Healing and clogging of Bure claystone

Chuanrui Wang

CENTRALE LILLE

THESE

Présentée en vue
D'obtenir le grade de

DOCTEUR

En

Spécialité: Mécanique des solides, des matériaux, des structures et des surfaces

Par

Chuanrui WANG

DOCTORAT DELIVRE PAR CENTRALE LILLE

Titre de la thèse

Cicatrisation et colmatage de l'argilite de Bure

Soutenue le 14 décembre 2021 devant le jury d'examen

Président	Jianfu-SHAO, Professeur, Université de Lille
Rapporteur	Albert GIRAUD, Professeur, Université de Lorraine
Rapporteur	Siavash GHABEZLOO, HDR, Ecole des Ponts ParisTech
Examinateur	Séverine Levasseur, Ingénieur/Docteur, ONDRAF/NIRAS
Directeur de thèse	Catherine DAVY, Professeur, Centrale Lille
Co-Directeur de thèse	Frédéric SKOCZYLAS, Professeur, Centrale Lille
Invité	Jean TALANDIER, Ingénieur/Docteur, ANDRA

Thèse préparée dans le Laboratoire de Unité de catalyse et de chimie du solide (UCCS)

Ecole Doctorale SMRE 104

Acknowledgement

I would like first to express my deepest thanks to my thesis supervisor, Prof. Frédéric SKOCZYLAS. During the past three years, I have learned a lot from you. It was a great honor to work with you and I have gained a lot of knowledge.

I also thank Andra for the supply of samples. Special thanks are given to Dr. Jean TALANDIER for the friendly discussion and precious advice. I would like to thank Prof. Albert GIRAUD and HDR Siavash GHABEZLOO for being rapporteurs for this dissertation. I really appreciated the reviews and advice from other members of the jury, Dr. Séverine LEVASSEUR, Prof. Jianfu SHAO.

I would like to thank all the members of our laboratory: Franck AGOSTINI, Thierry DUBOIS, Marie-Claude WILLEMETZ, Ludovic POTIER, Nicolas GAY, Laurent LECONTE for their many help. I also thank Zhibo DUAN, Dongmei ZHANG, Takoua LAMOUCHI, Sandy LANIER and Baptiste MARCHAND for working together during my thesis.

The final thanks I would like to give to my parents, thank you for your selfless dedication and for helping me to develop the right values and outlook on life. In the future, I will do my best to be an honorable and optimistic person.

Résumé

Depuis le XXe siècle, l'utilisation de l'énergie nucléaire est plus important pour les activités humaines. Par exemple, selon l'Agence internationale de l'énergie atomique (AIEA), l'énergie nucléaire représente 70,6 % de l'électricité totale en France en 2019 (AIEA 2020). Tout en profitant les avantages de l'énergie nucléaire, la question qui se pose est de savoir comment éliminer les déchets radioactifs en toute sécurité. Pendant des décennies, les pays industrialisés ont mené des recherches approfondies sur le stockage géologique des déchets radioactifs *moyenne activité and haute activité* (MA & HA). En France, l'argile du bassin de Bure (formation du Callovo-Oxfordien (COx)) est considérée comme la roche hôte. Ce matériau présente une importante capacité de la cicatrisation lors de la resaturation. Bien que des recherches approfondies aient été consacrées d'étanchéité de l'argile du COx, un certain nombre de questions liées à ces phénomènes physico-chimiques ne sont toujours pas complètement résolues.

Cette thèse se concentre sur la cicatrisation de l'argile du COx. Six carottes d'argile COx provenant de différentes profondeurs (du laboratoire de recherche souterrain de Meuse/Haute Marne) ont été testées avec différentes expériences, y compris la diffraction quantitative des rayons X (XRD), l'analyse de la capacité d'échange cationique (CEC), le test d'adsorption d'azote, le test de gonflement et poro-mécanique, et le test d'auto-étanchéité. Cette recherche a été menée sous trois angles différents, à savoir les mécanismes de gonflement multi-échelle, la mesure des propriétés poro-mécaniques avec de l'eau, et l'évaluation du gonflement et des propriétés de transport du matériau guéri.

Mécanismes de gonflement multi-échelle

Cette étude des mécanismes de gonflement multi-échelle de l'argile COx a été réalisée par une série de tests gonflement, complétés par des mesures quantitatives de XRD, de capacité d'échange cationique (CEC) et d'adsorption d'azote. Le matériau testé provient de cinq sites géologiques différents, fournis par l'Andra. Les analyses de XRD, de CEC et de sorption d'azote ont été réalisées sur des échantillons de poudre, tandis que les tests de gonflement ont été effectués sur des échantillons cylindriques. Les échantillons cylindriques ont été recalibrés à partir de différents cellule T1 et prééquilibrés à 75% d'humidité relative pour éliminer l'effet de la saturation. Les effets des teneurs en minéraux argileux et des états d'endommagement (c'est-à-dire la fissuration) sur le comportement de gonflement (amplitude et cinétique) ont été étudiés. Pendant l'essai de gonflement, l'échantillon a d'abord été placé dans une cellule triaxiale à une pression de confinement constante de 14 MPa. Lorsque la masse de l'échantillon a été stabilisée, de l'eau synthétique a été injectée par les deux extrémités de l'échantillon à une pression constante de 5 MPa. Les données expérimentales obtenues

sont l'évolution de la déformation d'expansion de l'échantillon en fonction du temps. L'amplitude de gonflement et la cinétique de gonflement sont évaluées en comparant les échantillons entre eux.

L'analyse de la composition minéralogique montre que la smectite est le seul minéral gonflant dans le COx, et qu'elle est intercalée dans deux types d'agrégats I/S dans le COx, à savoir R1-I/S (contient 30% de smectite) et R0-I/S (contient 78% de smectite). Les données de sorption de l'azote révèlent que le gonflement du COx n'est pas seulement déterminé par la teneur en smectite mais correspond également au volume des pores et à la surface accessibles à l'eau. Cette conclusion est valable de l'échelle nanométrique à l'échelle du mètre.

Des déformations anisotropes ont été mesurées pendant l'essai de gonflement. En particulier, la déformation de gonflement parallèle aux plans de litage ($\varepsilon_{//}^{S}$) est utilisée pour être liée aux minéraux liés à la smectite. Du point de vue de l'amplitude de gonflement, le résultat révèle que $\varepsilon_{//}^{S}$ a la corrélation la plus élevée avec R1-I/S, alors qu'il a la corrélation la plus faible avec R0-I/S. Cela illustre que l'effet de la distribution de la smectite sur le gonflement du matériau est toujours valable à l'échelle centimétrique. Par conséquent, un modèle conceptuel est proposé pour donner un aperçu du mécanisme de gonflement multi-échelle de ce matériau. Quant à la cinétique de gonflement, aucune corrélation n'a été trouvée entre le temps d'expansion et la composition minérale ou les propriétés des pores, ce qui indique que la cinétique correspond à un processus de couplage plus complexe.

En outre, l'effet des microfissures sur le gonflement a été étudié en comparant le gonflement d'échantillons intacts et microfissurés. Les résultats impliquent que les microfissures entraînent une plus grande amplitude de gonflement du matériau et une cinétique de gonflement initiale plus élevée. Et les microfissures induites par la compression sont plus susceptibles d'être parallèles aux plans de litage, ce qui entraîne une expansion plus prononcée dans cette direction.

Mesurer des propriétés poro-mécaniques avec l'eau synthétique

Lorsque l'essai de gonflement susmentionné est terminé, les échantillons sont complètement saturés. Un test poro-mécanique a été effectué sur le matériau saturé. L'objectif principal de ce travail est de mesurer le coefficient de Biot en utilisant de l'eau synthétique (proche de l'eau in-situ) pour contrôler la pression de pore. Dans le cadre de la poroélasticité, le coefficient de Biot est déterminé par les déformations mesurées pendant le chargement et le déchargement séquentiels de la pression de confinement (Pc) et de la pression de pore (Pi). Ce type d'essai prend beaucoup de temps en raison des longs temps de saturation pour obtenir l'uniformité de la pression. Plusieurs essais ont été réalisés

avec succès au cours des deux dernières années, parmi lesquels quatre essais représentatifs sont présentés dans cette étude.

Les résultats ont clairement démontré que, malgré une anisotropie significative du matériau, le tenseur de Biot est isotrope avec une composante unique "b". Ce résultat important, cohérent avec certains calculs théoriques, ne signifie pas que les déformations, dues au changement de pression de pore, sont isotropes. Un autre résultat important est que "b" a été trouvé très proche de 1. Cela signifie que, dans les conditions de laboratoire, l'argile COx se comporte comme un matériau de Terzaghi. Ce résultat crucial a été obtenu sur des échantillons d'argile saturés en eau, qui présentaient une certaine déstructuration après les essais. Il est néanmoins cohérent avec de nombreuses observations faites avec du gaz (hélium) comme étant le fluide permettant de contrôler la pression interstitielle, ce qui conduisait le plus souvent à un tenseur de Biot quasi isotrope avec "b" $\approx$ 1. Dans ce cas, les expériences avec le gaz ont été réalisées sur des matériaux partiellement saturés (de sec à presque saturé) donc sans la déstructuration observée avec l'eau.

Ce travail complète les résultats obtenus avec du gaz et met en évidence que cette argile saturée transversalement isotrope se comporte toujours comme un matériau de Terzaghi. Il contribue également à clarifier la valeur du coefficient de Biot qui doit être choisie dans les simulations numériques, en particulier celles qui sont cruciales pour lesquelles l'activité thermique des déchets est prise en compte.

Évaluation des propriétés de gonflement et de transport de la COx après la guérison

Une série d'essais d'auto-étanchéité à "faible confinement" a été conçue et réalisée pour étudier les propriétés de gonflement et de transport de l'argile COx rescellée. Grâce à cette expérience, le changement de la pression apparente de gonflement (P_{app}) et de la perméabilité à l'eau pendant la re-saturation et la pression de percée du gaz (GBP) après le scellement ont été mesurés. Ces données de mesure directe fourniraient des références importantes pour la reproduction numérique.

Les résultats montrent que Papp a augmenté avec le temps et que la valeur de l'échantillon UT est d'environ 1 MPa, alors qu'elle varie de 3 à 5 MPa pour les échantillons UA. En comparant les échantillons d'une même carotte, les échantillons macro-fissurés présentent une cinétique plus rapide que l'échantillon intact, tandis que l'échantillon intact présente un P_{app} légèrement plus élevé que les échantillons macro-fissurés. Cette différence est principalement attribuée à la présence de fissures qui augmentent la surface de contact entre l'eau et les minéraux argileux et génèrent plus d'espace pour le gonflement. La Papp présente également une meilleure linéarité avec R1-I/S qu'avec R0-I/S. Ce résultat est cohérent avec l'observation de la contrainte de gonflement en fonction des minéraux liés

à la smectite (chapitre 2). Du point de vue de la technologie des tests, la sorption d'azote est une approche plus simple et plus efficace que la XRD pour évaluer la capacité de gonflement du COx.

Pour les matériaux UT et UA, la présence de macro-fissures entraîne une augmentation significative de la perméabilité, jusqu'à 2 à 4 ordres de grandeur pour K_g et 5 à 6 ordres de grandeur pour K_w. L'auto-scellage du COx macro-fissuré peut provoquer des réductions significatives de la perméabilité à l'eau (Kw) de manière synchrone avec l'augmentation de Papp. La perméabilité à l'eau finale des échantillons UA est réduite de cinq ordres de grandeur et proche de celle de l'échantillon intact, tandis que la est réduite de quatre ordres de grandeur. Il convient de souligner que le K_w final de l'échantillon UT est supérieur d'environ deux ordres de grandeur à celui de l'échantillon intact. Ces résultats démontrent que, même en l'absence de confinement, le gonflement des minéraux argileux peut toujours conduire à la rescellation des macro-fissures de l'argile COx dans une certaine mesure. En outre, le COx UA présente une cinétique plus rapide que le COx UT, ce qui peut être attribué à l'impact de la teneur élevée en R1-I/S.

Après la guérison, les résultats des tests de percée de gaz illustrent que la valeur GBP du UT COx est d'environ 0-0.2 MPa, tandis que la valeur du UA COx est comprise entre 0.8 et 1.46 MPa. Cela confirme que le UA COx possède une meilleure efficacité d'étanchéité que le UT COx, même pour le transport de gaz, ce qui est cohérent avec l'observation de la diminution du K_w. Comparé à Papp et K_w, GBP est plus sensible à l'intégrité de l'échantillon. En utilisant la loi de Poiseuille, la valeur GBP de l'échantillon scellé est du même ordre de grandeur que la pression capillaire équivalente des fissures résiduelles, ce qui indique que la migration du gaz dans l'argile COx scellée se produirait principalement à travers la fissure scellée résiduelle et serait contrôlée par des phénomènes capillaires.

Table of Contents

General introduction

Industrial context

Since the 20th century, the use of nuclear energy has become increasingly important for human activities. For instance, according to the International Atomic Energy Agency (IAEA) nuclear energy accounts for 70.6% of total France electricity power generation in 2019 (IAEA 2020). While obtaining the benefits of nuclear energy, the ensuing issue is how to safely dispose of radioactive waste. Radioactive waste refers to the materials produced after nuclear reactions (nuclear fission), which generally remain radioactive and harmful to the environment. Different countries have their own classification methods for radioactive waste. In France, the classification is done with reference to the radioactivity and the half-life duration of nuclear species, which is shown below in Fig.1. Radioactive waste is divided into four categories: Very Low Activity (VLA or TFA for *Très Faible Activité* in French), Low Activity (LA or FA for *Faible Activité* in French), Medium Activity (MA also for *Moyenne Activité* in French), and High Activity (HA also for *Haute Activité* in French). Based on the radionuclide half-life period, it is also divided into 3 types: very short-lived (< 100 days, labeled VTC for *Vie Très Courte* in French), short-lived (≤ 31 years, labeled VC for *Vie Courte* in French), and Long-Lived (LL or VL for *Vie Longue* in French, ≥ 31 years and up to hundreds of thousand years).

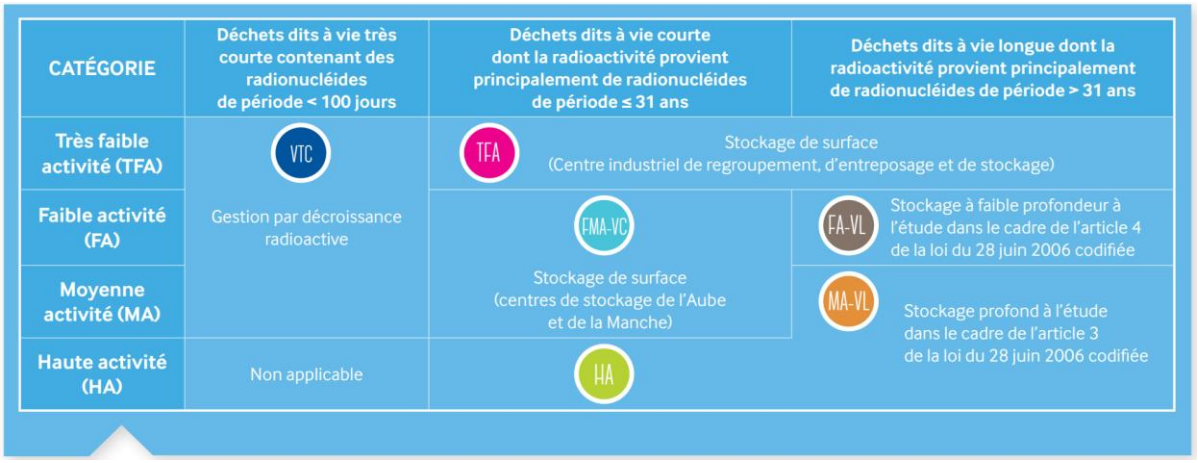

Figure 1: French classification of radioactive waste for their management (ANDRA, 2015)

For decades, industrialized countries have conducted extensive research on the management and storage of MA and HA-LL radioactive waste. Several management options have been proposed, e.g. deep underground repository (or disposal), waste burning under the seabed or under the Arctic ice sheet (Philberth 1977), or abandonment to space (Coopersmith, 1999). In order to fully account for a number of societal issues, including environmental protection (and in particular an effective isolation from the biosphere for a very long time), deep geological repository has been widely accepted as a privileged method for MA and HA-LL waste. This solution refers to waste storage in a geological

formation at a depth of several hundred meters below ground surface, either in clayey materials or in granitic bedrocks. Table 1 briefly summarizes the rock formation choices in several nuclear-industrial countries. Low permeability and availability at a large scale are the two main reasons for choosing suitable formations.

Table 1: Natural barrier options for the long term storage of radioactive waste for different industrial countries

Countries	Host Rock	Geological location
France	Callovo-Oxfordian claystone	420-550 m depth
Switzerland	Opalinus clay	Approx. 300 m depth with a thickness of 90 m
Belgium	Boom clay (plastic clay)	Approx. 230 m with a thickness of 100 m
Canada	Stanstead granitic rock	240-420 m depth
Sweden	Småland granites	200-460 m depth
China	Beishan granites	Approx. 560 m depth
Finland	Olkiluoto granitic rock	Approx. 345 m depth

Depending on the radioactivity of the waste, different storage solutions and different types of repositories are proposed. For instance, in France, the CIGEO project is operated by the French National Agency for Radioactive Waste Management (ANDRA for Agence Nationale de gestion des Déchets RAdioactifs) to explore plausible storage solutions for different categories of waste, see Figure 2. The HA waste are typically vitrified and placed in steel overpacks, while the MA waste (under the form of hulls and pieces) are directly sealed in overpacks. MA waste are then placed in concrete disposal containers after reception from waste producers. As shown in Figure 2, two different kinds of tunnels are excavated from the main gallery parallel to the claystone formation. One kind of tunnel is of several meters in diameter and supported by a concrete wall; such tunnels are used to store the MA waste concrete containers. After placing the containers inside the tunnels, the vacant space are filled by buffer material (based on bentonite) and sealing by bentonite/sand and concrete plugs. For the HA waste packages, they are stored in the other kind of tunnel, which is of only tens of centimeters in diameter and contains a layer of steel interior wall. The HA waste packages are stored head-to-tail in the tunnel, then sealed by clayey materials (bentonite for instance) and concrete plugs.

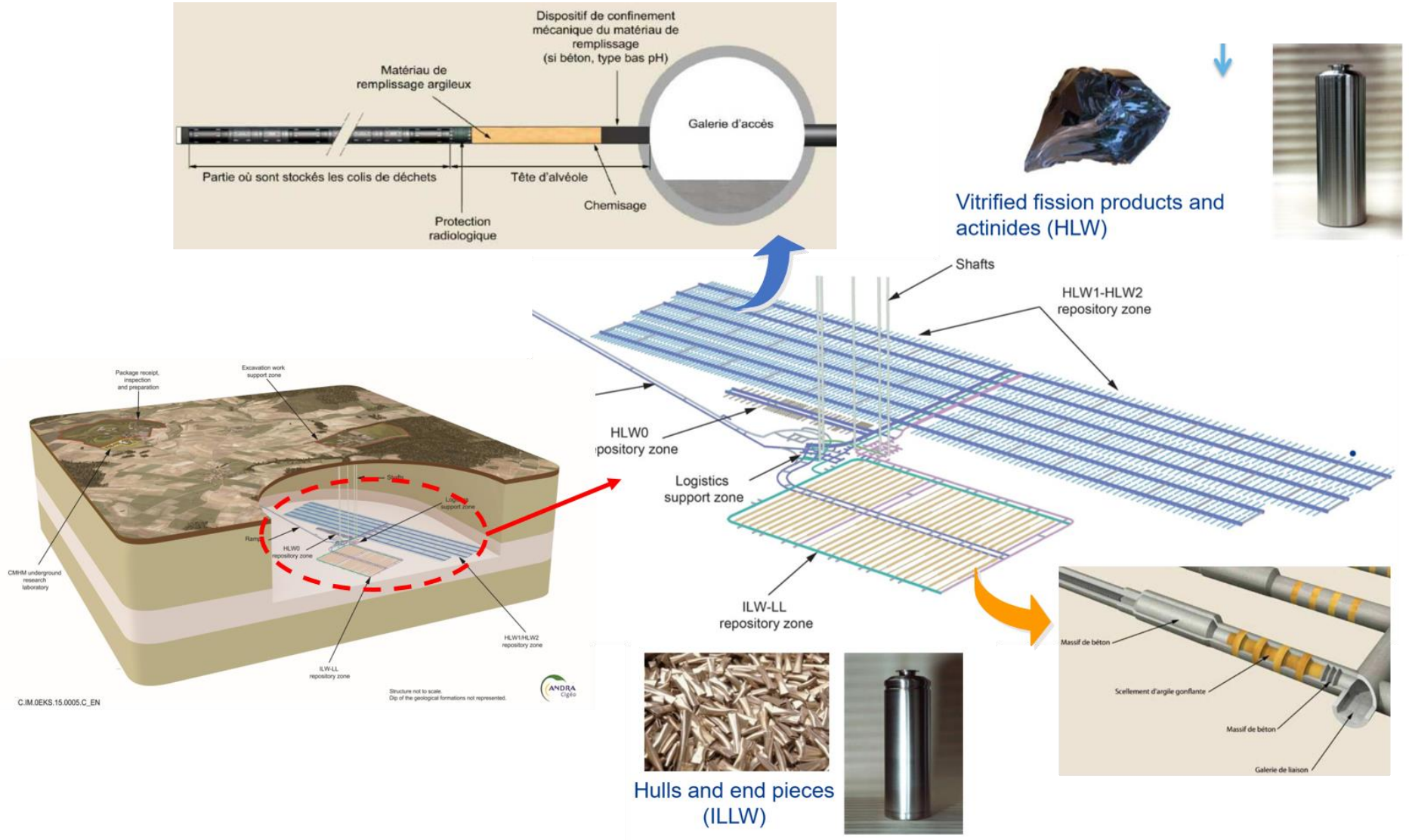

Figure 2: The CIGEO facility for HA and MA nuclear waste storage

In terms of geological location, the MA and HA radioactive waste would be stored in a claystone formation of Callovo-Oxfordian (COx) age. The CIGEO repository design for radioactive waste includes two anti-radiation protective barriers, which are the engineered barrier (composed of man-made structures, and mainly high performance concrete) and the natural barrier (i.e. the claystone itself). This claystone is chosen as the natural barrier thanks to its low permeability, excellent retention of radionuclides, favorable swelling characteristics, and self-sealing properties (Van Geet et al. 2008; Giot et al. 2019).

Preliminarily to any actual industrial storage, the feasibility of building a radioactive waste disposal facility within the COx is analyzed by ANDRA. To this purpose, an Underground Research Laboratory (URL) has been built, which is located in Bure, on the border of the Meuse and Haute-Marne districts of the eastern Paris Basin, France (Fig. 3). Since the start of the URL excavations in August 2000, two shafts have been drilled and provide access to drifts at different depth levels. Numerous COx cores have also been extracted from different depths, and are used for understanding the lithology, mineralogy and other properties of COx claystone. Overall, the URL is established for scientific purposes, which will provide useful knowledge for the future industrial CIGEO project (i.e. the actual repository).

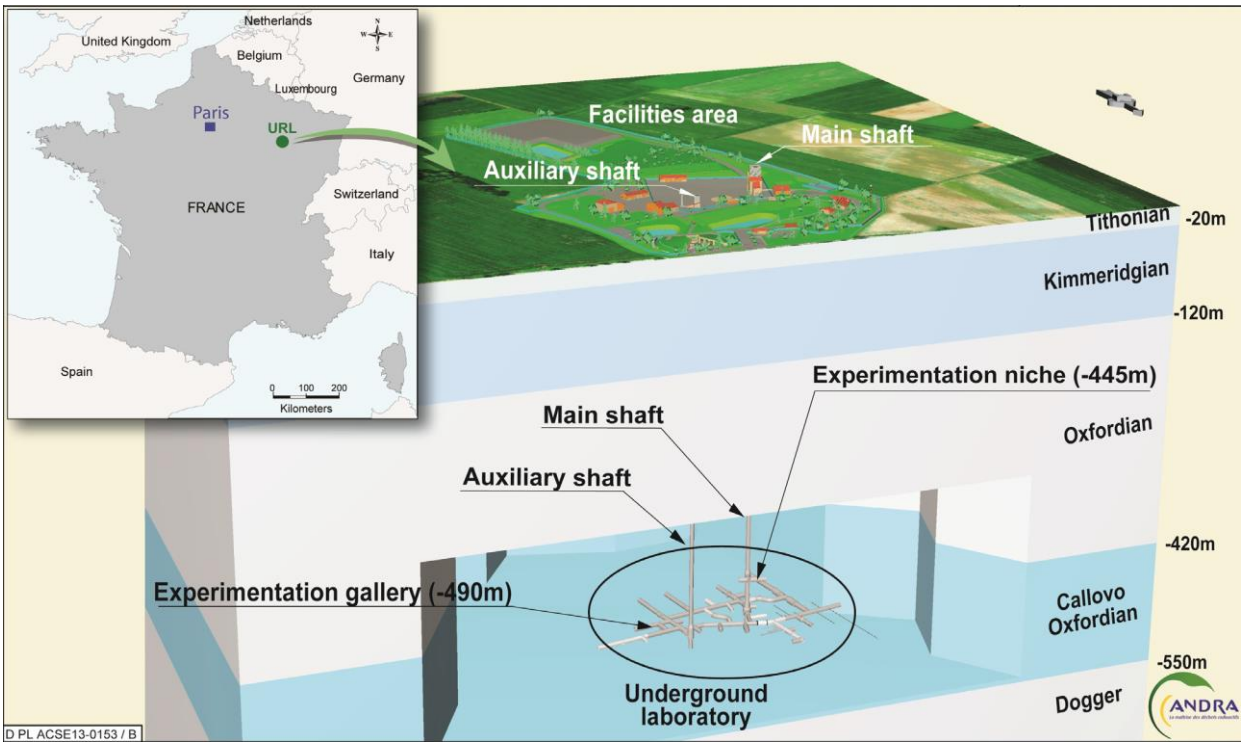

Figure 3: Meuse/Haute-Marne Underground Research Laboratory (in Bure locality): location and geology (de La Vaissière et al. 2015)

On the Bure site, the COx claystone layer was formed 152 - 158 million years ago and covers an area of approximately 200 km², the thickness of which is about 130 m and lies at a depth of 422–552 m (Yven et al. 2007). Figure 3 shows the vertical lithological and mineralogical evolution at around 365-560 m depth of the Bure basin. Based on its mineralogy content, the COx formation corresponds to strata sequences C3 and C2, and it can be further subdivided into three lithophysical units, with, in order from shallow to deep, the silty-carbonated unit (USC), the transition unit (UT), and the clay unit (UA), respectively.

The geological distribution of these different units shown in Figure 4. More precisely, the USC is located at depths around 420m and 440m; it generally has the highest carbonate and tectosilicate contents. Beneath the USC is the UT located at about 440m-460m depth in Figure 4; it has a contrasted mineralogy (Conil et al. 2018). The clay unit (UA) is located at the base of the COx formation, at depths ranging approximately from 460m to 550m; it covers two-thirds of the total COx formation thickness. Compared to the USC and the UT, the UA has the biggest proportion of clay minerals and comprises clay minerals, carbonates and tectosilicates contents of around 45-50%, 27%, and 24%, respectively (Giot et al. 2019).

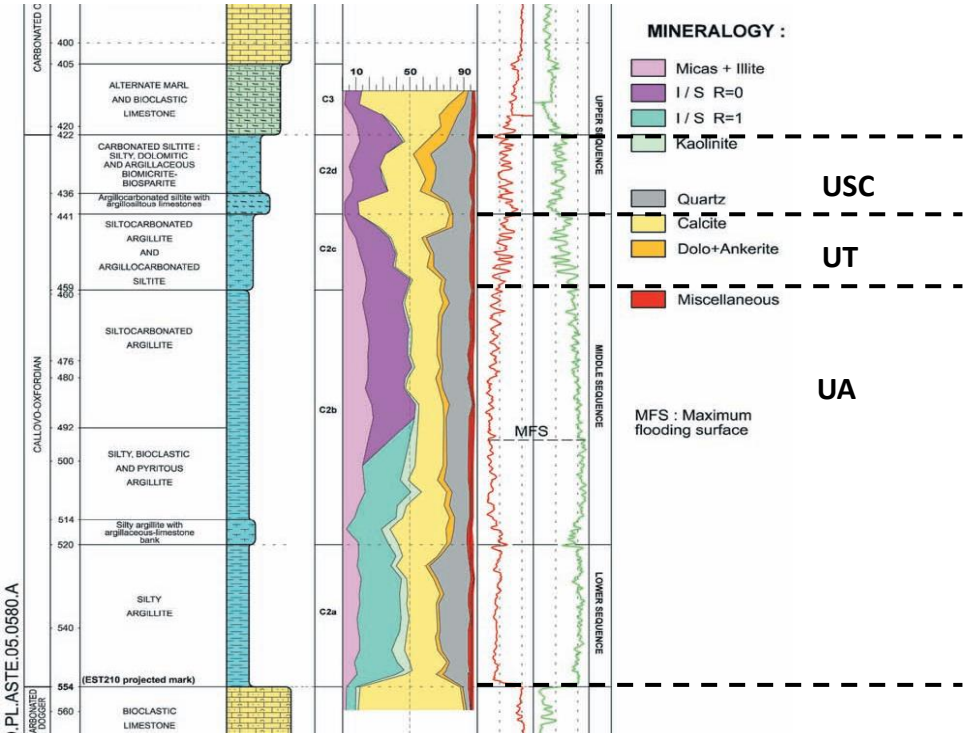

Figure 4: Lithology and mineralogy of the entire COx claystone (Yven et al. 2007)

These analyses show that the COx claystone becomes more clayey with the increase in geological depth. The carbonate content decreases with increasing clay content. A general mineralogical

composition table of the entire claystone formation is shown in Table 2, where SD is the standard deviation.

Table 2: Average mineralogical composition of the three different lithophysical units of the COx claystone (Conil et al. 2018)

COx	Phyllosilicates		Carbonates		Tectosilicates	
	Average (%)	SD (%)	Average (%)	SD (%)	Average (%)	SD (%)
UA	46	7	27	8	24	6
UT	43	8	26	8	28	8
USC	26	11	42	18	30	10
Total	42	11	30	12	25	8

Self-sealing of COx claystone

During excavation and building of the repository tunnels, an Excavation Damaged Zone (EDZ) is formed in the COx formation (Zhang 2011). The cracks in EDZ could be generated during the excavation and ventilation of underground tunnels. Moreover, the thermal dissipation of radioactive waste during long-term storage may also lead to cracking. After the repository closure, the EDZ will be subjected to re-saturation due to underground water seepage. Thanks to the self-sealing capacity, cracks in EDZ could be partially closed. The self-sealing process is a well-known phenomenon, which have been widely studied during the past 20 years (Blümling et al. 2001; Horseman 2001; Bastiaens et al. 2007; Davy et al. 2007; Van Geet et al. 2008; Zhang 2011; Giot et al. 2019; Bossart et al. 2019, etc). In presence of underground water and confining pressure, the permeability of damaged COx claystones can be reduced by several orders of magnitude and to levels approaching the permeability of undisturbed material (Figure 5).

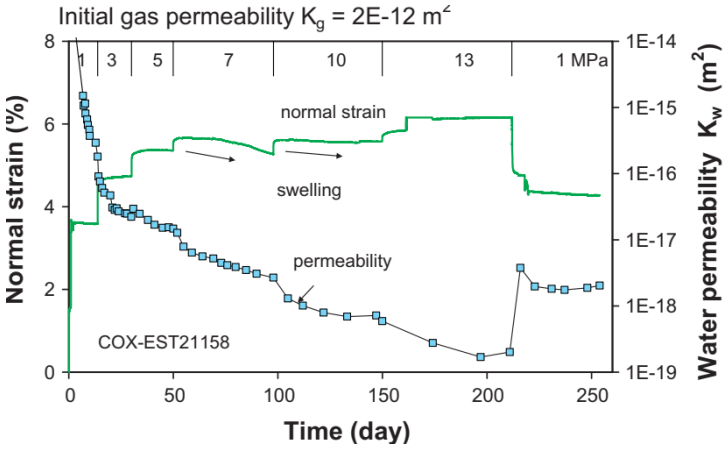

Figure 5: Evolution of normal strain and permeability parallel to fractures during water flowing under different confining stresses (Zhang 2011).

Compared with granitic rocks, clayey materials have a unique ability to self-seal, which can effectively improve the safety of the repository. Scientists have identified several factors affecting the extent of self-sealing of COx claystone. Such as the effect of confining pressure (e.g. Davy et al. 2007; Zhang and Rothfuchs 2008), the swelling of specific clay minerals (smectite) (e.g. Heidug and Wong 1996; Saiyouri et al. 2000), and the dynamic rearrangement of clay and non-clay particles in the micro-cracks (e.g. Marschall et al. 2005; Desbois et al. 2009, 2017). A detailed literature review on the self-healing of clayey rock will be presented in Chapter 1.

Aims and methodology of the research

Despite extensive research has been focused on the self-sealing of COx claystone, there is still a number of questions related to these physical-chemical phenomena still not completely solved. For instance, it has long been proven that clay (i.e. smectite) swelling has significant impact on the self-sealing. However, since smectite does not exist as a single phase in COx, its content and distribution are highly anisotropic. There is still no quantitative evaluation of the contribution of clay swelling to self-sealing. Another interesting scientific question is that, the claystone exhibits greater swelling potential at high relative humidity (>98% RH) rather than at the moderate and low relative humidity (Saiyouri et al. 2000; Valès 2008; Wang et al. 2015). There is still no reasonable explanation for the underlying mechanisms. After the repository closure, underground water will infiltrate from the undisturbed zone to the unsaturated zone around the galleries, resulting in the pore pressure redistribution. Whether the hydro-mechanical coupling will affects the poro-mechanical behavior of the material remains unclear.

To sum up, the objectives of this thesis are to provide answers to these questions, by a series of laboratory tests carried out on different COx claystone cores. The experimental program is divided into three main parts, as follows.

Part 1: Mineralogical and microstructural analysis

This part of work focuses on: 1) mineralogical analysis of samples from all the cores tested during the thesis, in order to quantitatively determine the proportions of the principal phases (clay minerals, carbonate or silicate or other minerals, such as pyrite). This work is an extension of (Song et al. 2016). 2) using the SEM imaging techniques to observe the microstructure of cracks, i.e. the spatial rearrangement of the clay and non-clay mineral fragments under the condition of without damage (refer to intact), after micro- and macro-cracked, and after self-sealing. The results obtained from this part of the work will be applied to the subsequent analysis of the swelling tests and self-sealing tests.

Part 2: Swelling of intact and micro-cracked COx claystone

The swelling experiments are carried out on the COx claystone samples from four different geological locations at Bure URL. The tested samples are cylindrical cores with diameter 20mm and height 40mm, all samples are from the UA type (relative high clay mineral content and swelling potential). The swelling tests are carried out in the original designed triaxial cell in our laboratory, and for each test, the confinement is of 14 MPa while the water injection pressure is 5 MPa. The volumetric deformations of the COx claystone are measured by strain gauges (glued on the sample side surface) over time. In this part, the effects of injected fluid, mineralogical composition, damage state, and saturation state on the swelling capacity are investigated. For one micro-cracked sample, the X Ray micro-tomography technique, based on the ISIS4D platform (University of Lille), is used to record the visible cracks with the resolution of the device (5 to 20 microns) before and after sealing, and then analyze the possible cracks evolution of the sample.

Part 3: Poro-mechanical tests - Biot's coefficient measurement

After the swelling tests, the fully saturated sample are keep stay in the triaxial cell and under confinement, and we performed the poromechanics tests on several fully saturated samples (initially intact or micro-cracked) by using water as the pore pressure change fluid. The objective of this kind of test is to measure the Biot's coefficient of fully saturated COx claystone, and to compare with the former works carried out in our laboratory (Cariou et al. 2012; Yuan et al. 2017).

Part 4: Self-sealing of macro-cracked COx claystone – under low confinement

In this part, the macro-cracked COx claystone samples are initially cored as diameter/height = 37mm/40mm and then split by Brazilian splitting tests. The Brazilian splitting tests can provide artificial shear and tensile cracks, which are very close to the *in-situ* cracks around the tunnel. Two original experimental devices are designed and implemented to investigate: 1) the swelling pressure of macro-cracked COx claystone under low confinement and 2) the self-sealing efficiency of COx claystone under (or without) low confinement. These devices are inspired by that used on the swelling pressure measurement of bentonite-sand mixtures (Liu et al. 2014). All sample types tested in part2 are also tested in this part.

The self-sealing tests are carried out with a device especially designed for this work. During the test, the initial gas permeability is first measured before water injection, the apparent swelling pressure (see further) and the water permeability are recorded over time. The gas breakthrough pressure is determined once the self-sealing is achieved.

References

Anderson RL, Ratcliffe I, Greenwell HC, et al (2010) Clay swelling — A challenge in the oilfield. Earth-Science Reviews 98:201–216.

ANDRA (2015) Inventaire national des matieres et dechets radioactifs.

ANDRA (2005) Dossier 2005 Argile. Collection les Rapports.

Armand G, Conil N, Talandier J, Seyedi DM (2017) Fundamental aspects of the hydromechanical behaviour of Callovo-Oxfordian claystone: From experimental studies to model calibration and validation. Computers and Geotechnics 85:277–286.

Auvray C, Morlot C (2015) X-RAY TOMOGRAPHY APPLIED TO SELF-HEALING EXPERIMENTS ON ARGILLITES. 3rd International Conference on Tomography of Materials and Structures, Lund, Sweden, 26-30 June 2017, ICTMS2017-144

Bernier F, Li XL, Bastiaens W, et al (2007) Fractures and Self-sealing within the Excavation DIsturbed Zone in Clays (SELFRAC). Report.

Bossart P, Nussbaum C, Schuster K (2019) Generation and Self-Sealing of the Excavation-Damaged Zone (EDZ) Around a Subsurface Excavation in a Claystone. In: Dewers T, Heath J, Sánchez M (eds) Geophysical Monograph Series, 1st edn. Wiley, pp 125–143

Cariou S, Duan Z, Davy C, et al (2012) Poromechanics of partially saturated COx argillite. Applied Clay Science 56:36–47

Conil N, Talandier J, Djizanne H, et al (2018) How rock samples can be representative of in situ condition: A case study of Callovo-Oxfordian claystones. Journal of Rock Mechanics and Geotechnical Engineering 10:613–623. https://doi.org/10.1016/j.jrmge.2018.02.004

Coopersmith J Disposal of IDGH-Level Nuclear Waste in Space. Space Studies Institute (SSI) 111–115.

Davy CA, Skoczylas F, Barnichon J-D, Lebon P (2007) Permeability of macro-cracked argillite under confinement: Gas and water testing. Physics and Chemistry of the Earth, Parts A/B/C 32:667–680.

de La Vaissière R, Armand G, Talandier J (2015) Gas and water flow in an excavation-induced fracture network around an underground drift: A case study for a radioactive waste repository in clay rock. Journal of Hydrology 521:141–156.

Desbois G, Höhne N, Urai JL, et al (2017a) Deformation in cemented mudrock (Callovo–Oxfordian Clay) by microcracking, granular flow and phyllosilicate plasticity: insights from triaxial deformation, broad ion beam polishing and scanning electron microscopy. Solid Earth 8:291–305.

Desbois G, Höhne N, Urai JL, et al (2017b) Deformation in cemented mudrock (Callovo–Oxfordian Clay) by microcracking, granular flow and phyllosilicate plasticity: insights from triaxial deformation, broad ion beam polishing and scanning electron microscopy. Solid Earth 8:291–305.

Desbois G, Urai JL, Kukla PA (2009) Morphology of the pore space in claystones – evidence from BIB/FIB ion beam sectioning and cryo-SEM observations. eEarth Discuss 4:1–19.

Dormieux L, Lemarchand E, Coussy O (2003) Macroscopic and Micromechanical Approaches to the Modelling of the Osmotic Swelling in Clays. Transport in Porous Media 50:75–91

Giot R, Auvray C, Talandier J (2019) Self-sealing of claystone under X-ray nanotomography. Geological Society, London, Special Publications 482:213–223.

Gratier JP, Jenatton L, Tisserand D, Guiguet R (2004) Indenter studies of the swelling, creep and pressure solution of Bure argillite. Applied Clay Science 26:459–472.

Heidug, Wong (1996) Hydration swelling of water-absorbing rocks: a constitutive model. International Journal for Numerical and Analytical Methods in Geomechanics 20:403–430

Hemes S, Desbois G, Urai JL, et al (2012) Variability of the morphology of the pore space in Boom Clay from BIB- SEM, FIB and MIP investigations on representative samples. RWTH Aachen University, Aachen.

Klaver J, Desbois G, Littke R, Urai JL (2015) BIB-SEM characterization of pore space morphology and distribution in postmature to overmature samples from the Haynesville and Bossier Shales. Marine and Petroleum Geology 59:451–466.

Lenoir N, Bornert M, Desrues J, et al (2007) Volumetric Digital Image Correlation Applied to X-ray Microtomography Images from Triaxial Compression Tests on Argillaceous Rock. Strain

Liu JF, Davy CA, Talandier J, Skoczylas F (2014) Effect of gas pressure on the sealing efficiency of compacted bentonite–sand plugs. Journal of Contaminant Hydrology 170:10–27.

Marschall P, Horseman S, Gimmi T (2005) Characterisation of Gas Transport Properties of the Opalinus Clay, a Potential Host Rock Formation for Radioactive Waste Disposal. Oil & Gas Science and Technology - Rev IFP 60:121–139.

Philberth K (1977) The Disposal of Radioactive Waste in Ice Sheets. J Glaciol 19:607–617.

Saiyouri N, Hicher PY, Tessier D (2000) Microstructural Approach and Transfer Water Modelling in Highly compacted Unsaturated Swelling Clays. Mechanics of Cohesive-frictional Materials 5:41–60.

Song Y Water retention and fine microstructure of Bure argillite. PhD thesis, Ecole Centrale de Lille, 2014.

Song Y, Davy CA, Bertier P, Troadec D (2016) Understanding fluid transport through claystones from their 3D nanoscopic pore network. Microporous and Mesoporous Materials 228:64–85.

Song Y, Davy CA, Troadec D, et al (2015) Multi-scale pore structure of COx claystone: Towards the prediction of fluid transport. Marine and Petroleum Geology 65:63–82.

Valès F (2008) Modes de déformation et d'endommagement de roches argileuses profondes sous sollicitations hydro-mécaniques. PhD thesis, Ecole Polytechnique.

Van Geet M, Bastiaens W, Ortiz L (2008) Self-sealing capacity of argillaceous rocks: Review of laboratory results obtained from the SELFRAC project. Physics and Chemistry of the Earth, Parts A/B/C 33:S396–S406.

Wang LL, Bornert M, Yang DS, et al (2015) Microstructural insight into the nonlinear swelling of argillaceous rocks. Engineering Geology 193:435–444.

Wang LL, Yang RW, Chanchole S, Zhang GQ (2017) The time-dependent swelling of argillaceous rock under resaturated conditions. Applied Clay Science 146:186–194.

Yuan H, Agostini F, Duan Z, et al (2017) Measurement of Biot's coefficient for COx argillite using gas pressure technique. International Journal of Rock Mechanics and Mining Sciences 92:72–80.

Yven B, Garcia MG, Chabiron AC (2015) Geometry and Rock Properties Modelling of the Callovo-Oxfordian Claystone from a 3D High Resolution Seismic Cube. Almeria, Spain.

Yven B, Sammartino S, Geraud Y, et al (2007) Mineralogy, texture and porosity of Callovo-Oxfordian argillites of the Meuse/Haute-Marne region (eastern Paris Basin). Mémoires: Société Géologique de France 178, 73–90.

Zhang C-L (2011) Experimental evidence for self-sealing of fractures in claystone. Physics and Chemistry of the Earth, Parts A/B/C 36:1972–1980.

Zhang C-L, Rothfuchs T (2008) Damage and sealing of clay rocks detected by measurements of gas permeability. Physics and Chemistry of the Earth, Parts A/B/C 33:S363–S373.

1. Chapter 1 - State of the art : Callovo-Oxfordian claystone – microstructure, dimensional stability, transport and self-sealing

1.1.Microstructure of the COx claystone

Callovo-Oxfordian (COx) claystone consists of solid components (clay minerals and non-clay minerals) and complex porous networks. Understanding the structure of COx claystone is vital for the nuclear waste geological storage. Figure 1.1 gives a sketch of the COx claystone structures from the centimeter scale to the nanometer scale. Under an atmosphere environment, the sporadically visible impurities and cracks can be observed on a centimetric sample. On the μm-scale, Figure 1.1 middle, COx claystone is composed of individual non-clay minerals and clay matrix, massive amounts of pores and micro-cracks take place in the inter-particle space. When focusing on the nanoscale, the clay mineral particle, e.g. smectite particle in Figure 1.1 left, is composed of stacked layers with a certain space between two neighbor layers (Wang et al. 2015). It should be emphasized that these observation was made under ambient conditions of approx. 300 K and 1 bar, while the underground condition is more complex and far less information is available.

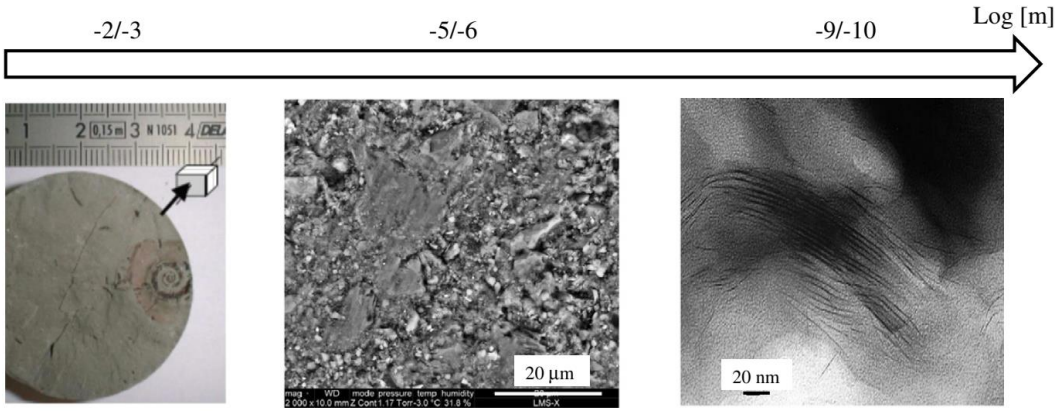

Figure 1.1. Multiscale structures of COx claystone (Wang et al. 2015)

Many researchers have conducted extensive studies on the microstructure (both the solid structure and the pore structure) of COx claystone. In this chapter, we will discuss the research methodology and the reported research findings in detail.

1.1.1. Solid Structure

The mineral compositions and distributions have a strong influence on the rock petro-physical properties. As many sedimentary rocks, COx claystone exhibits strong transverse isotropy due to its

layered structure. From the perspective of mineralogy, COx claystone includes two main components: clay minerals and non-clay minerals. The clay minerals refer to the aluminum phyllosilicates that were formed by the weathering and decomposition of igneous rocks. In general, the COx claystone is composed of clay minerals and non-clay minerals. Since the material transport and mechanical properties are highly related to the minerals (particularly the clays), it is important to have comprehensive understanding of the mineralogical compositions and distributions in COx claystone.

For COx claystone, the bulk mineralogical composition and clay composition can be analyzed by quantitative X-Ray Diffraction (XRD), while the chemical activity of clay minerals can be further quantified by Cation Exchange Capacity (CEC) test. Both the Quantitative XRD and CEC analysis are indirect methods since they do not give a visual observation of each mineral.

1.1.2. Quantitative XRD

Based on the Rietveld method, the overall mineralogical composition can be quantified by quantitative XRD (Rietveld 1969; Bish 1993; Zhou et al. 2018). Generally, using the Rietveld method to quantify the non-clay minerals is of high accuracy, with a deviation below 1%. However, it is difficult to assess the accuracy of clay composition due to the lack of standards. The bias of clay minerals quantification is mainly associated with the preferred orientation effects and the mistaken of quantifying illite as smectite as they have very similar structures (Seemann et al. 2017; Zhou et al. 2018). Yven et al. (2007) have reported the XRD results of a bunch of COx claystone samples. It is reported that the non-clay minerals in COx claystone include carbonates (calcite, dolomite, aragonite, ankerite, and siderite, etc.), tectosilicates (quartz, feldspars, and plagioclase), and the clay minerals (illite and muscovite, interstratified illite/smectite, kaolinite, and chlorite). Besides, small quantities of pyrite, oxides (anatase, rutile, and magnetite), and organic matter are presented in COx claystone as well (Andra 2005; Yven et al. 2007; Song et al. 2017). From the viewpoint of geological location, the mass proportions of each mineral vary from the different geological sequences of the COx formation. Particularly, the content (by weight) of phyllosilicates in the COx formation increasing with depth and varies from 20-60%. The content of carbonates decreasing with depth and varies from 15-80%. The distribution of tectosilicates is irregular, significantly variable and constitutes approximately 10 to 40% of the claystone. One plausible impact factor of these variations is the sea level at the time of the deposit. By recording the maximum flooding surface, the mineral analysis exhibits that higher sea level corresponds to greater clay content and lower carbonate content. The portions of pyrite, oxides and organic matter are less than 5% in total and show no tendency with the depth for the whole COx formation (Yven et al. 2015; Conil et al. 2018; Giot et al. 2019).

We illustrate in the general Introduction that the COx formation can be divided into three units from shallow to deep: the silty-carbonated unit (USC), the transition unit (UT), and the clay-rich unit (UA), where UA has the highest clay fraction. Table 1.1 and table 1.2 show the representative mineralogy characterization of this unit, extract from Song et al. (2016, 2017). Quantitative XRD and Cationic Exchange Capacity (CEC) analysis were carried out on seven samples from different cores (all from the UA unit, coming from different geological depths within a range between 476m and 507m). The quantitative XRD results of two UA samples (EST27405 and EST26095) only include the general clay minerals content, the tectosilicate content, and the carbonate content. The results of the rest five UA samples are more precise and give more detailed information, see Table 1.2. The present results illustrate that the clay minerals (illite, interstratified illite/smectite, kaolinite, and chlorite), calcite and quartz are the primary minerals whereas dolomite, ankerite, siderite, feldspar and pyrite make up together the secondary mineral phases. Besides, the total organic matter (not present in Table 1.1 and Table 1.2) also existed and forming less than 1% of the total.

Table 1.1. General mineralogy results of seven UA type samples by quantitative XRD (Song et al. 2016a)

Sample	EST42139, EST44140, EST44277, EST48401, EST48398	EST27405	EST26095
Coring depth (m) measured from the tunnel roof	490.98; 499.49 476.18; 489.7 489.73	481.08	507
Total clay content (wt%)	36.8–51.9	50 ± 10	37 ± 7.4%
Comprising illite + I/S + mica (wt%)	31.5–46.8	N/A	N/A
kaolinite (wt%)	2.2–5.2	N/A	N/A
chlorite (wt%)	0.6–1.7	N/A	N/A
Tecto-silicate content (wt%)	22.9–29.9	23 ± 4.6	19 ± 4%
Carbonate content (wt%)	19.9–38.8 (calcite, dolomite ankerite, siderite)	23 ± 4.6	44 ± 9% (calcite and dolomite)
Pyrite (wt%)	0.9–1.5	N/A	N/A
Anatase (wt%)	0.0	N/A	N/A
CEC (meq/100 g)	9.1–13.8	N/A	4–12
Porosity (%)	12.2; 14.6 12.5; 17.8; 16.6	–	15.8
BET SSA (m^2/g) Gurvich total PV (cm^3/g)	30.4–41.1 0.044–0.062	N/A N/A	N/A N/A

Table 1.2. Detailed mineralogy results of five UA type samples by quantitative XRD (Song et al. 2017)

Sample	EST42139	EST44140	EST44277	EST48401	EST48398
Borehole	POS1601	OHZ1608	OHZ1606	TPV1301	TPV1301
/orientation	/Horizontal	/Horizontal	/Horizontal	/Horizontal	/Horizontal
Nb. of samples For porosity Assessment	3	7	3	10	8
Quartz (wt%)	18.5	15.4	21.2	21.2	18.6
K-feldspar (wt%)	7.0	7.1	6.8	7.9	7.9
Albite (wt%)	0.7	0.4	1.9	0.5	0.4
Calcite (wt%)	30.8	33.3	24.4	17.9	17.1
Ankerite (wt%)	3.7	3.6	1.4	1.2	1.2
Dolomite (wt%)	1.1	1.4	1.4	1.3	1.5
Siderite (wt%)	0.4	0.5	0.1	0.1	0.2
Pyrite (wt%)	0.9	0.9	0.9	1.5	1.2
Total clay content (wt%)	36.8	37.4	41.7	51.7	51.9
Illite + Muscovite +I/S (wt%)	33.6	31.5	38.8	46.1	46.8
Kaolinite (wt%)	2.6	5.2	2.2	4.2	3.3
Chlorite (wt%)	0.6	0.7	0.7	1.4	1.7
CEC (meq/kg)	101	91	118	138	136
BET SSA (m^2/g)	31.1	30.4	31.3	41.1	35.9
t-plot pore area (m^2/g)	5.6	3.4	6.5	6.9	6.1
Gurvich total PV (cc/g)	0.045	0.051	0.044	0.062	0.057

1.1.3. Cation Exchange Capacity (CEC)

Cation exchange capacity (CEC), which is an inherent characteristic of clayey material, refers to the ability of a material to hold exchangeable cations in a saline aqueous solution. The common exchangeable cations on the outer surfaces of clay platelets are Ca^{2+}, K^{+}, and Na^{+}, etc (Anderson et al. 2010). The value of CEC is quantified in milligram equivalents (meq) of exchangeable cations per 100 grams of dry sample, and in many cases, for easy calculation, CEC is also expressed in millimoles of exchangeable cations per grams (mmol/g) of dry sample. For the COx claystone, CEC is not only determined by the proportions of clay minerals and organic matter but also by the type of clay mineral and the maturity of organic matter (Seemann et al. 2017). Empirically, the exchange capacity of 2:1 type clay minerals is higher than 1:1 type clay minerals. For instance, the CEC of smectite (2:1 type) is approximately 80 - 120 meq/100g while it is around 1 – 10 meq/100g for kaolinite (1:1 type). For organic matter, the exchange capacity varies from 100 to 300 meq/100g (Meier and Kahr 1999; Al-Ani and Sarapää 2008; Bergaya et al. 2013). In COx claystone, since the organic content is negligible, CEC is considered to be only determined by clay minerals.

The workflows of a CEC test are demonstrated in Figure 1.2. For a sample X-clay, it is firstly titrated by adding solution with index cation A (T1) (repeat several cycles). After the titration, the value of CEC is derived by performing steps E1, E2, and E3. In certain cases, it is necessary to perform another titration (T2) to replace the cations A by the index cations B, and subsequently applying steps E4, E5, and E6. Detailed operation procedures and precautions can be found in (Bergaya et al. 2013; Stanjek and Künkel 2016).

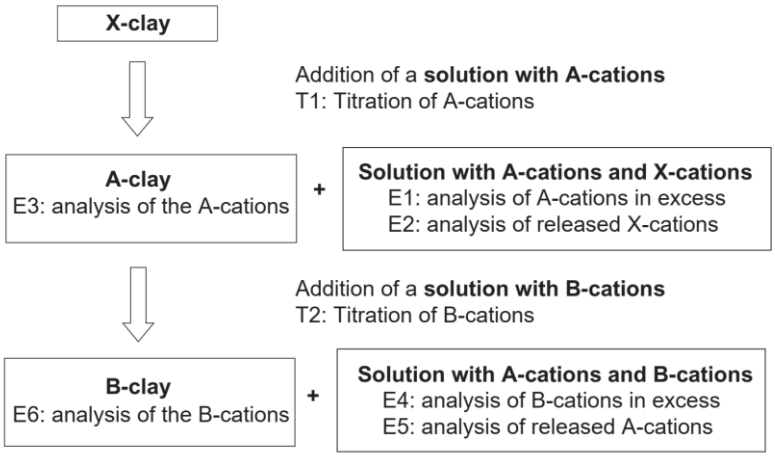

Figure 1.2. workflows of CEC determination (Bergaya et al. 2013)

Numerous exchange cations have been used to determine the CEC of bulk materials, such as Cu-ethylenediamine, methylene blue, protons, ammonium acetate, alkali or alkaline-Earth cations, organic cations, etc. (Bergaya et al. 2013). Nowadays, the most common index cation for clayey rock is Cu^{2+}-Trien as it has sufficient affinity for complete exchange with clay minerals. The reproducibility and accuracy by using Cu^{2+}-Trien have been exhaustively analyzed can be found in the literature (Stanjek and Künkel 2016).

Song et al. (2017) measured the CEC of five UA-type COx claystone samples, the measured CEC values are shown in Table. 2. CEC is ranging between 91 and 138 meq/kg (i.e., 9.1 -13.8 meq/100g), which is much lower than the purified 2:1 clay and slightly higher than the purified 1:1 clay. It exhibits a general trend that the CEC value increases with the total clay content, but EST44140 is an exception.

Further research has proven that the CEC of claystone is more related to the swelling clay mineral content. Przelaskowska et al. (2015) investigated the CEC of various claystone with different interstratified illite/smectite (I/S) layers, and the CEC value increases with the total I/S contents which consist with Song et al. (2017). Moreover, CEC is highly interrelated with the swelling mineral (i.e. smectite) content. A potential explanation is that the CEC value positively relates to the water-sorption capacity, as smectite adsorbs the most water molecules. Seemann et al. (2017) did the linear regression analysis of the measured CEC value and the water vapor (in moles) uptake of COx claystone at different relative humidity, see Figure 1.3, a good correlation is observed between the two properties. The result demonstrates that when the relative pressure range from 0.1 to 0.7, CEC and the total water sorption capacity have a good linear relationship. The calculated hydration numbers (H_2O/cation) range from 2.5 to 12.5 H_2O/cation (based on the obtained slope). By measuring different claystone samples, the total effective hydration numbers are calculated between 10.6 to 62.7 H_2O/cation (at p/p° of 0.98), such big variation suggests that the water sorption is not attributed exclusively to the interlayer cation hydration of clay minerals, there are still other water sorption regimes during the hydration of claystone. Furthermore, the effect of the exchangeable cation type (essentially refer to the effect of hydration energy) is also discussed in (Seemann et al. 2017). They first utilizing Na^+ and Mg^{2+} to completely exchange cations on the unexchanged COx claystone, the CEC values were then measured on exchanged samples to compare with the value of the unexchanged one. No distinguished results were observed between exchanged and unexchanged samples. This means that the clay surface cation type is not the major influence factor on the CEC.

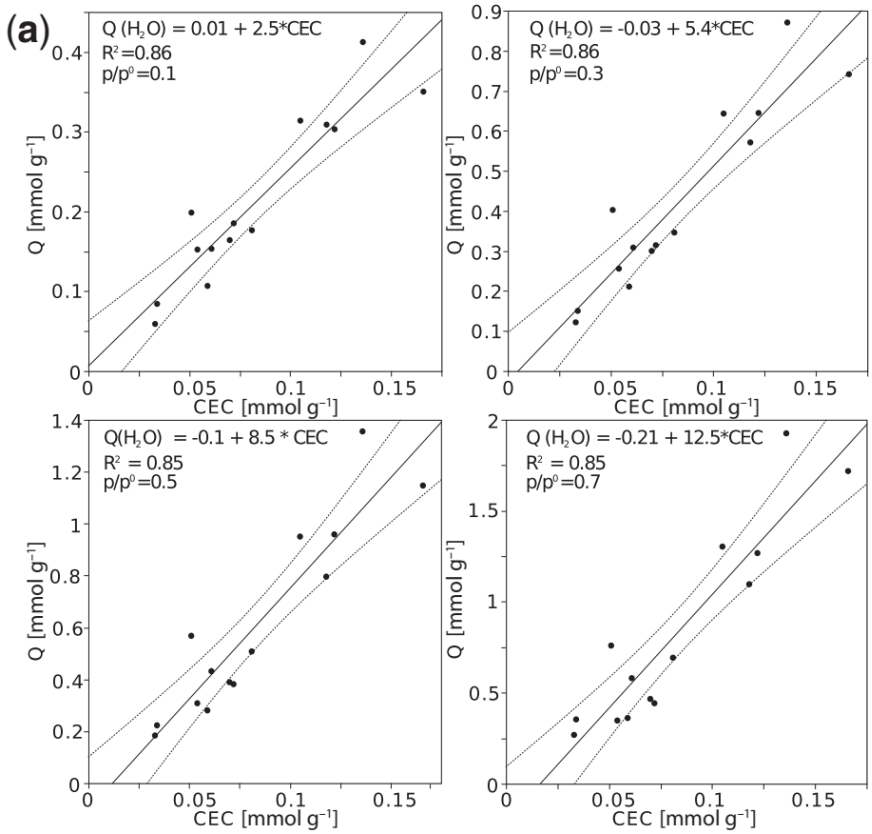

Figure 1.3. Molal water uptake (Q (mmol g21)) at 0.1, 0.3, 0.5 and 0.7 p/p° as a function of CEC (Seemann et al. 2017)

1.2.Pore-fracture structures

The pore-fracture network has a major effect on the mechanical and transport properties of COx claystone. To this date, the microstructural studies on the claystone are in rapid development. The pore-fracture network is a complex multi-scale system and consists of voids from macroscopic (millimeter-scale) to mesoscopic (micron-scale) and to microscopic (nano-scale). At different scales, various techniques can be used. Table 1.3 exhibits pore-fracture categories of claystone and the corresponding characterization approaches. Generally, investigation techniques can be divided into indirect and direct methods. In Table 1.3, mercury intrusion porosimetry and gas adsorption are indirect methods since they need simplified pores models to be analyzed. Micro-computed tomography (Micro-CT) and Scanning Electron Microscopy (SEM) are direct methods as they can be used to directly observe the real pore-fracture network at different scales. In this section, we will discuss these mainstream techniques and their application to COx claystone characterization.

Table 1.3. The definition of claystone pore categories in relation to various detected methods

<table>
<tr><td rowspan="2">Void category</td><td colspan="3">Pores radius</td><td rowspan="2">Fractures</td></tr>
<tr><td>Micropores</td><td>Mesopores</td><td>Macropores</td></tr>
<tr><td>Void size</td><td><2 nm</td><td>2-50 nm</td><td>50 nm -μm</td><td>μm-mm</td></tr>
<tr><td rowspan="4">Investigation techniques and resolution scales</td><td></td><td colspan="3">Mercury intrusion porosimetry (3 nm-10 mm)</td></tr>
<tr><td colspan="2">Gas physisorption (0,5 nm-0,35 μm)</td><td></td></tr>
<tr><td colspan="2"></td><td colspan="2">Micro-computed tomography (μm-mm)</td></tr>
<tr><td colspan="2"></td><td colspan="2">Scanning Electron Microscopy (nm-mm)</td></tr>
</table>

1.2.1. Mercury intrusion porosimetry

Mercury intrusion porosimetry (MIP) is a well-known technique for measuring the porosity and the pore size distribution of porous materials. Although mercury is metal, it behaves like a non-wetting fluid under atmospheric and vacuum conditions while maintaining extremely strong inter-molecule force. Moreover, mercury does not exhibit irregular thermal motion mass transfer pattern like gas. Thanks to the abovementioned advantages, one can use the MIP to get pore information. During the test, the invaded volume and the corresponding injection pressure are recorded. Before the test, the sample needs first to be dried to remove all pre-existing porous liquid. Theoretically, the minimum pore diameter that can be detected by MIP is around 3-4 nm, (Abell et al. 1999; Diamond 2000). The test carries out by progressively increasing the intruded mercury pressure on the vacuum sample. The intruded porosity (φ_{Hg}) can be directly calculated by the ratio of intruded mercury volume V_{Hg} to the total specimen volume V_{specimen}:

$$\varphi_{\mathrm{Hg}} = \frac{V_{\mathrm{Hg}}}{V_{\mathrm{specimen}}} \tag{1.1}$$

Besides, one can derive the information of pore size distributions (PSD) by linking the cumulative invaded mercury volume to the pore size. To generate the PSD information, a premise is that the pore system consists of numerous cylindrical tubes with various diameters. These cylindrical bundles are not interconnected, and each of them penetrates through the material and enters the outside of the sample. The famous Washburn equation (also called the Young-Laplace equation) is used to determine the intruded pore diameter (d):

$$d = -4\sigma \cos\theta / P_{\mathrm{Hg}} \tag{1.2}$$

where σ is the mercury-solid interfacial tension, θ is the mercury-solid contact angle, and P_{Hg} is the mercury intruded pressure. MIP has been widely used in claystone microstructure studies for years. For instance, ANDRA has charged several research institutions to study the porosity of COx claystone with different mineralogy contents by applying mercury intrusion. Table 1.4 summarized the porosity data of the predecessors, the porosity varies from different geological sequences with an average value equal to 16%.

Table 1.4. Water content and porosity of the at different Callovo-Oxfordian claystone sequences (Conil et al. 2018)

Water content (w)									
Totality		USC		UT + UA3 + UA2		UA1		−490 m depth	
Average (%)	SD (%)	Average (%)	SD (%)	Average (%)	SD (%)	Average (%)	SD (%)	Average (%)	SD (%)
7.1	1.7	6.7	2	8	1.2	6.2	1.3	7.9	0.6
Porosity (ϕ)									
Totality		USC		UT + UA3 + UA2		UA1 + RIO		−490 m depth	
Average (%)	SD (%)	Average (%)	SD (%)	Average (%)	SD (%)	Average (%)	SD (%)	Average (%)	SD (%)
16	3.3	15.1	4.2	17.7	1.9	14.2	2.3	17.5	1.2

Note: RIO is the Repère Inférieur Oolithique for petroleum geologist.

The porosity deduced from the mercury-pressure method is always underestimated. This is due to the limitation of the experiment apparatus allowing pores detection with a diameter greater than 3 nm. Moreover, most pores communicate the outside through a long seepage chain of intermediate pores of varying sizes and shapes, thus some pores connected to very fine necks will not be detected (Diamond 2000). Boulin et al. (2008) found that the MIP porosity gives around 75% of the total porosity for COx claystone. Menaceur et al. (2016) used MIP to measure the porosity of UA COx claystone is ca. 70% - 77% total porosity, this result is consistent with the observation in (Boulin et al. 2008).

Mercury intrusion test also provides information on pore size distribution, two typical result of COx claystone are shown in Figure 1.4. According to intrusion curves, the mean pore diameter of the UA sample is around 10-20 nm, while the value of the UT sample is around 50-100 nm. This implies that the higher the clay content, the smaller the mean pore diameter. For both UA and UT samples, the mean diameter deduced from extrusion curves is relatively higher than from the intrusion curves. The mean accessible pore size of overall COx formation varies between 3 nm and 60 nm, which belongs to the category of mesopores (Andra 2005; Yven et al. 2007).

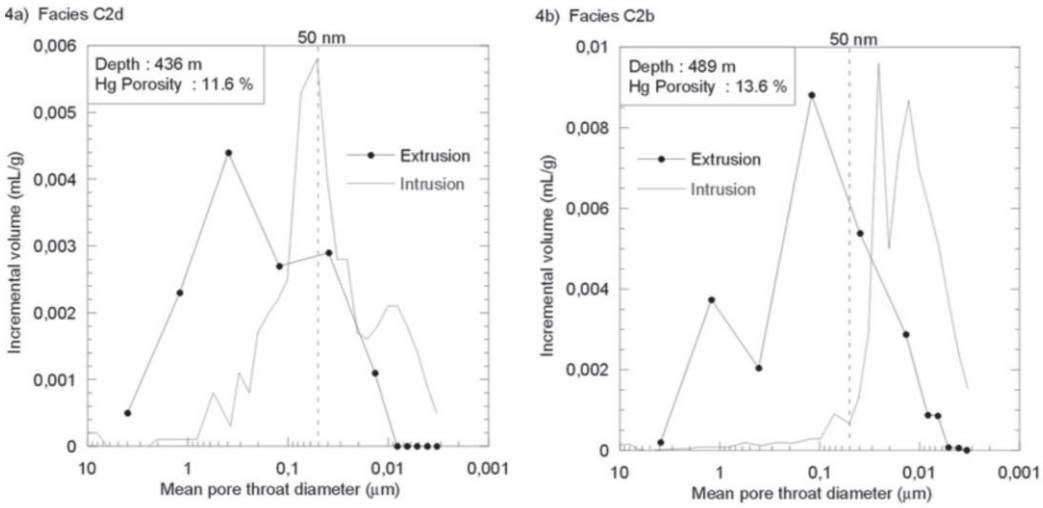

Figure 1.4. Typical pore size distribution of UT (left) unit and UA unit (right) (borehole EST205) (Yven et al. 2007)

However, Diamond (2000) reported that the PSD calculated based on the Washburn equation (rel. (1.2)) is typically one orders of magnitude smaller than the actual case. Several factors are proven can lead to this underestimation, such as the intrinsic defect of the cylindrical pores model, water status inside the clay particles, pore geometry effect, etc. (Horseman et al. 1999; Desbois et al. 2009; Houben et al. 2013; Klaver et al. 2015; Menaceur et al. 2016).

In summary, MIP can provide pore information between 3nm-300µm, with the mean pore-throat diameter between 3 nm and 60 nm, depends on the clay content. However, due to the intrinsic defect of the method, this is an underestimated value. Therefore, many researchers prefer to use another method with better accuracy, namely gas physisorption.

1.2.2. Gas physisorption

Gas physisorption is a pioneering approach to detect the pore textual properties of geomaterials. It is originally developed and applied in the physical-chemistry field of material sciences disciplines. Comparing to the Mercury intrusion porosimetry, gas physisorption not only provides a wider range of pore information, but also characterize the pore surface, pore volume, and other structural messages based on some well-established theories.

1.1.1.1 Principle of the gas physisorption

The term “physisorption” refers to a physical process of gas molecules penetrate into and gather at pore surface under van der Waals forces. Nitrogen is the most common gas that is used in laboratory studies, which has a boiling point at 77K and a corresponding saturation pressure of 101.3kPa. Using nitrogen (at 77K) can access a wide range of pore spectrum, from 0.36nm to 0.35µm (Thommes et al.

2015; Seemann et al. 2017). Recently, other gases such as water vapor (at 303K) and CO_2 (at 273K) are also developed for gas physisorption studies (Seemann et al. 2017; Lahn et al. 2020). For clay-rich rock, nitrogen and water vapor are the most common used gases. Therefore, only the results using these two gases are discussed here.

Based on the hypothesis that pore surface properties are homogeneous, the amount of adsorbed gas molecules is a function of relative pressure (p/p°) at a constant ambient temperature, where the p/p° is the ratio of the absolute gas pressure and the saturation pressure. Theoretically, the physisorption is thermodynamically reversible under isothermal conditions, thus the available original data is the adsorption/desorption isotherm.

The adsorption process consists of different stages with the increase of relative pressure (p/p°) and the adsorbed space expanded from ultra-micropores to macropores (Thommes et al. 2015). The dominant adsorption mechanisms with the increase of p/p° successively are: volume filling ($0.001<p/p°<0.15$), statistical monolayer and multilayer sorption ($0.15<p/p°<0.42$), capillary condensation ($0.42<p/p°<0.99$) and the clustering & spilling of molecules ($p/p°>0.99$). Figure 1.5 gives an exhaustive description of adsorption process by using nitrogen at 77K. When the $0.001<p/p°<0.01$, molecules start filling the micropores within the range of 0.35-1nm (i.e., the ultra-micropores), this process is termed “the primary filling”. The subsequent process is called “the secondary filling”, which occurred at slightly higher relative pressure range ($0.01<p/p°<0.15$) to fill wider micropores (up to 2nm). When p/p° increase from 0.15 to 0.42, statistical monolayer and multilayer adsorption successively occurs in the mesopores. Meniscus interfaces appear in the individual pores and move steadily up to the pore entrance (Hamamoto et al. 2006). Capillary condensation start at p/p° =0.42. Theoretically, all pores are fully filled and molecules start spilling when p/p° exactly equals 1. The concentration of gas is maintained constant in both the surrounding environment and the porous system when p/p° = 1. It is empirically considered that all the macropores are radically filled at a relative pressure p/p° greater than 0.99 (Bertier et al. 2016).

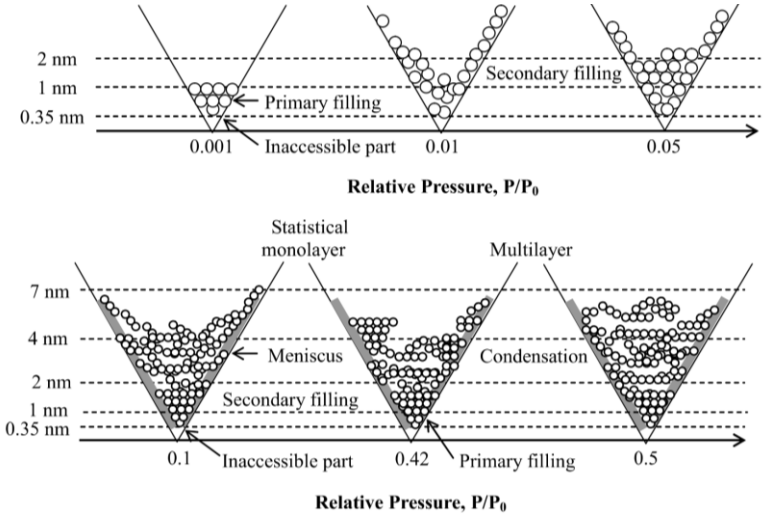

Figure 1.5. Main steps of physisorption of N2 at 77K (Hamamoto et al. 2006)

Desorption refers to the adsorbed gas molecules escape from the pores when p/p° decreases from 1 to 0. For material with complex pore structures (such as COx claystone), wider pores connect with very narrow throats. During desorption, high pore/throat ratio could result in the wider pores will remain filled until the throats empty at much lower pressures. Such effect is reflected in the isotherm as a hysteresis of the desorption phase. Theoretical and experimental studies reveal that the hysteresis is controlled by the comprehensive effects of several mechanisms (Rouquerol et al. 2013; Thommes and Cychosz 2014) According to the IUPAC2015 report, network effects and pore blocking are the dominant mechanisms for clayey materials.

1.1.1.2 Applications on the study of COx claystone

Based on several developed analysis theories, the pore textural properties can be converted from the isotherms (Bertier et al. 2016). The most used properties for characterizing COx claystone are: Gurvich specific pore volume ($V_{Gurvich}$) calculated from the Gurvich rule, specific surface area (SSA) derived by the Brunauer-Emmett-Teller (BET) theory, and the pore size distributions derived by the combination of Barrett-Joyner-Halenda (BJH) and Dubinin-Astakhov (DA) theories. In the following of this section, we will introduce in detail each theory and the related properties of COx claystone.

Gurvich rule

Assuming all pores are filled and the gas has liquid density at the operational temperature (e.g. -196 °C for N_2) at p/p^0 close 1, the up limite adsorbed pore volume is the so-called Gurvich specific pore volume ($V_{Gurvich}$), is calculated as follow:

$$V_{Gurvich} = \frac{Q_{max}}{1000} V_m \quad (3)$$

where Q_{max} is the maximum sorption capacity of the adsorbate, in unit of mmol/g; V_m is the liquid molar volume of the adsorbate, in unit of cm^3/mmol. If the tested material contains micropores, $V_{Gurvich}$ is underestimated due to the blocking of micropores (Thommes and Cychosz 2014; Bertier et al. 2016). Unlike porosity, which is expressed as a percentage, $V_{Gurvich}$ is quantified in cm^3/g. If the density of the absorber is known, $V_{Gurvich}$ can be converted to porosity by the following equation:

$$\varphi_{Gurvich} = \frac{V_{Gurvich}}{\frac{1}{\rho} + V_{Gurvich}} \tag{1.4}$$

where $\varphi_{Gurvich}$ is the Gurvich porosity, ρ is the grains density of the absorbent.

Song et al. (2017) performed the nitrogen adsorption analysis on five dry COx samples, with a total clay content varying between 36.8 and 51.9% (in mass). The measured $V_{Gurvich}$ varied between 0.044 cm^3/g and 0.062 cm^3/g. Moreover, water vapor adsorption was performed on two of the five samples using quick static desiccator method, see Figure 1.6. Results demonstrate that the total adsorbed volume ($V_{Gurvich}$) measured by water vapor is larger than that by nitrogen. This can be interpreted as the water-clay interaction increases the pore volume. Lahn et al. (2020) found that the nitrogen $V_{Gurvich}$ increase with decreasing relative humidities (RH) of the COx claystone. This means the $V_{Gurvich}$ of COx claystone depends on the water content.

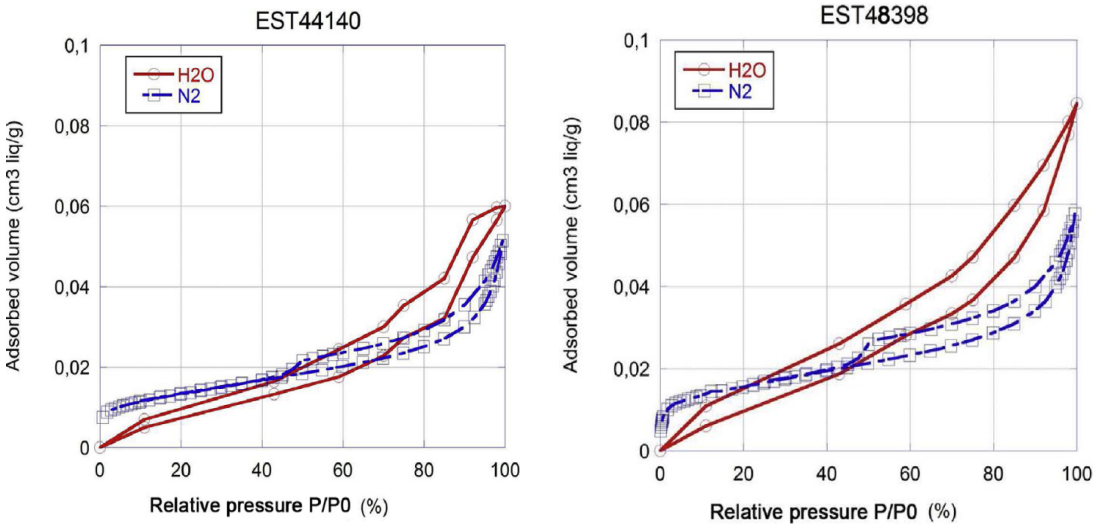

Figure 1.6. Comparison of the adsorption/desorption isotherms of nitrogen and water vapor (Song et al. 2017)

Brunauer-Emmett-Teller theory

The Brunauer-Emmett-Teller (BET) theory is an optimization of the classic Langmuir theory (Brunauer et al. 1938). The BET theory follows several assumptions, such as the adsorbent surface is

supposed to be uniform, no interactions between the molecules in the same layer, gas molecules can adsorb countless layers on a solid surface (Rouquerol et al. 2007). It considers both mesoporous multilayer adsorption and microporous molecule filling in the model, which is often used to quantify the adsorbable pore surface of the porous material.

From the isotherms, two important properties can be converted according to the BET theory, namely the monolayer capacity (Q_{mono}) and the specific surface area (SSA). Q_{mono} is determined by transforming the isotherms into the BET plot (in the form of $\frac{1}{[Q(1-p/p°)]}$ VS. p/p°) with the following equation:

$$\frac{1}{[Q(1-p/p°)]} = \frac{1}{Q_{mono}C} + \left[\frac{(C-1)}{Q_{mono}C}\right](p/p°) \tag{1.5}$$

where Q is the specific amount of adsorptive (mmol/g) at the relative pressure p/p°, and C is an empirical constant that is determined by measuring the adsorbent-adsorbate interaction. Rel. (1.8) illustrates that Q_{mono} linearly corresponds to the relative pressure (p/p°), thus only data from the straight part of BET plot is used for calculation. For practical purpose, Brunauer et al (1938) proposed that the useful data to adapt rel. (1.8) corresponds to p/p° range in [0.05, 0.35], which is can be slightly different from each specific adsorptive and adsorbent (Rouquerol et al. 2007).

The specific surface area (SSA) is determined by a mathematical calculation of knowing Q_{mono} and the molecule cross-sectional area σ_m of the adsorptive molecule (e.g. 0.162 nm² for Nitrogen at 77K), expressed as:

$$SSA = Q_{mono} \cdot N_A \cdot \frac{\sigma_m}{m} \tag{1.6}$$

where N_A is the Avogadro number, 6.022×10^{23}/mol; m is the mass of the adsorbent. Essentially, SSA cannot be treated as the real physical surface area but an "effective (or apparent)" surface area because it is derived from a simplified pore model. However, with the strict operation and well-controlled experiment conditions, SSA is still useful for characterizing the available adsorption area of porous materials (Rouquerol et al. 2007; Thommes and Cychosz 2014).

Yven et al. (2007) reported the nitrogen SSA varies between 17 and 39 m²/g for COx claystone samples from different depths. Particularly, samples originate from C2b sequence (belong to UA unit, includes higher clay contents) corresponds to relatively high values (Table 1.4). That is to say, the material with higher clay contents exhibits higher SSA.

Table 1.5. the information of pore surface area determined by: N_2 adsorption (at 77K) (Yven et al. 2007)

Depth (m)	Lithofacies	BET method	
		Specific surface area ($m^2 \cdot g^{-1}$)	Energy constant
422.1	C2d	29.5	205
430.2		23.8	185
442.4	C2c	16.7	155
451.9		34.2	180
460.7	C2b	31.7	195
464.4		28.4	170
470.4		34	210
475.2		30.5	175
480.8		38.3	185
485.8		30.7	175
491.9		38.7	160
495.9		38.1	150
500.2		33.4	140
509.8		33.5	135
520.3	C2a	24.5	90
526.6		22.2	140

Seemann et al. (2017) performed nitrogen adsorption measurements on 13 different clayey materials (including COx claystone), by using water vapor at 303K and nitrogen at 77K respectively. For COx claystone, the nitrogen Q_{mono} and SSA are 0.36 mmol/g and 35.1 m²/g, respectively. The corresponding values of water vapor are 0.73mmol/g and 46 m²/g, respectively, which are lower than that of water vapor. However, by comparing all 13 different clayey materials, the use of different adsorbents does not lead to significant differences in the results of Q_{mono} and SSA.

Barrett-Joyner-Halenda (BJH) theory + Dubinin-Astakhov (DA) theory

The pore size distribution (PSD) is a very important property. It can be obtained based on two theories: Barrett-Joyner-Halenda (BJH) theory and the Dubinin-Astakhov (DA) theory. The Barrett–Joyner–Halenda (BJH) theory is utilized to calculate PSD of pores larger than 4 nm, and the Dubinin-Astakhov (DA) theory is adopted for deriving the micropore size distribution (pore diameter < 2 nm).

The Barrett–Joyner–Halenda (BJH) theory was first established by Barrett, Joyner, and Halenda (Barrett et al. 1951). This method has two hypotheses: (1) all pores are in the shape of cylindrical geometry and (2) the retention of adsorbate is controlled by two mechanisms, namely the multilayer adsorption on the pore walls and the capillary condensation in the capillary bundles. Hence the pore radius (r_{BJH}) is the sum of the statistical multilayer thickness (t) and the Kelvin radius (r_k) of the liquid-vapor interface:

$$r_{BJH} = t + r_k \tag{1.7}$$

The multilayer statistical thickness (t) is deduced from the t-curve and an empirical equation by linking the reciprocal of multilayer-adsorption-pressure to the statistical multi-layer thickness (t):

$$t = k\left(\frac{1}{\ln\left(p°/p\right)}\right)^{\frac{1}{s}} \tag{1.8}$$

where the parameters k and s are both empirical constants, depending on the pore surface chemistry.

Dependent upon the macroscopic thermodynamic principles, the Kelvin radius (r_k) is calculated via the classic Kelvin equation:

$$r_k = -2\,V_M \cdot \sigma_w \cdot \cos\theta / \ln(p/p°)RT \tag{1.9}$$

Using rel. (1.7) - (1.9), Yven et al. (2007) have reported the prevailing pores in COx claystone are restricted to small mesopores (2.5 - 3.7 nm). It is worth underlining that these calculated value pore diameters are underestimated because using BJH theory to calculate pore size < 10 nm would yield underestimates of up to 20-30% (Thommes and Cychosz 2014). Nevertheless, r_{BJH} is still useful to compare between samples as the computational errors do not affect the qualitative results.

For the micropores PSD analysis, Dubinin-Astakhov (DA) theory is a prioritized approach recommended by both ISO15901 and IUPAC. Based on the theory of volume filling (micropores) (TVF(M)), the molar work of adsorption (A) in micropores is defined as equal to the loss of Gibbs free energy ($-\Delta G$). Thus A can be predicted by involving the thermodynamics principles: $\mathrm{A} = -\Delta G = -RT\ln(p/p°)$ (Seemann et al. 2017). Since A and Q can be derived from the isotherm data, the Dubinin-Astakhov equation gives a mathematical method to determine the pore size distribution (Dubinin and Astakhov 1971):

$$\Theta = \frac{Q}{Q_0} = \exp\left[-\left(\frac{A}{E}\right)^n\right] \tag{1.10}$$

where Θ is the fraction of filled micropore volume, Q_0 is the limiting micropore capacity (cm^3/g) for a certain pore diameter, E is the characteristic energy (KJ/mol) of the adsorption system, n is the adjustable exponent. Both Q_0 and E are the inherent properties of the adsorbtion system and can be obtained by non-linear curve fitting rel. (1.10) (Seemann et al. 2017). The equivalent micropore radius (r_e) can be calculated by the simplified van der Waals equation:

$$r_e = \sqrt[3]{-\frac{k}{\Delta G}} \tag{1.11}$$

where k is the interaction constant. According to Janssen and Van Oorschot (1989), k_{N_2} is estimated to be 2.96 KJ·cm^3/mol.

In Seemann et al. (2017), both BJH theory and DA theory were used to assess pore size distributions of 13 different claystone samples. Results demonstrate that the most popular pore size measured with nitrogen is slightly below 20 nm, while using water vapor leads to smaller pore size. This can be interpreted by the water vapor adsorption process being highly sensitive to rock properties (such as contact angle) and the BJH theory is not of good accuracy. As shown in Figure 1.7, DA micropore volume (Q_0) is linearly related to the BET monolayer adsorption volume (Q_{mono}). This implies that the Q_{mono} does not only relate to the monolayer adsorption capacity and specific surface area, but also being a quantization parameter of micropore volume.

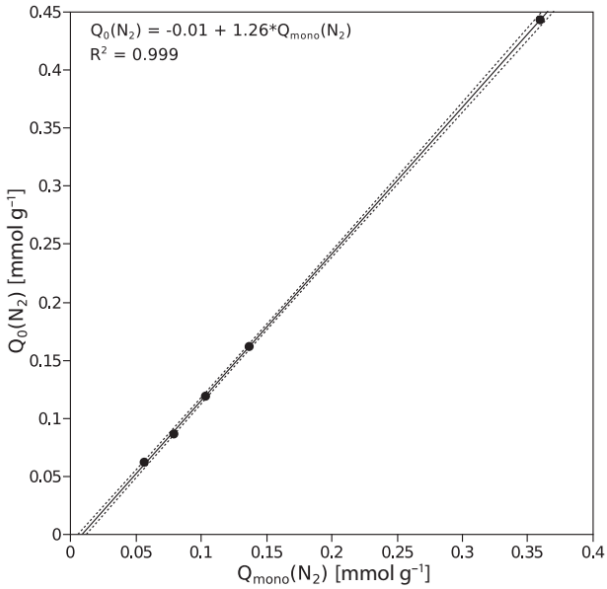

Figure 1.7. The relationship between Dubinin-Astakhov (DA) micropore volume (Q_0) and the BET monolayer capacity (Q_{mono}) of moisture-equilibrated COx claystone (Seemann et al. 2017)

It has been reported that the gas sorption is highly affected by the saturation of clayey materials. Figure 1.8 shows the cumulative pore-size distribution of COx claystone at different relative humidities (RH). One can find that the adsorption capacity decreases with the increase of RH. Results also demonstrate that nitrogen can be still adsorbed in micropores and narrow small mesopores (diameter lower than 10 nm) at high relative humidity (up to 94%RH), but the adsorbed volume sharply decrease with RH increase. This means that partial microporosity is still accessible even at high saturation.

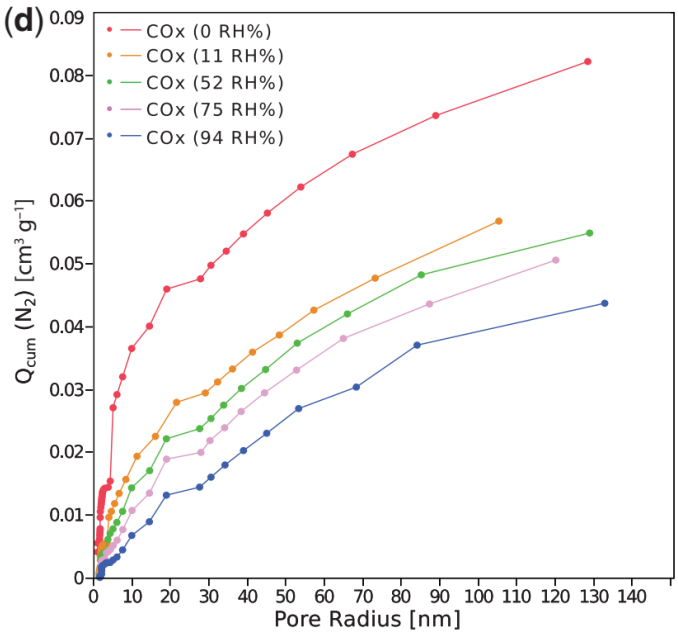

Figure 1.8. cumulative pore-size distribution (BJH + DA) derived from nitrogen sorption isotherms of COx claystone at different relative humidities (RH) (Seemann et al. 2017)

Overall, under some intrinsic hypotheses (e.g. the adsorbent surface is uniform), the gas physisorption can be used to analyze the microstructure of clayey materials. In particular for the measurement of COx claystone, nitrogen (77K) and water vapor (303K) are the most used adsorbate. Results indicate that its complex pores system consists of a large amount of mesopores and a small amount of micropores and macropores. The Gurvich pore volume ($V_{Gurvich}$) is a property derived based on the Gurvich rule, which can be used to quantify the total adsorption capacity of the material. The monolayer capacity (Q_{mono}) and the specific surface area (SSA) (of mesopores) are derived from BET theory. They are both "apparent" rather real properties, but can still be used to compare between samples. The PSD of meso- and micro-pores can be deduced by applying BJH theory and DA theory, respectively. Previous studies also proven that the above mentioned properties are highly affected by saturation states.

Nowadays, the most accurate approaches are density functional theory (DFT) and Monte Carlo simulation, which based on the fundamental principles of statistical mechanics. However, the two methods are based on models with certain homogeneous pore geometry, and none of these is well fitted for complex composite pore systems. Therefore, using the classical theories (i.e. Gurvich, BET, BJH, and DA theory) are still elegant solutions for characterizing gas physisorption on claystone.

1.2.3. Micro-Computed Tomography (Micro-CT)

Micro-Computed Tomography (Micro-CT) is an imaging technique used to observe pore structures from mesoscale (μm) to millimeter-scale (mm). The principle of this technique is to scan the sample horizontally with an X-ray to obtain a series of 2D images with the same spacing in the vertical direction. The 2D images are then superimposed in the vertical direction to construct a 3D image. The 3D image is composed of two parts: the skeleton and the pore network. Micro-CT is a non-destructive method because there is no need to pre-treat the sample and the sample can remain integrity after scanning.

Zacher et al. (2015) investigated the triaxial compress damaged Opalinus clay core of ca. 100 mm in diameter. The bedding planes and cracks with low resolutions (around 0.3 mm) were observed by the high-speed scanning (Figure 1.9 (a)) and more detailed structures were observed by using high-resolution (approx. 60 μm) scanning (Figure 1.9 (b)). Kaufhold et al. (2016) balanced the relationship between scanning speed and resolution and studied the minerals and fractures spatial distribution of the Opalinus clay.

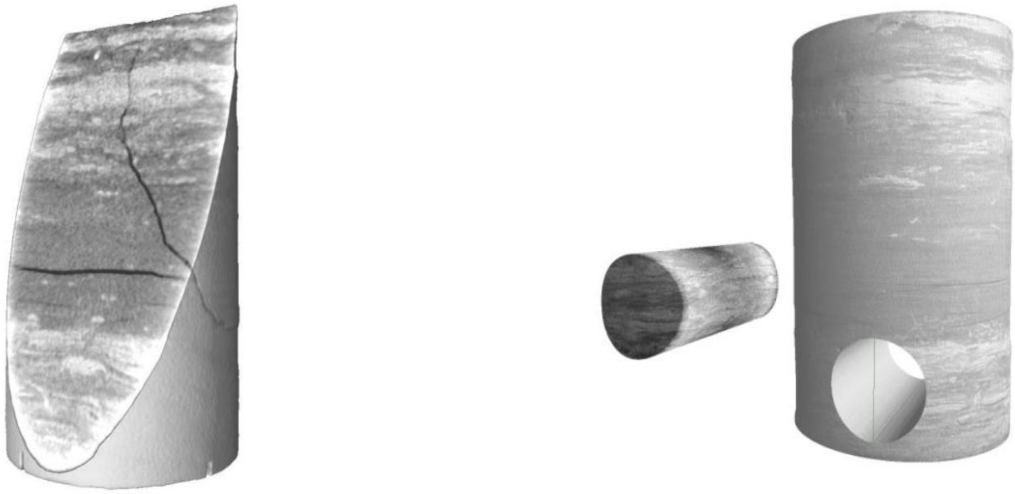

(a) (b)

Figure 1.9. 3D images of the Oplinus clay sample after triaxial compression tests: (a) acquired via high-speed CT (b) acquired via high-resolution CT (Zacher et al. 2015)

Similarly study but has been performed on shale samples (Cała et al. 2017). They focused on using Micro-CT to study the morphological evolution of fractures (tens to hundreds of microns) under uniaxial compression (Figure 1.10). The volume fraction of cracks, tortuosity and crack aperture spatial distribution are analyzed based on the information of micro-CT images.

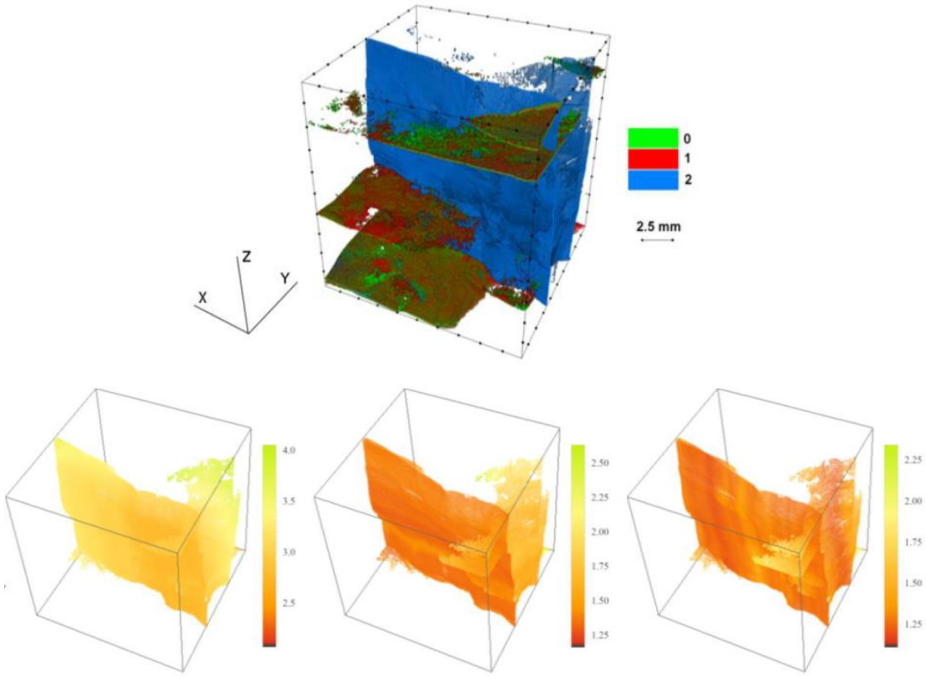

(a) X-direction (b) Y-direction (c) Z-direction

Figure 1.10. 3D reconstruction of crack network at subsequent loading stages and spatial distribution of tortuosity at three directions by Micro-CT (Cała et al. 2017)

Some researchers have visualized the stress variations in materials by combining Micro-CT with digital image correlation (DIC) techniques. For instance, Bésuelle and Hall (2011) used the two techniques to investigate the 3D strain field evolution of COx claystone under triaxial compression (with the pixel size of 14×14 µm²), see Figure 1.11. The strain field consists of a series of subsets, which are cubes in the reference images, each of them containing 20^3 fundamental voxels. The local pattern quality of the strain field highly relies on the resolution of the CT images.

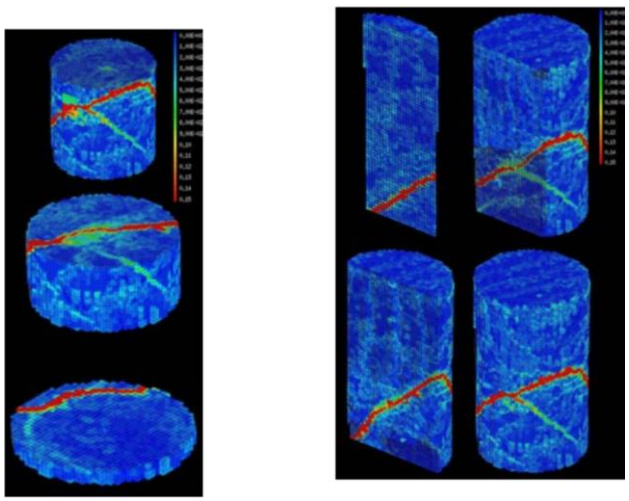

Figure 1.11. 3D shear strain increment field in the post-peak increment, represented by horizontal cuts at different heights (left), and vertical cuts (right) (Bésuelle and Hall 2011)

Giot et al. (2019) used high-resolution Micro-CT with a resolution of 24 µm to study the self-sealing of the artificially cracked COx claystone samples. Before inject water into the sample, an artificial crack is fabricated axially through the sample with the thickness of 100µm (or 800µm). The test is carried out under a continuous confinement pressure (12MPa) and the crack volume was monitored with the self-sealing process (Figure 1.12). This is direct evidence of COx claystone crack closure during hydration.

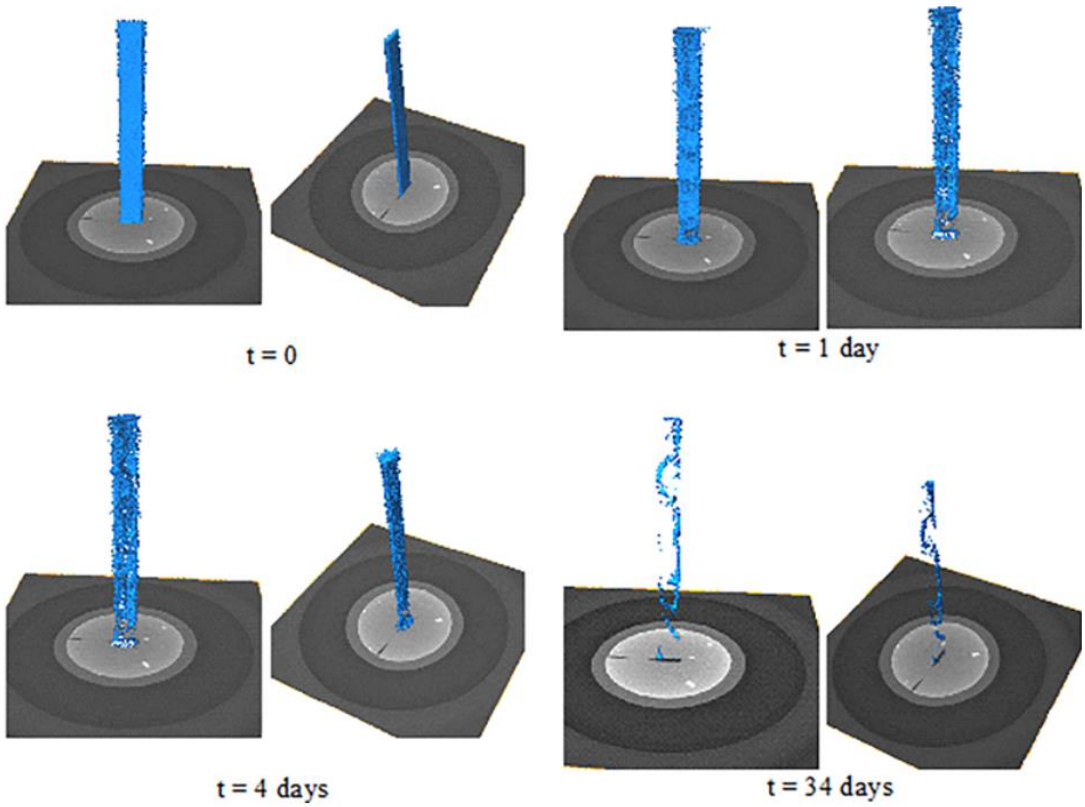

Figure 1.12. 3D Micro-CT of the crack volume evolution during the water injection (Giot et al. 2019)

In summary, Micro-CT can be used to directly characterize the pore structure of materials from macroscopic to mesoscopic scales. The resolution is very important for microstructure studies because it affects the processing time and the local information of the images. The latest Micro-CT techniques can reach an accuracy of a few microns (Iglauer and Lebedev 2018).

1.2.4. Scanning Electron Microscopy (SEM)

The size of mineral grains and the inter-mineral pores of COx claystone are often at the meso- even microscale. Hence, the Micro-CT is not sufficient to study these objectives and higher precision technique, i.e. Scanning Electron Microscopy (SEM), is needed.

Using SEM can acquire high-resolution images at very high magnification, thanks to the thermionic incident electrons and the atoms on (or approx. 0.5-1 micron below) the sample surface are interacting. During the scanning, low currents primary electron beam will slightly sputter and raster the target surface, and generate Secondary Electrons (SE) and BackScattered Electrons (BSE). SE images can characterize the sample topography (three-dimensional appearance), with relatively bright steep surfaces and edges and dark flat surfaces. For the standard thermionic SEM, the SE images can maintain a relatively high resolution at high magnification, which can be up to approx. 50-100 nm (depending on the electrical conductivity of the material surface). BSE are produced by the interactions of atoms down to approximately 0.5-1 micron below the surface. Due to the different chemical properties of the atoms, the BSE exhibit a contrasting brightness in images: the heavier the atom, the brighter the area observed in the images. Therefore, detailed mineral information can be obtained from the BSE images (Song 2014). Generally, the BSE images have a lower resolution than SE images. Figure 1.13 (a), (b) and (c) exhibits the micropores and micro-cracks within the clay matrix of Opalinus clay that observed by SE-SEM at nanoscale. Figure 1.13 (d) is the BSE-SEM image of the mineral composition and spatial distribution of Opalinus clay(μm-scale) (Houben et al. 2013).

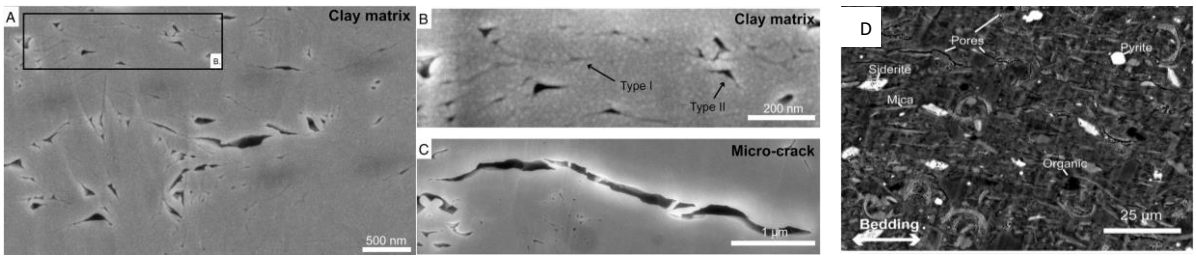

Figure 1.13. SE-SEM images of Opalinus clay: (A) micropores within the clay matrix (B) two different pore types in the clay matrix. (C) the elongated micro-crack with jagged edges in the clay matrix. (D) is the BSE-SEM images overview of the typical microstructure of Opalinus clay (Houben et al. 2013)

The processing of the sample surface is a very important part of the scanning test. Broad Ion Beam (BIB) polishing method is often used to acquire neat observe cross-sections. By bombarding the target surface with a heavy ions beam (typically argon), a certain mass of sample material is removed and a truly planar surface with less than 5 nm topography deviation is formed. The polished cross section varies from hundreds microns up to 1-2 millimeters in diameter (Philipp et al. 2017). Figure 1.14 shows a series of BSE-SEM images of COx claystone, the yellow lines indicate the boundaries of the BIB polished areas. It can be found that although the images are in black and white, the micro-cracks and the mineral grains still can be distinguished by the geometric boundary and different grayscale value.

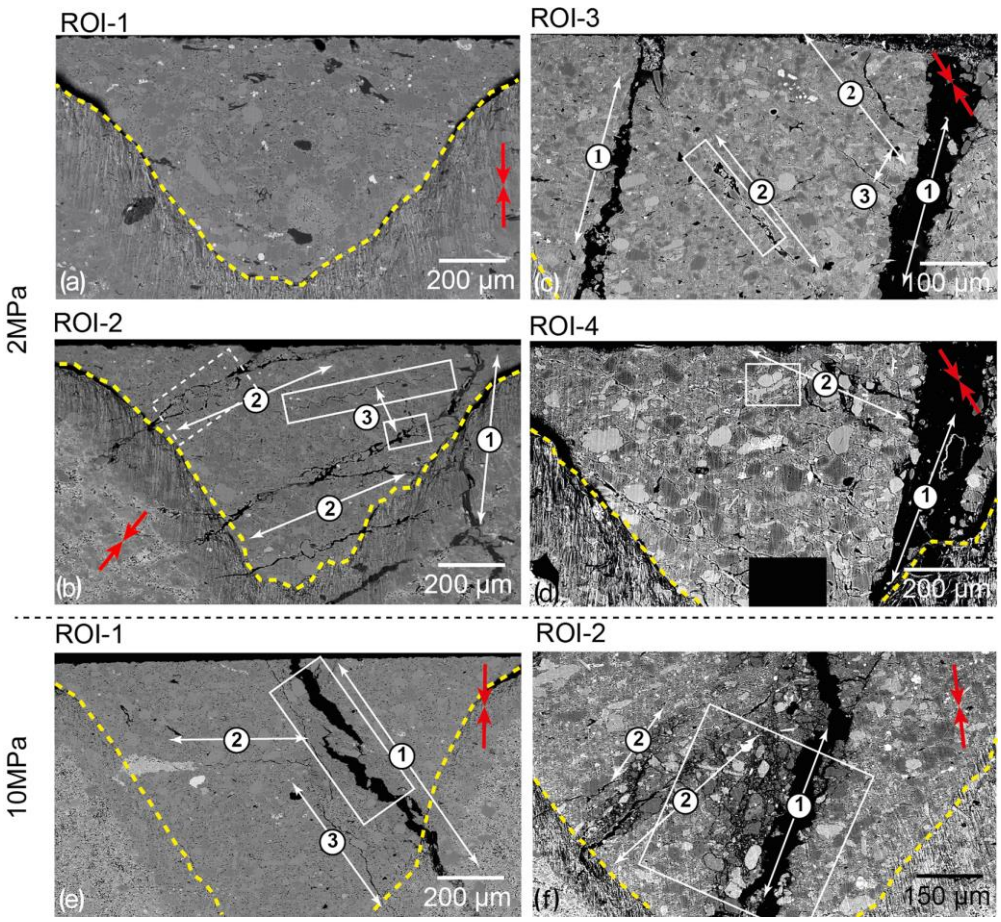

Figure 1.14. BSE-SEM micrographs of the BIB cross section overviews of COx claystone (Desbois et al. 2017)

To this day, it is possible to reconstruct the 3D microstructure of the porous material at nanometric size by combining SEM and Focused Ion Beam (FIB) techniques (Klaver et al. 2015; Song et al. 2016a, b, 2019; Keller 2016; Davy and Adler 2017; Keller et al. 2017; Brisard et al. 2018; Keller and Holzer 2018; Song et al. 2020). For the 3D reconstruction, a strong current finely focused ions beam (usually gallium) is used to cut a U-shaped hole to isolate a cube volume on the sample surface, see Figure 1.15 (a). Then cube-shaped sample is cutted into slices by focused ion beam at a constant thickness of 10-50 nm along ***z***-axis. Once a fresh surface is cut, it will immediately be captured as an SEM image with an inclined angle of 52° to the ***x-y*** plane. All 2D images are stacked in order to reconstruct a synthetic 3D image. Figure 1.15 (b) shows a The reconstructed raw sample volume (Figure 1.15 (b)) can be as small as 61 μm^3 with the voxel sizes of $5.9 \times 7.5 \times 10$ nm^3 (Song et al. 2019).

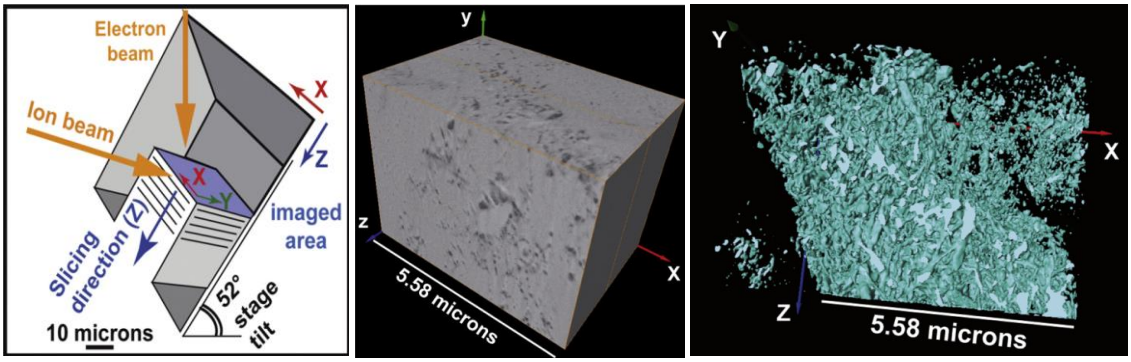

Figure 1.15. (a) principle of alternating action of focused ion and electron beams and a carved cube sample for observing; (b) reconstructed raw FIB/SEM 3D image; (c) reconstructed FIB/SEM 3D image of whole pore network of (Song et al. 2019)

Using a combination of the aforementioned microstructure (solid matrix and pore network) characterization techniques, Yven et al. (2007) reported a well-known conceptual model of multiscale porosity and of minerals distribution (Figure 1.16). It is widely used to in the field of mechanical and transport properties study of COx claystone.

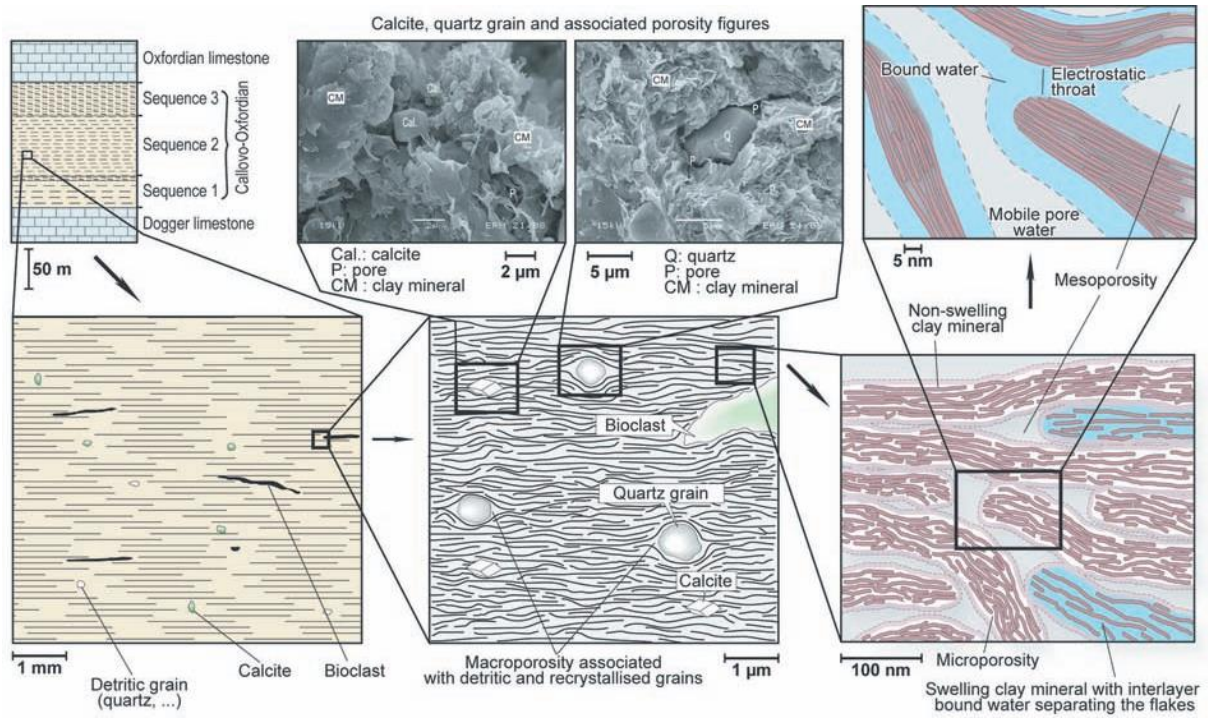

Figure 1.16. Multiscale pore structure and mineral composition in COx claystone (Yven et al. 2007)

Inspired from the previous works, various techniques are used in this research to investigate the multiscale pores and cracks evolution during the self-sealing of COx claystone. Precisely, the relationship between microscopic clay hydration and the macroscopic volume expansion is studied by

combining Quantitative XRD, CEC, and gas physisorption. The contribution of clay swelling to self-sealing is quantified by using Micro-CT and SEM.

1.3. Deformability of COx claystone: shrinkage, swelling, and poro-mechanics

Numerous studies have proven that COx claystone shrinks during desaturation and swells during hydration. Moreover, the deformation of this material always exhibits strong anisotropy due to the inherent layered sedimentary characteristics. During the construction of a radioactive waste repository, the tunnel ventilation can lead to shrinkage (even cracking) of the surrounding formation (i.e. EDZ, has been illustrated in Introduction). After the repository closure, COx claystone will be subjected to long-term hydro-mechanical loading. Such hydro-mechanical loading will lead to the self-sealing of desaturated & cracked EDZ, which has been validated by *in-situ* and laboratory experiments (Boulin et al. 2008; Van Geet et al. 2008; Zhang 2011; Wang et al. 2015; Harrington et al. 2017; Giot et al. 2019; Bossart et al. 2019). Obviously, the desaturation/resaturation cycles (in the presence of *in-situ* stress) can lead to a significant impact on the transport and mechanical properties of COx claystone. Therefore, understanding these phenomena is crucial for the stability and safety of the repository.

1.3.1. Shrinkage and swelling

It was generally observed that the volumetric behavior exhibits strong transverse isotropy. The swelling/shrinkage strain amplitude is found to be more pronounced in the direction perpendicular to the beddings. Submitting one COx claystone sample to several drying/wetting cycles (Yang et al. (2012)) reveals that the strain induced by hydration is more heterogeneous at the µm-scale than at the millimeter scale. This can be interpreted by minerals having specific orientations at the µm-scale. Whatever the direction, strain always shows non-linearity and a decreasing trend of amplitude after several drying/wetting cycles, which is attributed to the micro-cracking during the cycles (Yang et al. 2013). Wan et al. (2013) measured the water content and porosity of COx claystone by applying different suctions on the COx claystone. Results demonstrate that for suction varying from 0 to 150 MPa, the water content of such material changes between 12% to 3%, with a porosity range in 16.5% to 23%. The volumetric strain exhibits shrinkage of 1.4% at 150 MPa suction and a 7% swelling at 0 suction. After several drying/wetting cycles, water content and saturation appeared to be reversible while the volumetric strains are observed irreversible (Figure 1.17).

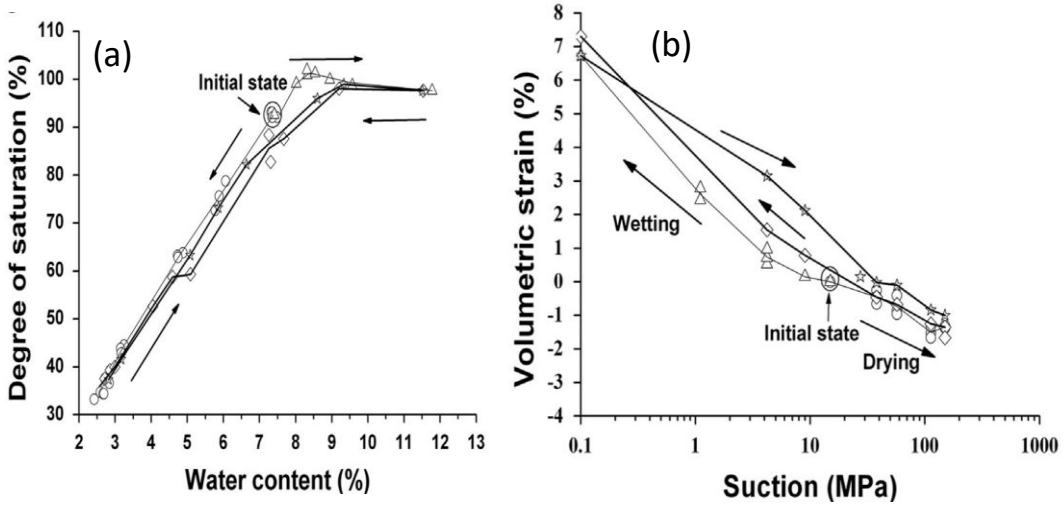

Figure 1.17. drying/wetting test on the COx claystone (a) water content VS. saturation degree (b) volumetric strain obtained during drying/wetting cycles (Wan et al. 2013)

Mineralogists have confirmed that smectite is the only clay mineral in clayey materials that interacts with groundwater (Altaner and Bethke 1988; Laird 1996). In the natural word, smectite particles are usually flake-shaped and consist of tens to hundred elementary platelets, see Figure 1.18 (a). The elementary platelet is composed of an octahedral sheet between two tetrahedral sheets (also called TOT structure) and with a basal spacing of 9.6 Å (Mitchell and Soga 2005), see Figure 1.18 (b).

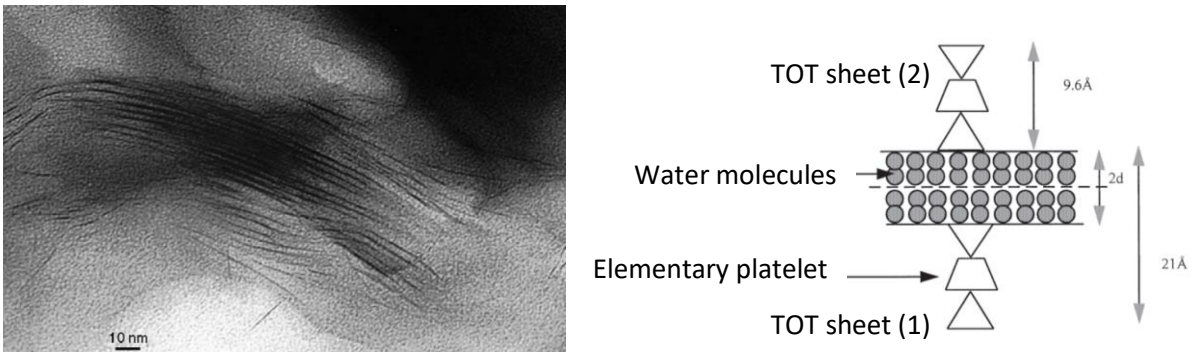

(a) (b)

Figure 1.18. (a) High-resolution transmission electron micrograph showing the arrangement of individual layers within a smectite particle (Laird 2006); (b) schematic distance between two layers of smectite (Saiyouri et al. 2000).

Saiyouri et al. (2000) carried out a leading research to investigate the swelling mechanism of highly compacted (one-dimensionally compacted the powder up to 60 MPa) smectite clay (smectite content > 80%). Similar to the suction controlled method in (Wan et al. 2013), the material was wetted by placing sample into desiccators with different suctions. Combining with the XRD analysis, results reveal that with the decrease of suction pressure, the smectite inter-platelet distance can be 9.6, 12.6, 15.6, 18.6

or 21.6 Å and corresponds to 0, 1, 2, 3, 4 water layers within the adjacent smectite platelets (Figure 1.19). This swelling mechanism is known as the crystalline swelling.

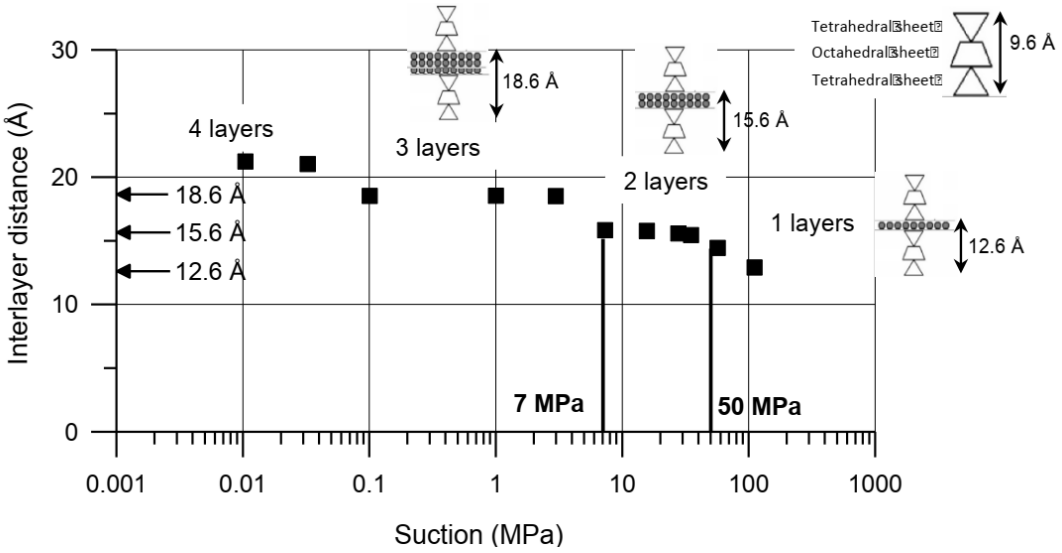

Figure 1.19. the schematic of the smectite interlayer distance changes with suction (Menaceur et al. 2016)

For gel or powder materials, the smectite swelling in the suspension was up to more than 100 Å (Delvaux 1992). That is to say, the swelling amplitude can reach a much greater value than crystalline swelling. Such a swelling mechanism is the so-called osmotic swelling. Essentially, osmotic swelling is attributed to the repulsion effect of neighbor particles. Due to the individual subdivided smectite particle carries negative charges on its surface, the inter-layer spacing will increase when adjacent particles are close enough to each other (Anderson et al. 2010).

Saiyouri et al. (2000) proposed a conceptual swelling model that consists of two microscopic mechanisms, demonstrated in Figure 1.20. Crystalline swelling results in the subdivision of the initial particles. The crystalline swelling amplitude of two adjacent layers varies from 3 to 12 Å, depends on the saturation level. When the material is close to fully saturated (saturation > 90%), Osmotic swelling occurs. If given enough swelling space, osmotic swelling (d_2 in Figure 1.20) can lead to an order of magnitude greater expansion than crystalline swelling (d_1 in Figure 1.20) (Anderson et al. 2010).

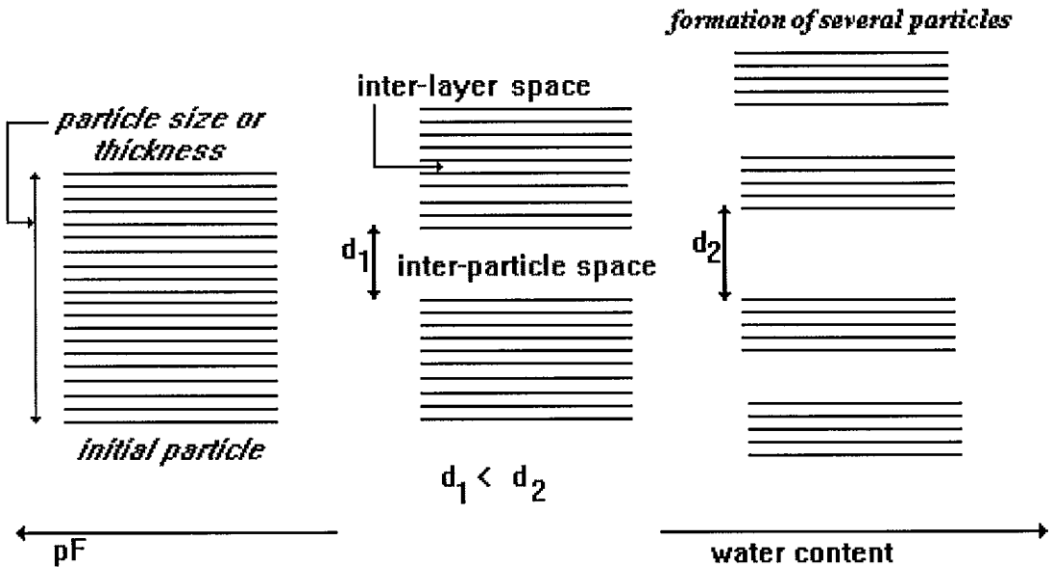

Figure 1.20. swelling model of smectite including two mechanisms (Saiyouri et al. 2000)

Menaceur et al (2016) studied the hydration effect on the volumetric change of COx claystone. At 34 MPa suction (saturation = 79.1%), the smectite hydro-state of the material is characterized and corresponds to a 2-layers of water molecules. From Figure 1.21, one can find that the saturation increases from 79.1% to 98.1% when the suction decrease from 34 MPa to 9 MPa, while only slight volumetric strain is observed. However, when the suction is reduced from 9 MPa to 0, the saturation increased from 98.1% to 100% and results in a significant volume swelling (Figure 1.21 (c)).

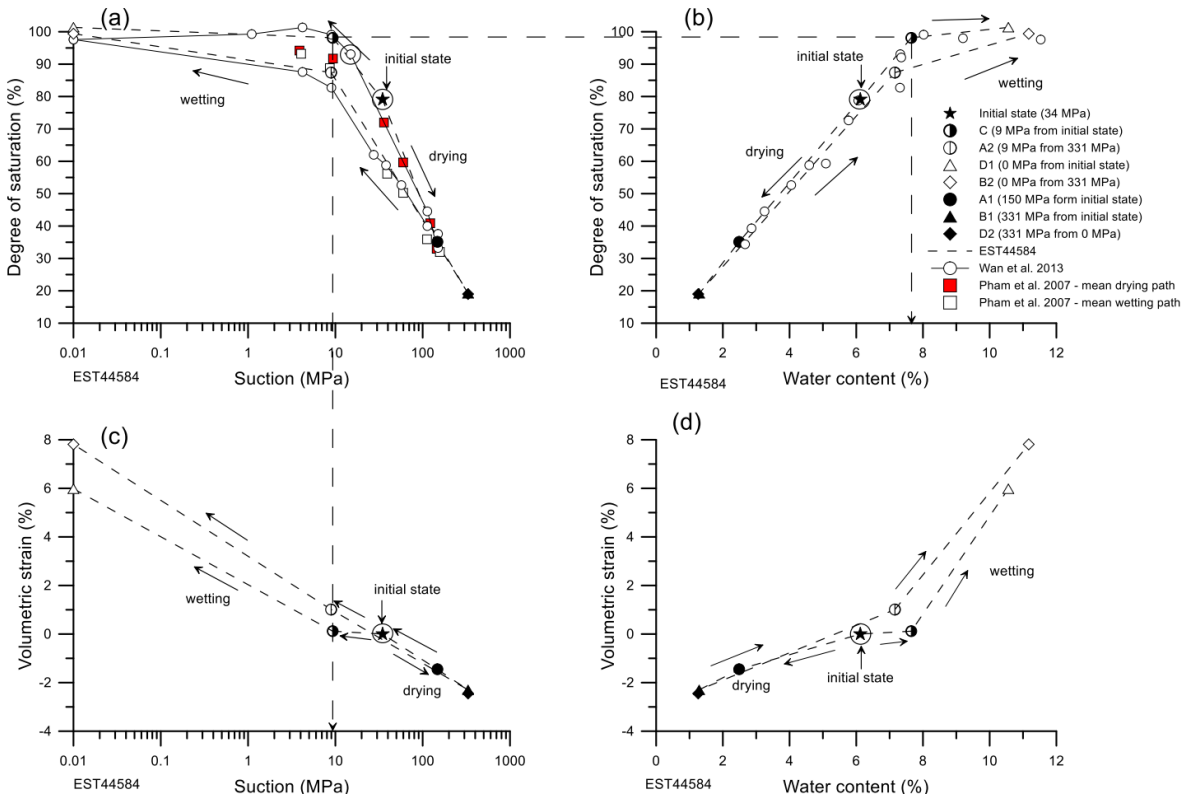

Figure 1.21. Water retention properties and volume changes obtained by suction control in terms of changes in degree of saturation and volume changes with respect to i) suction changes (a and c, respectively) and ii) water content (b and d, respectively) (Menaceur et al. 2016)

Minardi et al (2016) studied the swelling anisotropy of Opalinus clay, the clay mineral composition of which is similar to COx claystone. In their test, strain gages were directly glued on the sample side surface to measure the volume change of the material. The strain change demonstrates a more significant deformation perpendicular to, rather than along, the bedding planes. In particular, the wetting episode typically shows a profound strain variation than the drying episode. Results also indicate that a higher proportion of total clay mineral (including interstratified I/S, illite, muscovite, kaolinite, and chlorite) corresponds to a larger swelling pressure in all directions.

Thanks to the intriguing works of Saiyouri et al. (2000) and other researchers, we can have a basic knowledge of the two swelling mechanisms of smectite. From the viewpoint of the deformation scale, the two mechanisms corresponding to two different pore scales: the crystalline swelling occurs in micropores (3 to 12 Å) while the osmotic swelling occurs in mesopores (up to 10 nm). In the natural word, smectite does not appear as a single-phase but is interspersed in I/S aggregates, and I/S aggregates are mixed with other clay and non-clay minerals in COx claystone. With such a complex microstructure, the current understanding of COx claystone swelling usually remains phenomenological, the underlying relationship between multi-scales swelling mechanisms is still not completely understood.

1.3.2. Poro-mechanical properties

Numerous studies have confirmed that the water content change typically leads to the stiffness change of COx claystone (Ibrahim 2008; Cariou et al. 2012a; Zhang et al. 2019). COx claystone is known as a transverse isotropic material, thus its mechanical properties analysis should be carried on from two directions: along bedding planes (⊥) and perpendicular to bedding planes (‖). Cariou et al (2012a) reported the drained bulk moduli K_β ($\beta \in \{\perp, \parallel\}$), which is obtained by a series of "change in pore pressure" poro-mechanical tests, see Figure 1.22. Results demonstrate that $K_\parallel$ is typically greater than $K_\perp$, and dried samples exhibit higher values.

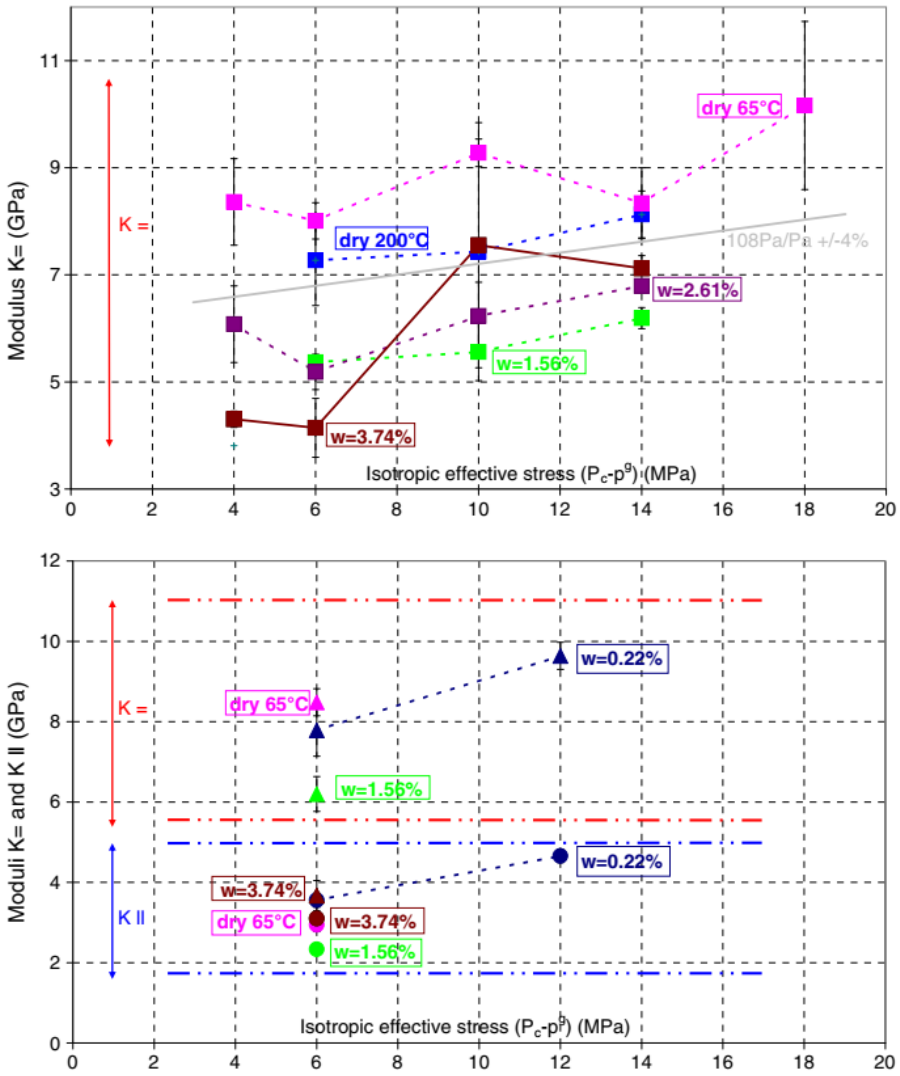

Figure 1.22. Evolution of moduli (K=) and Kzz(K‖) with the isotropic effective stress for samples 33957 (top) and 27404 (bottom) (Cariou et al. 2012a)

Since the water dilation coefficient is higher than the COx claystone one, the hydro-mechanical loading on the material may causes different effective tensile stresses due to water overpressure and low rock permeability (10^{-20} to 10^{-21} m^2 water permeability). Hence, understanding the poro-

mechanical properties of COx at different water saturations is crucial for the stability and safety of the nuclear waste repository (Duan et al., 2021; Hu et al., 2014). For instance, radioactive wastes are thermally active and temperature increase up to 90°C is expected by Andra. This effective stress is obviously linked to the material poro-elastic behavior and particularly to its Biot's tensor.

It has thus long been evidenced that this material exhibits a transverse isotropic behavior (Zhang and Rothfuchs, 2004; Guillon et al., 2012; Cariou et al., 2012) but most of the (very few) studies related to its poro-mechanical properties do not really take into account this important fact. It is may be due to the extreme difficulty in performing accurate measurements of strains (due to pore pressure) during a very long experimental time (weeks and/or months for a single test – see in the following). For such an anisotropy, the effective stress cannot be "a priori" calculated with a single Biot's coefficient b but with a two order Biot's tensor, which contains two independent components in the structural material axes. However, due to major difficulties to measure these components, many researchers simplified the experimental analyses, i.e. the tests were analyzed as if the COx claystone was isotropic (Bemer et al., 2004; Vincke et al., 1998). As a consequence, many experimental studies found in the literature, consider an "isotropic" Biot's tensor within the framework of isotropic poro-elasticity.

The measured Biot's coefficient of COx claystone found in the literature, is scattered in a large range - between 0.26 and 1. The reliability of such results can therefore be questioned. For a long period of time, Andra had used 0.6 as average b-value as a reference for numerical studies (Andra, 2005). Such disperse values evidence the difficulty to carry out "accurate" measurements. When compared with other rocks or porous materials, Biot's coefficients lower than 0.5 - 0.6 seem unlikely. b= 0.2-0.3 is met for some salts (Zhang et al., 2020) with a porosity less than 1%, 0.5 - 0.7 are quite common for concrete (Pei et al., 2019) or sandstones (Wang et al., 2018) but these kinds of material are far from being comparable to claystone, which remains a soft rock, especially in a fully water saturation state.

Some researchers have recently taken into account the transverse isotropy to consider the Biot's tensor with two components b_1 (along the bedding planes) and b_3 (in the vertical direction). Suarez-Rivera and Fjær (2013) put in light Biot's tensor anisotropy of Haynesville and Bossier shales. He et al. (2016) found that the Biot's tensor components of Bakken shales were between 0.57 and 0.70 and also exhibited a slight anisotropy. Belmokhtar et al. (2017) measured Biot's components of COx claystone between 0.85 and 0.98, with (slightly) higher values perpendicular to the bedding planes. Holt et al. (2018) also measured the anisotropy of Biot's tensor components of saturated soft shales, whereas the back-calculated bulk Biot's modulus leads to Biot's coefficient close to 1. This value is also confirmed by (Giot et al., 2018). More recently, a study of (Braun et al., 2021) showed two Biot's tensor

components close to 1 and depending on the confining pressure. However, the measurement methods were not direct and the Biot's coefficients were often obtained from back-calculations.

Our laboratory has carried out a series of poro-mechanical studies on COx claystone during the past decade (Cariou et al., 2012, 2013; Yuan et al., 2017; Hu et al., 2020). In contrast to many results reported in the literature, these studies clearly showed that, despite the structural anisotropy, the Biot's tensor was isotropic leading to a coefficient very close to 1.

However, these previous works were carried out on partially saturated material and used gas as the fluid to control pore pressure. It was particularly demonstrated by (Cariou et al., 2012) that any increase in gas pressure at both sample ends led to the same increase in pressure for the water and gas phases present into the material porous structure. This showed that gas was theoretically a convenient fluid to perform such experiments. However, doubts remained about their equivalence with measurements using water to control the pore pressure and to maintain a full saturation state.

Due to the low water permeability (about 10^{-20} to 10^{-21} m²), using water as the pore fluid to change pore pressure of saturated samples can be very time-consuming. Recently, Hu et al (2020) first use water as the pore fluid to identify the Biot's tensor of COx claystone. Results implies that even though the material exhibits anisotropic strain behavior, the Biot's tensor is isotropic and, given inherent experimental uncertainties is lying into the range 0.9 to 1 (Figure 1.23). From a theoretical viewpoint, the *in-situ* COx claystone can be considered as comprising of an isotropic solid matrix and an anisotropic pore network.

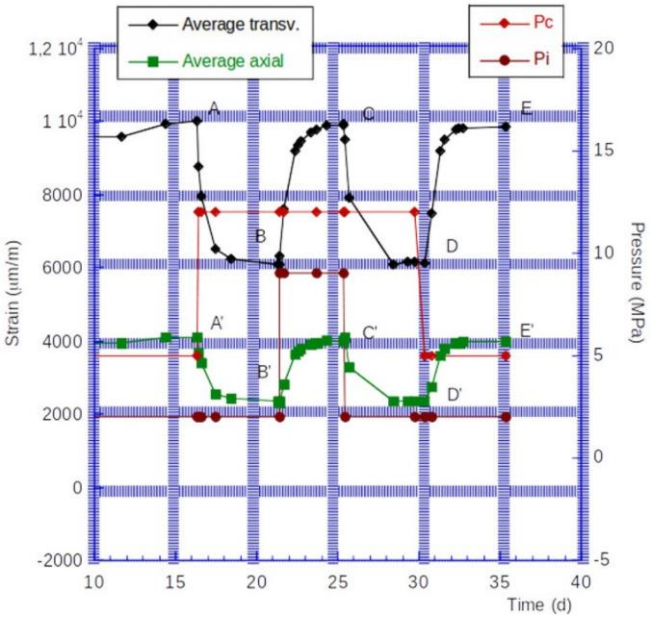

Figure 1.23. a typical result of the "change in pore pressure" test for COx claystone (Hu et al. 2020)

The multi-scales swelling plays an important role in the self-sealing of EDZ. In the literature, swelling can lead to the increase of water content and porosity. The swelling amplitude increases with the sample saturation degrees and smectite content. However, the effect of smectite distribution in the interstratified illite/smectite phases has not been reported. Moreover, the link between smectite swelling-clay matrix deformation and macroscopic swelling of COx claystone is still poorly understood. Therefore, understanding the multi-scales swelling mechanisms of COx claystone at different saturation states is crucial. In this thesis, it is concerned particularly with the underlying dominant swelling mechanisms as saturation changes.

Pore water content can significantly increases during the hydration of COx claystone. Due to the low rock permeability, pore pressure will cause effective tensile stresses on the solid phase during hydro-mechanical loadings. In the laboratory conditions, the Biot coefficient can be determined by the "change in pore pressure" test. The Biot coefficient of dried and partially saturated COx claystone with gas is confirmed to be isotropic (Hu et al. 2020) and close to 1 (Cariou et al. 2012a; Yuan 2017), while the Biot coefficient of saturated material is still needed to be further investigated. In this thesis, experiments have been designed to complete gas experiments and to verify whether they are consistent with water experiments. Reconstituted synthetic water (close to the in-situ one) was used to measure the Biot's components in the saturated state. Two main results had to be confirmed: Biot's tensor isotropy and a unique coefficient close to 1.

1.4.Fluid transport: permeability, self-sealing and gas breakthrough

The continuous heat release of the long-life radioactive waste can reduce the strength of the engineering barrier (Reinhardt and Jooss 2003). Once the engineered barrier is damaged, the radionuclide can dissolve in the groundwater and percolate into the COx formation and causing contamination of the biosphere. On the other hand, degradation of the engineered barrier would allow reverse groundwater infiltration, this will cause a moist reservoir environment inside the repository. Chemical interactions between groundwater and metal facilities can cause metal corrosion and gases generation (usually hydrogen) around the waste repository. When the gas generation rate is much greater than its dissolution rate, a gas pressure gradient arises and the preferential gas pathways are bound to form and propagate, which may allow the radionuclides migrate through to the formation. Hence, it is essential to understand, analyze, and quantify the water or gas transport in COx claystone.

1.4.1. Permeability of COx claystone

1.4.1.1 Mono-phase fluid transport

For mono-phase flow, the fluid transport is essentially dominated by the fluid pressure gradient and follows Darcy's law. The analysis of Darcy's law is different for the incompressible fluid (such as water or oil, etc.) and the compressible fluid, i.e. a gas phase. Assuming the flow is unidimensional and neglecting the effect of gravity, Darcy's law for water can be simplified as:

$$\frac{Q}{A} = V_x = -\left(\frac{K_{\text{water}}}{\mu}\right)\frac{dP(x)}{dx} = \frac{K_{\text{water}}}{\mu}\frac{(P_1 - P_2)}{L} \tag{1.12}$$

where V_x is the average flow velocity in the direction of $\vec{x}$, which can be derived by the ratio of volume flow rate Q and cross-sectional area A; K_{water} is the water permeability along $\vec{x}$, μ is the liquid viscosity. P_1 and P_2 are respectively the gas pressure at upstream and downstream sides of the sample. From rel. (1.12), one can find that K_{water} is an inherent property of the material that theoretically should not depend on the experimental setting conditions, such as sample size and temperature. In fact, water interacts with clay rock (and also with many low porosity materials – concrete for example) and K_{water} is not an intrinsic property. When compared to gas permeabitliy K_{gas}, orders of magnitude difference can be usually found.

For a gas transport process, the gas flux state is governed by its pressure, volume, and temperature. Assuming the gas is perfect, the ideal gas law can be used as the mass balance equation:

$$PV = nRT \tag{1.13}$$

Assuming the use of an ideal gas and under isothermal conditions rel. (1.13) leads to

$$\frac{P}{\rho} = \frac{dP}{d\rho} = cste \tag{1.14}$$

According to rel. (1.12) – (1.13) or (1.14) and the mass balance equation, the Darcy's law for a compressible media (i.e. a gas) (K_{gas}^{app}) leads to:

$$\frac{Q}{A} = \frac{K_{gas}^{app}}{2\mu L}\frac{(P_1^2 - P_2^2)}{P_2} \tag{1.15}$$

In rel. (1.15), Q is the volumetric gas flow rate at downstream sample side. Researchers found that the calculated gas permeability using experimental data and rel. (1.15) is not constant but linearly decreases with increasing mean gas pressure (Klinkenberg 1941; Tanikawa and Shimamoto 2006; Chen et al. 2013; Song 2014; Sabet et al. 2019). This phenomenon relates to the pressure- and temperature-dependent mean free path of the gas molecules (Klinkenberg 1941; Sabet et al. 2019). When the gas pressure is low and the average pore diameter is small, the mean free path shortens and increases the frequency of collision between gas molecules and pore walls and results in an additional gas slip flow along the wall surface (Klinkenberg 1941). This effect is termed "Klinkenberg effect" or "slippage effect" and can be written as:

$$K_{gas}^{app} = K_{gas}^{int}\left(1 + \frac{\beta}{P_m}\right) \tag{1.16}$$

where β is the Klinkenberg coefficient, which is related to the temperature and the average pore diameter for gas transport, P_m is the average gas pressure: $P_m = (P_1 + P_2)/2$. Generally, a so-called "Klinkenberg correction" method is used to remove the Klinkenberg effect. It is achieved by recording the measured apparent permeability at different average gas pressure i.e. K_{gas}^{app} as a function of $(1/P_m)$. Extrapolating the trend curve to infinite pressure ($1/P_m \rightarrow 0$), the intrinsic gas permeability can be estimated, see Figure 1.24.

Experiments confirmed that Klinkenberg coefficient depends on the gas type. Boulin et al. (2008) studied the nitrogen flow in COx claystone and found that rel. (1.16) is only valid for gas pressure larger than 5 bar. This reveals that the Darcy's flow is not the dominant transport mechanism at low gas pressure. Chen et al. (2012) used argon and helium to study gas transport properties of two concrete materials. Results illustrate that the Klinkenberg effect is less pronounced by using argon than helium (Figure 1.24 (a)). This can be explained by the molecule size of argon is bigger than helium and lead to a less significant slippage effect. Skoczylas (2011) and M'Jahad (2012) used argon to study the permeability of COx claystone and found that the Klinkenberg coefficient appears in a relatively small value when injected gas pressure is between 1 to 3 MPa, regardless the sample cracked or not (Fig.1.24 (b)). In literature, the water permeability of saturated COx claystone ranges in 10^{-20} – 10^{-21} m², and the

Klinkenberg corrected gas permeability of which is found located between 10^{-17} m² and 10^{-19} m² (Davy et al. 2007a; M'Jahad 2012; Song et al. 2016a; Liu et al. 2016).

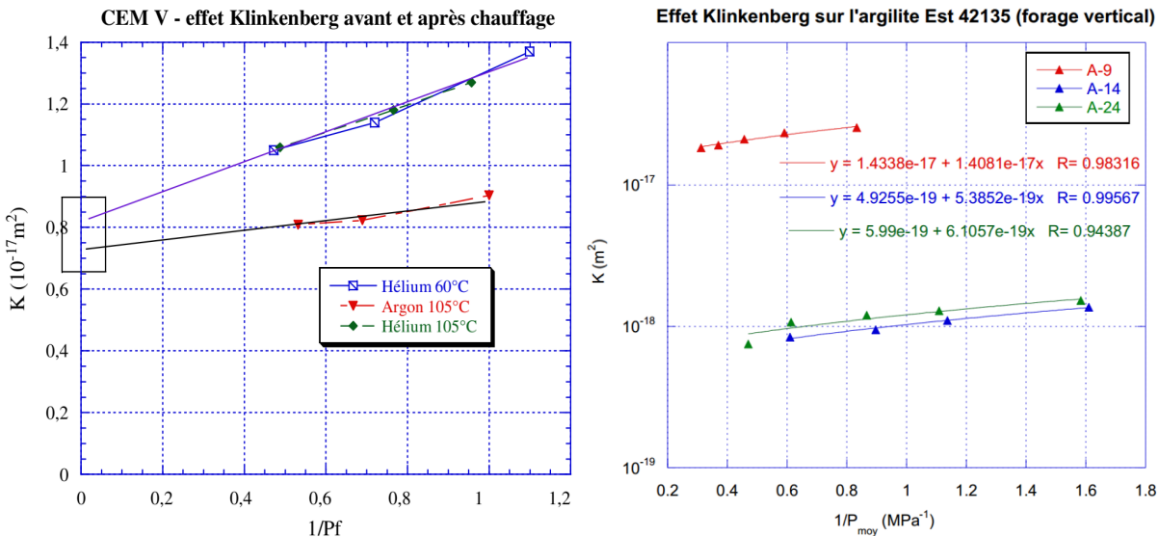

(a) (b)

Figure 1.24. evolution of apparent gas permeability vs. the inverse of average gas pressure of: (a) CEMV concreate, using helium and argon as the injected gas; (b) COx claystone EST42135, sample A-9 is cracked while samples A-14 and A-24 remain "intact" (Chen et al. 2012; M'Jahad 2012)

1.4.1.2 Two-phase fluid transport

If a porous material contains two or more immiscible fluids (e.g., water, gas, oil, etc.), the mass transfer in the pore network is called two-phase (or multi-phase) flow. In the context of nuclear waste storage, the two-phase flow in COx claystone is comprised of underground water and corrosion-induced gas. Four transport mechanisms have been documented in the literature that leads to gas migration: diffusion, two-phase capillary flow, dilatancy-controlled flow, and gas fracturing (Horseman et al. 1999; Hildenbrand et al. 2002; Marschall et al. 2005). Among them, the dilatancy-controlled flow and gas fracturing only occur when the initial gas pressure is extremely high (at least exceed the confining pressure), which is not the potential scenario around the nuclear storage repository. Hence, only diffusion and two-phase flow are discussed here below.

Diffusion refers to gas molecule migration by means of dissolving in pore water, in the dispersed organic matter, and long mineral surfaces. This process can occur at very low gas pressure because it is mainly controlled by the gas concentration difference, the ambient temperature, and the organic matter maturity level (Amann-Hildebrand et al. 2012, 2013). The effective diffusion coefficient (D_{eff}) is used to represent the bulk diffusion efficiency of claystone, expressed by Fick's first law:

$$J_D = -D_{\text{eff}} \frac{dC_{bulk}}{dx} \tag{17}$$

Where J_D is the diffusive flux (mol/m²/s), D_{eff} is the effective diffusion coefficient (m²/s), C_{bulk} is the bulk gas concentration (mol/m³) comprising contributions by pore water, organic matter, and matrix mineral surface, x is the sample length (m) that along the direction of concentration gradient. In the claystone, diffusion mainly occurs in the water-saturated pores, and D_{eff} can be characterized by the product of the gas diffusion coefficient in free water (D_{water}) and the water-saturated porosity (ϕ):

$$D_{\mathrm{eff}} = \tau \cdot D_{\mathrm{water}} \cdot \phi \tag{1.18}$$

τ is a corrective factor that is able to take into account the porous network tortuosity.

By definition, diffusion is a continuous and ubiquitous process as long as the gas phase is present. However, compared with the pressure gradient-driven transport (Darcy's flow), its transport efficiency is very limited. In analogy to heat transport, Amann-Hildenbrand et al. (2012) used the dimensionless Peclet number (*Pe*) (sample length×fluid velocity/effective gas diffusion coefficient) to express the ratio of convective to diffusive transport. Results indicate that pressure-driven flow is the dominating process when *Pe* >> 1 while diffusion dominates the transport process when *Pe* << 1. Typically, a Peclet number close to 1 corresponds to an effective permeability coefficient less than 10^{-22} m². For most laboratory gas transport tests on COx claystone, the value of *Pe* is found much larger than 1 even if only a small gas pressure (several bars) is applied.

Two-phase capillary flow refers to a pressure gradient-driven two immiscible fluids volume flow in the porous network. Fluid phases are not synchronized during a two-phase capillary flow, and each fluid phase has its own effective permeability (K_{eff}). When the material is 100% saturated by one fluid, K_{eff} of the fluid is equal to its intrinsic permeability (K_{int}) independent of the fluid type. When the sample is partially saturated, the ratio of K_{eff} and K_{int} of a certain fluid phase is defined as its relative permeability (K_{rel}).

Sometimes, K_{rel} is very difficult to measure directly especially if concerning the wetting phase. For example it is quite easy to measure effective gas permeability for a partially water saturated material since effective water permeability is almost non directly measurable for low porosity materials. If the saturation is known, K_{rel} can be estimated by the van Genuchten-Mualem (vGM) model (Schaap and Leij 2000; Marschall et al. 2005; M'Jahad et al. 2017) as:

$$\begin{aligned} K_{\mathrm{rg}} &= (1 - S_w)^{\eta} \left(1 - S_w^{\frac{1}{m}}\right)^{2m} \\ K_{\mathrm{rw}} &= S_w{}^{\eta} \left[1 - \left(1 - S_w^{\frac{1}{m}}\right)^{m}\right]^2 \end{aligned} \tag{1.19}$$

where K_{rg} and K_{rw} are the relative gas permeability and relative water permeability, respectively; η and m are empirical shape factors. η describes the pore connectivity of the material while m corresponds to the pore size distribution. S_w is the water saturation degree, which can be determined by weighing the sample or by knowing the capillary pressure (M'Jahad et al. 2017):

$$S_w = \frac{m_{\text{current}} - m_{\text{dry}}}{m_{\text{saturated}} - m_{\text{dry}}} = \left(1 + \left(\frac{P_{\text{cap}}}{P_r}\right)^{\frac{1}{1-m}}\right)^m \tag{1.20}$$

where $m_{current}$ is the present sample mass, m_{dry} is the dry mass, and $m_{saturated}$ is water-saturated mass. P_{cap} refers to the present capillary pressure, and P_r is interpreted as the gas entry pressure (see section 3.3).

It is worth noticing that the empirical parameters η and m vary significantly between materials. For COx claystone, η is generally pick 0.5 (Marschall et al. 2005) and ANDRA (2005) suggest that m is around 0.329. However, Cariou et al. (2012b) found that using rel. (1.19) to fit K_{rg} vs. saturation data, m equal to 0.817. Such a variation in m can be interpreted by the different clay mineral contents between samples, which in turn affect the geometry of the morphology of pores. In fact, with gas for which direct measurements are available, these two coefficients can be regarded more as fitting properties without real physical meanings.

1.5.Self-sealing of COx

One of the favorable properties of the EDZ is that cracks tend to close over time after the repository closure, i.e. self-sealing. In terms of fluid transport, self-sealing leads to a significant decrease in gas/water permeability (Davy et al. 2007a; Delay et al. 2014; Bossart et al. 2019). Self-sealing is a very important property since it can delay the radionuclides migration along the water and gas flow channels. Although the term "self-healing" is mentioned in some European projects for integrated research on the nuclear waste geological storage (such as SELFRAC and NEA), most observations reveal that the EDZ of COx claystone can only self-sealed or partially self-healed (de La Vaissière et al. 2015).

Table 1.7 exhibits an overview of the classical experimentally research on the self-sealing of different clayey materials. We can summarize from Table 1.5 that in both *in situ* and laboratory experiments, the self-sealing of claystone mainly reflects on the closure of cracks and the decrease in permeabilities. Table 1.7 also illustrates various artificial fractures that were used to simulate the cracks in laboratory experiments, such as cylindrical tiny holes, hollowed samples, neat cracks cut by diamond saw, and compressed shear cracks. A 3D visualization of the excavation-induced fracture network is shown in

Figure 1.25. One can find that the shear cracks are considered to be the closest type to the natural EDZ cracks.

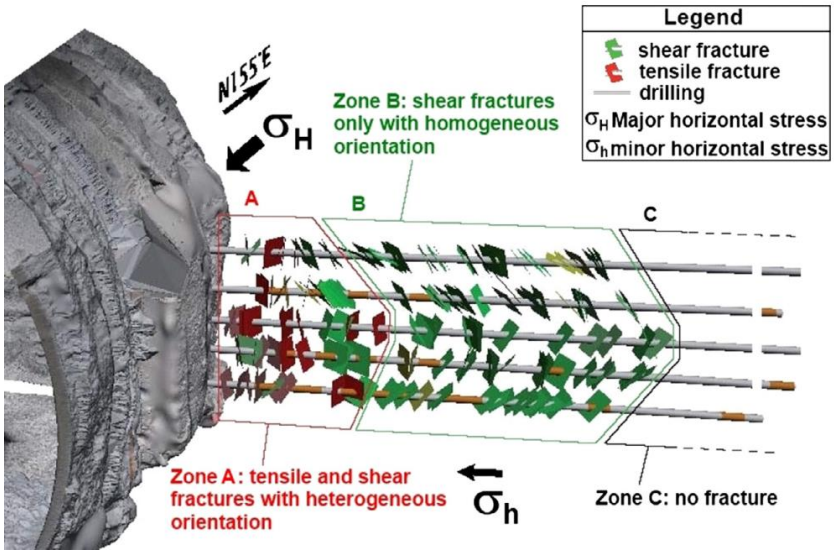

Figure 1.25. 3D visualization of typical excavation-induced fracture network (de La Vaissière et al. 2015)

Table 1.7. laboratory studies on the self-sealing of claystones

Category of rock	Source	Damaged state	Experiment conditions	Evaluation parameters
COx claystone	Davy et al. (2007)	Split-cracked along the beddings	Change confining pressure	Kw VS. Cc; Kg VS. Cc
	Zhang & Rothfuchs (2008)	Shearly cracked by deviatoric stress	Re-compression via various loading paths Re-saturation by inject water	Kg VS. Pc; Kg VS. Time
	Zhang (2011, 2015, 2017)	Compress-cracked parallel to beddings	Deviatoric compressed; Re-saturation under various RH; Thermal loading	Kg VS. Crack aperture Kg VS. Strain; Kw VS. *T*
	Giot et al. (2019)	Cutted with a diamond saw along the beddings	Re-saturation at constant confinement	Kw VS. Time Geometry of crack (μCT)
Boom clay & Opalinus clay	Bernier et al. (2007)	Artificially cracked hollow sample	Acoustic emission/isostastic	Strain VS. Time; Kw VS. Time
	Bastiaens et al. (2007)	Cut fractures parallel to the beddings	Re-saturation at constant confinement; *In situ* measurement	Pp VS. Time; P-wave VS. Time Geometry of crack (μCT)
	Van Geet et al. (2008)	Drilled a tiny hole through the axis of the sample & Artificial cracks	Inject various solutions	Kw VS. Time Geometry of crack (μCT)
	Monfared et al. (2012)	Shearly cracked hollow sample	Re-saturation; Heating-cooling loading	Pp VS. *T*; Strain VS. *T*
	Chen et al. (2014)	Drilled a tiny hole through the axis of the sample, parallel to the beddings	Perform heating cycles after sealing	Kw VS. Time; Kw VS. *T* Geometry of crack (μCT)
	Bossart et al. (2019)	EDZ at Mont Rock Laboratory	*In situ* pneumatic-hydraulic tests *In situ* miniseismic tests	Kw VS. Location; Pp VS. Time P-wave (S-wave) VS. Depth

Notions: Kw/Kg: water/gas permeability; Cc: crack closure; Pc/Pp: confining/pore pressure; *T*: temperature

Many field experimental studies have been conducted on the effect of self-healing on permeability. For instance, ANDRA performed a series of one-year repetitive *in-situ* hydration tests on the EDZ of COx formation in Bure URL, France. By monitoring the change of hydraulic conductivity around excavated tunnels over time, the hydraulic conductivities of all the observed points decreased and stabilized below 10^{-10}m/s, shown in Figure 1.26. However, field experiment is limited to the qualitative description of sealing process, the self-sealing mechanisms and quantitative analysis need to be studied by laboratory experiments.

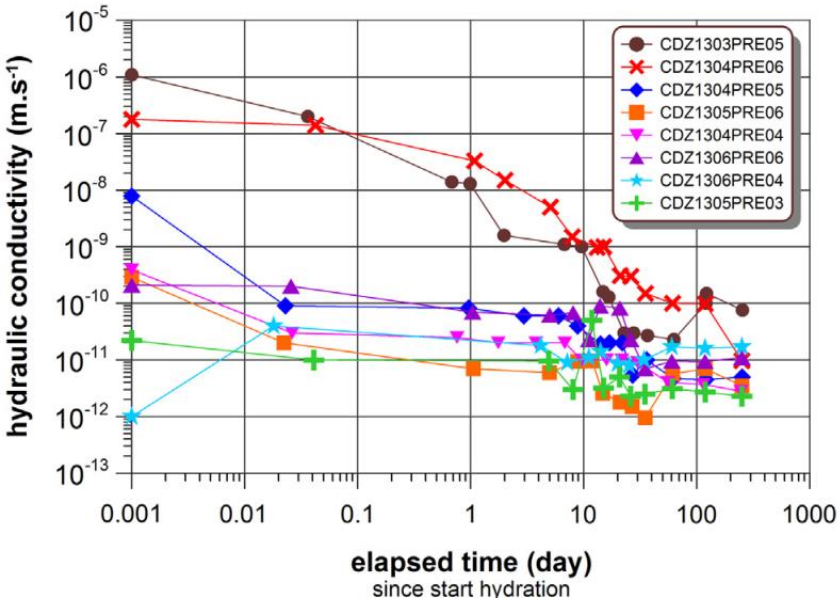

Figure 1.26. the change of hydraulic conductivity during the hydration tests (de La Vaissière et al. 2015)

In the laboratory experiments, the *in-situ* stress is reproduced by loading confining pressure on re-cored samples. Various laboratory techniques (e.g. LVDT, strain gauges, wave velocity, etc.) were used to study the effect of confining pressure on self-sealing. Davy et al (2007) reported that loading confining pressure leads to an irreversible decrease of the crack aperture in COx claystone. Figure 28 exhibits the evolution of crack closure (cc) subjected to cycles of loading/unloading confining pressure (P_c), the corresponding gas permeability (K_g) VS. confining pressure (P_c), and gas permeability (K_g) VS. crack closure (cc). One can find in Figure 1.27 (a) that despite the close amplitude is different for each sample, P_c VS. cc tends to be linear after the first cycle, and each loading almost identical to the other. This means that during increasing P_c cracks first irreversibly closed then behaved elastically. Figure 1.27 (b) shows that K_g keeps in the same order of magnitude after several cycles of loading/unloading P_c, this means that increasing Pc can lead to an irreversible decrease of Kg.

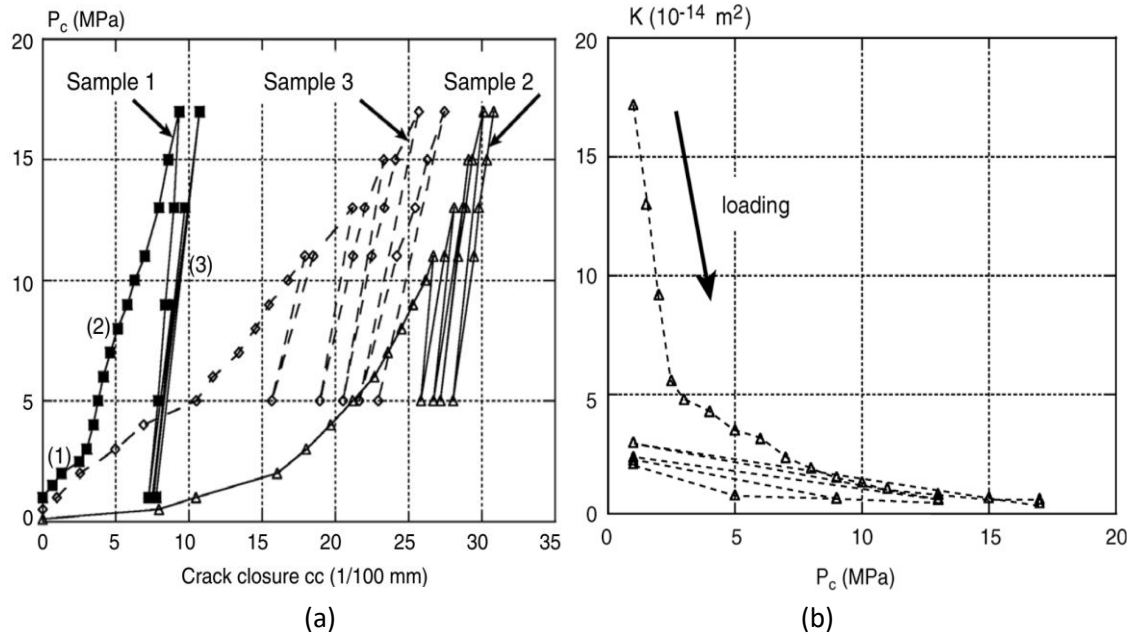

(a) (b)

Figure 1.27. confining pressure Pc vs. crack closure cc for three COx samples (Davy et al. 2007a)

Thermal impact on self-sealing is studied by measuring the relationship between the intrinsic permeability (K_{int}) and temperature. Some researchers noted out that increasing temperature will result in a slight increase of intrinsic permeability which is attributed to the fluid viscosity and density as they will decrease with increasing the temperature (Chen et al. 2014; Zhang 2018). Chen et al. (2014) measured the K_{int} of both cracked and un-cracked Boom Clay under different temperatures by using three salt solutions and results showed that temperature has no adverse effect on the self-sealing of Boom Clay (Fig. 1.28 (a)). Similar conclusions are also reported in the study of COx claystone (Delage et al. 2000; Monfared et al. 2012; Zhang 2018). However, the self-sealing of Opalinus Clay proved to be more temperature-dependent. Figure 1.28 (b) exhibits that by injecting with three different solutions, the permeability of Opalinus Clay reduces by tens times when temperature goes up from 20°C to 80°C.

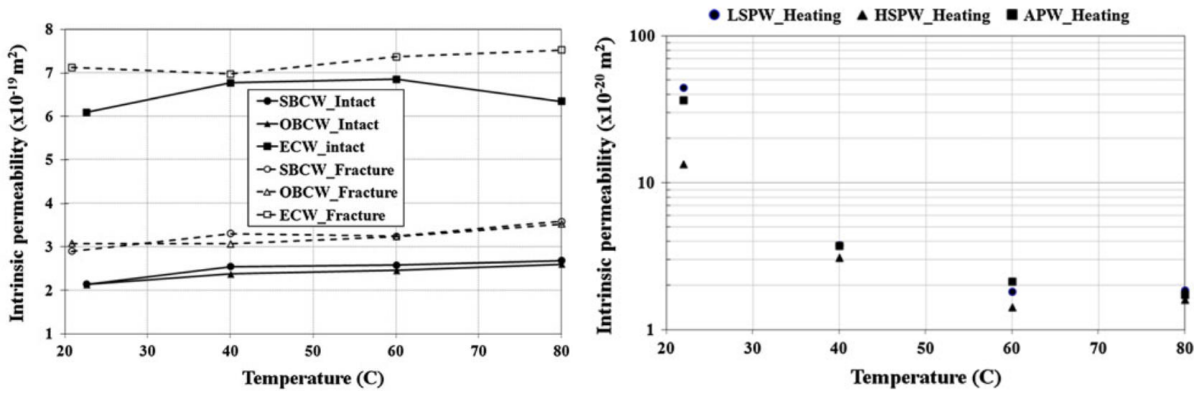

(a) (b)

Figure 1.28. (a) Intrinsic permeability VS. Temperature of Boom Clay; (b) intrinsic permeability VS. temperature of Opalinus Clay (Chen et al. 2014)

Besides the effect of confining pressure and thermal aspects, the clay minerals swelling during re-saturation has an important effect on self-sealing also. The principle of volumetric swelling is the interaction between underground water and specific clay mineral (i.e. smectite), which was already discussed in section 2.2. Table 1.8 shows the water permeability measurements of GDR-FORPRO research program, the macro-cracked COx claystone water permeability decreases by one to three orders of magnitude during 4-21 days, with a volumetric swelling amplitude between 0.03-0.18mm. Davy et al (2007) performed pulse water injection tests on the macro-cracked COx claystone samples, results demonstrated that the water permeability decreases by two or three orders of magnitude during 2-10 days, which is in consistency with the results of GDR-FORPRO.

Table 1.8. Water permeability tests from GDR-FORPRO research program (Davy et al. 2007)

Sample no.	Plug no.	Max crack closure (mm)	Max positive crack closure (mm)	Swelling (mm)	K_0 (m^2)	K_f (m^2)	Test duration (days)
2	MSE761	0.03	0.07	0.03	9.1×10^{-18}	3×10^{-21}	4
3	MSE761	0.06	0.11	0.07	2.8×10^{-18}	3×10^{-21}	6
4	MSE748	0.05	0.06	0.04	6×10^{-20}	7.9×10^{-21}	5
5	MSE748	0.06	0.16	0.18	1.5×10^{-19}	1×10^{-21}	21

The volumetric swelling is quantitatively analyzed by monitoring the deformation of strain gauges on the sample surface (Zhang 2011, 2018; Minardi et al. 2016). Particularly, Zhang (2011) carried out the water injection and compression tests simultaneously on an axially cracked COx sample, the deformation and water permeability are monitored over time. Figure 1.29 illustrates the synthetic impact of hydrostatic stress and water-clay mineral interaction. After water injection, the swelling effect is significant even under hydrostatic stress loading. The swelling-induced sealing reflects on: 1) the non-stop decrease over time of water permeability at each elevated confining stress; 2) by unloading the sample to 1 MPa, the rebounded water permeability is still three orders of magnitude lower than the initial value before self-sealing.

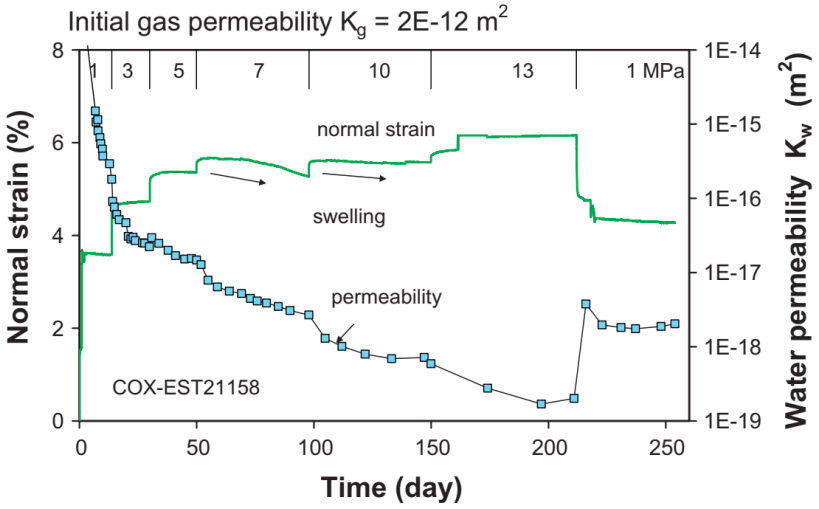

Figure 1.29. Evolution of normal strain and water permeability of a axial-parallel cracked COx sample, under the hydrostatic stress loading and water injection (Zhang 2011)

By visualizing the cracked zone and the water permeability over time, Giot et al. (2019) proposed a useful conceptual model to describe the self-sealing mechanisms of clay-rich samples (UA type), which involved the crystalline swelling and osmotic swelling and the mineral particle clogging of the crack zone. Technically, the *in-situ* volume swelling behavior is not as easy to analyze as confining pressure and temperature because it is difficult to evaluate separately from the confining pressure.

To sum up, the self-sealing and (partially) self-healing of EDZ is a complex long-term thermal-hydro-mechanical coupling process, depending on the morphology of the fracture network, stress filed re-distribution, thermal impacts, and swelling capacity of smectite.

1.6. Gas breakthrough pressure

Since the instantaneous gas pressure (mainly hydrogen) around the repository is not like to exceed the formation stress (approx. 14 MPa in Bure URL), the dilation of flow passages and gas fracturing are not the plausible dominant gas transport mechanisms in the COx claystone. According to the laboratory experimental data, the equivalent gas permeability of diffusion in COx claystone is orders of magnitude smaller than that of the pressure-driven transport process (Hildenbrand et al. 2002, 2004; Amann-Hildebrand et al. 2012). Based on the Laplace's law, the mobility of the gas phase in the pressure-driven transport is determined by capillary process. The capillary process is affected by interfacial tension, wetting angle, and pore geometry (Hildenbrand et al. 2002, 2004; Busch and Amann-Hildenbrand 2013). Generally, Young-Laplace's equation (rel. (1.2)) is used to determine the threshold pressures during the gas migration process.

Figure 1.30 illustrates that the relationship between capillary pressure and gas saturation during two-phase flow. Assuming the pore system is initially water-saturated and the gas pressure increase continuously from zero, the gas saturation does not increase until gas starts to enter the porous system at a certain pressure, which is termed *capillary entry pressure* (P_{Entry}). At P_{Entry}, the gas phase will drive the pore water to start moving towards the largest (not necessarily interconnected) pores. By increasing the gas pressure, the gas will successively invade the porous structure and drive the free water out of the pore network. When the first interconnected gas flow path appears, the corresponding capillary pressure is called *gas breakthrough pressure* ($P_{\text{Breakthrough}}$). After breakthrough, the gas saturation and effective gas permeability increase with capillary pressure. When no more water is extruded from the rock body, we can obtain the corresponding maximum gas saturation and irreducible water saturation. The maximum gas saturation and the irreducible water saturation correspond to the biggest effective gas permeability and the smallest effective water permeability, respectively. With successive decreases in the capillary pressure from this point, water will gradually refill the pore network. When the last inter-connected gas flow path is closed, the corresponding

pressure is called *snap-off pressure* ($P_{snap\text{-}off}$) (or *residual pressure*). $P_{snap\text{-}off}$ is typically smaller than P_{Entry} and $P_{Breakthrough}$ (Egermann et al. 2006). Amann-Hildebrand et al (2012) reported that the $P_{snap\text{-}off}$ of limestone and shale are about half the $P_{Breakthrough}$.

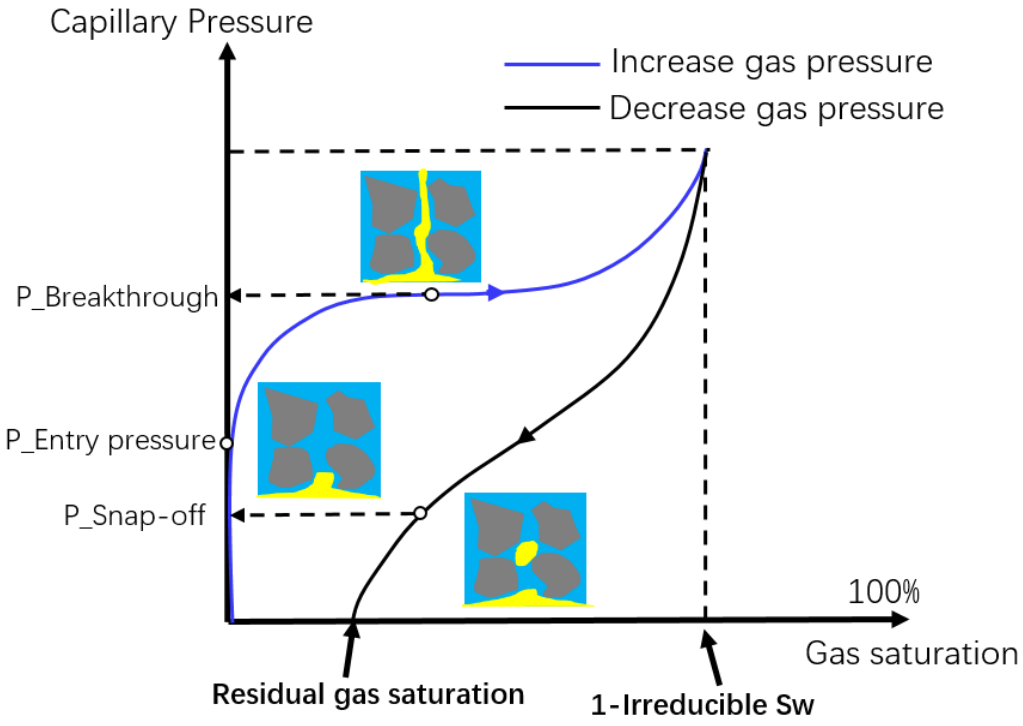

Figure 1.30. The capillary pressure of the gas phase as a function of water saturation in a two-phase flow process, modified according to Amann-Hildebrand et al. (2002)

Generally, there are two approaches to measured the $P_{Breakthrough}$: steady-state approach and non-steady-state approach. For a steady-state approach, the sample is first subjected to a constant confining pressure, then a reservoir is connected to its upstream with constant gas pressure and the downstream connects to the atmosphere. Stepwise increasing the upstream gas pressure, $P_{Breakthrough}$ is determined by a continuous gas flow leading to pressure detected at downstream, see Figure 1.31 (a). For a non-steady-state experiment, both ends of the sample are connected to a gas reservoir. By imposing an instantaneously high gas pressure at upstream (exceeding the expected GBP), the gas will migrate under the pressure gradient, the breakthrough is assessed when the downstream pressure start to increase, see Figure 1.31 (b). With the non-steady-state experiments, we can also get both $P_{Breakthrough}$ and $P_{snap\text{-}off}$.

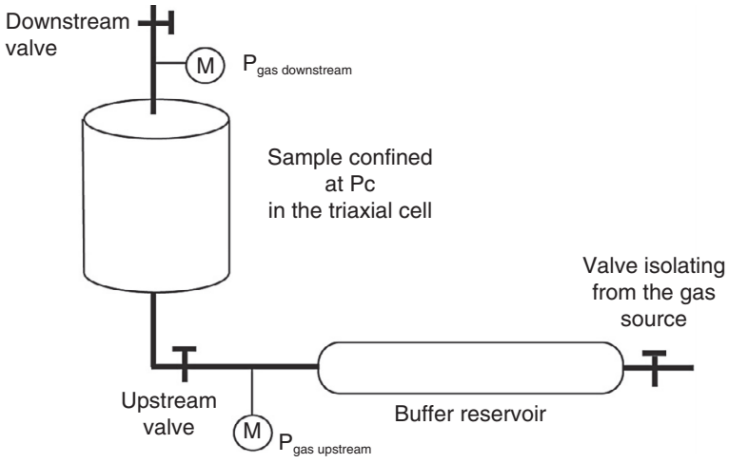

(a)

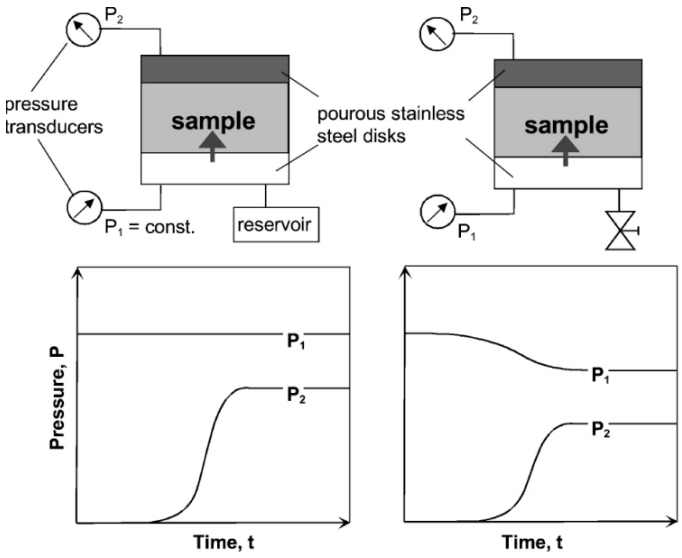

(b)

Figure 1.31. Schemes of two approaches of the gas breakthrough experiments (a) steady-state experiment with a constant upstream pressure (Song et al. 2016a) (b) non-steady-state experiment with a fixed upstream volume (Hildenbrand et al. 2002)

In the field of oil exploration and CO_2 storage, both the steady-state approach and the non-steady-state approach are widely used to study the gas transport in various sedimentary rocks (such as claystone, limestone, sandstone, etc.) using different gases. Results reveal that the transport porosity account for a very small fraction of the total porosity regardless the gas type. The study on the COx claystone shows that, the maximum gas effective permeability after breakthrough decreases with capillary pressure, eventually stabilizes at a value one to several orders of magnitude lower than the intrinsic permeability (Zhang 2015). For different gas type, nitrogen have the biggest GBP while CO_2 corresponds to a lowest, the interfacial tension and wetting angles of different gases seem to be the key impact factors to the breakthrough pressure (Hildenbrand et al. 2004; Busch and Amann-

Hildenbrand 2013). The snap-off pressure is a rock type-dependent parameter and varies from 0.06 to 6.7 MPa for different claystone (Hildenbrand et al. 2002).

For nuclear waste storage, steady-state approach is used to simulate the gradual accumulation effect of gas pressure around the repository. Davy et al. (2009) used this method to study gas migration through saturated bentonite/argillite (COx claystone) plugs. The effective swelling pressure after water injection is around 7.5 MPa, while the "gas critical pressure" (i.e. the injection pressure when the first gas bubble is detected at downstream, often called discontinuous $P_{Breakthrough}$) equal to 4.35 MPa $\pm$ 0.95. Liu et al. (2014) performed similar experiments on bentonite/sand plugs. The effective swelling pressure of such mix material is 7.32 MPa $\pm$ 0.11, which is compatible with the value of bentonite/argillite plugs. $P_{Breakthrough}$ is sensitive to the plug saturation state: when the sample is fully saturated, the continuous $P_{Breakthrough}$ is equivalent or slightly higher than the swelling pressure; when the plug is de-saturated (by imposing gas in one of the end surfaces), both the discontinuous and continuous breakthrough pressure are lower than for the fully saturated cases. M'Jahad et al. (2017) found that $P_{Breakthrough}$ is very sensitive to the damage state of COx claystone even under high confining pressure. This means that it is a useful *in-situ* materials damage detector.

References

Abell, Willis, D.A. Lange (1999) Mercury Intrusion Porosimetry and Image Analysis of Cement-Based Materials. Journal of Colloid and Interface Science 211:39–44. https://doi.org/10.1006/jcis.1998.5986

Al-Ani, Sarapää (2008) CLAY AND CLAY MINERALOGY. Geological survey of Finland

Altaner, Bethke (1988) Interlayer order in illite/smectite. American Mineralogist 73:766–774

Amann-Hildebrand A, Bertier P, Busch A, Krooss BM (2013) Experimental investigation of the sealing capacity of generic clay-rich caprocks. International Journal of Greenhouse Gas Control 19:620–641

Amann-Hildebrand A, Ghanizadeh A, Krooss BM (2012) Transport properties of unconventional gas systems. Marine and Petroleum Geology 31:90–99

Anderson RL, Ratcliffe I, Greenwell HC, et al (2010) Clay swelling — A challenge in the oilfield. Earth-Science Reviews 98:201–216

Andra (2005) Dossier 2005 Argile. ANDRA, Collection les Rapports

Barrett EP, Joyner LG, Halenda PP (1951) The Determination of Pore Volume and Area Distributions in Porous Substances. I. Computations from Nitrogen Isotherms. J Am Chem Soc 73:373–380. https://doi.org/10.1021/ja01145a126

Bergaya F, Lagaly G, Vayer M (2013) Cation and Anion Exchange. In: Developments in Clay Science. Elsevier, pp 333–359

Bertier P, Schweinar K, Stanjek H, et al (2016) On the use and abuse of N2 physisorption for the characterization of the pore structure of shales. pp 151–161

Bésuelle P, Hall SA (2011) Characterization of the Strain Localization in a Porous Rock in Plane Strain Condition Using a New True-Triaxial Apparatus. In: Bonelli S, Dascalu C, Nicot F (eds) Advances in Bifurcation and Degradation in Geomaterials. Springer Netherlands, Dordrecht, pp 345–352

Bish DL (1993) Studies of clays and clay minerals using X-ray powder diffraction and the Rietveld method. Clay Minerals Society, San Diego, CA, pp 79–122

Bossart P, Nussbaum C, Schuster K (2019) Generation and Self-Sealing of the Excavation-Damaged Zone (EDZ) Around a Subsurface Excavation in a Claystone. In: Dewers T, Heath J, Sánchez M (eds) Geophysical Monograph Series, 1st edn. Wiley, pp 125–143

Boulin, Angulo-Jaramillo, Daian, et al (2008) Experiments to estimate gas intrusion in Callovo-oxfordian argillites. Physics and Chemistry of the Earth, Parts A/B/C 33:S225–S230

Brisard, Davy, Michot, et al (2018) Mesoscale pore structure of a high-performance concrete by coupling focused ion beam/scanning electron microscopy and small angle X-ray scattering. J Am Ceram Soc jace.16059

Brunauer S, Emmett PH, Teller E (1938) Adsorption of Gases in Multimolecular Layers. J Am Chem Soc 60:309–319. https://doi.org/10.1021/ja01269a023

Busch, Amann-Hildenbrand (2013) Predicting capillarity of mudrocks. Marine and Petroleum Geology 45:208–223

Cała M, Cyran K, Kawa M, et al (2017) Identification of Microstructural Properties of Shale by Combined Use of X-Ray Micro-CT and Nanoindentation Tests. Procedia Engineering 191:735–743. https://doi.org/10.1016/j.proeng.2017.05.239

Cariou S, Duan Z, Davy CA, et al (2012a) Poromechanics of partially saturated COx argillite. Applied Clay Science 56:36–47

Cariou S, Skoczylas F, Dormieux L (2012b) Experimental measurements and water transfer models for the drying of argillite. International Journal of Rock Mechanics and Mining Sciences 54:56–69. https://doi.org/10.1016/j.ijrmms.2012.05.014

Cases JM, Berend I, Besson G, et al (1992) Mechanism of adsorption and desorption of water vapor by homoionic montmorillonite. 1. The sodium-exchanged form. Langmuir 8:2730–2739. https://doi.org/10.1021/la00047a025

Chen, Caratini, Davy, et al (2013) Coupled transport and poro-mechanical properties of a heat-treated mortar under confinement. Cement and Concrete Research 49:10–20

Chen GJ, Maes T, Vandervoort F, et al (2014) Thermal Impact on Damaged Boom Clay and Opalinus Clay: Permeameter and Isostatic Tests with µCT Scanning. Rock Mech Rock Eng 47:87–99

Chen, Liu, Brue, et al (2012) Water retention and gas relative permeability of two industrial concretes. Cement and Concrete Research 42:1001–1013

Conil N, Talandier J, Djizanne H, et al (2018) How rock samples can be representative of in situ condition: A case study of Callovo-Oxfordian claystones. Journal of Rock Mechanics and Geotechnical Engineering 10:613–623

Davy, Adler (2017) Three-scale analysis of the permeability of a natural shale. Phys Rev E 96:063116

Davy CA, Skoczylas F, Barnichon J-D, Lebon P (2007a) Permeability of macro-cracked argillite under confinement: Gas and water testing. Physics and Chemistry of the Earth, Parts A/B/C 32:667–680. https://doi.org/10.1016/j.pce.2006.02.055

Davy CA, Skoczylas F, Barnichon JD, Lebon P (2007b) Permeability of macro-cracked argillite under confinement: Gas and water testing. Physics and Chemistry of the Earth, Parts A/B/C 32:667–680

Davy, Skoczylas, Lebon, Dubois (2009) Gas migration properties through a bentonite/argillite interface. Applied Clay Science 42:639–648

de La Vaissière R, Armand G, Talandier J (2015) Gas and water flow in an excavation-induced fracture network around an underground drift: A case study for a radioactive waste repository in clay rock. Journal of Hydrology 521:141–156

Delage P, Sultan N, Cui YJ (2000) On the Thermal Consolidation of Boom Clay. Canadian Geotechnical Journal 37:343–354

Delay J, Bossart P, Ling LX, et al (2014) Three decades of underground research laboratories: what have we learned? Geological Society, London, Special Publications 400:7–32

Delvaux B (1992) Morphology, Texture, and Microstructure of Halloysitic Soil Clays as Related to Weathering and Exchangeable Cation. Clays and Clay Minerals 40:446–456. https://doi.org/10.1346/CCMN.1992.0400409

Desbois G, Höhne N, Urai JL, et al (2017) Deformation in cemented mudrock (Callovo–Oxfordian Clay) by microcracking, granular flow and phyllosilicate plasticity: insights from triaxial deformation, broad ion beam polishing and scanning electron microscopy. Solid Earth 8:291–305. https://doi.org/10.5194/se-8-291-2017

Desbois G, Urai JL, Kukla PA (2009) Morphology of the pore space in claystones – evidence from BIB/FIB ion beam sectioning and cryo-SEM observations. eEarth Discuss 4:1–19. https://doi.org/10.5194/eed-4-1-2009

Diamond S (2000) Mercury porosimetry An inappropriate method for the measurement of pore size distributions in cement-based materials. Cement and Concrete Research 9

Dormieux L, Lemarchand E, Coussy O (2003) Macroscopic and Micromechanical Approaches to the Modelling of the Osmotic Swelling in Clays. Transport in Porous Media 50:75–91

Dubinin MM, Astakhov VA (1971) DEVELOPMENT OF THE CONCEPTS OF VOLUME FILLING OF MICROPORES IN THE ADSORPTION OF GASES AND VAPORS BY MICROPOROUS ADSORBENTS COMMUNICATION I. CARBON ADSORBENTS. Physical Chemistry 1:5–11

Egermann P, Lombard JM, Bretonnier P (2006) A Fast and Accurate Method to Measure Threshold Capillary Pressure of Caprocks Under Representative Conditions. Trondheim, Norway

Giot R, Auvray C, Talandier J (2019) Self-sealing of claystone under X-ray nanotomography. Geological Society, London, Special Publications 482:213–223

Hamamoto Y, Alam KCA, Saha BB, et al (2006) Study on adsorption refrigeration cycle utilizing activated carbon fibers. Part 1. Adsorption characteristics. International Journal of Refrigeration 29:305–314. https://doi.org/10.1016/j.ijrefrig.2005.04.008

Harrington JF, Cuss RJ, Talandier J (2017) Gas transport properties through intact and fractured Callovo-Oxfordian mudstones. Geological Society, London, Special Publications 454:131–154. https://doi.org/10.1144/SP454.7

Hildenbrand A, Schlomer S, Krooss BM (2002) Gas breakthrough experiments on fine-grained sedimentary rocks. Geofluids 2:3–23

Hildenbrand, Schlomer, Krooss, Littke (2004) Gas breakthrough experiments on pelitic rocks: comparative study with N2, CO2 and CH4. Geofluids 4:61–80

Horseman ST, Harrington JF, Sellin P (1999) Gas migration in clay barriers. Engineering Geology 54:139–149

Houben ME, Desbois G, Urai JL (2013) Pore morphology and distribution in the Shaly facies of Opalinus Clay (Mont Terri, Switzerland): Insights from representative 2D BIB–SEM investigations on mm to nm scale. Applied Clay Science 71:82–97. https://doi.org/10.1016/j.clay.2012.11.006

Hu C, Lemarchand E, Dormieux L, Skoczylas F (2020) Quasi-isotropic Biot's Tensor for Anisotropic Porous Rocks: Experiments and Micromechanical Modelling. Rock Mech Rock Eng 53:4031–4041. https://doi.org/10.1007/s00603-020-02147-7

Ibrahim N (2008) Caractérisation des propriétés mécaniques des géomatériaux par technique de micro indentation. PhD thesis, Université des Sciences et Technologies de Lille

Iglauer S, Lebedev M (2018) High pressure-elevated temperature x-ray micro-computed tomography for subsurface applications. Advances in Colloid and Interface Science 256:393–410. https://doi.org/10.1016/j.cis.2017.12.009

Janssen MJG, Van Oorschot CWM (1989) The Characterization of Zeolites by Gas Adsorption. In: Studies in Surface Science and Catalysis. Elsevier, pp 633–642

Kaufhold A, Halisch M, Zacher G, Kaufhold S (2016) X-ray computed tomography investigation of structures in Opalinus Clay fromlarge-scale to small-scale after mechanical testing. Solid Earth 7:1171–1183. https://doi.org/10.5194/se-7-1171-2016

Keller LM (2016) Pore geometry effects on elastic properties of Opalinus Clay. GEOPHYSICS 81:D543–D551. https://doi.org/10.1190/geo2015-0452.1

Keller LM, Holzer L (2018) Image-Based Upscaling of Permeability in Opalinus Clay. Journal of Geophysical Research: Solid Earth 123:285–295. https://doi.org/10.1002/2017JB014717

Keller LM, Schwiedrzik JJ, Gasser P, Michler J (2017) Understanding anisotropic mechanical properties of shales at different length scales: In situ micropillar compression combined with finite element calculations. Journal of Geophysical Research: Solid Earth 122:5945–5955. https://doi.org/10.1002/2017JB014240

Klaver J, Desbois G, Littke R, Urai JL (2015) BIB-SEM characterization of pore space morphology and distribution in postmature to overmature samples from the Haynesville and Bossier Shales. Marine and Petroleum Geology 59:451–466. https://doi.org/10.1016/j.marpetgeo.2014.09.020

Klinkenberg LJ (1941) THE PERMEABILITY OF POROUS MEDIA TO LIQUIDS AND GASES. American Petroleum Institute, Drilling and Productions Practices 200–213

Lahn L, Bertier P, Seemann T, Stanjek H (2020) Distribution of sorbed water in the pore network of mudstones assessed from physisorption measurements. Microporous and Mesoporous Materials 295:109902

Laird DA (1996) Model for Crystalline Swelling of 2:1 Phyllosilicates. Clays and Clay Minerals 44:553–559. https://doi.org/10.1346/CCMN.1996.0440415

Laird DA (2006) Influence of layer charge on swelling of smectites. Applied Clay Science 34:74–87. https://doi.org/10.1016/j.clay.2006.01.009

Liu J-F, Davy CA, Talandier J, Skoczylas F (2014) Effect of gas pressure on the sealing efficiency of compacted bentonite–sand plugs. Journal of Contaminant Hydrology 170:10–27

Liu J-F, Song Y, Skoczylas F, Liu J (2016) Gas migration through water-saturated bentonite–sand mixtures, COx argillite, and their interfaces. Can Geotech J 53:60–71. https://doi.org/10.1139/cgj-2014-0412

Marschall P, Horseman S, Gimmi T (2005) Characterisation of Gas Transport Properties of the Opalinus Clay, a Potential Host Rock Formation for Radioactive Waste Disposal. Oil & Gas Science and Technology - Rev IFP 60:121–139

Meier LP, Kahr G (1999) Determination of the Cation Exchange Capacity (CEC) of Clay Minerals Using the Complexes of Copper(II) Ion with Triethylenetetramine and Tetraethylenepentamine. Clays and Clay Minerals 47:386–388

Menaceur H, Delage P, Tang AM, Talandier J (2016) The Status of Water in Swelling Shales: An Insight from the Water Retention Properties of the Callovo-Oxfordian Claystone. Rock Mech Rock Eng 49:4571–4586

Minardi A, Crisci E, Ferrari A, Laloui L (2016) Anisotropic volumetric behaviour of Opalinus clay shale upon suction variation. Géotechnique Letters 6:144–148

Mitchell JK, Soga K (2005) Fundamentals of Soil Behavior, 3rd Edition. John Wiley & Sons, Ltd, New Jersey

M'Jahad S (2012) Etude du l'impact de la fissuration sur les proprietes de retention d'eau et de transport de gaz des betions, de l'argilite et des interfaces argilite/beton. Application au stockage geologique des dechets radioactifs. PhD thesis, Ecole Centrale de Lille

M'Jahad S, Davy CA, Skoczylas F, Talandier J (2017) Characterization of transport and water retention properties of damaged Callovo-Oxfordian claystone. Geological Society, London, Special Publications 443:159–177

Monfared M, Sulem J, Delage P, Mohajerani M (2012) On the THM behaviour of a sheared Boom clay sample: Application to the behaviour and sealing properties of the EDZ. Engineering Geology 124:47–58

Philipp T, Amann-Hildenbrand A, Laurich B, et al (2017) The effect of microstructural heterogeneity on pore size distribution and permeability in Opalinus Clay (Mont Terri, Switzerland): insights from an integrated study of laboratory fluid flow and pore morphology from BIB-SEM images. Geological Society, London, Special Publications 454:85–106

Przelaskowska A, Łykowska G, Klaja J, et al (2015) Application of the cation exchange capacity parameter (CEC) to the characterisation of the swelling capacity of lower Paleozoic, Carpathian Flysch and Miocene Carpathian Foredeep clay rocks

Rietveld HM (1969) A profile refinement method for nuclear and magnetic structures. J Appl Crystallogr 2:65–71. https://doi.org/10.1107/S0021889869006558

Rouquerol J, Llewellyn P, Rouquerol F (2007) Is the bet equation applicable to microporous adsorbents? In: Studies in Surface Science and Catalysis. Elsevier, pp 49–56

Rouquerol J, Rouquerol F, Llewellyn P, et al (2013) Adsorption by Powders and Porous Solids: Principles, Methodology and Applications. Academic Press

Sabet S, Barisik M, Mobedi M, Beskok A (2019) An extended Kozeny-Carman-Klinkenberg model for gas permeability in micro/nano-porous media. Physics of Fluids 31:112001. https://doi.org/10.1063/1.5125434

Saiyouri N, Hicher P-Y, Tessier D (2000) Microstructural Approach and Transfer Water Modelling in Highly compacted Unsaturated Swelling Clays. Mechanics of Cohesive-frictional Materials 5:41–60

Schaap MG, Leij FJ (2000) Improved Prediction of Unsaturated Hydraulic Conductivity with the Mualem-van Genuchten Model. Soil Sci Soc Am J 64:843–851. https://doi.org/10.2136/sssaj2000.643843x

Seemann T, Bertier P, Krooss BM, Stanjek H (2017) Water vapour sorption on mudrocks. Geological Society, London, Special Publications 454:201–233

Song, Davy, Troadec, Bourbon (2019) Pore network of cement hydrates in a High Performance Concrete by 3D FIB/SEM — Implications for macroscopic fluid transport. Cement and Concrete Research 115:308–326

Song W, Yin Y, Landry CJ, et al (2020) A Local-Effective-Viscosity Multirelaxation-Time Lattice Boltzmann Pore-Network Coupling Model for Gas Transport in Complex Nanoporous Media. SPE Journal. https://doi.org/10.2118/203841-PA

Song Y (2014) Water retention and fine microstructure of Bure argillite. PhD thesis, Ecole Centrale de Lille

Song Y, Davy CA, Bertier P, et al (2017) On the porosity of COx claystone by gas injection. Microporous and Mesoporous Materials 239:272–286

Song Y, Davy CA, Bertier P, Troadec D (2016a) Understanding fluid transport through claystones from their 3D nanoscopic pore network. Microporous and Mesoporous Materials 228:64–85

Song Y, Davy CA, Nguyen Kim T, et al (2016b) Two-scale analysis of a tight gas sandstone. Phys Rev E 94:043316

Stanjek H, Künkel D (2016) CEC determination with Cu-triethylenetetramine: recommendations for improving reproducibility and accuracy. Clay miner 51:1–17. https://doi.org/10.1180/claymin.2016.051.1.01

Tanikawa W, Shimamoto T (2006) Klinkenberg effect for gas permeability and its comparison to water permeability for porous sedimentary rocks. Hydrol Earth Syst Sci Discuss 3:1315–1338. https://doi.org/10.5194/hessd-3-1315-2006

Thommes, Kaneko, Neimark, et al (2015) Physisorption of gases, with special reference to the evaluation of surface area and pore size distribution (IUPAC Technical Report). Pure and Applied Chemistry 87:1051–1069

Thommes M, Cychosz KatieA (2014) Physical adsorption characterization of nanoporous materials: progress and challenges. Adsorption 20:233–250

Van Geet M, Bastiaens W, Ortiz L (2008) Self-sealing capacity of argillaceous rocks: Review of laboratory results obtained from the SELFRAC project. Physics and Chemistry of the Earth, Parts A/B/C 33:S396–S406

Wan M, Delage P, Tang AM, Talandier J (2013) Water retention properties of the Callovo-Oxfordian claystone. International Journal of Rock Mechanics and Mining Sciences 64:96–104

Wang L, Bornert M, Yang D, et al (2015) Microstructural insight into the nonlinear swelling of argillaceous rocks. Engineering Geology 193:435–444

Yang, Bornert, Chanchole, et al (2012) Dependence of elastic properties of argillaceous rocks on moisture content investigated with optical full-field strain measurement techniques. International Journal of Rock Mechanics and Mining Sciences 53:45–55

Yang, Chanchole, Valli, Chen (2013) Study of the Anisotropic Properties of Argillite Under Moisture and Mechanical Loads. Rock Mech Rock Eng 46:247–257

Yuan H (2017) Caractérisation expérimentale des propriétés de poromécaniques et de transfert de l'argilite du COx. PhD thesis, Ecole Centrale de Lille

Yven B, Garcia MG, Chabiron AC (2015) Geometry and Rock Properties Modelling of the Callovo-Oxfordian Claystone from a 3D High Resolution Seismic Cube. Almeria, Spain

Yven B, Sammartino S, Geraud Y, et al (2007) Mineralogy, texture and porosity of Callovo-Oxfordian argillites of the Meuse/Haute-Marne region (eastern Paris Basin). Bulletin de la Société Géologique de France 178:73–90

Zacher G, Paul T, Kaufhold A, Grasle W (2015) X-ray Computed Tomography Investigation of Structures in Claystone at Large Scale and High Speed. ASEG Extended Abstracts 2015:1–2. https://doi.org/10.1071/ASEG2015ab021

Zhang (2015) Investigation of gas migration in damaged and resealed claystone. Geological Society, London, Special Publications 415:75–93

Zhang C-L (2018) Thermo-hydro-mechanical behavior of clay rock for deep geological disposal of high-level radioactive waste. Journal of Rock Mechanics and Geotechnical Engineering 10:992–1008

Zhang C-L (2011) Experimental evidence for self-sealing of fractures in claystone. Physics and Chemistry of the Earth, Parts A/B/C 36:1972–1980

Zhang C-L, Armand G, Conil N, Laurich B (2019) Investigation on anisotropy of mechanical properties of Callovo-Oxfordian claystone. Engineering Geology 251:128–145. https://doi.org/10.1016/j.enggeo.2019.02.008

Zhou X, Liu D, Bu H, et al (2018) XRD-based quantitative analysis of clay minerals using reference intensity ratios, mineral intensity factors, Rietveld, and full pattern summation methods: A critical review. Solid Earth Sciences 3:16–29

2. Chapter 2 - Experimental study of the multi-scale swelling mechanism of Callovo-Oxfordian claystone

In this chapter, the multi-scale swelling mechanism of Callovo-Oxfordian (COx) claystone was experimentally investigated with samples extracted from different depths of the Bure Underground Research Laboratory (URL), France. Data from this study demonstrate that two types of illite/smectite (I/S) aggregates act as the swelling phases in COx, namely R1-I/S (contains 30% smectite) and R0-I/S (contains 78% smectite). Compared with R0-I/S, R1-I/S has less smectite proportion but provides more water-accessible void volumes and surface areas (from nano-scale to cm-scale) for water, resulting in R1-I/S is better correlated to the volumetric swelling of this material than R0-I/S. A conceptual model is proposed to characterize the multi-scale swelling mechanism of intact COx claystone based on the experimental data. In addition, the effect of compress-induced micro-cracks on swelling was also studied, demonstrating that micro-cracks can lead to a greater swelling amplitude and higher initial swelling kinetics, more important in the direction perpendicular to the crack orientation.

2.1. Clay swelling in COx claystone

In general, COx claystone is considered to be composed of non-clay minerals and clay minerals. The non-clay minerals (such as calcite-$CaCO_3$, silica-SiO_2) are considered as rigid inclusions (Fig.2. 1 left) and will not swell. The clay minerals include illite, muscovite, interstratified illite/smectite aggregates (abbreviated as I/S) and small amounts of kaolinite and chlorite. Massat et al. (2016) reported that I/S aggregates are the only swelling mineral in COx claystone. From Fig. 2.1 middle, one I/S aggregate includes tens (even hundreds) illite and smectite particles, both of them are flake-shaped and consist of numerous elementary platelets. The structure of the elementary platelet is the same for illite and smectite, which is composed of an octahedral sheet between two tetrahedral sheets and with a basal spacing of 9.6 Å (Mitchell and Soga, 2005), see Fig. 2.1 right. Each elementary platelet is negatively charged on its external surface owing to atom substitutions of the lattice structure. Thus, some cations will exist in the inter-platelet region to achieve the system electric balance. The inter-platelet cations differ between illite and smectite: the illite lattice spaces are filled with K^+, whereas the smectite lattice spaces are filled with Na^+ and Ca^{2+}. Early XRD results showed that the larger the inter-platelet cation size is, the stronger its association with the platelet surfaces will be. (Mooney et al., 1952; Slade, 1991; Boek et al., 1995). Since the diameter of K^+ is greater than that of Na^+ and Ca^{2+}, the structural stability of illite is therefore weaker than that of smectite. Such a difference in structural stability will result in different sensitivity to water. Compared with smectite, illite is almost insensitive to relative humidity

(RH) and exhibits almost no swelling capacity (Hensen and Smit, 2002). This means that the swelling capacity of I/S aggregates is only determined on the smectite.

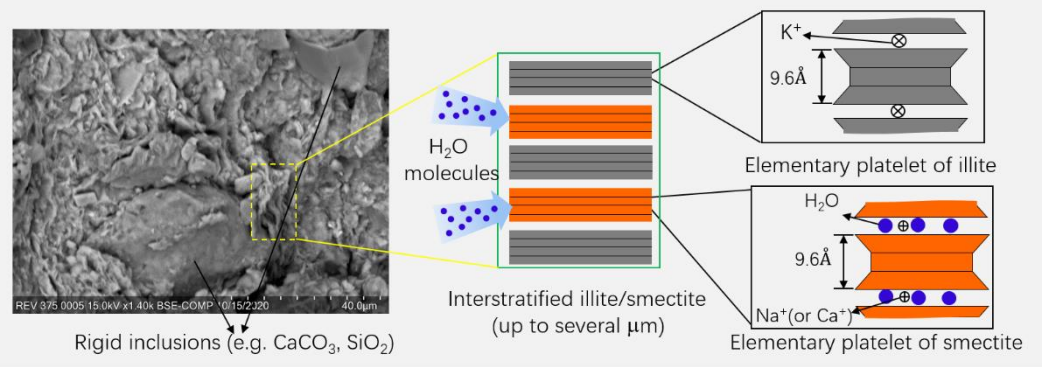

Figure 2.1. Microstructure of swelling clay mineral in COx claystone

Another swelling mechanism that occurs in COx claystone is called osmotic swelling. It is driven by repulsive force between the adjacent smectite platelets, which eventually leads to the decomposition of smectite particles (Anderson et al., 2010; Daab et al., 2018). Osmotic swelling depends on the surface charge density and localization, the nature of cations in aqueous solutions and the potential swelling space (i.e. pores) (Bish, 1988; Daab et al., 2018). If sufficient swelling space is available (e.g. submerge the material in dilute suspensions), osmotic swelling results in significantly larger amplitude (up to ca. 130 Å) than crystal swelling (Michot et al., 2013; Pusch et al., 2019). With the aid of environmental scanning electron microscopy technique, Carrier et al. (2013) and Wang et al. (2013) observed the osmotic swelling mainly involving the deformation of mesopores.

During hydration, smectite exhibits a non-linear free swelling behavior upon wetting (Wang et al., 2015). This is attributed to the fact that the two expansion mechanisms occur at different saturation stages (Massat et al., 2016). From a scale viewpoint, crystalline swelling and osmotic swelling occur at the microscale and mesoscale, respectively (Slade, 1991; Dormieux et al., 2003; Menaceur et al., 2016; Daab et al., 2018). This means that at a macroscopic scale, COx swelling is the consequence of combine multi-scale effects. It should also be underlined that COx claystone exhibits a strong swelling anisotropy (Duan et al., 2021). This can be interpreted by the layered structure of the material leading to swelling heterogeneities (Wang et al., 2017).

Despite smectite swelling mechanisms have been extensively studied, complementary researches on COx swelling of are still necessary, especially at the macroscopic scale. It is commonly believed that the macro-scale swelling of COx is directly determined by smectite content (Menaceur et al., 2016). However, smectite does not appear as a single-phase but is interspersed in I/S aggregates (Fig 2.1). The deformation of these I/S aggregates and structural effects, occurring at larger scales, remain poorly

understood. Therefore, this work aims at investigating the multi-scale swelling behavior of COx claystone with a focus at the macroscopic level. To achieve this, the mineralogical compositions, pore structure and the swelling behavior of centimetric samples were analyzed by X-ray diffraction (XRD), cation exchange capacity (CEC), nitrogen sorption tests and a series of specially designed swelling tests.

2.2.Material and sample preparation

2.2.1. Origination of material

Five COx claystone samples retrieved from different boreholes of the Meuse/Haute Marne Underground Research Laboratory (URL) (Bure, France) were tested in this study, see Table 2.1. Classified by geological sequences, the core EST51133 comes from the transition unit (UT), drilled perpendicular to bedding planes; the other four cores are from the clay-rich unit (UA) and drilled parallel to the bedding plane. The difference between UT and UA claystone is mainly of the content of clay minerals, which will be detailed in section 2.4.1.

When received in the laboratory, all samples were sealed in the "T1 cells" to maintain a compression state. They were re-cored into small cylinders (detailed in the following section). To avoid water loss before further treatment, these cylinders were wrapped in plastic film and sealed in vacuum bags, then immersed in oil and stored in a temperature-controlled room. An exception is the EST 51133 cylinders, which were actually re-cored in 2016 and are not well protected. It has been dried to 36.7% during the long time storage.

Table 2.1. Information of the tested material

Core number	Geological sequence	Initial saturation (before swelling test)
EST 51133	UT	36.7%
EST 57903	UA	86.8%
EST 58128	UA	85.5%
EST 58145	UA	84.3%
EST 62665	UA	84.3%

2.2.2. Powders: for Quantitative XRD, CEC, and nitrogen sorption measurements

A small amount of fragments (several grams) from each core was used for quantitative mineralogical characterization and nitrogen sorption. The fragments were micronized in ethanol for 15 minutes and then spray dried. Milling in ethanol can avoid further strain, heat damage and dissolution of the material. This step allows obtaining dried and homogenized powder samples with particle sizes of 400-800 microns. Powders with such particle sizes can be directly used for CEC analysis.

For samples used for XRD analysis, an additional processing step was required prior to milling. Corundum (Al_2O_3) is to be added as the internal standard into the COx fragments, with a proportion of 0.2 g/g. The internal standard serves as the precision control material to improve the accuracy of the analysis.

The powder samples used in nitrogen sorption were handled differently from the above two. The fragments of each core were first gently manually crushed and sieved. After sieving, particles with a size between 63 and 400 µm are selected for measurement. The powder samples (several grams) were outgassed in a *VacPrep 061* machine (Micromeritics Instrument Corporation, Norcross, Georgia, USA) for 12 hours at an ambient temperature (22 °C), then dried at 130 °C for 12 hours (under vacuum) to remove excess water prior to the sorption measurement.

2.2.3. Cylinders: for swelling tests

Each T1 cores were re-cored into several small cylinders (40 mm in length and 20 mm in diameter) using a low-speed diamond saw. Although the sample dimension is smaller than the ASTM (or ISRM) standards, the length/diameter ratio (equal to 2) is still enough to avoid the end effects. Moreover, due to the low permeability of the material (between 10^{-20} m² and 10^{-21} m²), a relatively small sample size can significantly reduce the testing time (Yuan, 2017). In this study, cylinders without further manipulation are called “intact” samples. It is worth mentioning that “intact” does not mean the sample is perfect because they might have been slightly damaged due to the decompression, desaturation and drilling operation.

As illustrated in Figure 2.2, the cylinders were either cored perpendicular (along axis 3, Figure 2.2 (a)) or parallel (along axis 1 or 2, Figure 2.2 (b)) to the bedding planes. The swelling deformation of samples was measured by the strain gauges. Two cross-strain gauges (5mm length each) were symmetrically glued on each sample side surface. For both core orientations, gauges were glued parallel to axis 1 (or 2) and axis 3, illustrated Figure 2.2 (a) and (b). Before gluing gauges, a small amount of water was sprayed on one sample end (or the side surface of EST51133) to let the bedding plane be visible, see Figure 2.2 (c). In the following, gauges parallel to the bedding planes are called $J_{\parallel}$ and gauges perpendicular to the beddings are $J_{\perp}$. The swelling strains measured by $J_{\parallel}$ and $J_{\perp}$ are called $\varepsilon_{\parallel}^{S}$ and $\varepsilon_{\perp}^{S}$, respectively.

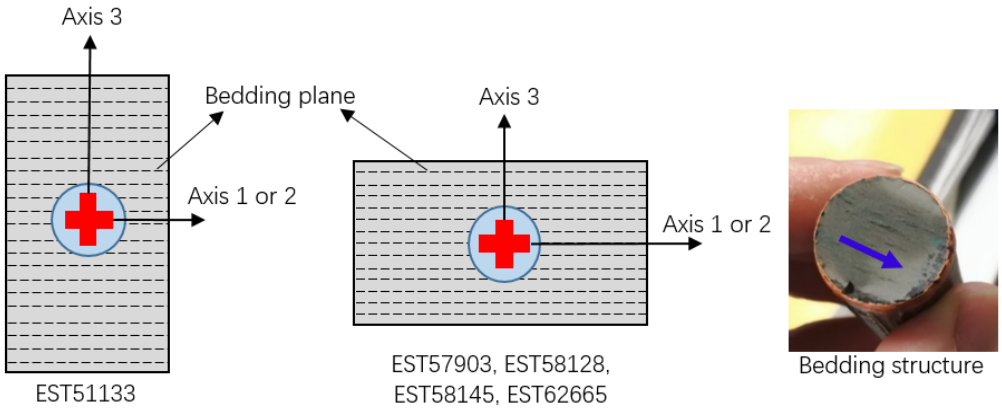

Figure 2.2. Samples cored (a) perpendicularly to the bedding plane and (b) parallel to the bedding plane; (c) exhibits the bedding structure of the material by spraying water on the sample end surface

The effects of clay minerals contents and damage states (i.e.additional cracking) on swelling behavior (amplitude and kinetics) were investigated in this study. Cylindrical samples were divided into two groups depending on the study objectives, as shown in Table 2.2. All swelling tests were conducted using synthetic water with a mineralogical composition close to that of the ground water (provided by Andra). Intact samples from different cores were used to study the effect of clay mineral contents (group 1 in Table 2.2 (a)). Mass samples were first stabilized at 75% relative humidity (RH) to minimize the effect of initial pore water condition. The resulting water saturation (S_w) is determined by:

$$S_w = \frac{m_{RH} - m_{dry}}{m_{saturated} - m_{dry}} \tag{2.1}$$

where m_{RH} is the mass at 75% RH, $m_{saturated}$ is the saturated mass weighed after swelling, m_{dry} is the stable mass after drying in the oven at 105 °C for 48 hours. For the whole set of samples, the resulting water saturation was measured between 73 and 77%.

Table 2.2: Summary of samples used for swelling tests

(a) Group 1. Intact samples, dried at 75% RH

Sample ID	Drilling orientation	Damage state	drying procedure
EST 51133	Vertical	Intact	75% RH
EST 57903	Horizontal	Intact	75% RH
EST 58128	Horizontal	Intact	75% RH
EST 58145	Horizontal	Intact	75% RH
EST 62665	Horizontal	Intact	75% RH

(b) Group 2. Two intact and two micro-cracked samples, initial saturation

Sample origin	Sample ID	Damage state	saturation
EST 58128	I-1	Intact	85.5%
	MC-1	Micro-cracked	85.5%
	I-2	Intact	85.5%
	MC-2	Micro-cracked	85.5%

Recently, Duan et al. (2021) reported that cracks parallel to bedding planes can significantly enlarge the swelling strain, especially the $\varepsilon_{\perp}^{S}$ value. To verify this result, two intact and two micro-cracked samples from core EST 58128 were used for studying the effect of the initial damage states, see Table 2.2 (b). The micro-cracked samples were obtained by performing uniaxial compression tests on "intact" ones. An intact sample was initially loaded with uniaxial stress until failure to determine its uniaxial compressive strength (UCS). The micro-cracked state was then obtained by uniaxial loading until 80% UCS (Figure 2.3). Figure 2.3 (a) and Figure 2.3 (b). respectively give axial/lateral and volumetric strain changes during loading/unloading. A non-linear stress-strain behavior and a significant volume dilatancy were observed, indicating that micro-cracks occurred within the sample even if no visible cracks appeared on the outer surface.

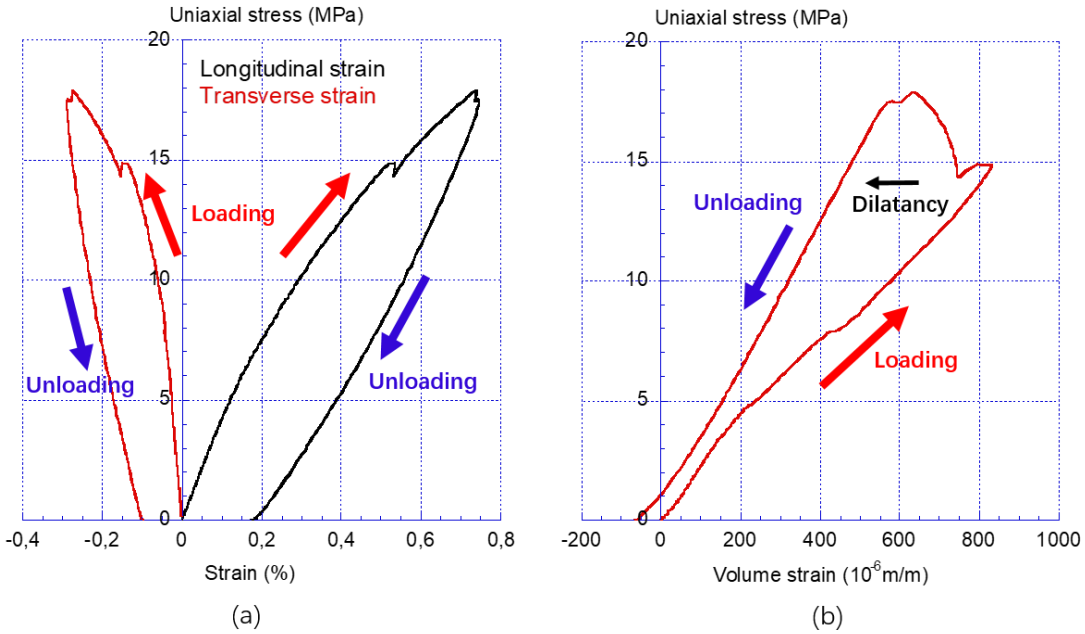

Figure 2.3 Uniaxial compression test of sample EST58128: (a) stress-strain behavior and (b) volume strain during loading/unloading unixial stress

2.3. Experimental methodology

2.3.1. Quantitative XRD

The XRD measurements were carried out with the CuKα-radiation produced at 40 kV and 30 mA. To reduce the textural effect on the result, the powder samples were side-loaded in the sample holder and the top layer was removed. During the test, the powder samples were illuminated through a divergence slit (1.7 mm) and a spacing collimator (0.2 mm). The diffracted beam was recorded by a scintillation detector for every 5 seconds at a step size of 0.02° 2θ, with an angle interval of [2°, 82°] 2θ. Bulk mineralogical compositions were analyzed by the Rietveld refinement method (Rietveld,

1969). The BGMN-Profex software was used with customized clay mineral structures based on (Ufer and Kleeberg, 2015).

The clay-content analysis was performed on the material with a size of below 2 μm. Such size particles were obtained by centrifugation after thorough chemical treatment to remove cementing agents of the samples (including carbonates, organic matter, and iron/manganese oxides/hydroxides). This procedure is also known as the "Jackson treatment" (Jackson and Abdel-Kader, 1978). After centrifugation, only clay minerals were retained. They were then saturated with Ca^{2+} to remove other exchangeable cations. Such an exchange greatly facilitates the identification and quantification of the clay minerals in the oriented preparations that were prepared. The oriented preparations were made by sedimentation on a porous ceramic plate. Samples were subsequently analyzed by X-ray diffraction while the first reflections (001) of the clay minerals were recorded.

Due to the lack of standard clay materials, the precision of the subdivided clay mineral content is very difficult to quantify. Through a large number of repetitive experiments, it was found that the accuracy is generally better than 0.001g/g for phases with mass content over 0.02g/g. In this study, the two important minerals used for data analysis are R1-I/S and R0-I/S, which mass contents are greater than 0.02g/g in UA samples and slightly smaller than 0.02g/g in UT samples. This means that the accuracy of XRD results is sufficient to avoid the logical bias of this study.

2.3.2. Cation exchange capacity (CEC)

Cation exchange capacity (CEC) reflects the ability of the material to hold exchangeable cations in the saline aqueous solution. In this study, the CEC was measured using the Co (III)-hexamine method (Meier and Kahr, 1999). The micronized powders (ca. 0.5 g) were dried at 110°C and subsequently exchanged with the Co (III)-hexamine solution. The material was then homogenized after ultrasonic treatment (20 kHz, 400 W, 5 min) and the absorption of the supernatant solution was measured using an ultraviolet-visible (UV-Vis) spectrophotometer. The absorption measurement was repeated several times to guarantee a reliable value of the number of exchangeable cations.

2.3.3. Nitrogen sorption measurements

The nitrogen sorption was carried out on the initially dried and degassed materials, with a cryogenic nitrogen bath (-196 °C). The physisorption isotherms were obtained by recording 55 relative pressure points within a relative pressure interval of 0.001-0.995 p/p^0. Precisely, 31 points for adsorption and 24 points for desorption were recorded for each measurement. The saturation pressure (p^0) was re-calibrated independently for every relative pressure point. The thermodynamic equilibrium of sorbate-sorbent was assumed when the pressure fluctuation was less than 0.01% over 10 s. The

adsorption/desorption isotherm provides abundant information related to the pore structures. Using the isotherm data, several important textural properties of the material were able to be indirectly deduced. The applied theories and related results are further detailed in section 4.2.

2.3.4. Swelling tests

Unlike many tests using swelling pressure to evaluate the swelling capacity of clayey material, this work uses a specially designed hydrostatic disposal to directly measure the sample strain (Figure 2.4). The sample was wrapped with a rubber sleeve. Both two sample ends were connected to the ISCO water pump successively through a metallic porous disc, a stainless steel hollow cylinder and a pipe. This design allowed to apply constant pore water pressure (P_i) from both ends. The assemblage was then placed into a hydrostatic cell and immersed in oil. A Gilson^{TM}-type oil pump was connected to the cell to control the confining pressure (P_c) applied on the sample. The strains were recorded by an external digital strain-meter (with an accuracy of ± 10^{-6} m/m). All the tests were carried out in a temperature-controlled room to avoid thermal perturbative effects. For each test, P_c was first slowly loaded to 14 MPa and kept constant. When the strain values were stabilized, 5 MPa pore pressure P_i was applied and kept constant. The swelling strain values were recorded until complete stabilization.

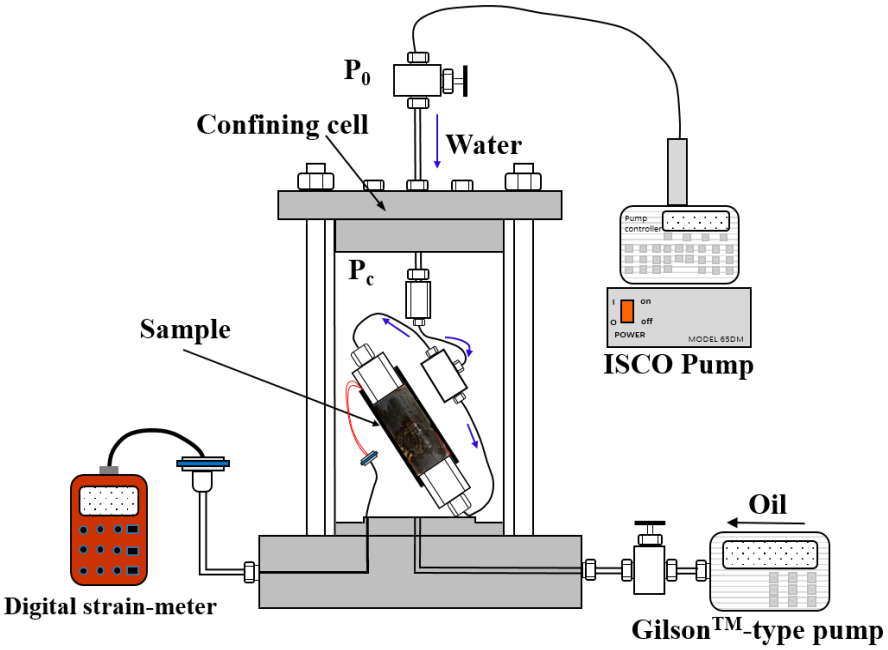

Figure 2.4. Diagram of the experimental setup for swelling test

2.4.Results and analysis

2.4.1. Mineralogical characterization

XRD and CEC analysis were performed twice for each core, summarized in Table 2.3. The XRD result shows that UT and UA samples have similar bulk mineral compositions but only differ in proportions.

Powder samples originated from the UT core (EST51133) consist of ca. 95% non-clay minerals (ca. 79% carbonates and ca. 15% quartz) and 5% clay minerals (mainly 2:1 clay minerals). For powder samples from UA cores, the non-clay minerals are composed of around 24% carbonates and around 28% quartz, while the clay mineral content is between 40% - 50%. The subdivided clay mineral analysis indicates that two types of interstratified illite/smectite phases exist in both UT and UA COx, named R1-I/S and R0 –I/S respectively. The difference between the two I/S phases lies in the content and arrangement of illite and smectite (Altaner and Bethke, 1988). In terms of proportions, R1-I/S is composed of 70% illite and 30% smectite while R0-I/S has 22% illite and 78% smectite. From a structural viewpoint, in R1-I/S, every smectite particle is sandwiched between two illite particles (e.g. ISII.. or IISI..). In contrast, both smectite and illite particles are randomly distributed in R0-I/S (e.g. ISSI… or SSII…). From Table 2.3, the amounts of R1-I/S and R0-I/S are close to each other in UT COx, while the R1-I/S content is three to four times higher than that of R0-I/S in UA COx.

Table 2.3. Quantitative XRD and CEC analysis of the tested samples (in mass percentage)

Sample	**EST 51133-1**	**EST 51133-2**	**EST 57903-1**	**EST 57903-2**	**EST 58128-1**	**EST 58128-2**	**EST 58145-1**	**EST58145-2**	**EST62665-1**	**EST62665-2**
Geological sequence	UT	UT	UA	UA	UA	UA	UA	UA	UA	UA
Carbonates	76	82.6	29.5	27.7	22.1	21.0	22.6	22.7	19.6	21.1
Tectosilicates	17.1	13.5	28.6	26.8	26.9	26.9	29	28.6	25.3	26.9
Secondary minerals (pyrite, anatase, etc.)	0.5	0.3	1.9	1.8	2.1	1.9	1.7	1.9	1.6	1.9
Non-clay minerals	93.7	96.3	59.9	56.3	51.0	50.0	53.3	53.2	46.5	49.8
Kaolinite	/	/	2.2	2.7	3.3	3.4	2.9	3.0	3.4	3.1
Chlorite	0.1	0.1	1.1	1.4	1.5	1.7	1.7	1.7	1.7	1.6
Illite & muscovite	2.8	1.6	4.7	12.9	13.1	14.3	18.8	20.2	12.7	13.4
R1-I/S (70% illite /30% smectite)	1.7	1.2	23.5	20.6	22.6	23.2	24.2	23.4	28.3	25.5
R0-I/S (22% illite /78% smectite)	1.8	0.7	8.5	6.1	8.5	7.4	6.2	6.0	7.3	6.5
Total smectite	1.87	0.94	13.7	10.9	13.4	12.7	12.1	11.7	14.2	12.7
Total clay minerals	6.4	3.6	40.1	43.7	49.0	50.0	46.8	46.7	53.5	50.2
CEC (meq/100g)	1.9	1.4	14.6	13.1	17.6	16.8	15.2	14.2	21.3	20.8

CEC results are presented in Table 2.3. The value of UT material (i.e. EST 51133) is lower than 2 meq/100g, which is much smaller than that of UA materials (13.1 - 21.3 meq/100g). Fig. 2.5 (a)-(c) depict the correlation between CEC, total smectite, R1-I/S and R0-I/S of both UT and UA samples, with the Pearson coefficients (R^2) equal to 96.7%, 94.5% and 83.4%, respectively. From Fig. 2.5 (a), one can note that the smectite in COx is responsible for the chemical interaction with aqueous solutions. However, the structural effect, i.e. the impacts of different I/S layers on CEC, is observed by comparing Fig. 2.5 (b) and (c) that the linear quality of CEC vs. R1-I/S is better than that of CEC vs. R0-I/S.

Inspection of Fig. 2.5 (a)-(c) suggests that the data is always distinguished into two sets: UT samples correspond to small CEC values while UA samples exhibit much higher CEC values. This can always lead to a kind of linear correlation between the two sets. As the UA and UT samples have very different natural properties, they should be analyzed as two different materials. Thus, it would be worth excluding the UT samples and only analyzing the UA material, see Fig. 2.5 (d)-(f). From Fig. 2.5 (d), one can note that the relation of CEC & smectite content keeps linear. Compared to Fig. 2.5 (a), the decrease in R^2 is significant (equal to 8.6%) but still sufficient to show a linear tendency, validating the fact that smectite is in charge of the chemical activity of COx. Comparison of Fig. 2.5 (e) and (f) demonstrates that the structural effect is more significant when only analyzing UA samples. This implies an unexpected result: R1-I/S has less smectite content but plays a more significant role.

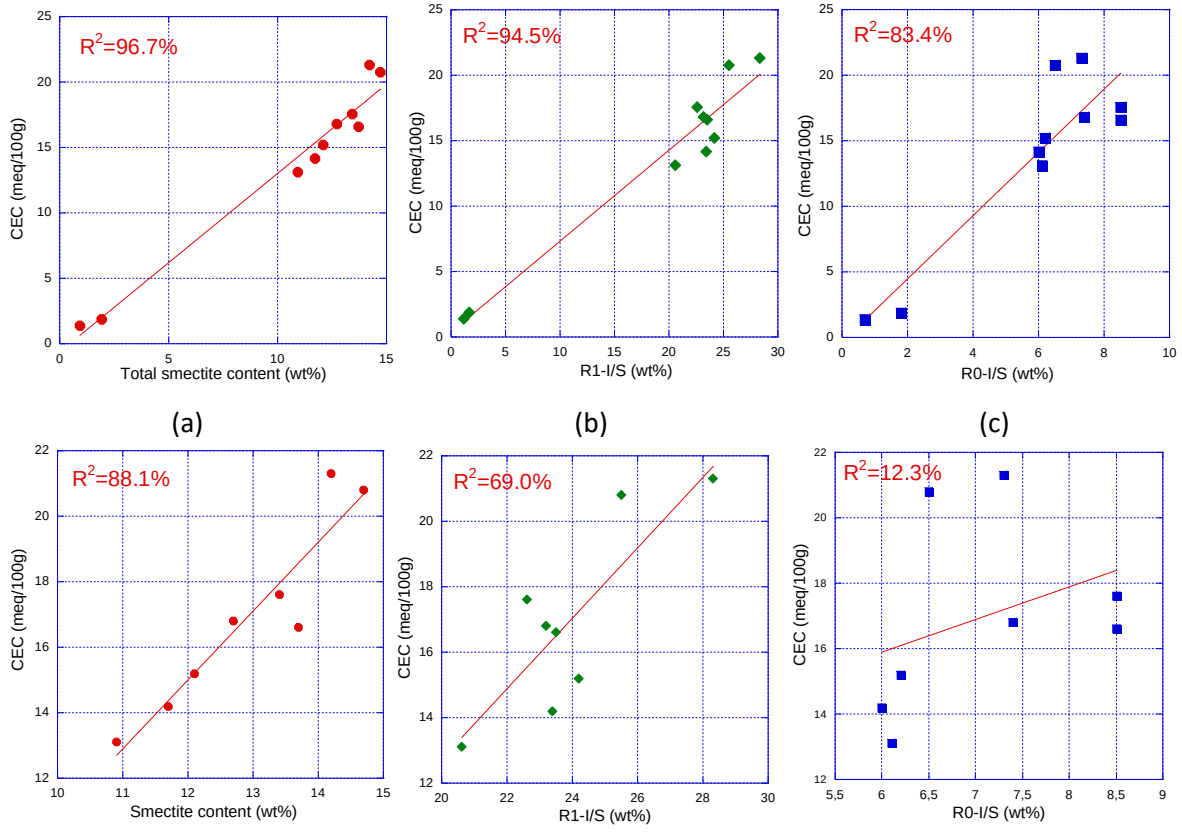

Figure 2.5. The relationship between CEC, total smectite content, R1-I/S and R0-I/S. (a)-(c) show results for both UT and UA samples; (d)-(f) exhibit results for only UA samples.

2.4.2. Nitrogen sorption isotherms

The sorption isotherms of different cores are shown in Figure 2.6. According to the IUPAC classification (Thommes et al., 2015), the five isotherms are all classified Type IV, indicating that all these cores contain pores of various sizes. A sample-dependent hysteresis loop (Type H3) is observed on the desorption branches at $p/p^0 \approx 0.45$ for all isotherms. The hysteresis loops are caused by complex pore structures such as narrow throats blocking and cavitation-induced evaporation of larger pores (Bertier et al., 2016). This suggests that the pore system of COx is mainly composed of a large amount of mesopores (2 nm < pore diameters < 50 nm) and a small amount of micropores (pore diameter < 2 nm) and macropores (pore diameters > 50 nm). This result is consistent with the reported values of this material (Seemann et al., 2017; Song et al., 2016).

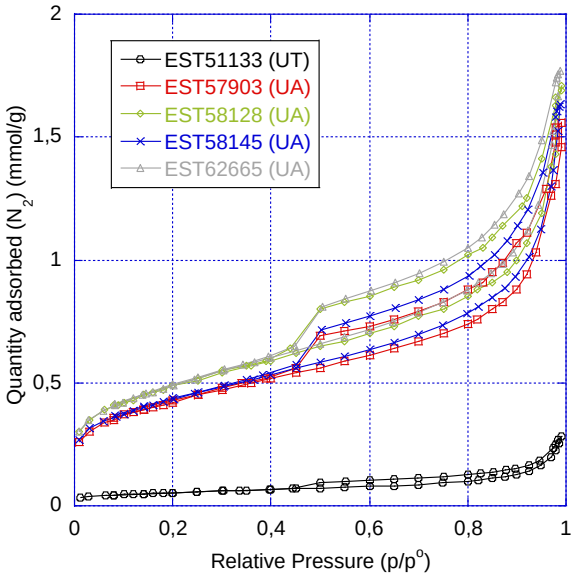

Figure 2.6. N_2 physisorption isotherms of COx samples from different cores, measured at 77 K.

Table 2.4 shows the pore textural properties derived from the nitrogen isotherm data based on different theories. The specific pore volume (V_{Gur}) was calculated using the Gurvich rule; the specific surface area (SSA) was deduced by the Brunauer-Emmett-Teller (BET) theory; E is the characteristic energy of the micropores and n the Dubinin-Astakhov exponent, both derived from the Dubinin-Astakhov (DA) theory. Moreover, the cumulative pore size distributions (PSD) were deduced by combining the Barrett-Joyner-Halenda (BJH) theory and the DA theory, as detailed in section 4.2.4.

Table 2.4. Texutral properties of tested COx claystone derived from the N_2 adsorption isotherms. V_{Gur} is the Gurvich specific pore volume, SSA is the BET specific surface area, Q_0 is the Dubinin-Astakhov limiting micropore volume, E is the characteristic energy and n the Dubinin-Astakhov exponent

Core numbers	V_{Gur} (cm^3/g)	SSA (m^2/g)	Q_0 (cm^3/g)	E (kJ/mol)	n
EST 51133	0.013	4.12	0.001	15.4	1.6
EST 57903	0.069	32.72	0.011	16.7	1.9
EST 58128	0.076	37.51	0.012	17.2	1.7
EST 58145	0.073	33.56	0.014	16.2	1.6
EST 62665	0.079	37.98	0.012	17.1	1.6

2.5.2.1 Gurvich specific pore volume vs. clay contents

The calculation of V_{Gur} involves two hypotheses: 1) the whole pore system is filled at $p/p^0 \approx 1$ and 2) the gas density is close to the liquid one at the operational temperature (-196 °C for N_2). According to the Gurvich rule, V_{Gur} is given by:

$$V_{Gur} = \frac{Q_{total}}{1000} \cdot V_m \tag{2.2}$$

where Q_{total} (mmol/g) is the total adsorbed N_2 quantity at p/p^0 equal to 0.99; V_m is the liquid molar volume of N_2, $cm^3/mmol$. Technically, V_{Gur} measured by nitrogen is associated with pores below 0.35 μm (Seemann et al., 2017). From Figure 2.6, no obvious plateau is observed at p/p^0 close to 1. This implies that V_{Gur} cannot represent the real total pore volume. The measured V_{Gur} values vary between 0.28 and 1.77 mmol/g and exhibit a strong sample dependency, see Table 2.4. Figure 2.7 (a) shows that V_{Gur} linearly increases with the smectite-related clay contents whatever the clay categories. This implies that higher clays content results in greater adsorption pore volume. The R^2 of R1-I/S and total smectite are close to each other, equal to 97.8% and 96.7%, respectively. It is unexpectedly found that R0-I/S corresponds to the R^2 value of 86.9%, which is the lowest among all smectite-related clays. This means that even though R0-I/S includes 78% smectite in mass, it provides less pore space for the connection of water and smectite. This is consistent with the result reported in (Wang et al., 2021a)

It is also observed that V_{Gur} increases exponentially with the CEC value (R^2=98.5%), see Figure 2.7 (b). Such a non-linear tendency can be interpreted by the effect of R0-I/S proportion. As a phase containing a large amount of smectite (78%), R0-I/S accounts for about 50% of the total I/S for low CEC samples i.e. the UT one, while it accounts for only 1/4 of the total I/S for high CEC samples (UA cores) (Table 2.3). This indirectly confirms that compared to R1-I/S, R0-I/S provides less pore spaces for free water molecules to contact with smectite.

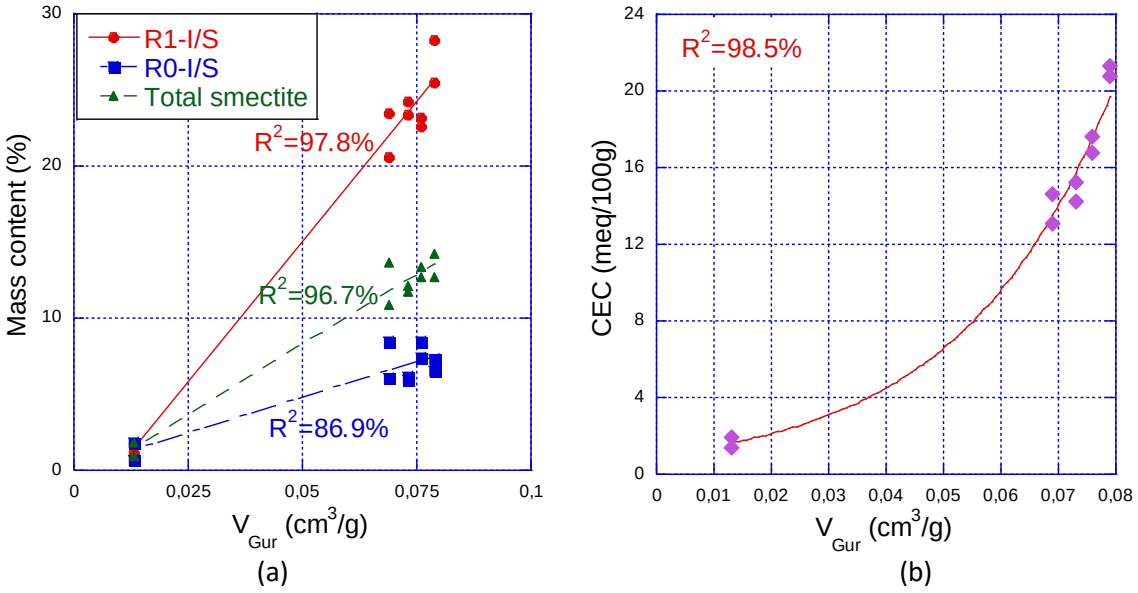

Figure 2.7. Analysis of the relationship between V_{Gur} and clay mineral contents (a) Different clay mass contents are linearly related to V_{Gur}; (b) the exponential relationship between CEC and V_{Gur}.

2.5.2.2 BET specific surface area vs. clay contents

The BET theory was used to assess the specific surface area (SSA) (Bertier et al., 2016). Following several assumptions (see Rouquerol et al. (2007)), the isotherm data corresponds to p/p^0 range in [0.05, 0.35] can be transformed into the BET plot:

$$\frac{1}{[Q(1-p/p°)]} = \frac{1}{Q_{mono}C} + \left[\frac{(C-1)}{Q_{mono}C}\right](p/p°) \tag{2.3}$$

where C is the BET constant, Q_{mono} is the monolayer adsorbed quantity. Both C and Q_{mono} are determined by using rel. (2.3) to fit isotherm data. The specific surface area (SSA) is given by:

$$SSA = Q_{mono} \cdot N_A \cdot \frac{\sigma_m}{m} \tag{2.4}$$

where N_A is the Avogadro number, 6.022×10^{23} mol^{-1}; σ_m is the N_2 molecule cross-sectional area, 0.162 nm^2; m is the total mass of the adsorbent. The SSA of the UT sample EST 51133 is 4.12 m^2/g, which is significantly smaller than the value of UA samples (32.72-37.98 m^2/g). See Figure 2.8 (a), SSA showed a linear relationship with all smectite-related clay minerals. Similar to the observation in Figure 2.7 (a), the lowest correlation (R^2 = 87.8%) is observed for R0-I/S, while the R^2 values for R1-I/S and total smectite are both equal to 96.8%. This implies that despite R0-I/S contains more smectite, R1-I/S not only provides more pore volume V_{Gur} but also a greater specific surface area for gas adsorption than R0-I/S. An exponential relationship is also observed between CEC and SSA, with an R^2 of 97.0% (Figure 2.8 (b)). Once again, it can also be explained by the effect of the change of R0-I/S proportion in total I/S. From Figure 2.7 and Figure 2.8, $V_{Gurvich}$ and SSA exhibit similar sensitivity to the smectite-related

clay minerals. The structure of R1-I/S seems to be more favorable for the water-smectite interaction than that of R0-I/S.

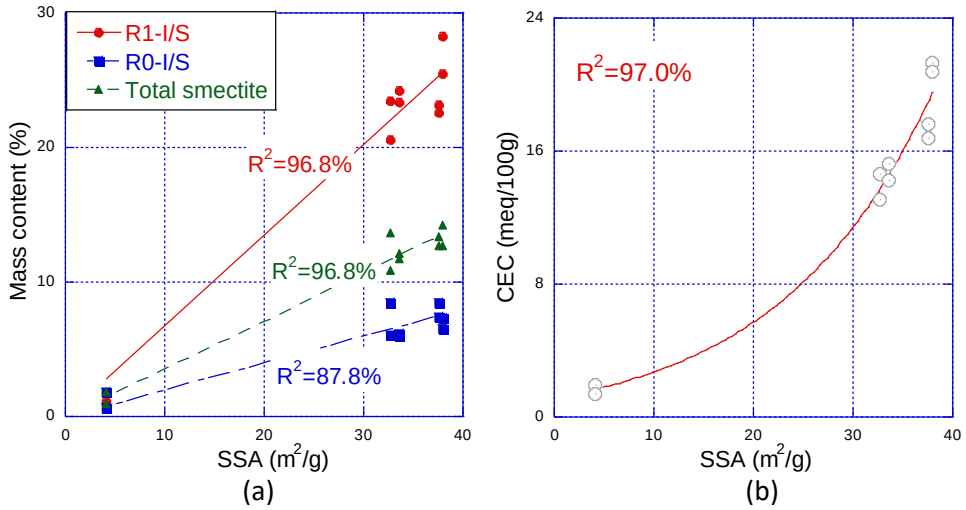

Figure 2.8. Analysis of the relationship between SSA and smectite-related mineral contents (a) Different clay mass contents are linearly related to the SSA; (b) the exponential relationship between CEC and SSA.

2.5.2.3 Micropore textural properties vs. crystalline and osmotic swelling

Based on thermodynamic relations, Dubinin-Astakhov (DA) theory assumed that the molar work of adsorption (A) in micropores (pore size<2nm) is equal to the loss of Gibbs free energy ($-\Delta G$), i.e. $\mathrm{A} = -\Delta G = -RT\ln(p/p°)$. Dubinin-Astakhov equation gives the relationship between the adsorbed gas volume Q in micropores and the relative pressure $p/p°$:

$$Q = Q_0 \cdot \exp\left[-\left(\frac{A}{E}\right)^n\right] = Q_0 \cdot \exp\left[-\left(\frac{-RT\ln(p/p°)}{E}\right)^n\right] \quad (2.5)$$

where Q_0 (cm^3/g) is the limiting micropore volume, E (kJ/mol) is the characteristic energy; and n is the adjustable DA exponent. Q_0, E and n are all derived from non-linear curve fitting the isotherm data using rel. (2.5).

From Table 2.3, the limiting micropore volume Q_0 of UA samples differed from UT by an order of magnitude while the difference between UA samples is not significant. The relationship between Q_0 and the smectite-related minerals is illustrated in Figure 2.9. Obvious similarities between Figure 2.7 (a) and Figure 2.9 can be underlined. As for V_{gur}, Q_0 exhibits the best linear correlation with R1-I/S (R^2=93%), whereas the worst one is observed with R0-I/S (R^2=76.4%). This seems to suggest that R1-I/S provides more pore volume than R0-I/S for pore sizes < 2 nm when concerning both UT and UA samples, which is quite logical as the UT sample data are significantly smaller than that of UA samples.

However, this tendency of Q_0 may be changed when focusing on UA samples only, which are detailed later.

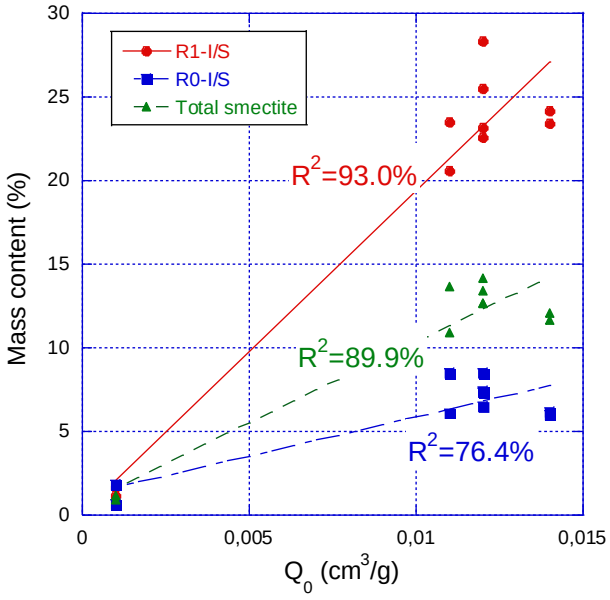

Figure 2.9. Linear relationship between Q_0 and smectite-related mineral contents

However, there is no significant difference between the calculated E and n of different core samples (Table 2.5). This means that samples from different stratigraphic locations have similar micropore surface chemistry. Since the crystalline swelling occurs in micropores, the consistency of E and n between samples indirectly confirms the fact that only a specific clay (i.e. smectite) has such swelling capacity. Lahn et al. (2020) reported that pores below 10 nm will be blocked or fully filled when the relative humidity exceeds 97% for clayey materials. This means that the inter-platelet crystal swelling (0.96 - 2 nm) and the osmotic swelling in small mesopores (2 - 10 nm) cease at (or very close to) saturation state. In the meantime, osmotic swelling continues to occur in pores larger than 10 nm since they remain accessible at high relative humidity. Hence, it is concluded that when unsaturated COx starts to hydrate, crystalline swelling immediately occurs and stops close to 100% saturation. In parallel osmotic swelling initiates at high saturation level (Massat et al., 2016) and continues until the system hydro-mechanical equilibrium.

2.5.2.4 Pore size distributions vs. clay contents

The pore size distribution (PSD) of the material was obtained by two theories: Barrett-Joyner-Halenda (BJH) theory and the DA theory. BJH theory is used to calculate the PSD of pores larger than 4 nm (meso- and macropores) and is the result of the Kelvin equation and a statistical thickness equation (Lammers et al., 2015). The calculated pore radius is the sum of Kelvin radius (r_k) and a multilayer

thickness (t) (Barrett et al., 1951). Kelvin radius (r_k) is calculated by the classic Kelvin's equation (Seemann et al., 2017). The statistical multilayer thickness (t) is a function of the partial pressure p/p^0 (Halsey, 1948). In particular, the Harkins-Jura equation (with Faas correction) is used for the nitrogen-claystone system (Harkins and Jura, 1944). By definition, the BJH theory is only applicable for $p/p^0 > 0.15$ to measure the PSD of meso and macropores. At lower relative pressures ($p/p^0 < 0.15$), the DA theory was used to evaluate the PSD of micropores (pore diameter < 2 nm) (Dubinin and Astakhov, 1971). Assuming gas adsorption in micropores follows the volume filling theory (TVF), the micro-PSD can be derived by combining the Dubinin-Astakhov equation (rel. (2.5)) and the Van Der Waals equation (consider surface effects) (Janssen and Van Oorschot, 1989).

Figure 2.10 (a) shows the cumulative pore size distributions (including micropores to macropores) calculated with a combination of BJH and DA theories. The total pore volume of UA samples is significantly higher than that of the UT sample, implying that clay minerals provide a significant pore volume within a wide size (or radius) range. All samples exhibited a rapid increase in cumulative pore volume between 0 and 45 nm pore size, and then a plateau occurs between around 45-75 nm. Such a plateau indicates the COx has relatively few pores in this size range. Following the plateau, the pore volume smoothly increases (compared with the range of 0-45 nm) until reaching the maximum measurable pore size (ca. 160 nm). Statistically, the volume of 0-45 nm pores represents 78.6%-82.4% total pore volume for UA samples and 69.6% for the UT one. This is consistent with the fact that the majority of pores in COx are micropores and mesopores (Song et al., 2016). From the viewpoint of the clay composition, the differences in adsorption capacity between samples are mainly related to the clay content associated with smectite. Since pores between 0-45 nm correspond to the largest pore volume part, the cumulative PSD in this range was correlated with smectite-related minerals for the analysis, see Figure 2.10 (b). Once again, the mineral with the best correlation is still R1-I/S, with R^2 =98.6%. Combining with Figure 2.7 (a), such a result illustrates that the effect of smectite distribution on adsorption capacity is valid from nano-scale to μm-scale.

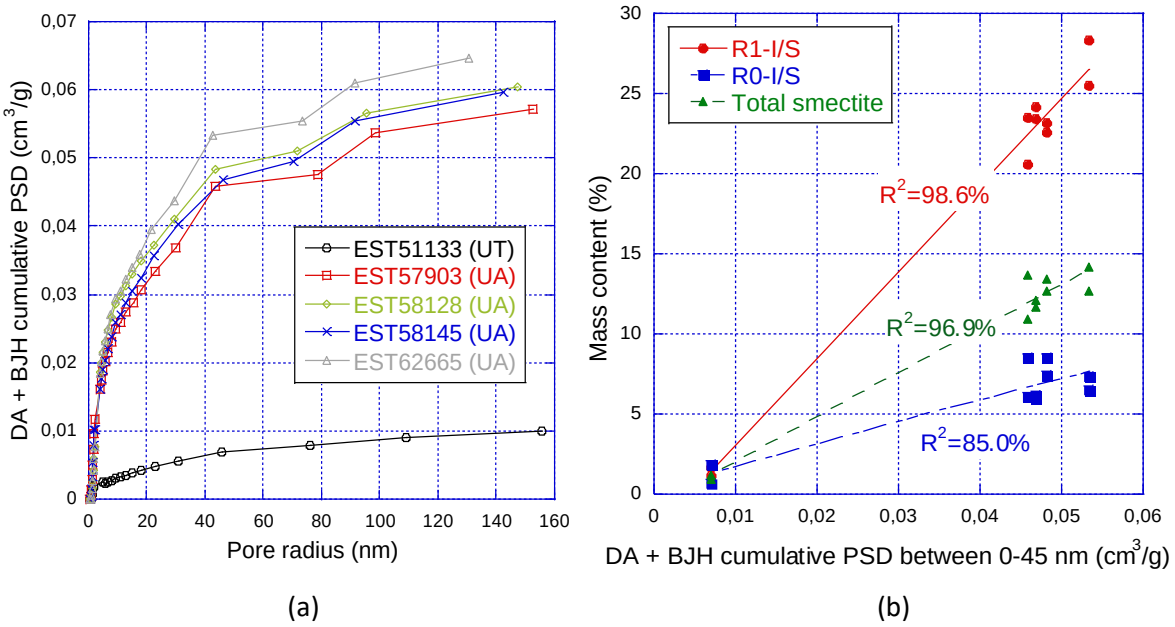

(a) (b)

Figure 2.10. Cumulative pore-size distributions based on the combination of DA and BJH theories

2.5.2.5 Focusing on UA material

Fig. 2.11 depicts the relationship between smectite-related clays and pore textural properties of UA samples. In comparison with the analyses concerning both UT and UA samples (Fig. 2.7 to Fig. 2.10), R^2 values decreased in all relations, indicating that the linear tendency is less significant for UA samples. One reasonable interpretation is that the inherent errors of XRD analysis, i.e. the deviation of mass content of R1-I/S and R0-I/S are magnified and leading to lower R^2 values when focusing on a relatively narrow range. Nevertheless, inspections of data in Fig. 2.11 (a) and (b) indicate that the macropore properties (V_{Gur} and SSA) still linearly increase with R1-I/S, even though R^2 values are dramatically decreased. In contrast, there is almost no correlation between R0-I/S and the macropore properties. This means that the total pore volume and surface area in UA type COx claystone are possibly mainly provided by R1-I/S. On the other hand, Fig. 2.11 (c) shows the micropore volume Q_0 has no relation with R1-I/S even negatively related to R0-I/S, indicating that the accessible micropore volume of UA samples does not depend on clay species. Hence, it can be concluded here that the structural effect on adsorption capacities of UA material is mainly concentrated in meso- and macropores, while the adsorption capacity of micropores seems not to be affected by the I/S types.

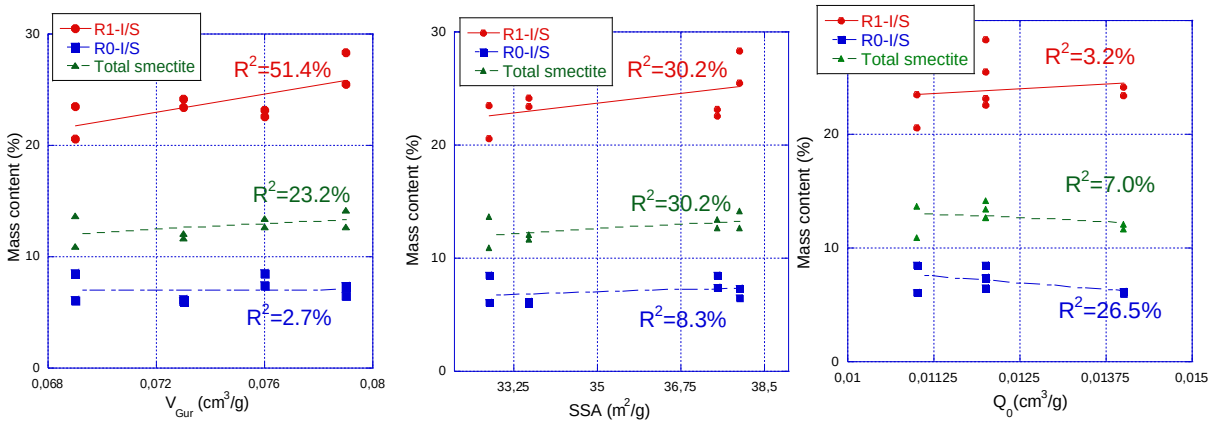

(a) (b) (c)

Fig. 2.11. Relationships between material properties and the smectite-related clays for only UA samples

2.5.2.6 Partially conclusion

XRD and CEC analysis demonstrate that smectite is the most chemical active mineral in COx, while the structure of R1-I/S is more favorable than that of R0-I/S for the interaction between smectite and pore water. In comparison between UT and UA samples, nitrogen adsorption data demonstrates that all void spaces (from the nanoscale to mesoscale) increase significantly with the clay content, in particular with the R1-I/S. When focusing on UA samples only, the absorptive macro- and mesopore volume are still likely linearly increase with the R1-I/S, while the linear correlation with R0-I/S no longer exists. Meanwhile, the available micropore volume seems not sensitive to the change of smectite-related clays. Thus, it can be concluded that the structural effect on CEC may be attributed to the fact that compared to R0-I/S, R1-I/S provides more available macro- and mesoscale pores for the smectite-water reaction. To examine the upscaling consequence of this structural effect, a series of swelling tests were carried out to link the microstructure properties to the macroscopic swelling strains.

2.5. Swelling experiments

2.5.1. Accuracy of strains

For each sample, the average strain of the two lateral (or vertical) gauges (see Fig. 2.2) was calculated and called $\varepsilon_{\parallel}$ (or $\varepsilon_{\perp}$). COx claystone is a transversely isotropic material and more deformable perpendicular to bedding planes during wetting, i.e. $\varepsilon_{\parallel} < \varepsilon_{\perp}$ (Minardi et al., 2016). During the sample preparation, there are always some uncertainties about the bedding planes vs. the gauge orientation. Precisely, the $J_{\perp}$ of UA samples and the $J_{\parallel}$ of the UT one are not strictly perpendicular to bedding planes due to the sample curvature and unavoidable geometrical uncertainties and consequently, the measured $\varepsilon_{\perp}$ of UA samples (or $\varepsilon_{\parallel}$ of UT sample EST51133) are inevitably biased. To minimize these uncertainty of results, the $\varepsilon_{\parallel}$ of each sample is therefore used for comparison between different

samples and/or sample states. It must be nevertheless mentioned that the strain results for UT did not exhibit significant anisotropy. This is highlighted in Fig. 2.12 in which are plotted the strain measurements on the UT sample. One can find that the measured $\varepsilon_{\parallel}$ and $\varepsilon_{\perp}$ of the UT sample are obviously very close to each other, which is far to be the case for UA samples. As the smectite content of the UT sample is much lower than that of other UA ones, the measured $\varepsilon_{\parallel}$ is much smaller than that of UA samples. This denotes that the $\varepsilon_{\parallel}$ value of EST51133 can be logically used for a purpose of comparisons between UT and UA materials.

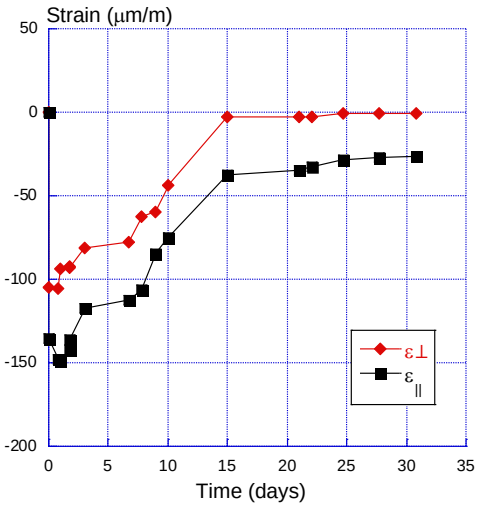

Figure 2.12. Swelling strains of four gauges of the UT sample EST51133 (initially mass stabilized at 75%RH)

Despite the uncertainty in $\varepsilon_{\perp}^{S}$ of UA samples, it is obvious that this strain remains a good tool to evaluate the sample sensitivity for swelling. In this study, they were used to investigate the effect of initial damage states on swelling i.e. of cracks suspected to be present in the bedding planes.

2.5.2. Swelling amplitude vs. clay contents & N2 sorption properties

Figure 2.13 (a) depicts the overall swelling process of the tested samples. As discussed in section 2.3, the pre-stable of sample masses at 75% RH leads to similar initial saturation values between samples, whatever the mineralogical compositions are. A typical test starts with a confining pressure P_c loading up to 14 MPa before water injection - see the left small graph of Figure 2.13 (a). Comparing the initial contraction (due to P_c) between samples is not very meaningful, because: (1) differences in mineral contents may affect the mechanical properties, and (2) the possible pre-damage varies among samples (interpreted in section 2.3). Nevertheless, it was generally observed that the contraction of the UT sample is much smaller than that of all UA samples, this means that the material stiffness decreased with increasing clay content. After water injection with P_i = 5 MPa, significant swelling was observed under a "Terzaghi effective pressure" of 9 MPa. Some structural effects occurred during a short time

and they were attributed to some transient pore pressure phenomena, see the orange and black curve of Figure. 13 (a). After these, all the samples started to swell after pressurization. The swelling time varied widely between samples, ranging from around 10 to 60 days (Figure 2.13 (b)). It can be underlined that the shortest time (10 days) was obtained for UT sample, which contains less clay than the UA ones. The sample swelling is therefore the superposition of pure swelling and poromechanical effect due to pore pressure increase. It is nevertheless obvious that, even if the Biot's coefficient was found close to one (Wang et al., 2021b), the strain due to this effect is much smaller than the measured swelling observed here. As Pi=5MPa, the maximum strain due to poromechanical effect could be roughly estimated (or capped) at 5/14 time the strain due to P_c=14MPa.

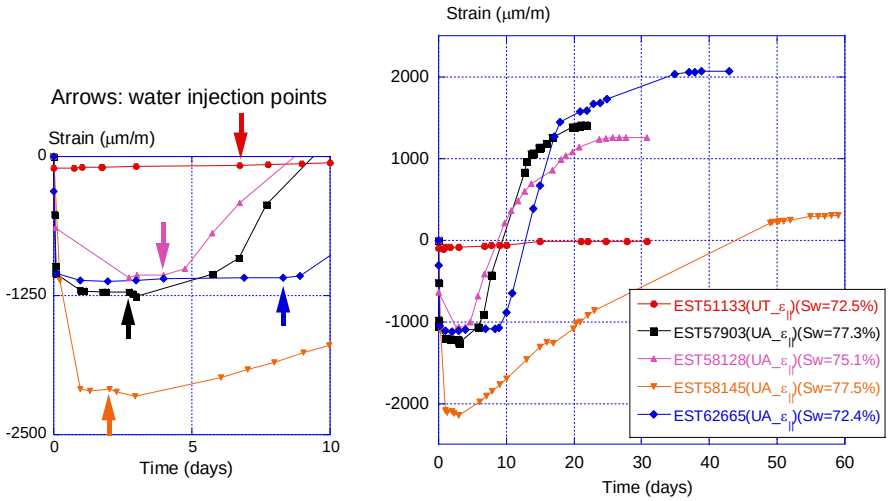

(a)

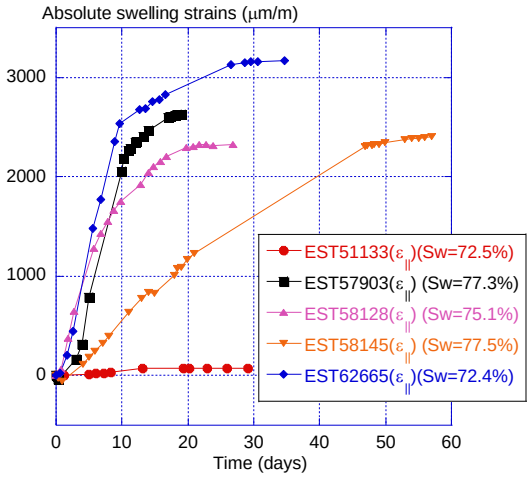

(b)

Figure 2.13. Strains evolution (parallel to bedding planes) of different samples, with P_c =14 MPa and P_i =5 MPa. (a) The overall strain evolution. The small chart on the left illustrates the water injection points after loading P_c; (b) absolute swelling behavior during loading P_i.

Fig. 2.14 shows the linear relations between $\varepsilon_{||}$ and smectite-related clays for both UT and UA materials. Inspections of data suggest that $\varepsilon_{||}$ vs. R1-I/S corresponds to the highest R^2 (96.0%) while

the worst correlation is $\varepsilon_{\parallel}$ vs. R0-I/S (R^2=77.2%). In the comparison of Fig. 2.14 with Fig.2.7-2.9, one can note that the mm-scale property $\varepsilon_{\parallel}$ has similarities with the µm-scale and nm-scale pore properties (i.e. V_{Gur}, SSA and Q_0). This implies that the structural effect seems to be sitll valid at different scales.

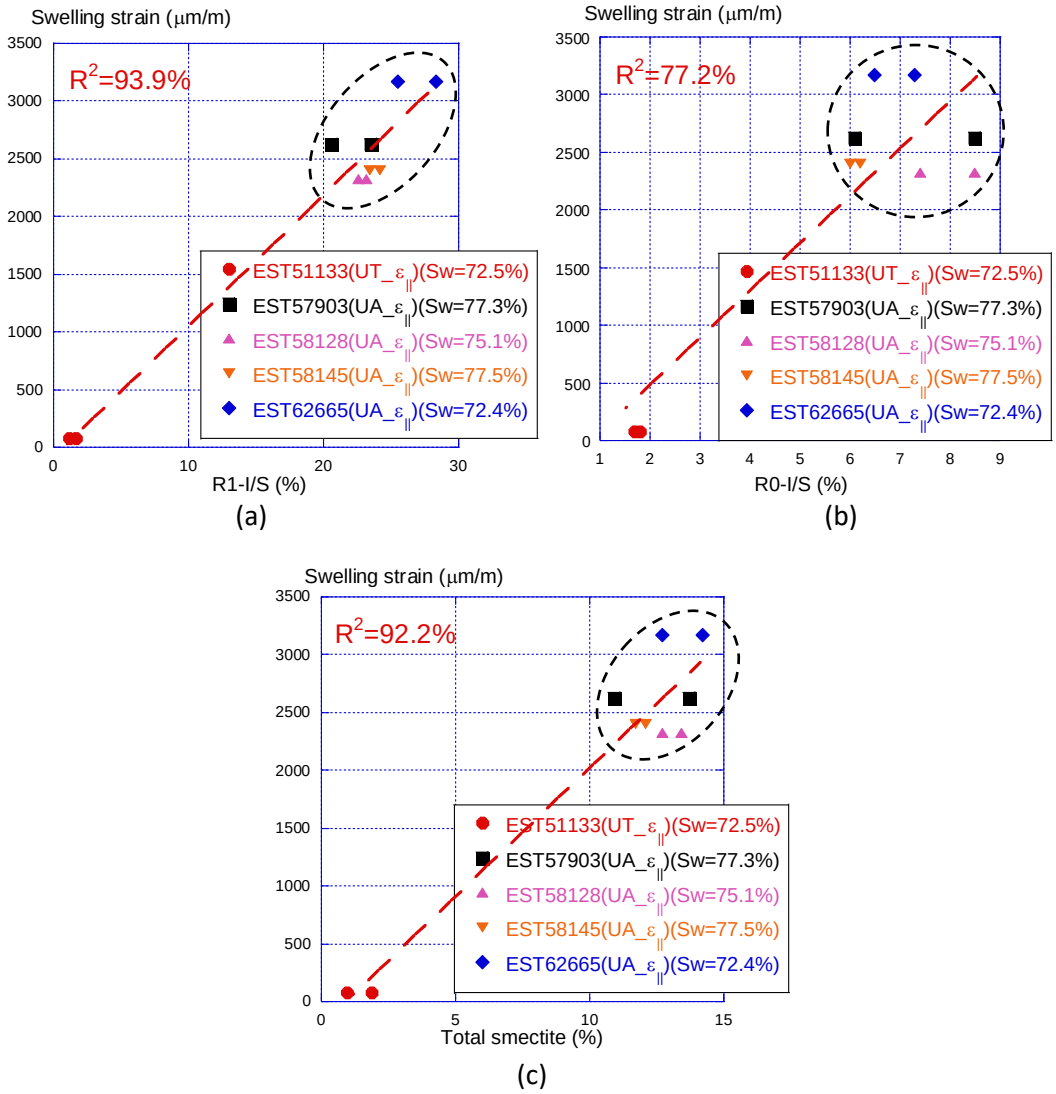

Fig. 2.14. Swelling amplitude vs. smectite-related clay contents for both UT and UA samples

This assumption can be confirmed by correlating $\varepsilon_{\parallel}$ to multi-scale pore textural properties, see Fig. 2.15. Fig. 2.15 (a) and (b) show that $\varepsilon_{\parallel}$ is well correlated with two mesoscopic pore properties, i.e. V_{Gur} (R^2=93.9%) and SSA (R^2=93.1%). This means that the expansion of centimetric samples is highly affected by the meso- and macropore volume and specific surface area. The micropore property Q_0 is also linearly related to $\varepsilon_{\parallel}$ with a relative smaller R^2 that equal to 84.7% (Fig. 2.15 (c)). This indicates that the expansion of micropores, which is a small part of the total pore volume, is also one of the drivers affecting macroscopic swelling strains. Hence, it can be concluded that the multiscale pores

swelling in all contribute to macroscopic volume expansion with 'in priori' contrasted swelling amplitudes.

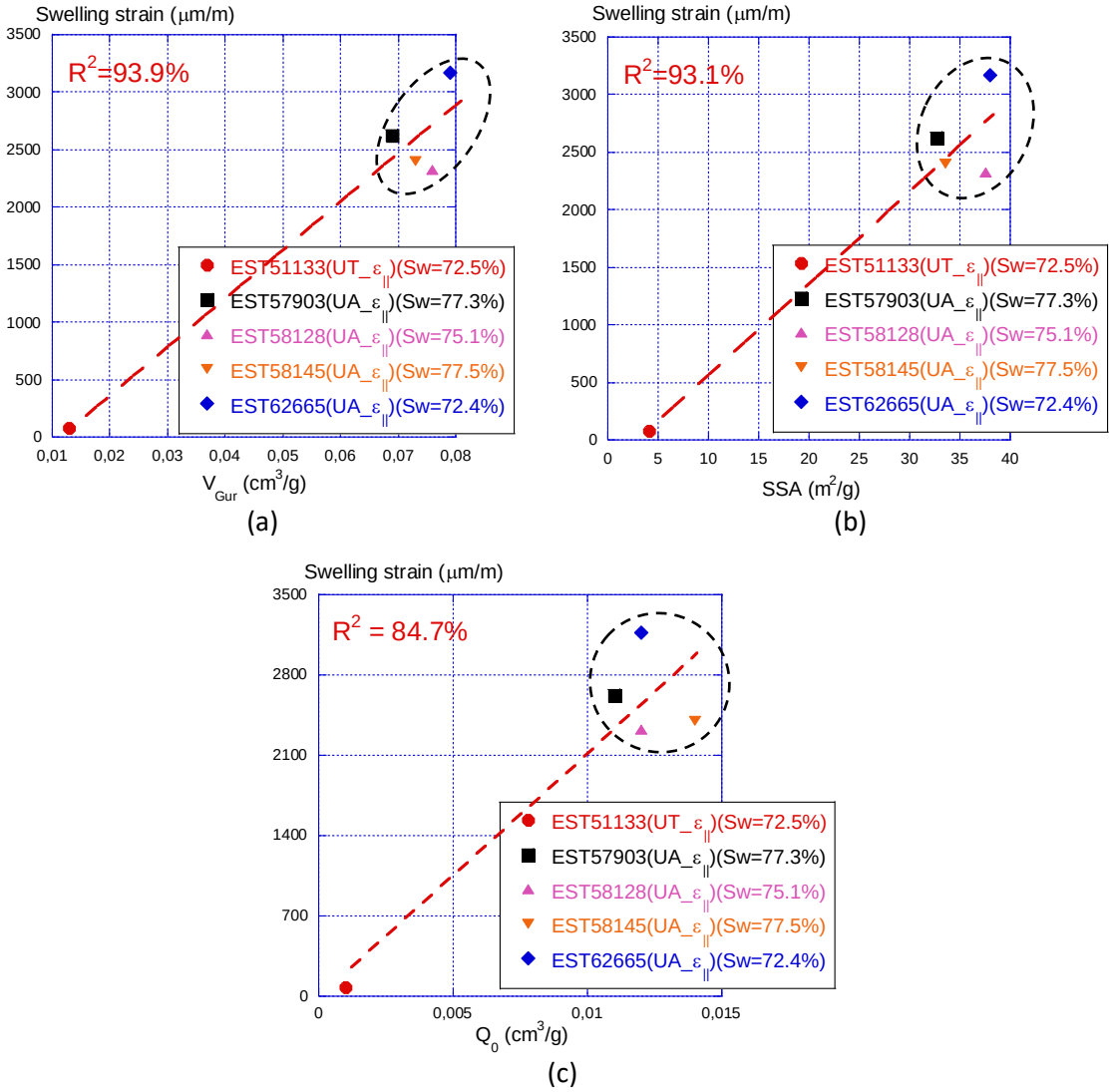

Fig. 2.15. Correlation between absolute swelling strain $\varepsilon_{\parallel}$ and multi-scale pore textural properties

Fig. 2.14 and Fig. 2.15 clearly show that the data again form two distinguished groups. This is logical because the large difference in clay content leads to significant variations in swelling capacity between UT and UA samples. By excluding the UT samples and only analyzing the UA samples (data highlighted by dash ovals in Fig. 2.14), one can note that the linear quality of all relations decreased, similar to the results presented in section 2.4.2.5. In addition, two general conclusions can be drawn by visual observation. Firstly, $\varepsilon_{\parallel}$ is clearly better linearly correlated with R1-I/S than R0-I/S, which could be explained by the smectite swelling in R1-I/S being more significant than in R0-I/S during re-saturation. This is a complementary result to section 2.4.2 and gives direct evidence for the structural effect of I/S at the macroscale. Secondary, inspections of data of UA samples in Fig. 2.15 indicate that the linear correlation of $\varepsilon_{\parallel}$ with V_{Gur} and SSA still exists while almost no correlation with Q_0. One could thus

conclude that $\varepsilon_{\parallel}$ is more related to the swelling of meso- and macropores than micropores. However, it should be noted that very little data is available in this study, more data are required for the validation of this conclusion.

2.5.3. Conceptual model for the COx swelling

As re-called in section 1.2, crystalline swelling occurs in the micropores, whereas osmotic swelling takes place in the mesopores. A conceptual model is proposed to give insights into the swelling process of COx claystone, see Figure 2.16.

As seen in Figure 2.16 (a) and (b), the inter-platelet region of smectite (in R1-I/S and R0-I/S) initially contains 0, 1, 2, and 3 layers of water molecules at different RH. With the increase of RH, crystalline swelling and osmotic swelling occur successively. Crystalline swelling is the first to appear by increasing the thickness of smectite particles (Figure 2.16 (c) and (d)). As shown in Figure 2.16 (left part), the smectite basal spacing increases with RH due to the increase of inter-platelet water layers. At 100% RH, the basal spacing value reaches the maximum value (21.6 Å) and the crystalline swelling is completed. It should be underlined that both R1- and R0-I/S exhibit an increase in layer thickness until the crystalline swelling is complete, without causing any structural damage.

After the crystalline swelling stops, osmotic swelling continues at high saturation levels. Free water molecules keep diffusing into the interlayer regions and lead to the cleavage of highly stacked interstratified I/S along the smectite inter-platelets. The osmotic swelling process is different in R1-I/S and R0-I/S. Thanks to the large pore volume and a small amount of smectite particles, the stacked R1-I/S layers can evolve to highly disaggregated smectite particles (Figure 2.16 (e)). Such a decomposition process produces many smectite “fragments” inducing more surface area for water molecules sorption. More importantly, since each smectite “fragment” carries negative charges on its surface, the system will absorb more water molecules to achieve the overall electrical balance. These water molecules cause an increase in the distance between adjacent fragments, which is coming along with an increase in osmotic pressure. In contrast, the decomposition of R0-I/S is less complete. Limited by the pore volume, the stacked R0-I/S is decomposed into illite clusters and smectite clusters (Figure 2.16 (f)). Apparently, the incomplete decomposition of R0-I/S results in a smaller volume expansion and surface area than that of R1-I/S. Consequently, the swelling amplitude of the centimetric sample with high R1-I/S content (Figure 2.16 (g)) would be greater than the one with high R0-I/S content (Figure 2.16 (h)).

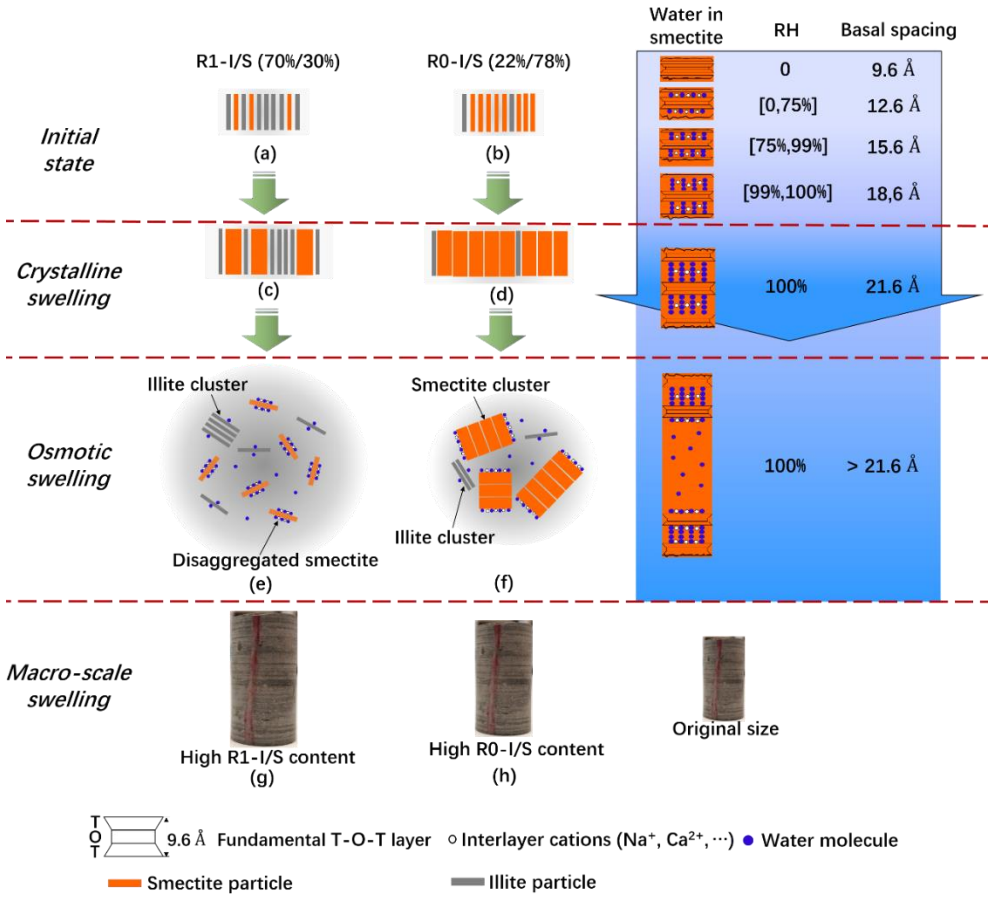

Figure 2.16. Conceptual model of multi-scale swelling mechanism of COx claystone. (a) and (b) illustrate the unsaturated R1-I/S and R0-I/S, respectively. Smectite particles are inserted in the interstratified I/S phases. With the increase of RH, the initial water layer state in the smectite inter-platelet space corresponds to 1-3 water layers; (c) and (d) show the crystalline swelling of R1-I/S and R0-I/S, respectively, corresponding to 100% RH. Smectite inter-platelet spaces are filled by four layers of water molecules; (e) and (f) are the osmotic swelling of R1-I/S and R0-I/S. The material saturation maintains 100% RH during the osmotic swelling process; (g) is the sample with high R1-I/S content after swelling, while (h) is the sample with high R0-I/S content after swelling.

2.5.4. Swelling kinetics vs. clay contents & N2 sorption properties

From Figure 2.13, one can observe that it takes around 10 days to achieve the strain stabilization for the UT sample (EST51133), whereas the time to stabilize UA samples is between 19 and 56 days. It can be logically concluded that materials containing more smectite require longer swelling reaction times. However, no specific linear relationship was observed between the swelling kinetics and the used pore structure properties. One possible interpretation is that the mineralogical composition of UA material was too close to highlight the differences in swelling rate and time between samples (see the black, blue and pink curves in Figure 2.13 (b)). Although sample EST 58145 (orange one in Figure 2.13) has a longer swelling time than that of other UA samples, this cannot be explained through the available data. Hence, more samples and data are needed for further analysis. For instance, macroscopic properties such as permeability and diffusivity are likely to play a major role in swelling kinetics.

2.5.5. Swelling vs. micro-cracks

In order to study the effect of micro-cracking on the swelling behavior, $\varepsilon_{\parallel}$ and $\varepsilon_{\perp}$ were recorded and analyzed, respectively shown in Figure. 2.17 (a) and (b). Despite the existence of micro-cracks, neither $\varepsilon_{\parallel}$ and $\varepsilon_{\perp}$ exhibited a significant difference in contraction during confinement loading. The difference is mostly visible after water injection (P_i= 5 MPa),which is followed by a pronounced effect of micro-cracking. This effect is clearly involved in the swelling amplitude. Both $\varepsilon_{\parallel}$ and $\varepsilon_{\perp}$ of micro-cracked samples (MC-1 and MC-2) are greater than the intact ones (I-1 and I-2). $\varepsilon_{\parallel}$ of micro-cracked samples are around twice that of intact samples, while $\varepsilon_{\perp}$ of micro-cracked ones are almost three times greater than that of intact ones. The micro-cracking effect is more significant for $\varepsilon_{\perp}$, which is consistent with a more intense micro-cracking parallel to the beddings. This leads to more swelling space and less rigidity (i.e. the material becomes more deformable) perpendicularly to the beddings. For a short period of time after starting water injection (several days), micro-cracked samples (particularly the MC-2) exhibit higher swelling kinetics than the intact samples. This can be attributed to the presence of cracks creates more contact surface for initial water imbibition, allowing pore water to contact the smectite in the clay matrix more rapidly at the beginning of the test. Obviously cracking induces increases in permeability and diffusivity. This reinforces the fact, mentioned before, that these properties play a major role in the swelling kinetics. For engineering implications, *in-situ* COx claystone swells under a quasi-constant volume, and the presence of micro-cracks can significantly affect the cumulative expansion pressure generated over time.

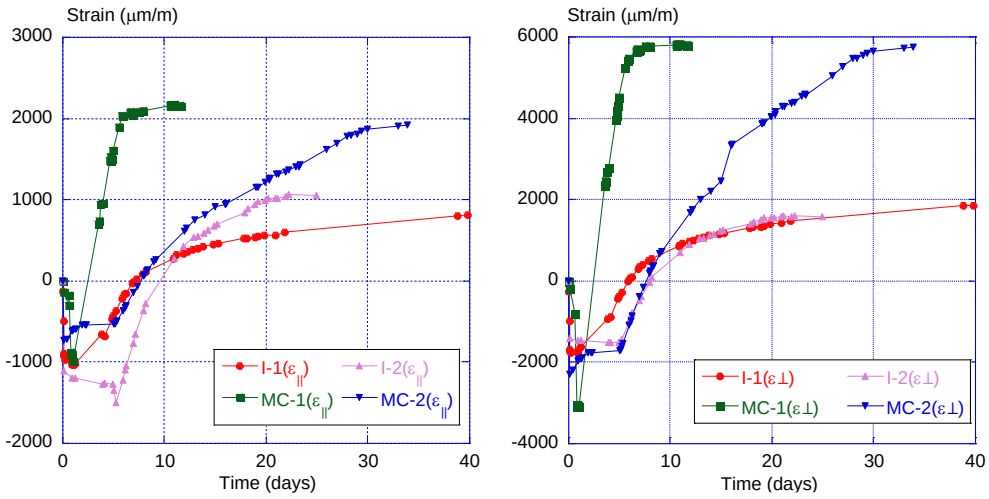

(a) (b)

Figure 2.16. Comparison of swelling between intact and micro-cracked samples of sample EST58128 (a) swelling strain parallel to bedding planes ($\varepsilon_{\parallel}^{S}$) (b) swelling strain perpendicular to bedding planes ($\varepsilon_{\perp}^{S}$)

2.6. Chapter summary

This chapter focuses on investigating the effect of clay minerals (specifically smectite-related clays) and pore structure on the swelling behavior of COx claystone. Five COx samples (one UT sample and four UA sample) originated from different geological locations were tested with different approaches. Quantitative XRD and cation exchange capacity (CEC) analysis indicates that smectite is the only swelling clay in COx. It exists in two types interspersed in I/S aggregates, namely R1-I/S (30% smectite) and R0-I/S (78% smectite).

Based on different models, nitrogen isotherms were used to study the pore textual properties, such as Gurvich specific volume (V_{Gur}), BET specific surface area (SSA) and micropore volume (Q_0). It is found that these pore properties have the highest correlation with R1-I/S and the lowest correlation with R0-I/S. This means that from microscale to macroscale, the interstratified I/S phase with lower smectite content consistently corresponds to greater pore volume and surface. Characteristic energy E and Dubinin-Astakhov exponent n are the micropore textural properties necessary to apply the Dubinin-Astakhov theory. No apparent difference of the two properties was observed between UT and UA samples, which can be explained by the swelling mechanism in micropores, i.e. crystalline swelling is identical for all COx samples. The cumulative pore size distribution derived from Barrett-Joyner-Halenda + Dubinin-Astakhov theories, indicates that increasing smectite-related clay content mainly increases the pore volume between 0 and 45 nm. This means that the macroscopic volume expansion mainly originates from the swelling of these pores. Within this pore size range, both crystalline swelling and osmotic swelling are promoted.

A series of swelling tests were carried out to investigate the anisotropic swelling behavior under constant confining pressure. Swelling strain parallel to bedding planes ($\varepsilon_{\parallel}^{S}$) is used to analyze the effect of smectite-related minerals, due to it is hardly affected by layered structure. Linear correlation of $\varepsilon_{\parallel}^{S}$ with smectite-related clay minerals revealed that R1-I/S has the highest correlation, while R0-I/S shows the lowest correlation. Combined with the nitrogen sorption data to analyze, it can be concluded that the macroscopic strain amplitude is mainly determined by two microscopic factors: the total content of smectite in interstratified I/S phases and the accessible pores for water-smectite contact. A conceptual model is proposed to describe a multi-scale swelling mechanism of COx claystone.

The effect of micro-cracks on swelling was studied showing that micro-cracking causes the material to exhibit a greater swelling amplitude and higher initial swelling kinetics. In particular, the compress-induced micro-cracks are more likely to parallel to the bedding planes, leading to a more pronounced expansion in the direction perpendicular to the bedding planes. Results also indicate the swelling kinetics of intact sample not solely depends on the clay content and pore structures, but is likely to depend on other properties like permeability and diffusivity.

References

Altaner, Bethke, 1988. Interlayer order in illite/smectite. American Mineralogist 73, 766–774.

Anderson, R.L., Ratcliffe, I., Greenwell, H.C., Williams, P.A., Cliffe, S., Coveney, P.V., 2010. Clay swelling — A challenge in the oilfield. Earth-Science Reviews 98, 201–216.

Andra, 2015. Inventaire national des matieres et dechets radioactifs.

Barrett, E.P., Joyner, L.G., Halenda, P.P., 1951. The Determination of Pore Volume and Area Distributions in Porous Substances. I. Computations from Nitrogen Isotherms. J. Am. Chem. Soc. 73, 373–380. https://doi.org/10.1021/ja01145a126

Bastiaens, W., Bernier, F., Li, X. ling, 2007. SELFRAC: Experiments and conclusions on fracturing, self-healing and self-sealing processes in clays. Physics and Chemistry of the Earth, Parts A/B/C 32, 600–615.

Bernier, F., Li, X.L., Bastiaens, W., Ortiz, L., Van Geet, M., Wouters, L., Frieg, B., Blumling, P., Desrues, J., Viaggiani, G., Coll, C., Chanchole, S., De Greef, V., 2007. Fractures and Self-sealing within the Excavation DIsturbed Zone in Clays (SELFRAC). EIG Euridice GIE-BE.

Bertier, P., Schweinar, K., Stanjek, H., Ghanizadeh, A., Clarkson, C.R., Busch, A., Kampman, N., Prinz, D., Amann-Hildebrand, A., Krooss, B.M., Pipich, V., 2016. On the use and abuse of N2 physisorption for the characterization of the pore structure of shales. pp. 151–161. https://doi.org/10.1346/CMS-WLS-21.12

Bish, D.L., 1988. Smectite dehydration and stability: Applications to radioactive waste isolation at Yucca Mountain, Nevada (No. LA--11023-MS, 60343). https://doi.org/10.2172/60343

Boek, E.S., Coveney, P.V., Skipper, N.T., 1995. Monte Carlo Molecular Modeling Studies of Hydrated Li-, Na-, and K-Smectites: Understanding the Role of Potassium as a Clay Swelling Inhibitor. J. Am. Chem. Soc. 117, 12608–12617. https://doi.org/10.1021/ja00155a025

Carrier, B., Wang, L., Vandamme, M., Pellenq, R.J.-M., Bornert, M., Tanguy, A., Van Damme, H., 2013. ESEM Study of the Humidity-Induced Swelling of Clay Film. Langmuir 29, 12823–12833. https://doi.org/10.1021/la402781p

Daab, M., Eichstaedt, N.J., Habel, C., Rosenfeldt, S., Kalo, H., Schießling, H., Förster, S., Breu, J., 2018. Onset of Osmotic Swelling in Highly Charged Clay Minerals. Langmuir 34, 8215–8222. https://doi.org/10.1021/acs.langmuir.8b00492

Davy, C.A., Skoczylas, F., Barnichon, J.D., Lebon, P., 2007. Permeability of macro-cracked argillite under confinement: Gas and water testing. Physics and Chemistry of the Earth, Parts A/B/C 32, 667–680.

Dormieux, L., Lemarchand, E., Coussy, O., 2003. Macroscopic and Micromechanical Approaches to the Modelling of the Osmotic Swelling in Clays. Transport in Porous Media 50, 75–91.

Duan, Z., Skoczylas, F., Wang, C., Talandier, J., 2021. Hydric Cycle Impacts on COx Argillite Permeability and Young's Modulus. Rock Mech Rock Eng 54, 1129–1147. https://doi.org/10.1007/s00603-020-02258-1

Dubinin, M.M., Astakhov, V.A., 1971. DEVELOPMENT OF THE CONCEPTS OF VOLUME FILLING OF MICROPORES IN THE ADSORPTION OF GASES AND VAPORS BY MICROPOROUS ADSORBENTS COMMUNICATION I. CARBON ADSORBENTS. Physical Chemistry 1, 5–11.

Halsey, G., 1948. Physical Adsorption on Non-Uniform Surfaces. Journal of Chemical Physics 16, 931–937.

Harkins, W.D., Jura, G., 1944. Surfaces of Solids. XIII. A Vapor Adsorption Method for the Determination of the Area of a Solid without the Assumption of a Molecular Area, and the Areas Occupied by Nitrogen and Other Molecules on the Surface of a Solid. J. Am. Chem. Soc. 66, 1366–1373. https://doi.org/10.1021/ja01236a048

Hensen, E.J.M., Smit, B., 2002. Why Clays Swell. J. Phys. Chem. B 106, 12664–12667. https://doi.org/10.1021/jp0264883

Jackson, M.L., Abdel-Kader, F.H., 1978. Kaolinite Intercalation Procedure for All Sizes and Types with X-Ray Diffraction Spacing Distinctive from Other Phyllosilicates. Clays and Clay Minerals 26, 81–87. https://doi.org/10.1346/CCMN.1978.0260201

Janssen, M.J.G., Van Oorschot, C.W.M., 1989. The Characterization of Zeolites by Gas Adsorption, in: Studies in Surface Science and Catalysis. Elsevier, pp. 633–642. https://doi.org/10.1016/S0167-2991(08)61761-9

Lahn, L., Bertier, P., Seemann, T., Stanjek, H., 2020. Distribution of sorbed water in the pore network of mudstones assessed from physisorption measurements. Microporous and Mesoporous Materials 295, 109902.

Lammers, L.N., Brown, G.E., Bird, D.K., Thomas, R.B., Johnson, N.C., Rosenbauer, R.J., Maher, K., 2015. Sedimentary reservoir oxidation during geologic CO2 sequestration. Geochimica et Cosmochimica Acta 155, 30–46. https://doi.org/10.1016/j.gca.2015.02.001

Massat, L., Cuisinier, O., Bihannic, I., Claret, F., Pelletier, M., Masrouri, F., Gaboreau, S., 2016. Swelling pressure development and inter-aggregate porosity evolution upon hydration of a compacted swelling clay. Applied Clay Science 124–125, 197–210. https://doi.org/10.1016/j.clay.2016.01.002

Meier, L.P., Kahr, G., 1999. Determination of the Cation Exchange Capacity (CEC) of Clay Minerals Using the Complexes of Copper(II) Ion with Triethylenetetramine and Tetraethylenepentamine. Clays and Clay Minerals 47, 386–388.

Menaceur, H., Delage, P., Tang, A.M., Talandier, J., 2016. The Status of Water in Swelling Shales: An Insight from the Water Retention Properties of the Callovo-Oxfordian Claystone. Rock Mech Rock Eng 49, 4571–4586.

Michot, L.J., Bihannic, I., Thomas, F., Lartiges, B.S., Waldvogel, Y., Caillet, C., Thieme, J., Funari, S.S., Levitz, P., 2013. Coagulation of Na-Montmorillonite by Inorganic Cations at Neutral pH. A Combined Transmission X-ray Microscopy, Small Angle and Wide Angle X-ray Scattering Study. Langmuir 29, 3500–3510. https://doi.org/10.1021/la400245n

Minardi, A., Crisci, E., Ferrari, A., Laloui, L., 2016. Anisotropic volumetric behaviour of Opalinus clay shale upon suction variation. Géotechnique Letters 6, 144–148.

Mitchell, J.K., Soga, K., 2005. Fundamentals of Soil Behavior, 3rd Edition. ed. John Wiley & Sons, Ltd, New Jersey.

Mooney, R.W., Keenan, A.G., Wood, L.A., 1952. Adsorption of Water Vapor by Montmorillonite. II. Effect of Exchangeable Ions and Lattice Swelling as Measured by X-Ray Diffraction. J. Am. Chem. Soc. 74, 1371–1374. https://doi.org/10.1021/ja01126a002

Pusch, R., Kasbohm, J., Hoang-Minh, T., 2019. Degradation Mechanisms in Smectitic Clay for Isolating Radioactive Waste. Journal of Earth Sciences and Geotechnical Engineering 9, 115–130.

Rietveld, H.M., 1969. A profile refinement method for nuclear and magnetic structures. J Appl Crystallogr 2, 65–71. https://doi.org/10.1107/S0021889869006558

Rouquerol, J., Llewellyn, P., Rouquerol, F., 2007. Is the bet equation applicable to microporous adsorbents?, in: Studies in Surface Science and Catalysis. Elsevier, pp. 49–56. https://doi.org/10.1016/S0167-2991(07)80008-5

Saiyouri, N., Hicher, P.-Y., Tessier, D., 2000. Microstructural Approach and Transfer Water Modelling in Highly compacted Unsaturated Swelling Clays. Mechanics of Cohesive-frictional Materials 5, 41–60.

Seemann, T., Bertier, P., Krooss, B.M., Stanjek, H., 2017. Water vapour sorption on mudrocks. Geological Society, London, Special Publications 454, 201–233.

Slade, P.G., 1991. Crystalline Swelling of Smectite Samples in Concentrated NaCl Solutions in Relation to Layer Charge. Clays and Clay Minerals 39, 234–238. https://doi.org/10.1346/CCMN.1991.0390302

Song, Y., Davy, C.A., Bertier, P., Troadec, D., 2016. Understanding fluid transport through claystones from their 3D nanoscopic pore network. Microporous and Mesoporous Materials 228, 64–85.

Thommes, Kaneko, Neimark, Olivier, Rodriguez-Reinoso, Rouquerol, Sing, 2015. Physisorption of gases, with special reference to the evaluation of surface area and pore size distribution (IUPAC Technical Report). Pure and Applied Chemistry 87, 1051–1069.

Ufer, K., Kleeberg, R., 2015. Parametric Rietveld refinement of coexisting disordered clay minerals. Clay miner. 50, 287–296. https://doi.org/10.1180/claymin.2015.050.3.03

Van Geet, M., Bastiaens, W., Ortiz, L., 2008. Self-sealing capacity of argillaceous rocks: Review of laboratory results obtained from the SELFRAC project. Physics and Chemistry of the Earth, Parts A/B/C 33, S396–S406.

Wang, C., Davy, C.A., Skoczylas, F., Talandier, J., 2021a. Effect of mineralogical composition and pore structure on the swelling of COx claystone 39, 8.

Wang, C., Gay, N., Talandier, J., Skoczylas, F., 2021b. Poroelastic experiments on COx claystone: insight from the Biot's coefficient measurement with water. Engineering Geology.

Wang, L., Bornert, M., Chanchole, S., Yang, D., Héripre, E., Tanguy, A., Caldemaison, D., 2013. Micro-scale experimental investigation of the swelling anisotropy of the Callovo-Oxfordian argillaceous rock. Clay miner. 48, 391–402.

Wang, L., Bornert, M., Yang, D., Héripré, E., Chanchole, S., Halphen, B., Pouya, A., Caldemaison, D., 2015. Microstructural insight into the nonlinear swelling of argillaceous rocks. Engineering Geology 193, 435–444.

Wang, L., Yang, D., Chanchole, S., Zhang, 2017. The time-dependent swelling of argillaceous rock under resaturated conditions. Applied Clay Science 146, 186–194.

Yuan, H., 2017. Caractérisation expérimentale des propriétés de poromécaniques et de transfert de l'argilite du COx (PhD thesis). Ecole Centrale de Lille, Lille.

Zhang, C.-L., 2018. Thermo-hydro-mechanical behavior of clay rock for deep geological disposal of high-level radioactive waste. Journal of Rock Mechanics and Geotechnical Engineering 10, 992–1008.

Zhang, C.-L., 2011. Experimental evidence for self-sealing of fractures in claystone. Physics and Chemistry of the Earth, Parts A/B/C 36, 1972–1980.

3. Chapter 3 - Poroelastic experiments on COx claystone: insight from the Biot's coefficient measurement with water

This chapter focuses on Biot's coefficient measurement of saturated COx claystone. The tests were systematically conducted to provide clarification on its value as the available literature indicates quite erratic results from 0.26 to 1. The difficulty of this work mainly lies in the time that is necessary to stabilize each loading step (confining pressure and/or pore pressure) and also in sample preparation. Two main results were obtained: 1) Whatever the initial conditions were (confining pressure P_c amplitude, hydric state, damaged or not…), all samples exhibited a significant anisotropic swelling during the first water injection; 2) even being a transversely isotropic rock, its Biot's tensor is (quasi) isotropic thus leading to a unique coefficient "*b*" which is very close to 1. Such results are consistent with what was observed with gas as being the fluid to control pore pressure in partially saturated samples.

In contrast to many results reported in the literature, experimental studies carried out in our laboratory clearly showed that, despite the structural anisotropy, the Biot's tensor was isotropic leading to a coefficient very close to 1 (Cariou et al., 2012, 2013; Yuan et al., 2017; Hu et al., 2020). These previous works were carried out on partially saturated material and used gas as the fluid to control pore pressure. This showed that gas was theoretically a convenient fluid to perform such experiments. However, doubts remained about their equivalence with measurements using water to control the pore pressure and to maintain a full saturation state. This study had therefore been designed to complete gas experiments and to verify whether they are consistent with water experiments. Reconstituted synthetic water (close to the in-situ one) was used to measure the Biot's components in the saturated state. Two main results had to be confirmed: Biot's tensor isotropy and a unique coefficient close to 1.

3.1. Summary of the measurements of the Biot's claystone components using gas to control pore pressure

3.1.1. Constitutive relations in the case of transverse isotropy claystone

As mentioned before, the COx argillite from Bure is a transverse isotropic material. As shown in Figure 3.1, the isotropic plane is the bedding plane containing the structural axis 1, 2 and 3 being the *in-situ* vertical axis. Let us suppose that a crossed gauge is glued on a sample like in Figure 3.1. One gauge

direction is axis 1 or 2 (gauge J2) and the second one is along a direction “n” (gauge Jn). As the sample is a cylinder, axis ‘n’ can not exactly match with axis 3.

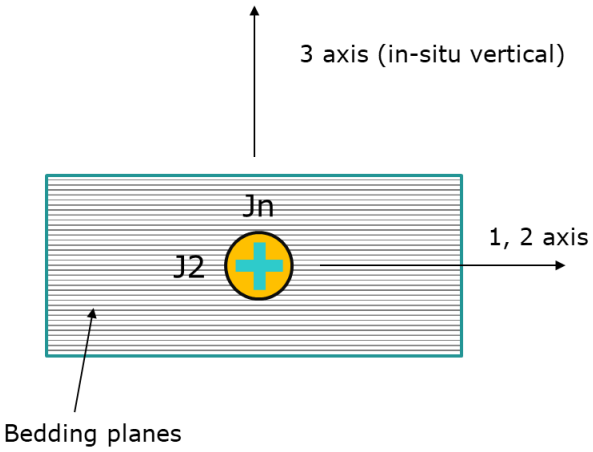

Figure 3.1. Scheme of the argillite sample with its bedding plane and equipped with crossed strain gages

Within the frame of Biot’s poro-elastic theory, the behavior of the material can be expressed with respect to its material axis using the following relation (Hu et al., 2020):

$$\begin{vmatrix}\varepsilon_{11}\\ \varepsilon_{22}\\ \varepsilon_{33}\\ \gamma_{12}\\ \gamma_{13}\\ \gamma_{23}\end{vmatrix} = \begin{vmatrix} \frac{1}{E_1} & \frac{-\nu}{E_1} & \frac{-\nu'}{E_1} & 0 & 0 & 0 \\ \frac{-\nu}{E_1} & \frac{1}{E_1} & \frac{-\nu'}{E_1} & 0 & 0 & 0 \\ \frac{-\nu'}{E_1} & \frac{-\nu'}{E_1} & \frac{1}{E_3} & 0 & 0 & 0 \\ 0 & 0 & 0 & \frac{2(1+\nu)}{E_1} & 0 & 0 \\ 0 & 0 & 0 & 0 & \frac{1}{G_{13}} & 0 \\ 0 & 0 & 0 & 0 & 0 & \frac{1}{G_{23}} \end{vmatrix} \begin{vmatrix}\sigma_{11}-bP_i\\ \sigma_{22}-bP_i\\ \sigma_{33}-b_3P_i\\ \sigma_{12}\\ \sigma_{13}\\ \sigma_{23}\end{vmatrix} \quad (3.1)$$

where compressive strengths are positive, and b, b_3 are the Biot’s tensor components used for a transverse isotropic behavior. A convenient approach to the identification of these components relies on the application of a hydrostatic loading P_c and/or a pore pressure P_i. One interesting case arises when b=b_3. When this specific case is verified, the following expressions for the three strain terms can be derived:

$$\left.\begin{aligned}\varepsilon_{11} &= \varepsilon_{11}(P_c)(1-\alpha b)\\ \varepsilon_{22} &= \varepsilon_{22}(P_c)(1-\alpha b)\\ \varepsilon_{33} &= \varepsilon_{33}(P_c)(1-\alpha b)\\ \gamma_{ij} &= 0\end{aligned}\right\} \quad (3.2)$$

where α=P_i/P_c , and

$$\varepsilon_{11}(P_c) = \varepsilon_{22}(P_c) = \frac{P_c}{E_1}[1 - (\nu + \nu')] \; and \; \varepsilon_{33}(P_c) = P_c(\frac{1}{E_3} - \frac{2\nu'}{E_1}) \quad (3.3)$$

A gauge Jn, glued in any direction n, will give $\varepsilon_{nn} = \bar{\bar{\varepsilon}}.\vec{n}.\vec{n}$, with $\vec{n}$: $\begin{vmatrix} n_1 \\ n_2 \\ n_3 \end{vmatrix}$. This leads to:

$$\varepsilon_{nn} = [\varepsilon_{11}(P_c)(n_1)^2 + \varepsilon_{22}(P_c)(n_2)^2 + \varepsilon_{33}(P_c)(n_3)^2](1 - \alpha b) \quad (3.4)$$

Rel. (3.4) shows that, whatever the gauge direction, the Biot's coefficient b can be derived from two measurements, which may be combined: hydrostatic loading with a confining pressure P_c and a change in pore pressure P_i. This is useful when the direction of axis 3 is not accurately known as it is the case for COx claystone samples. It can also be underlined that an "isotropic" Biot's coefficient does not mean that a change in pore pressure would lead to isotropic strain state (see relations (3.2) and (3.3)).

3.1.2. The use of gas to control pore pressure

In a poro-mechanical test intended to measure Biot's coefficient, loading/unloading P_i is always more difficult than controlling P_c. As the water permeability of COx claystone is in the range 10^{-20} to 10^{-21} m² (M'Jahad et al., 2017; Yuan, 2017), reaching a homogeneous pore pressure is not only time-consuming but very difficult to assess. It will be seen in the following that the strain stabilization due to P_i variation can be very long. Another specific property of COx claystone is that the material exhibits significant volumetric swelling from unsaturated to saturated state. Such process can also last for a very long time, depending on the material initial saturation state, swelling mineral content, and confinement (Anderson et al., 2010; Busch et al., 2020; IAEA, 2013). Another specificity is that experiments with gas do not change the sample saturation level, which allow Biot's coefficient measurements on a dry and/or partially saturated sample. This particular aspect is crucial as it means that gas pressure change ΔP_i, applied at both sample ends, leads to the same pressure ΔP_i for both gas and water phases inside the sample. This was demonstrated by Cariou and led to a very important consequence: gas pressure ΔP_i, even applied on a partially saturated sample, induces a uniform global pore pressure change ΔP_i, i.e. can be used to perform poro-mechanical experiments on a non-fully saturated material.

In conclusion, gas is a good choice to control pore pressure as it is involved in rel. (3.1). Technically, pore pressure equilibrium is easier to be reached by injecting the gas at both sample ends, which also significantly shortens the test time and avoids the swelling effect.

3.1.3. Results obtained with gas. A summary

Cariou et al. (2012) were the first to perform this kind of test on COx samples. By using argon as the pore fluid, results showed that the stiffness of COx claystone exhibits noticeable anisotropic property (Figure 3.2). It is evidenced by the strain amplitudes, due to Pc change, along bedding plane or perpendicular to it. This is a common result for all the tests having been performed for more than 10 years.

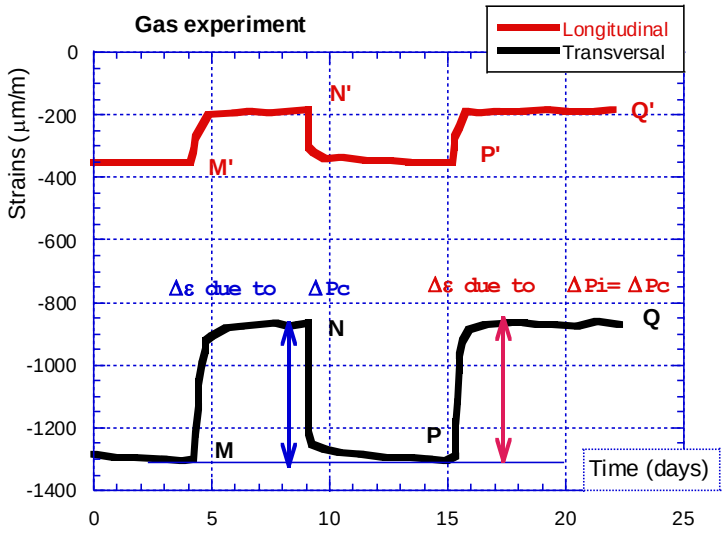

Figure 3.2. Anisotropic strain variations due to equivalent changes in Pc and Pi

As mentioned before, the results in Figure 3.2 are unambiguous as they indicate different strain values, depending on the direction, due to either P_c or P_i changes. What is more noticeable is that despite this behavior and whatever the direction is, the ratio $\varepsilon_i(\Delta P_i)/\varepsilon_i(\Delta P_c)$ is almost the same. This clearly evidences that the Biot tensor is isotropic. This result was also validated on a theoretical point of view (Hu et al., 2020). In the case illustrated in Figure 3.2, the ratio $\varepsilon_i(\Delta P_i = \Delta P_c)/\varepsilon_i(\Delta P_c)$ is 1 (or very close to 1 – see points M to N and P to Q). This was not a particular case as most of the results obtained in Cariou (2010) and Yuan (2017) confirmed this tendency.

It has been observed that the Biot's coefficient of partially saturated COx claystone is generally around 1, and hardly dependent on confining pressure and pore pressure (Yuan et al., 2017). However, it must be mentioned here that on dry material (or close to be) the measured Biot's components were higher than 1, which is theoretically not possible. This means that the strain due to variation of pore pressure ΔP_i, $\varepsilon_j(\Delta P_i{=}\Delta P_c)$, is higher than the one due to ΔP_c, $\varepsilon_j(\Delta P_c{=}\Delta P_i)$. A concomitant phenomenon was also observed by Song (2014) in porosity experiments performed with argon. This work evidenced argon adsorption in COx claystone. Biot's coefficient higher than 1 means an "over-swelling" due to pore pressure increase. Assuming that this swelling was due to adsorption, Yuan et al., (2017) focused

the research to compare the strains obtained either with argon or helium, which is a (quasi) non-adsorbable gas. Using helium led to consistent Biot's coefficient between (slightly higher than) 0,9 and 1 and never higher than 1 (Figure 3.3). Adsorption phenomena only occurred for dry (or quasi dry) material. This is quite logical as dry or quasi dry state means that the smallest pores are now free to be filled with gas whereas it is not true at higher level of water saturation. Adsorption is a surface phenomenon and it is well known that the smallest pores give the highest part of the material specific surface.

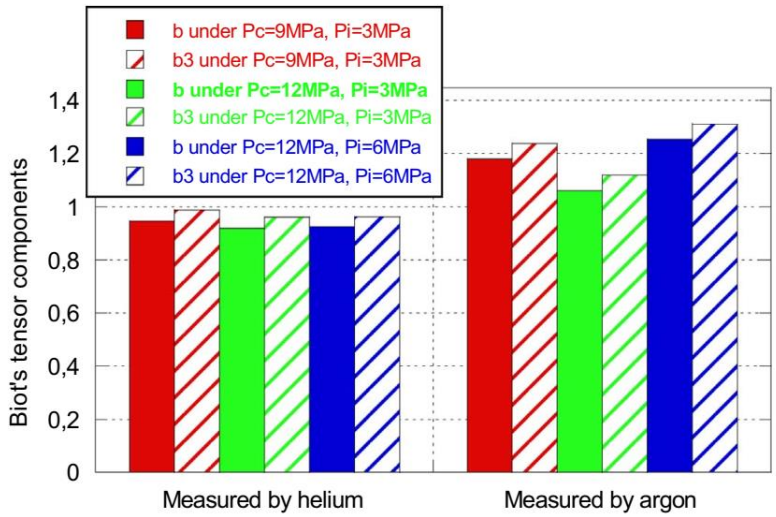

Figure 3.3. Measured Biot's tensor of COx claystone with helium and argon (Yuan et al., 2017)

3.1.4. Partial conclusion

Measuring Biot's coefficient with gas indicates that COx claystone exhibits a high isotropic Biot's coefficient (close to 1), despite a significant structural anisotropy. This is an inherent property of COx claystone, regardless the sample is dried or partially saturated. In the following section, such property is verified on fully saturated samples with synthetic water.

3.2. Measurements of the Biot's components with synthetic water

3.2.1. Sample preparation

COx claystone comes from the Meuse/Haute Marne Underground Research Laboratory (MHM-URL), France. The material had been initially sealed in a T1 cell (80 mm in diameter, 250 mm height cylinders). Due to the low permeability of COx, samples were cored into cylinders and of 40 mm in height and 20 mm in diameter in order to shorten the experiment duration i.e. to obtain a uniform pore pressure assessed by strain stability. Such a size is relatively smaller than the ASTM or the ISRM standard, but

still sufficient to avoid end effects with a slenderness of 2. For a transversely isotropic material it is important to identify the layer orientation. Hence, a small amount of water was sprayed on a sample end to highlight the layers, see Figure 3.4 left. It should be pointed out that this technique was not used for sample EST 57903-1, which led to a structural anisotropy effect less significant than for other tests. Nevertheless, thanks to rel. (3.4), the measured strains are still useful for the Biot's coefficient measurement.

Four strain gauges (5mm length) were glued on each sample. It should be noted here that this phase occurred after a specific sample surface treatment, which took a very long time to successfully develop so as to ensure a reliable gauge behavior over time (for weeks or months). This point is far to be insignificant as it is one of the main difficulties to conduct poro-mechanical experiments on this water saturated claystone. Two longitudinal gauges (in red) were diametrically placed along the sample bedding plane, while the two transverse gauges (in green) were respectively perpendicular to each longitudinal gauge, see Figure 3.4 middle. The two longitudinal gauges measured strains parallel to the beddings ($\varepsilon_{\parallel}$), and the two transverse gauges were used to measure strains perpendicularly to the beddings ($\varepsilon_{\perp}$). Despite their short length, transverse gauge axis cannot strictly be parallel to axis 3 due to the curvature of the sample. Nevertheless, $\varepsilon_{\perp}$ is still useful to be compared with $\varepsilon_{\parallel}$ and to calculate Biot's coefficient b (see rel. (3.4)).

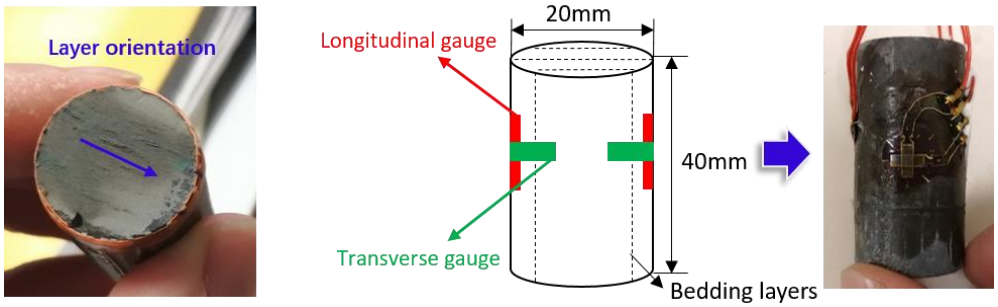

Figure 3.4. Specimen with gauges: two longitudinal gauges and two transverse gauges glued on the sample side surface.

Four samples, retrieved from three boreholes, were used for the tests. Different initial sample states were taken into account in order to evaluate their possible impact on Biot's coefficient measurements (see Table 3.1). A (quasi) dry sample was used (EST 51446) to be compared with highly saturated ones. A pre-damaged state, obtained with the uniaxial compressive test (UCT), was also considered (EST 58128).

Table 3.1. summary of the samples

Sample	Depth (m)	Curing	Initial saturation
EST 51446	-480	65°C	Close to 0
EST 57903-1	-490	-	86.8%
EST 57903-2	-490	-	86.8%
EST 58128	-490	Pre-damaged (UCT)	85.5%

3.2.2. Design of the experiments and measurement strategy

A special dedicated setup (see Figure 3.5) was designed to conduct experiments. It includes a hydrostatic cell, an ISCO syringe pump, a Gilson™ - type oil pump and a digital strain-meter. As the sample size is small, it was decided to simply dip it into oil pressure without linking it to the cell. This is more efficient to ensure the isotropic loading. For tightness and fluid injection purposes, samples were sandwiched between two porous stainless steel disks connected to capillary tubes via two steel hollow cylinders. They allow water pressure control (and injection) at both sample ends. The assembly of "sample + steel disks + steel hollow cylinders" was wrapped into a rubber jacket, then immersed in oil. During experiments, the loading/unloading of confining pressure (P_c) and interstitial water pressure (P_i) were applied by the Gilson™-type oil pump and the ISCO water pump, respectively. Strains were measured with a digital strain-meter having an accuracy of ± 10^{-6} m/m. Synthetic water, similar to in-situ water, was used in all poro-mechanical experiments. The mineralogical composition is detailed in Table 3.2.

Table 3.2. mineral composition of synthetic water

Mineral	NaCl	$NaHCO_3$	KCl	$CaSO_4,2H_2O$	$MgSO_4,7H_2O$	$CaCl_2,2H_2O$	Na_2SO_4	total
Concentration (g/L)	1.95	0.130	0.035	0.630	1.020	0.080	0.700	4.545

There are two different phases in the tests. They are necessary as, whatever the initial state is (dry to almost saturated – confining pressure intensity), there is always a significant swelling due to the first water injection (carried out to fully saturate the sample). This swelling is not only due to pore pressure effect as a large part of it attributed to specific clay swelling due to water molecules adsorption (Anderson et al., 2010; Carrier et al., 2013). Hence the first testing phase is to apply a couple (P_c, P_i),

which represents the initial state from which the so-called poro-mechanical experiment can start. It can be noticed here that this first phase can last weeks until strain stability, depending on the sample initial state and the content of swelling clay. The second phase follows with the measurement of Biot's components with water.

The experimental protocol is given as follows:

- Step 1: Maintaining the pore pressure constant (drained test), the initial isotropic confining pressure (P_c^1) is loaded to P_c^2, i.e. $P_c^2 = P_c^1 + \Delta P_c$. This step is often irreversible (not elastic) due to plastic deformation and/or micro-crack closure.
- Step 2: Pore pressure is varied under constant confining pressure. It is firstly increased by ΔP_i, with $\Delta P_i = \Delta P_c$. This step is regarded as being a unloading one as it leads to a decrease in effective isotropic pressure. Hence, this phase is likely to be elastic and leads to strain values ($\varepsilon_i(\Delta P_i)$) – ε_i is the strain recorded for gauge n°i. As soon as strain values are stabilized, the pore pressure is then decreased (by ΔP_i) back to its initial value P_i.
- Step 3: The pore pressure being constant, P_c^2 is decreased (by ΔP_c) down to P_c^1. This step is regarded as an elastic unloading path leading to $\varepsilon_i(\Delta P_c)$.

At this step $\varepsilon_i(\Delta P_c)$ and $\varepsilon_i(\Delta P_i = \Delta P_c)$ are compared and if the ratio $b = \varepsilon_i(\Delta P_i)/\varepsilon_i(\Delta P_c)$ is the same (or almost the same) for every gauge n°i, it can be concluded (rel. (3.2) to rel. (3.4)) that Biot's tensor is isotropic with a single component *b*, which is then the Biot's coefficient. If the ratio depends on the gauge direction (orientation) then the Biot's tensor is not isotropic and the situation begins to be trickier as the complete identification of this tensor would require other complementary experiments. It is also possible to use some kind of average value of the volumetric strain, which is difficult to measure if the structural axes are not perfectly identified. From this averaging, a mean "Biot's coefficient" can be obtained with the volumetric strains due to ΔP_c and ΔP_i. Such a method leads to a "mean" coefficient value but is not rigorous from a poro-mechanical point of view.

- Step 4: The Biot's coefficient is calculated by the ratio $b = \varepsilon_i(\Delta P_i)/\varepsilon_i(\Delta P_c)$ if it is independent on any gauge direction.

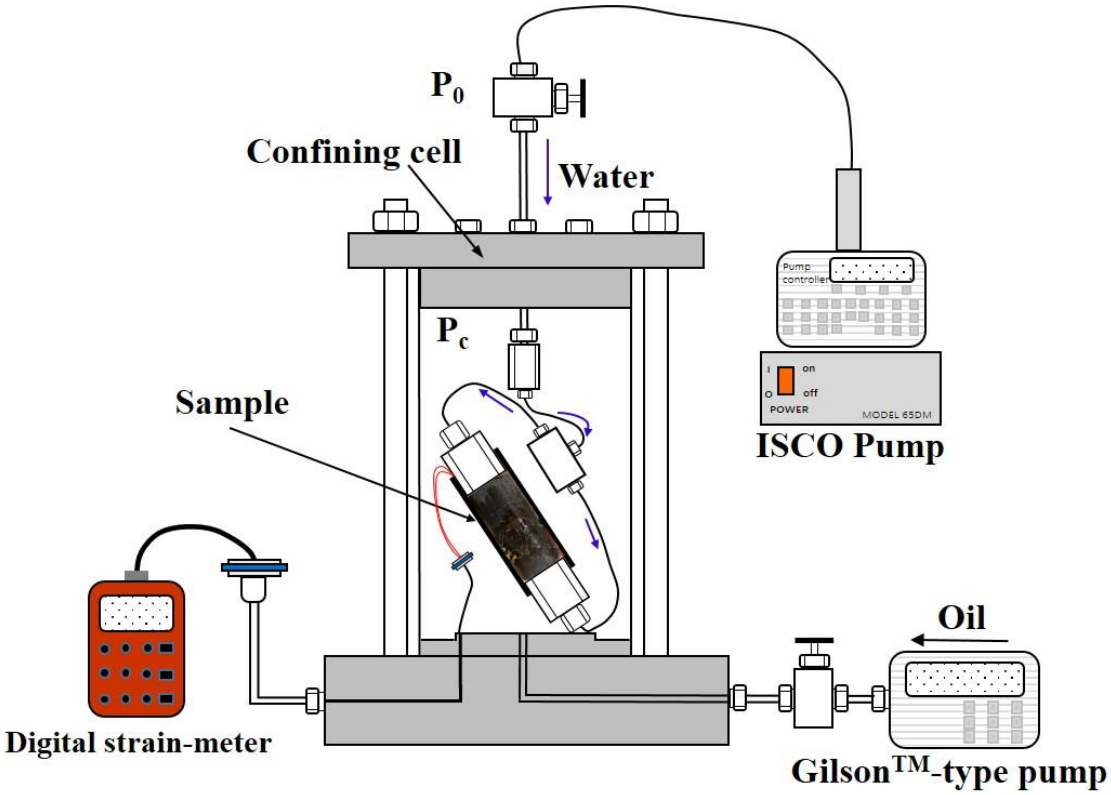

Figure 3.5. Experiment setup used for Biot's components measurement.

3.3.Results and discussion

The result presentation is divided into two parts to highlight: the swelling phase due to initial loading (P_c, P_i) and Biot's coefficient isotropy derived from the poro-mechanical loading phases. For a clearer analysis of strain variation, the average values of two longitudinal or transverse gauges were considered to represent the mean strain parallel or perpendicular to bedding planes.

3.3.1. Swelling due to initial loading (Pc, Pi)

Table 3.3 shows the initial loading (P_c, P_i) leading to P^{eff} (Terzaghi's effective pressure). The tests were generally performed with a first P_c loading followed by water injection in order to obtain P_i. Sometimes both P_c and P_i were simultaneously applied. An example is given in Figure 3.6. An important phenomenon has to be underlined here, which is linked to COx claystone re-saturation with liquid water. Even if the initial effective stress – indicated by P^{eff} – is isotropic compression, there is always a resulting absolute swelling. This swelling occurred whatever the initial conditions were (P_c amplitude, hydric state, damaged or not…). It is not the purpose of the present study to focus on this phenomenon as it is still under study in the laboratory. However, in the context of nuclear waste storage in COx rock, such a swelling effect facilitates the crack closure in the Excavation Damaged Zone

(EDZ) and leads to “self-sealing” (Wang et al., 2021). The swelling amplitude and kinetics are contrasted and variable. They depend on sample initial state and likely on its mineral composition.

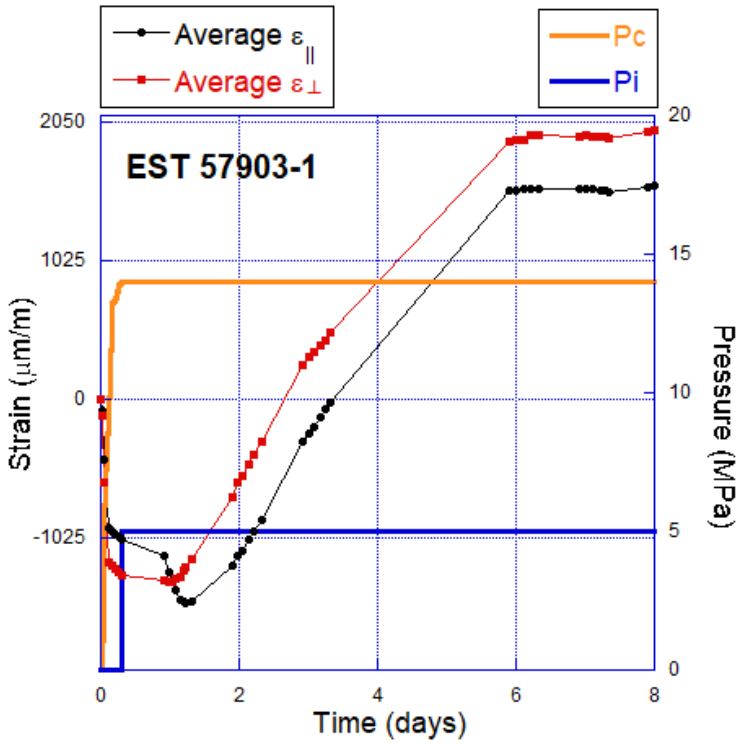

Figure 3.6. Example of a first loading phase of EST 57903-1: Pc and Pi were simultaneously applied. Positive strain is expansion

Table 3.3. Summary of initial pressure and swelling properties of tested samples

Sample	P_c (MPa)	P_i (MPa)	P^{eff} (MPa)	Absolute Swelling (μm/m)	Swelling time (days)
EST 51446	5	2	3	$\varepsilon_{\parallel}$=4101 $\varepsilon_{\perp}$=10027	9
EST 57903-1	14	5	9	$\varepsilon_{\parallel}$=1580 $\varepsilon_{\perp}$=1992	6
EST 57903-2	14	4	10	$\varepsilon_{\parallel}$=1645 $\varepsilon_{\perp}$=6505	11
EST 58128	14	5	9	$\varepsilon_{\parallel}$=1925 $\varepsilon_{\perp}$=5745	29

Notion: $\varepsilon_{\parallel}$ ($\varepsilon_{\perp}$) is the average of two longitudinal (transverse) gauges for each sample

Results in Table 3.3 evidence that the absolute swelling amplitude shows significant anisotropy, since $\varepsilon_{\perp}$ (along axis 3 in Figure 3.1) is always higher than $\varepsilon_{\parallel}$ (along axis 1 or 2 in Figure 3.1). The ratio $r = \varepsilon_{\perp} / \varepsilon_{\parallel}$ is variable and generally higher than the degree of mechanical anisotropy often found between 1.5 and 2 (Zhang et al., 2019). It is obvious that a part of the absolute swelling is a poro-mechanical effect, induced by pore pressure increase, completed by effects of water absorption of

swelling clay. From a microscopic point of view, the SEM image exhibits the elementary swelling-clay particles are layer-stratified in structure (Figure 3.7 left). As mentioned before in §2, during saturation, the water molecules are adsorbed in the inter-particle regions into one to several (up to four) water layers (Figure 3.7 right) (Menaceur et al., 2016). At a macroscopic scale, the material anisotropy results in less stiffness perpendicular to the beddings. It is therefore consistent to observe that $\varepsilon_{\perp}$ is greater than $\varepsilon_{\parallel}$ of samples. Moreover, it was also observed at a larger scale (Duan et al., 2021) a preferential cracking parallel to the bedding plane. This cracking, which is mainly due to material manipulation and sometimes drying, is likely to amplify the transverse swelling.

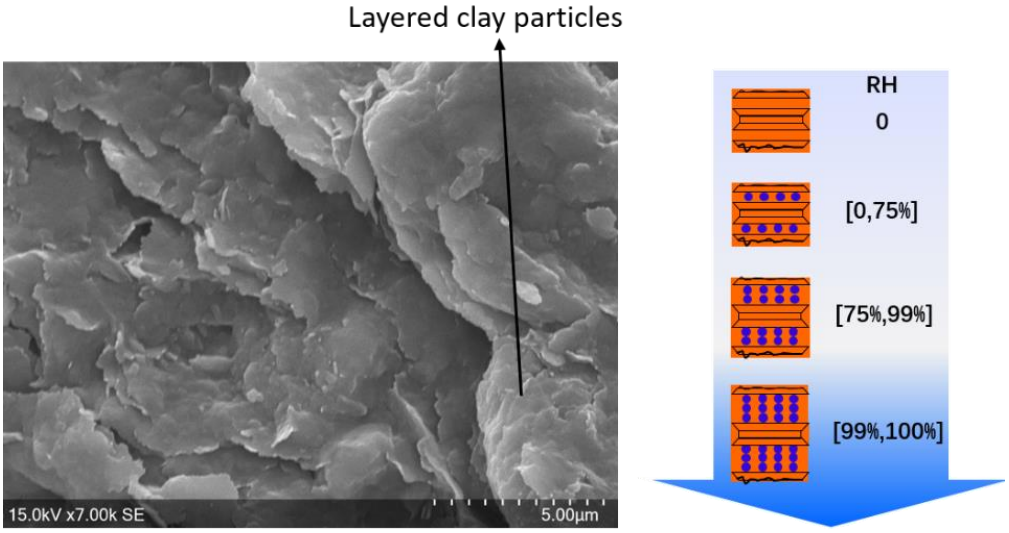

(a) (b)

Figure 3.7. (a) SEM image of an unpolished surface of COx claystone (EST 58128); (b) an conceptual illustration of water molecules distribution in a swelling clay

3.3.2. Biot's coefficient measurements, results and discussion

When the swelling phase is completed, the Biot's coefficient measurement was carried out according steps 1-4 (see section 3.2). Figure 3.8 presents the strain evolution during poro-mechanical loadings of the four samples. Red lines with solid squares indicate the average strain $\varepsilon_{\perp}$, whereas black lines with solid circles represent the average strain $\varepsilon_{\parallel}$. Strain variation A-B (or A'-B') and D-E (or D'-E') correspond to increasing and decreasing P_c, respectively; B-C (or B'-C') and C-D (or C'-D') are the strain induced by increasing and decreasing P_i, respectively. A complete test cycle can last around 20 to 30 days. Such a duration is likely to explain why many previous published results had given lower Biot's coefficient. It can be seen in Figure 3.8 that the necessary time to stabilize the strains, due to change in P_c and/or in P_i, is around 10 days (more or less) – even on these small samples, which are drained at both ends. It is consistent to assume that a large part of this time is controlled by the material water permeability, i.e. the time to obtain a uniform pore pressure inside the sample. It is also clear that, if

during injection test, the waiting time was insufficient, this would obviously lead to artificially smaller Biot's coefficient.

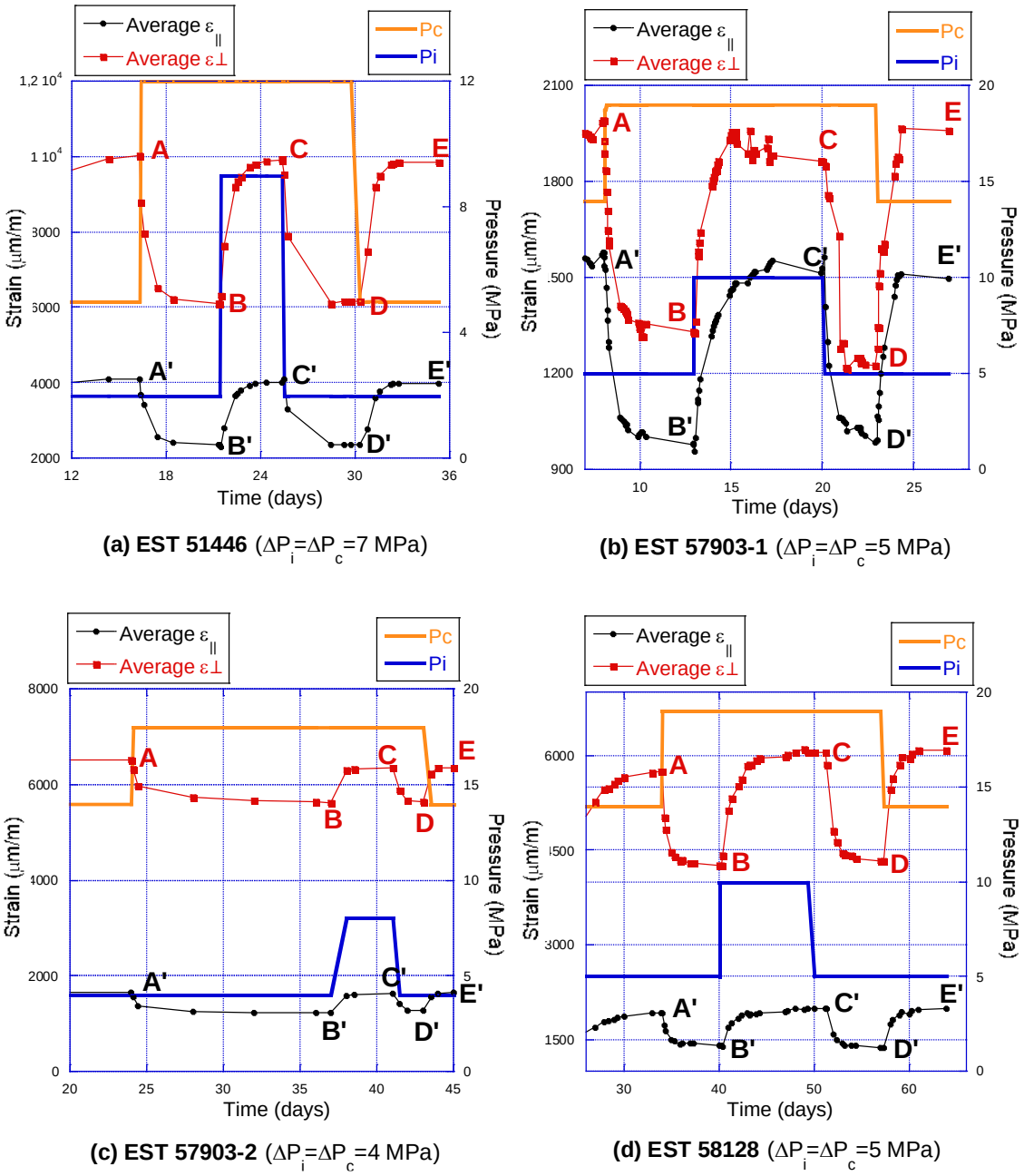

(a) EST 51446 (ΔP_i=ΔP_c=7 MPa)

(b) EST 57903-1 (ΔP_i=ΔP_c=5 MPa)

(c) EST 57903-2 (ΔP_i=ΔP_c=4 MPa)

(d) EST 58128 (ΔP_i=ΔP_c=5 MPa)

Figure 3.8. Strain evolution during poro-mechanical tests

As commented in section 3.2.2, Biot's coefficient has to be identified through elastic loading paths. It was then assumed that a decrease ΔP_c in P_c or an increase ΔP_i in P_i would lead to elastic strain recovery as they give a decrease in Terzaghi's effective pressure. A decrease in P_c (in Figure 3.8) results in strains from D to E (or D' to E') while an increase in P_i gives strains from B to C (or B' to C'). If P_c is kept constant during the P_i test, i.e. increase followed by decrease in P_i, then both paths must be elastic. Decrease in P_i leads to strains from C to D (or C' to D'). This can be easily verified in Figure 3.8

in which strains at B and D are virtually the same. There is an exception in Figure 3.8 (b) for the red curve. This is attributed to experimental artefact due to gauge malfunctioning. Hence either strain B-C (or B'-C') or strain C-D (or C'-D') can be taken as $\varepsilon_i(\Delta P_i)$ to calculate Biot's coefficient. The ΔP_c amplitude was chosen as ΔP_c=ΔP_i. This allows a direct comparison between $\varepsilon_i(\Delta P_i)$ and $\varepsilon_i(\Delta P_c)$. Results in Fig.9 show that C and E (resp. C' and E') are virtually at the same level of strains. This is detailed in tables Table 3.4 (1) and Table 3.4 (2).

Table 3.4. Strains and Biot's coefficient measured by gauges (a) perpendicular to the beddings and (b) parallel to the beddings

(a)

Sample	ΔP_c = ΔP_i (MPa)	B-C (m/m)	C-D (m/m)	$\frac{B-C}{C-D}$	D-E (m/m)	$\frac{C-D}{D-E}$	b
EST51446	7	3817	3772	1.011	3702	1.019	≈ 1
EST57903-1	5	532	637	0.835	733	0.87	
EST57903-2	5	722	698	1.034	696	1.003	
EST58128	5	1798	1716	1.048	1744	0.984	

(b)

Sample	ΔP_c = ΔP_i (MPa)	B'-C' (m/m)	C'-D' (m/m)	$\frac{B'-C'}{C'-D'}$	D'E' (m/m)	$\frac{C'-D'}{D'-E'}$	b
EST51446	7	1650	1655	0.997	1630	1.015	≈ 1
EST57903-1	5	548	541	1.013	511	1.059	
EST57903-2	5	406	357	1.137	368	0.970	
EST58128	5	587	619	0.948	611	1.013	

In both Tables 3.4 (a) and (b), the ratio B-C/C-D (resp. B'-C'/C'-D') is very close to one despite (sometimes) small gauge uncertainties, also leading to 'b' slightly greater than one – obviously experimental artefacts. It is nevertheless very clear that these ratio indicate that the path from B to D via C (resp. B' to D' via C') is elastic, which is consistent. C-D/D-E (resp C'-D'/D'-E') is the ratio b = $\varepsilon_i(\Delta P_i = \Delta P_c)/\varepsilon_i(\Delta P_c)$. From Table 3.4 (a) and (b) it comes that this ratio is the same for both gauge directions (whatever the gauge direction n°i). This completely confirm what was already observed with gas experiments i.e. b=b_3 (isotropic Biot's tensor) despite the global material anisotropy. Once again it should be mentioned here that this does not mean that the strains due to change in pore pressure are the same (i.e. C-D≠C'-D'). This is a first important and interesting point. The second one is that $b_1 \approx b_3 \approx \varepsilon_i(\Delta P_i = \Delta P_c)/\varepsilon_i(\Delta P_c) \approx 1$. This second and very important result evidences that, when fully water saturated (and under laboratory conditions), COx claystone behaves like a Terzaghi's material i.e. like a soil. Even if only 4 results are presented, this was observed on several other tests with UA claystone samples (clay-rich material). It is now clear that many previous studies indicated too low Biot's

coefficient and, in our opinion, it is mainly due to insufficient waiting times between two loading paths (either in P_c or in P_i).

Another important point must be mentioned as regards water vs gas measurements. After a complete (and very long) cycle of water saturation and poro-mechanical loading steps, the COx claystone is obviously de-structured, see Figure 3.9. After sample dismounted, water content measurements showed values as high as 9.5% while 7.5% (dry at 105°C) is considered to be the in-situ saturated material value. This means that the material, under these laboratory conditions, is over-saturated and deeply modified compared to the in-situ conditions.

Figure 3.9. Image of a sample after test. The sample is full of water and looks “pasty”

The destruction effect was also evidenced in a conventional triaxial test. Figure 3.10 shows the stress & strain behaviors of two COx samples (extracted from the same T1 core) at 9 MPa confining pressure under drained conditions, one is in its initial state (7.5% water content) and the other is over saturated (9.5% water content). Strong mechanical contrasts between the two samples were found, especially on strength and ductility. Hence, it could be supposed that $b \approx 1$ derived from this de-structuration. From there, the comparison with gas experiments brings new interesting highlights. They were indeed performed on partially saturated (or even dry) samples and with the same experimental technics. The sample is not de-structured under such hydric states and gas pore pressure tests obviously indicated that $b_1 = b_3$ and lies in the range [0.9, 1] as indicated with ‘helium’ results. As in the ‘in-situ’ conditions, the material is unlikely destructured as it is during ‘water’ laboratory experiments, it is plausible to consider that the range [0.9, 1] is the most consistent for COx claystone. This means that for simulations, the choice of Biot’s coefficient (between these two values) has to be made to ensure the worst case scenario so as to maximize safety.

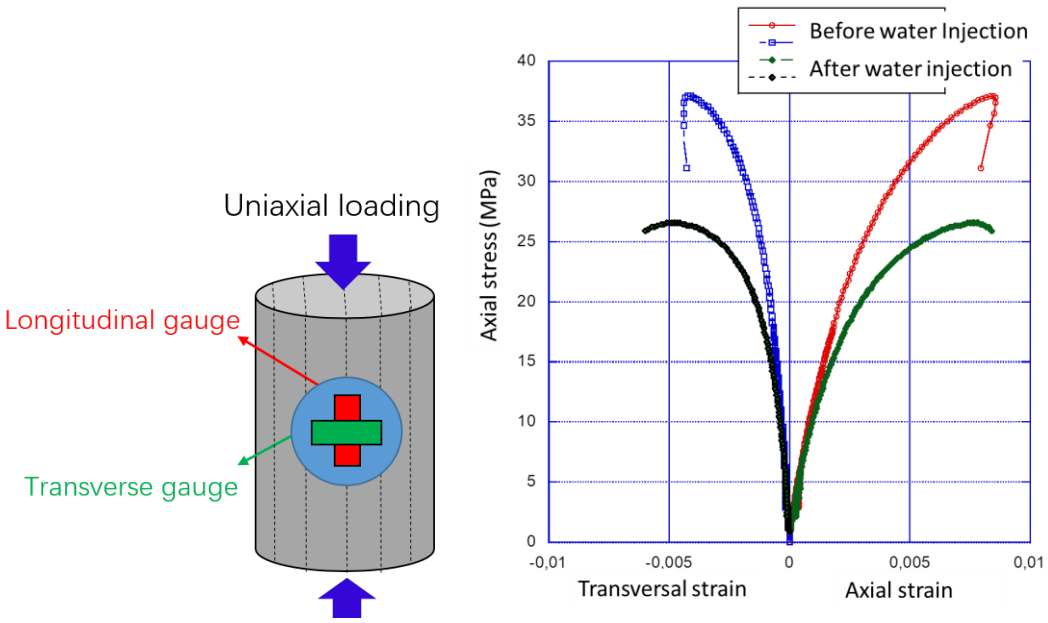

Figure 3.10 Conventional triaxial test results for partially and fully saturated COx samples (retrived from the same T-cell plug EST 58128).

3.4. Chapter summary

This contribution aimed at measuring the Biot's coefficient of COx claystone in a saturated state. In particular, synthetic water (close to *in-situ* water) was used as being the fluid to control pore pressure. The tests were very challenging due to difficulties: sample preparation, long saturation times to obtain pressure uniformity. Several tests were successfully performed for the past two years among which four representative ones are presented in this study. Several essential points can be highlighted.

A significant swelling during the first water injection was observed, regardless the initial sample states (hydric and/or damaged) and the initial loading path (couple P_c, P_i). This absolute swelling is due to the pore pressure loading (poro-mechanical effect) and the clay mineral swelling. The swelling amplitude was always found to be anisotropic with higher values perpendicular to bedding than the ones parallel to bedding. Such an anisotropy is consistent with the usual results found for this COx claystone i.e. a lower stiffness in the direction perpendicular to the beddings.

The poro-mechanical part of the tests was performed, after the first swelling stabilization, in order to measure Biot's coefficients on saturated samples. Results clearly demonstrated that, despite a significant material anisotropy, the Biot's tensor is isotropic with a unique component "*b*". This important result, consistent with some theoretical calculations, does not mean that the strains, due to pore pressure change, are isotropic. An other important result is that "*b*" was found very close to 1. This means that, under the laboratory conditions used, the COx claystone behaves as a Terzaghi

material. This crucial result was obtained on water saturated claystone samples, which exhibited some kind of de-structuration after the tests. It is nevertheless consistent with numerous observations made with gas (helium) as being the fluid to control pore pressure, which more often led to quasi isotropic Biot's tensor with "*b*" in the range [0.9, 1]. In this case gas experiments were performed on partially saturated materials (from dry to almost saturated) so without the de-structuration observed with water.

To summarize, this work completes the results obtained with gas and evidences that this saturated transversely isotropic claystone still closely behaves as a Terzaghi's material. It also contributes to clarify the Biot's coefficient value range that has to be chosen in numerical simulations, especially the crucial ones for which thermal activity of wastes is taken into account.

Note: This chapter has been written with a purpose of publication and submitted to 'Engineering Geology'

Reference

Anderson, R.L., Ratcliffe, I., Greenwell, H.C., Williams, P.A., Cliffe, S., Coveney, P.V., 2010. Clay swelling — A challenge in the oilfield. Earth-Sci. Rev. 98, 201–216.

Andra, 2005. Dossier 2005 Argile - Evolution phénoménologique du stockage géologique.

Belmokhtar, M., Delage, P., Ghabezloo, S., Tang, A.-M., Menaceur, H., Conil, N., 2017. Poroelasticity of the Callovo–Oxfordian Claystone. Rock Mech. Rock Eng. 50, 871–889. https://doi.org/10.1007/s00603-016-1137-3

Bemer, E., Longuemare, P., Vincké, O., 2004. Poroelastic parameters of Meuse/Haute Marne argillites: effect of loading and saturation states. Appl. Clay Sci. 26, 359–366. https://doi.org/10.1016/j.clay.2003.12.012

Braun, P., Ghabezloo, S., Delage, P., Sulem, J., Conil, N., 2021. Transversely Isotropic Poroelastic Behaviour of the Callovo-Oxfordian Claystone: A Set of Stress-Dependent Parameters. Rock Mech. Rock Eng. 54, 377–396. https://doi.org/10.1007/s00603-020-02268-z

Busch, A., Hangx, S.J.T., Marshall, J.D., Wentinck, H.M., 2020. Swelling clay minerals and containment risk assessment for the storage seal of the Peterhead CCS project. Int. J. Greenh. Gas Control. 94, 102924. https://doi.org/10.1016/j.ijggc.2019.102924

Cariou, S., 2010. Couplage hydro-mécanique et transfert dans l'argilite de Meuse/Haute-Marne: approches expérimentale et multi-échelle (PhD thesis). Ecole des Ponts ParisTech, Paris, France.

Cariou, S., Dormieux, L., Skoczylas, F., 2013. An original constitutive law for Callovo-Oxfordian argillite, a two-scale double-porosity material. Appl. Clay Sci. 80–81, 18–30. https://doi.org/10.1016/j.clay.2013.05.003

Cariou, S., Duan, Z., Davy, C.A., Skoczylas, F., Dormieux, L., 2012. Poromechanics of partially saturated COx argillite. Appl. Clay Sci. 56, 36–47.

Carrier, B., Wang, L., Vandamme, M., Pellenq, R.J.-M., Bornert, M., Tanguy, A., Van Damme, H., 2013. ESEM Study of the Humidity-Induced Swelling of Clay Film. Langmuir 29, 12823–12833. https://doi.org/10.1021/la402781p

Davy, C.A., Skoczylas, F., Talandier, 2013. Gas Migration through COx Claystone and Implications for Self-Healing, in: Poromechanics V. Presented at the Fifth Biot Conference on Poromechanics, American Society of Civil Engineers, Vienna, Austria, pp. 1615–1624.

Duan, Z., Skoczylas, F., Wang, C., Talandier, J., 2021. Hydric Cycle Impacts on COx Argillite Permeability and Young's Modulus. Rock Mech. Rock Eng. 54, 1129–1147. https://doi.org/10.1007/s00603-020-02258-1

Giot, R., Auvray, C., Conil, N., de La Vaissière, R., 2018. Multi-stage water permeability measurements on claystone by steady and transient flow methods. Eng. Geol. 247, 27–37. https://doi.org/10.1016/j.enggeo.2018.10.019

Guillon, T., Giot, R., Giraud, A., Armand, G., 2012. Response of Callovo-Oxfordian claystone during drying tests: unsaturated hydromechanical behavior. Acta Geotech. 7, 313–332. https://doi.org/10.1007/s11440-012-0172-9

He, J., Rui, Z., Ling, K., 2016. A new method to determine Biot's coefficients of Bakken samples. J. Nat. Gas Sci. Eng. 256–264.

Holt, R.M., Bakk, A., Stenebråten, J.F., Bauer, A., Fjær, E., 2018. Skempton's A — A Key to Man-Induced Subsurface Pore Pressure Changes. In: 52nd U.S. Rock Mechanics / Geomechanics Symposium, American Rock Mechanics Association, Seattle

Hu, C., Lemarchand, E., Dormieux, L., Skoczylas, F., 2020. Quasi-isotropic Biot's Tensor for Anisotropic Porous Rocks: Experiments and Micromechanical Modelling. Rock Mech. Rock Eng. 53, 4031–4041. https://doi.org/10.1007/s00603-020-02147-7

Hu, D.W., Zhang, F., Shao, J.F., Gatmiri, B., 2014. Influences of Mineralogy and Water Content on the Mechanical Properties of Argillite. Rock Mech. Rock Eng. 47, 157–166. https://doi.org/10.1007/s00603-013-0413-8

IAEA, 2013. Characterization of swelling clays as components of the engineered barrier system for geological repositories: results of an IAEA coordinated research project 2002-2007.

Menaceur, H., Delage, P., Tang, A.M., Talandier, J., 2016. The Status of Water in Swelling Shales: An Insight from the Water Retention Properties of the Callovo-Oxfordian Claystone. Rock Mech. Rock Eng. 49, 4571–4586.

M'Jahad, S., Davy, C.A., Skoczylas, F., Talandier, J., 2017. Characterization of transport and water retention properties of damaged Callovo-Oxfordian claystone. Geological Society, London, Special Publications 443, 159–177.

Pei, Y., Li, S., Agostini, F., Skoczylas, F., 2019. Effects of severe heating and rehydration on poro-mechanical properties of a mortar. Cem. Concr. Res. 115, 460–471. https://doi.org/10.1016/j.cemconres.2018.09.020

Song, Y., 2014. Water retention and fine microstructure of Bure argillite (PhD thesis). Ecole Centrale de Lille.

Suarez-Rivera, R., Fjær, E., 2013. Evaluating the Poroelastic Effect on Anisotropic, Organic-Rich, Mudstone Systems. Rock Mech. Rock Eng. 46, 569–580.

Vincke, O., Longuemare, P., Bouteca, M., Deflandre, J.P., 1998. Investigation of the Poromechanical Behavior of Shales in the Elastic Domain, in: SPE/ISRM Rock Mechanics in Petroleum Engineering. Presented at the SPE/ISRM Rock Mechanics in Petroleum Engineering, Society of Petroleum Engineers, Trondheim, Norway. https://doi.org/10.2118/47589-MS

Wan, M., Delage, P., Tang, A.M., Talandier, J., 2013. Water retention properties of the Callovo-Oxfordian claystone. Int. J. Rock Mech. Min. Sci. 64, 96–104.

Wang, C., Davy, C.A., Skoczylas, F., Talandier, J., 2021. Effect of mineralogical composition and pore structure on the swelling of COx claystone. AJCE 2021, 39, 9-16. https://doi.org/10.26168/ajce.39.1.3

Wang, Y., Jeannin, L., Agostini, F., Dormieux, L., Skoczylas, F., Portier, E., 2018. Experimental study and micromechanical interpretation of the poroelastic behaviour and permeability of a tight sandstone. Int. J. Rock Mech. Min. Sci. 103, 89–95. https://doi.org/10.1016/j.ijrmms.2018.01.007

Yuan, H., 2017. Caractérisation expérimentale des propriétés de poromécaniques et de transfert de l'argilite du COx (PhD thesis). Ecole Centrale de Lille, Lille.

Yuan, H., Agostini, F., Duan, Z., Skoczylas, F., Talandier, J., 2017. Measurement of Biot's coefficient for COx argillite using gas pressure technique. Int. J. Rock Mech. Min. Sci. 92, 72–80.

Zhang, C.-L., Armand, G., Conil, N., Laurich, B., 2019. Investigation on anisotropy of mechanical properties of Callovo-Oxfordian claystone. Eng. Geol. 251, 128–145. https://doi.org/10.1016/j.enggeo.2019.02.008

Zhang, C.-L., Rothfuchs, T., 2004. Experimental study of the hydro-mechanical behaviour of the Callovo-Oxfordian argillite. Appl. Clay Sci. 26, 325–336.

Zhang, D., Skoczylas, F., Agostini, F., Jeannin, L., 2020. Experimental Investigation of Gas Transfer Properties and Stress Coupling Effects of Salt Rocks. Rock Mech. Rock Eng. 53, 4015–4029.

4. Chapter 4 - Swelling and fluid transport of re-sealed Callovo-Oxfordian claystone

In this last chapter, a dedicated experimental device has been designed to measure the apparent swelling pressure, gas and water permeability, and gas breakthrough pressure of macro-cracked COx claystone. The experimental results are analyzed in parallel with mineralogical (quantitative XRD & CEC) and nitrogen adsorption data. Six COx claystone samples from four different geological locations of the Bure basin (France) are tested, five of which are macro-cracked and one remains intact. Sample swelling occurs, during re-hydration with liquid water, leading to the measurement of an apparent swelling pressure. The latter is continuously recorded with a dedicated device. The asymptotic apparent swelling pressure of macro-cracked UT (transitional unit) COx is approximately 1 MPa, while it varies from 3 to 5 MPa for macro-cracked UA (clayey unit) COx. Quantitative X-ray diffraction (QXRD) analysis demonstrates that the amount of smectite, which is a swelling clay, is weakly correlated with Papp. Meanwhile, the interstratified illite/smectite with higher illite content (R1-I/S) is highly correlated to Papp, and nitrogen isotherms data imply that the Gurvich total pore volume ($V_{Gurvich}$) and specific surface area (SSA) are linearly related to R1-I/S. This provide an easier and more effective technique than QXRD for assessing COx swelling capacity, as both $V_{Gurvich}$ and SSA have been proven as effective indicators.

For both UT and UA COx, self-sealing can cause significant reductions in water permeability. In particular, UA COx shows higher sealing efficiency and faster kinetics compared to UT COx. After sealing, the equivalent crack aperture (calculated from Poiseuille's law) decreases from tens of microns to less than 1 micron. According to the gas breakthrough tests, the gas breakthrough pressure (GBP) is of re-sealed macro-cracked COx is of the same order of magnitude as the equivalent capillary pressure of residual crack. This indicates that the gas migration in the re-sealed cracked COx claystone mainly occurs through the residual crack and is 'a priori' controlled by capillary processes.

4.1.Materials and sample preparation

4.1.1. Origin of COx claystone samples

Six COx claystone samples originating from four cores were used. The four cores, provided by Andra, were extracted at different depths of the COx formation. COx claystone is known as a transversely isotropic material, see Figure 4.1 (Cariou et al., 2012). The isotropic bedding planes contain the structural axis 1 and 2, and axis 3 is perpendicular to the bedding plane. All cores were extracted along the bedding planes (i.e. axis 1) and immediately sealed in T1 cells, which were developed by Andra to

keep the core under certain stress (Conil et al., 2018). The dimensions of the original core are around 300 mm length and 75 mm diameter. From each original core, several cylindrical samples parallel to the bedding planes were retrieved to obtain representative samples that fit the experimental set-up. After coring, and before swelling and sealing test, all samples were wrapped in plastic film, sealed in vacuum bags and then immersed in oil in order to minimize their desaturation. The re-cored samples were of a diameter of 37 mm and a length slightly greater than 40 mm. After placing the sample in the experimental device, its length was adjusted to 40mm by machining. The detailed preparation procedure of the sample is provided in the following subsection.

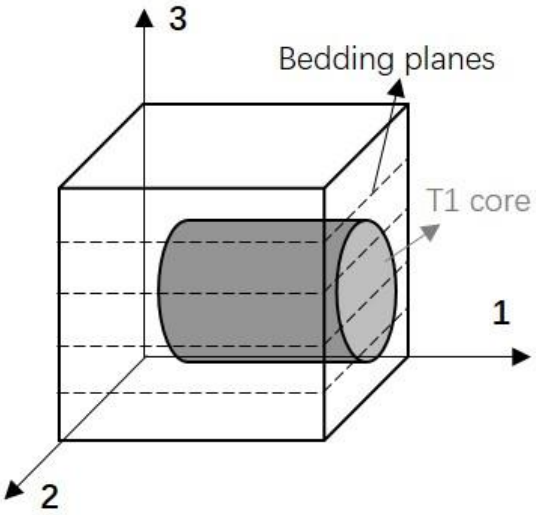

Figure 4.1. Schematic diagram of transversely isotropic COx claystone

All samples were extracted from the UT and UA unit, and referenced as UT-C, UA1-C, UA2-C, UA3-C1, UA3-C2, UA3-I, where UT refers to the transition unit and UA refers to the clay-rich unit; C means that the sample is macro-cracked and I means that it is in the intact state. Table 4.1 summarizes the information of all tested samples, including the sample label, geological unit, damaged state, and the initial physical properties. It is worth noticing that, as the COx claystone was subjected to decompression when extracted from T1 cells and slighlty de-saturated during coring, a small extent of cracks would have been generated in the samples (Duan et al., 2021). Nevertheless, these re-cored samples (without further processing or macro-cracking) are referred to “intact samples”.

Table 4.2. Basic information of the tested COx claystone samples

Sample label	Core number	Depth	Geological unit	Damage state	Saturation degree	Bulk density
UT-C	EST 57257	-457 m	UT	Brazilian splitting	-	2.58 g/cm^3
UA1-C	EST 57903	-490 m	UA	Brazilian splitting	86.8%	2.39 g/cm^3
UA2-C	EST 58128	-490 m	UA	Brazilian splitting	85.5%	2.37 g/cm^3
UA3-C1	EST 58145	-490 m	UA	Brazilian splitting	84.3%	2.37 g/cm^3
UA3-C2	EST 58145	-490 m	UA	Brazilian splitting	84.3%	2.37 g/cm^3
UA3-I	EST 58145	-490 m	UA	Intact	84.3%	2.37 g/cm^3

4.1.2. Sample preparation

4.1.2.1 Macro-cracking by Brazilian splitting test

Brazilian splitting tests were used to obtain a diametrical crack, which aperture can not be fully controlled. Multiple cracks were generated sometimes. After retrieving the 37 mm/40 mm samples from the original core, the Brazilian splitting tests (Davy et al., 2007) were conducted on five samples (detailed in Table 4.1). To avoid shattering, the side surfaces of the sample were first wrapped with insulating tapes. The uniaxial stress was applied perpendicularly to the bedding planes to prevent cracks propagation only along the bedding surface. A typical result is shown in Figure 4.2 (a). The Brazilian splitting tests were stopped when the macro crack was created throughout the sample, see Figure 4.2 (b). The numbers and diameter of cracks are significantly different from one sample to another. Apart from the split-cracked samples, an intact sample from EST 58145 was also used as the intact reference in our experiment.

Figure 4.2. Photograph of a Brazilian test (left) and the resulting diametral macro-crack (right)

4.1.2.2 Design of the “stainless steel tube-epoxy-sample” system

An originally designed set-up was used to investigate the sealing efficiency of compacted bentonite/sand plugs (Liu et al. (2014)). Innovatively, by placing the bentonite/sand plug in a stainless steel-epoxy tube, swelling occurred at almost constant volume during hydration. This allowed the asymptotic swelling pressure to be derived from the strain on the external surface of the tube. The system of “sample plug + stainless steel tube” is placed inside a triaxial cell and subjected to confining

pressure. Thanks to high rigidity of the metallic tube, it is able to prevent the sample from being subjected to high confining pressure. The same kind of experiment was conducted on the COx argillite since the sample was included in a rigid steel tube+epoxy resin. When water is injected, the sample swelling is partially prevented by the tube. As a consequence, the swelling sample will apply radial stress on the assemblage (tube + resin). This stress can be evaluated by calibration (see section 2.2.3) and be related to a kind of swelling pressure. On the other hand, most of the swelling/sealing tests were usually performed with a significant confining pressure. The combination of the sample swelling (due to re-hydration) and the confining pressure leads to sharp decrease in permeability. It is therefore difficult to evaluate the real role of the only swelling. As shown in Figure 4.3 (a), the system consists of a stainless steel tube with an external diameter of 65 mm and a cylindrical COx claystone sample with a diameter of 37 mm, the length of the whole system is 40 mm. The claystone sample is placed in the center of the tube, and the space between tube and sample is fully filled with degassed liquid epoxy resin. The harden resin sticks strongly to the sample surface and the tube internal surface and is considered impermeable, meanwhile it has a significant compressibility (flexibility). The internal pressure effects in the tube-epoxy structure can be evaluated with two strain gauges (with an accuracy of 10^{-6} m/m) symmetrically glued on the tube external surface, see Figure 4.3 (a). Thanks to a calibration process, the strain can be converted into an "apparent swelling pressure" (P_{app}), which is an adequate indicator of the swelling process duration and amplitude. Hence, the system (tube-epoxy-cracked sample) allows to measure the swelling kinetics, and an "apparent swelling pressure". It can also be used to evaluate the self-sealing efficiency with water permeability measurements. On the other hand, the sample is subjected to its own swelling pressure and not to an artificial level of confining pressure. This system needs a calibration phase to obtain the relationship between gas pressure into the tube and the strain. Both calibration and self-sealing tests are carried out with a triaxial cell, see Figure 4.3 (b). The experimental procedures are detailed in section 4.2.3.

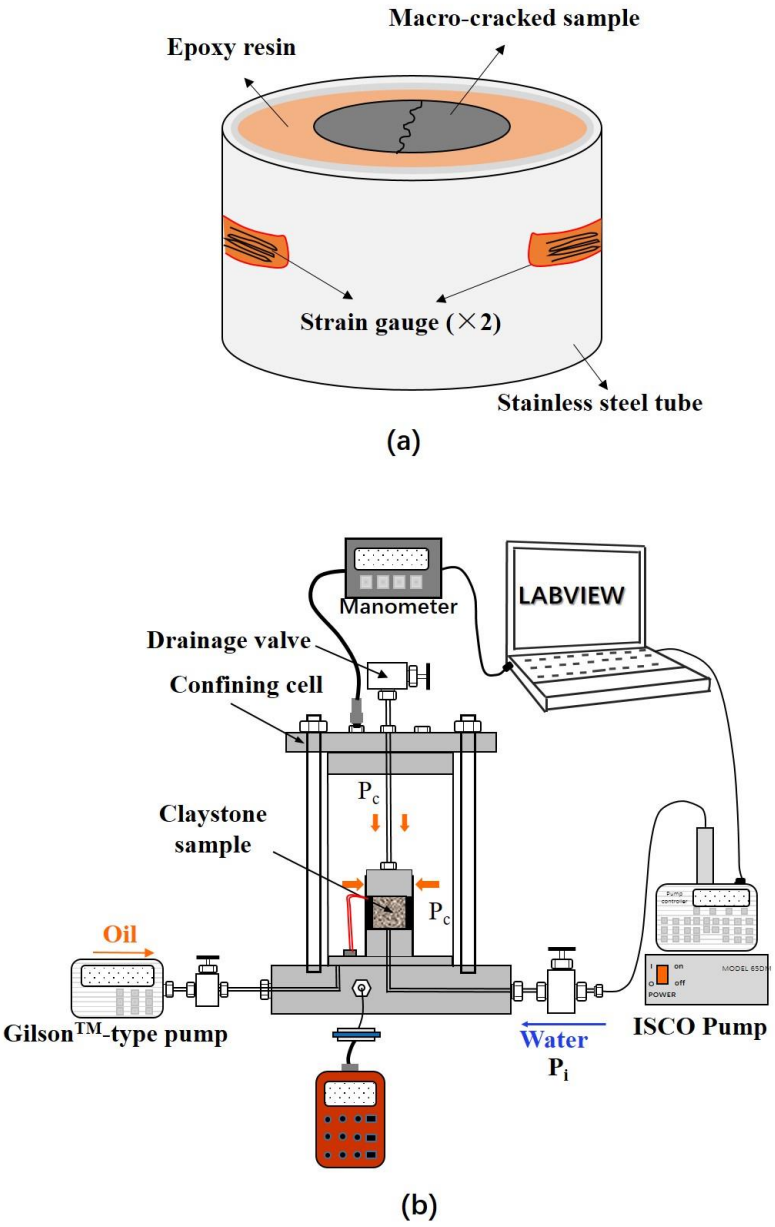

Figure 4.3. Sketch of the experimental set-up: (a) a system consists of steel-epoxy composite tube and a COx sample, the sample is placed in the tube center and two strain gauges are glued on the tube outer surface; (b) the hydrostatic triaxial cell used for the self-sealing experiments

4.2.Experimental methodology

4.2.1. Mineralogical analysis

The mineralogical analysis is determined by two measurements: quantitative X-ray diffraction (QXRD) and Cations Exchange Capacity (CEC). Quantitative X-ray diffraction (QXRD) is used to analyze the bulk mineralogical and the subdivided clay mineral composition. For the purpose of improving the reliability of the results, two different representative parts were extracted from each sample, then

analyzed and averaged. The detailed representative sample preparation and measurement procedures are exactly the same as illustrated in chapter 2.

Cation exchange capacity (CEC) is an inherent characteristic of a clayey material (such as soil and claystone), which refers to the ability of the solid to hold exchangeable cations in a saline aqueous solution. This property is mainly impacted by the content of clay minerals and organic matter (Mitchell and Soga, 2005)). Empirically, the CEC value of 2:1 type clay minerals (e.g. smectite) is approx. 80 - 120 meq/100 g, which is higher than 1:1 type clay minerals (e.g. kaolinite), around 1 – 10 meq/100 g. The CEC varies from 100 to 300 meq/100g for the organic matter (Al-Ani and Sarapää, 2008)). In order to determine the most active mineral component of the COx claystone during hydration, CEC analysis was simultaneously performed for each sample subjected to QXRD.

The detailed representative sample preparation and measurement procedures are exactly the same as illustrated in chapter 2.

4.2.2. Nitrogen physisorption measurement

As mentioned before, nitrogen adsorption/desorption experiments are used to obtain pore information of the tested COx samples. The main goal is to acquire the nitrogen isotherms, by recording the adsorbed nitrogen quantity at different relative nitrogen pressures. These isotherms are summarized in Figure 4.4, the sample preparation and measure procedures are already illustrated in chapter 2. These isotherms data can be used and analyzed with different theories to derive a series of textural parameters such as the total pore volume ($V_{Gurvich}$) and the Specific Surface Area (SSA), which were selected for this study. $V_{Gurvich}$ is the pore volume that is determined under the validity of Gurvich's rule (Ongari et al. (2017)): when $p/p_0 \geqslant 0.995$, the adsorbed nitrogen has a molar density of the liquid state at the operational temperature, and have no interaction with the solid framework. The $V_{Gurvich}$ is computed by:

$$V_{Gurvich} = \frac{n_{N_2}^{ads}}{\rho_{N_2}^{liq}} \tag{4.1}$$

Where $n_{N_2}^{ads}$ is the adsorbed amount of nitrogen (g of nitrogen/g of COx), $\rho_{N_2}^{liq}$ is the liquid nitrogen density, 0.808 g/cm^3. Theoretically, $V_{Gurvich}$ is an underestimated value of the total connected pore volume as nitrogen cannot fill the micropores with a diameter smaller than the N_2 molecules.

Specific Surface Area (SSA) is derived by the Brunauer-Emmett-Teller (BET) theory, which is an optimization of Langmuir theory. The BET theory can give the monolayer adsorbed capacity (Q_m) and the adsorbent's specific surface area (SSA). Data from the straight part of isotherms to fit the empirical

BET equation are used for these calculations (Seemann et al., 2017). One should notice that the BET theory is an approach based on several assumptions, thus the derived Q_m and SSA cannot be treated as the real physical properties (Lahn et al., 2020; Seemann et al., 2017). However, with well-contolled experimental conditions, they are still useful and effective for characterizing pore structure and to compare different materials (Rouquerol et al., 2007; Thommes and Cychosz, 2014).

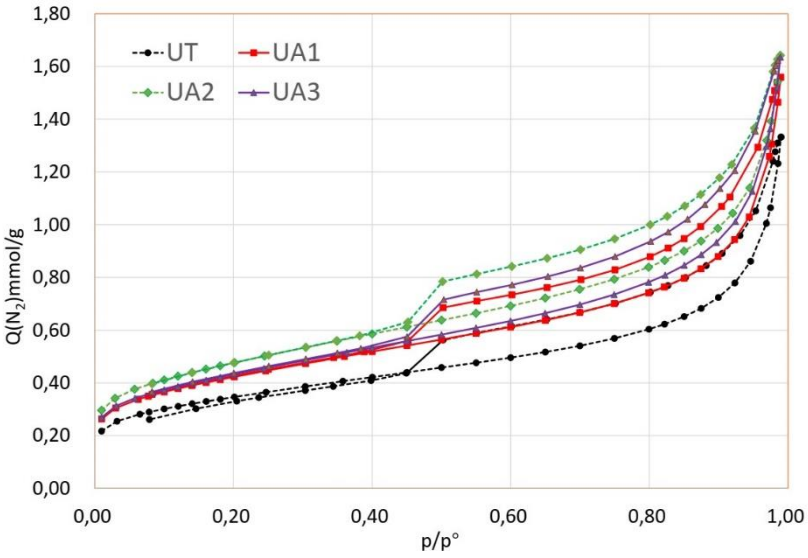

Figure 4.4. Nitrogen adsorption results of tested samples

4.2.3. Self-sealing experiments

Four results were recorded during the self-sealing measurements: evolution of the "apparent swelling pressure" (P_{app}), initial gas permeability (K_{inigas}), change of water permeability (K_w), and gas breakthrough pressure (GBP) after self-sealing. All the experiments were carried out in a temperature-controlled room in order to minimize the effect of temperature, with an average value of 21°C. In order to better simulate the interaction between the clay mineral and the underground water, a specially made synthetic water was used in all self-sealing tests. The detailed mineralogical composition is shown in Table 4.2.

Table 4.3. Mineral composition of the synthetic water (provided by Andra)

Mineral	NaCl	$NaHCO_3$	KCl	$CaSO_4$	$MgSO_4$	Na_2SO_4	$CaCl_2$	Total
Concentration (g/L)	1.95	0.13	0.035	0.63	1.02	0.08	0.7	4.545

The self-sealing experiment was carried out with a modified triaxial cell. The system (tube-epoxy-cracked sample) is first wrapped with a rubber jacket then installed in the triaxial cell (Figure 4.3 (b)). For saturation purpose, a Gilsons™ pump is used to control the confining pressure (P_c) of 4 MPa, the sample is then subjected to a wetting environment. More precisely, the saturation process is achieved

by injecting synthetic water into the cylindrical sample from one end surface until it passes through the sample. The drainage valve (Figure 4.3 (b)) is then closed to obtain uniform water pressure through the whole sample. This pressure (P_i) is of 0.5 MPa, which is lower than the confining pressure to avoid any leakage around the tube. The drainage valve is periodically opened to measure the sample water permeability (see section 4.3.3).

4.2.4. Apparent swelling pressure measurement

Before conducting the self-sealing experiment, the tube was calibrated. This is done with gas pressure into the tube ($P_{internal}$) linked to the corresponding average strain of both gauges $\varepsilon_{average} = (\varepsilon_1 + \varepsilon_2)/2$. A linear relationship between $P_{internal}$ & strain is shown in Figure 4.5. To improve the accuracy, several internal pressure loading/unloading cycles were performed on each tube submitted to various confining pressure. A special test was performed for which the gas pressure was applied on the "epoxy resin + stainless steel tube". The strains obtained were close to those recorded when the gas pressure was directly applied in the steel tube. Thanks to the tube calibration, the direct measurement data (strains of the two gauges) are constantly converted into P_{app}. P_{app} is followed until its stabilization.

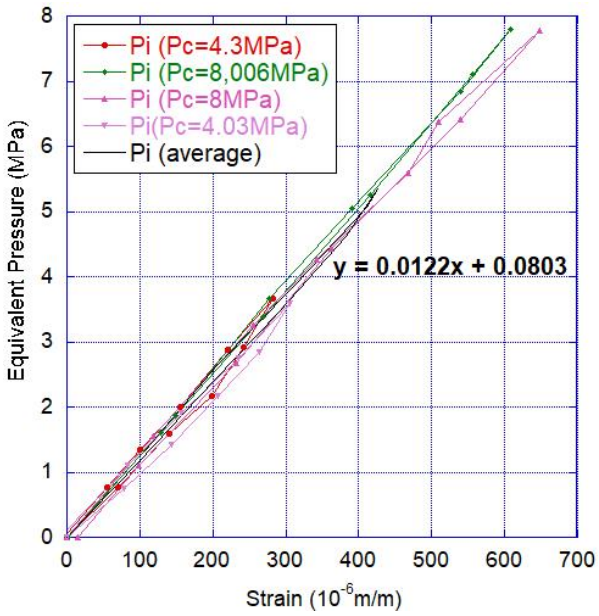

Figure 4.5. An example of tube calibration

Water can easily flow through the sample at the beginning of the test due to the presence of macro-cracks. Closing the drainage valve allows the sample to swell under (quasi) uniform water pressure without any perturbative drying risk. For the sample sizes used, the swelling process usually lasts for two weeks to one month. It should be underlined that P_{app} is the total stress applied on the tube so it

also depends on pore pressure (P_{pore}). This pressure was of the same value (0.5 MPa) for all tests. P_{app} can then be decomposed as follow:

$$P_{app} = P_{pore} + P_{swell} - \Pi_{epoxy} \tag{4.2}$$

where Π_{epoxy} represents the suppressing effect of epoxy resin on the transmission of sample swelling pressure to the tube. This value has been revealed to be very low during the calibration test. In any case, the presence of resin does not affect the comparison of P_{app} between different samples. As a consequence, the measured P_{app} is not the genuine value induced from sample swelling but it is still a reliable result for assessing and comparing the COx claystone swelling behavior (and kinetics).

4.2.5. Permeability assessment techniques

Some transfer properties of the cracked samples were measured: the initial gas permeability (K_{inigas}) and the water permeability (K_w) over time. The initial gas permeability is measured with argon gas under steady flow rate. The injection pressure is P_1 (at upstream side) since the sample is freely drained at $P_0 = P_{atm}$ at the downstream side (see Figure 4.6). A bronkhorst gas flowmeter with an accuracy of 0.01 ml/min is connected to the downstream side for the permeability test. Once a stabilized gas flow is detected, the classic Darcy's law for gas phase is applied to calculate the K_{inigas}:

$$K_{inigas} = \frac{2\mu Q L P_0}{A(P_1^2 - P_0^2)} \tag{4.3}$$

Where μ is the dynamic viscosity of argon at 21 ℃, equals to 2.2×10^{-5} Pa·s, Q is the volume flow rate measured at the downstream sample side, L is the sample length, A is the cross-sectional area of sample, P_1 is the upstream gas pressure, and P_0 is the downstream atmospheric pressure.

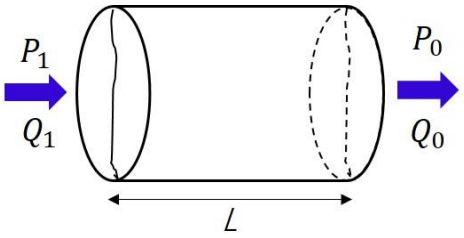

Figure 4.6. Schematic diagram of permeability test

The self-sealing efficiency is accessed via two properties: water permeability and gas breakthrough pressure (GBP). They were selected because they can quite easily be captured for the experimental procedure. Water permeability was periodically measured to be compared to the "intact" one. The latter is often in the range [10^{-19}m^2, 5×10^{-21} m^2], for laboratory measurements (M'Jahad et al., 2017). Therefore, for assessing the swelling-induced permeability decrease, the change of water permeability (K_w) is recorded over time as the sample hydrates and swells. If the differential pressure between the

sample inlet and outlet (Δ*P*) is known, the water permeability can be calculated using Darcy's law for liquid phase by recording the water flow rate *Q*, the equation is as follows:

$$K_{water} = \frac{\mu Q L}{A \Delta P} \tag{4.4}$$

Rel. (4.4) is valid under permanent flow rate. This was assumed in order to get an approximate value the water permeability K_w. Water permeability measurements were performed every one to two days, until the end of swelling. The drainage valve remained open during each permeability evaluation and was closed again as soon as the measurement was completed.

4.2.6. Gas breakthrough measurement techniques

GBP was chosen as being another swelling indicator. The gas breakthrough tests were carried out immediately after the swelling stabilized. It was compared to values obtained on different samples during previous laboratory experiments (M'Jahad et al., 2017). In terms of methodology, two methods are presented in the literature to study the gas migration in (partially) saturated porous materials: the steady-state approach and the non-steady-state approach (Horseman et al., 1999; Amann-Hildebrand et al., 2016; Liu et al., 2014). The non-steady-state approach leads to shorter test durations and can provide both breakthrough and residual pressures, however, it was chosen to use the steady-state approach in the GBP tests (i.e. slow increase of gas pressure until gas is detected at the downstream sample side). It is often assumed that this technique leads to more accurate GBP value and in the present case, it was thought to better reproduce the in-situ case for which gas pressure is supposed to increase slowly. When both P_{app} and K_w were stabilized, the ISCO water pump was dismounted and replaced by an argon injection system. To start the GBP test, argon is injected from the upstream side of the saturated sample, with 0.2 MPa increment every 24 h. The downstream (i.e. the drainage valve of the cell in Figure 4.3) is initially closed, which results in downstream pressure increase. This increase may be due to expulsed water from the sample (i.e. "pushed" by the upstream gas pressure) and/or to the gas (argon) breakthrough. A gas detection device was then used to detect (or not) this breakthrough. Detection is performed by placing an argon detector (accurate to ± 0.1 µl/s) close to the drainage valve. This valve is opened and the detector gives an indication whether argon is present at the downstream side. The valve is closed again after this operation. Different physical processes can be successively observed: water expulsion due to gas intrusion, discontinuous (transient) gas flow, and continuous gas flow (Liu et al., 2014). The inlet gas pressure leading to continuous gas flow is defined as being the breakthrough gas pressure of the tested sample.

4.3. Results and discussion

4.3.1. Mineralogical characterization

The bulk mineralogical compositions and the subdivided 2:1 clay minerals are summarized in Table 4.3. Through the QXRD analysis, the bulk mineralogical composition results demonstrate that the COx claystone contains similar primary minerals for both UA- and UT-type. They are mainly silicates (like quartz), carbonates (like calcite), and 2:1 clay minerals (layered clay content). The secondary mineral phases (such as kaolinite, chlorite, K-feldspar, pyrite, etc.) are also present in the COx claystone with lower quantities. Results show that the total clay content is slightly lower for the UT core (with values ranging between 30.4% and 39.3%) than for the UA cores (values in the range 40.1 to 50.0%). Moreover, they also demonstrate that, among all clay minerals, the illite/smectite mixed layers R1 and R0 constitute the vast majority. Indeed, the illite/smectite mixed layers are divided into two types: the R1-I/S, with 70% illite and 30% smectite, and the R0-I/S, with a proportion of 22% illite and 78% smectite. In R1-I/S, smectite is arranged in regular alternance with illite. Among these, smectite is the only one reputed to be a swelling clay.

Table 4.4. Quantitative XRD and CEC analysis for different cores of the tested COx claystone (in mass percentage)

Sample	EST 57257-1	EST 57257-2	EST 57903-1	EST 57903-2	EST 58128-1	EST 58128-2	EST 58145-1	EST58145-2
Geological unit	UT	UT	UA	UA	UA	UA	UA	UA
Carbonates	33.4	26.6	29.5	27.7	22.1	21.0	22.6	22.7
Tectosilicates	33.7	32.2	28.6	26.8	26.9	26.9	29	28.6
Secondary minerals	2.6	1.9	1.9	1.8	2.1	1.9	1.7	1.9
Kaolinite	/	/	2.2	2.7	3.3	3.4	2.9	3.0
Chlorite	0.9	1.2	1.1	1.4	1.5	1.7	1.7	1.7
2:1 clay minerals	29.5	38.1	36.8	39.6	44.1	44.9	42.2	42.0
of which Illite & muscovite	2.5	9.0	4.7	12.9	13.1	14.3	18.8	20.2
of which R1 illite/smectite (70/30)	14.2	13.3	23.5	20.6	22.6	23.2	24.2	23.4
of which R0 illite/smectite (22/78)	12.9	15.8	8.5	6.1	8.5	7.4	6.2	6.0
Total smectite	14.3	16.3	13.7	10.9	13.4	12.7	12.1	11.7
Total clay minerals	30.4	39.3	40.1	43.7	49.0	50.0	46.8	46.7
CEC (meq/100g)	16.8	19.2	14.6	13.1	17.6	16.8	15.2	14.2

In the 2:1 clay minerals group, the subdivided mineral contents are not consistent with the trend of the overall 2:1 clay minerals content. In other words, the subdivided mineral contents in 2:1 clay minerals are contrasted and there is no dominant mineral. In the presence of aqueous solution, specific minerals among the 2:1 clay minerals will be substituted with exchangeable cations in aqueous solution, and the interlayer spacing of which expands as a result of the adsorption of water molecules which are carried by the exchangeable cations. Therefore, in order to determine the most chemically active (i.e. the most swelling-related) mineral, the Cations Exchange Capacity (CEC) was carried out. Results demonstrate that the total smectite contents are linearly related to the CEC value, with the Pearson correlation coefficient (R^2) of 0.8035, see Figure 4.7. Hence, in COx claystone, smectite can be considered as the most swelling-related mineral among all 2:1 clay minerals. For the whole set of UA samples, the difference in the content of smectite was not significant and results in similar CEC values. The smectite content of the two UT representative samples (EST57257-1 and EST57257-2) is slightly higher than for UA samples. But this cannot generalized as the mineral composition of UT COx claystone varies greatly from one location to another (Andra (2005)).

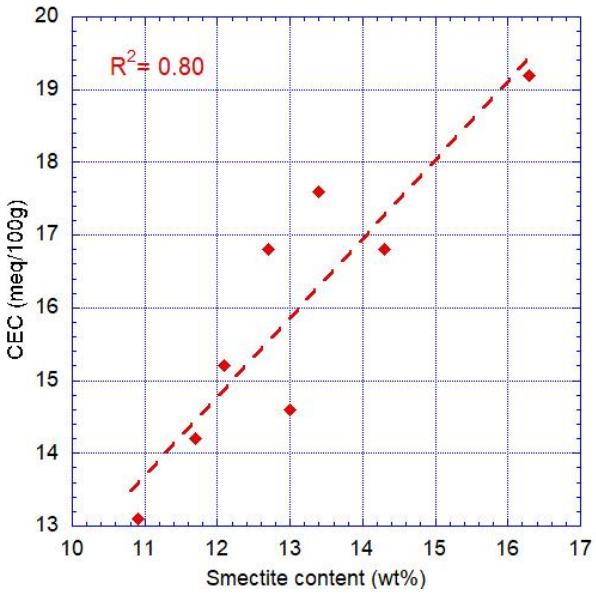

Figure 4.7. Relation between the CEC value and the Smectite content

4.3.2. Apparent swelling pressure (P_{app})

After a long period of geological evolution, the COx claystone matrix has been highly compacted and its hydration swelling is essentially due to the increase of pores volume. It was observed that crystalline swelling and osmotic swelling occur in the infra-clay micro-pores and inter-clay particle meso-pores, respectively (Saiyouri et al., 2000; Menaceur et al., 2016). Consequently, the measured apparent swelling pressure (P_{app}) is the reaction to the limited volume expansion of the COx sample. It

can be considered as the micro scale swelling pressure at the macro scale. The P_{app} change with time was recorded for each test and given in Figure 4.8. For the macro-cracked samples, the difference between P_{app} value of UA and UT samples is quite significant: the P_{app} of the UT-C is around 0.99 MPa, while for the four tested UA samples (UA1-C, UA2-C, UA3-C1, and UA3-C2), the value of P_{app} are in the range of 4.55-5.10 MPa. For comparison purposes, the swelling pressure of intact sample UA3-I was also measured (5.88 MPa) in parallel with the macro-cracked samples. The measured P_{app} range is smaller than that of samples with an "in-situ" void ratio (Zhang et al. 2020). This is a logical consequence, as the rebound and damage of the claystone during re-coring reduces the swelling capacity of the material. Moreover, the presence of steel tube and epoxy resin also suppressed the swelling strain. From the viewpoint of kinetics, the swelling time of UA3-C1 and UA3-C2 are both around five days, while it is 17 days for the intact sample UA3-I. Such difference in kinetics indicates that the presence of macro cracks creates more water-mineral contact area inside the sample, which accelerates the swelling process. P_{app} of UA3-I, 5.88 MPa, is relatively higher than P_{app} for UA3-C1 and UA3-C2. The difference in P_{app} between macro-cracked and intact samples is around 15%. One plausible interpretation of such difference is that the crack network leads to more swelling space, i.e. there is a logical decrease in P_{app}.

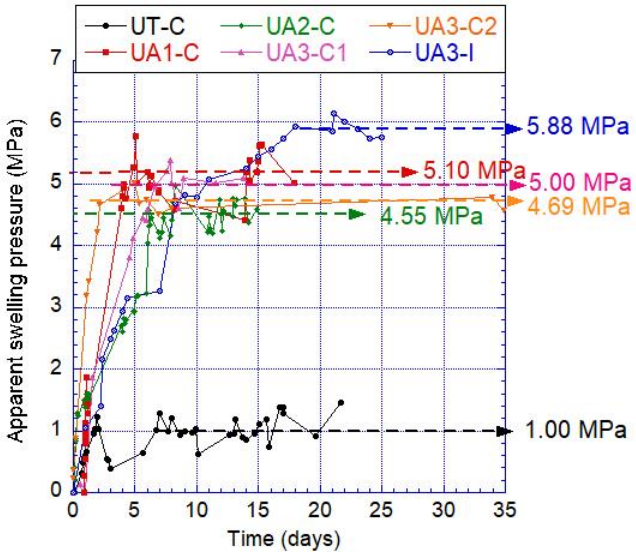

Figure 4.8. Evolution of apparent swelling pressure of the tested COx claystone sample

Knowing the quantitative XRD results, it can be analyzed whether there is a specific mineral that affects the swelling capacity of the COx claystone. To this purpose, the mass content of each clay mineral is linearly related (in the least squares sense) to the apparent swelling pressure P_{app}, see Figure 4.9. The total interstratified I/S exhibits an ambiguous relationship with P_{app}, with an Pearson coefficient R^2 of 44%. It is observed that the clay mineral most related to the swelling pressure P_{app} is R1-I/S, with an R^2 of 83%. On the opposite, the Pearson coefficient between smectite content and P_{app}

is of only 10%. The lowest correlation (R^2=6%) is obtained for R0-I/S, although it contains 78% smectite in mass. These results demonstrate that the total smectite amount and the content in mixed I/S clay are not the driving factors of the magnitude of P_{app} at the laboratory scale. Compared to other clay minerals in COx claystone, the R1-I/S structure that makes it easier for water molecules to enter the clay layers seems to be a more significant factor.

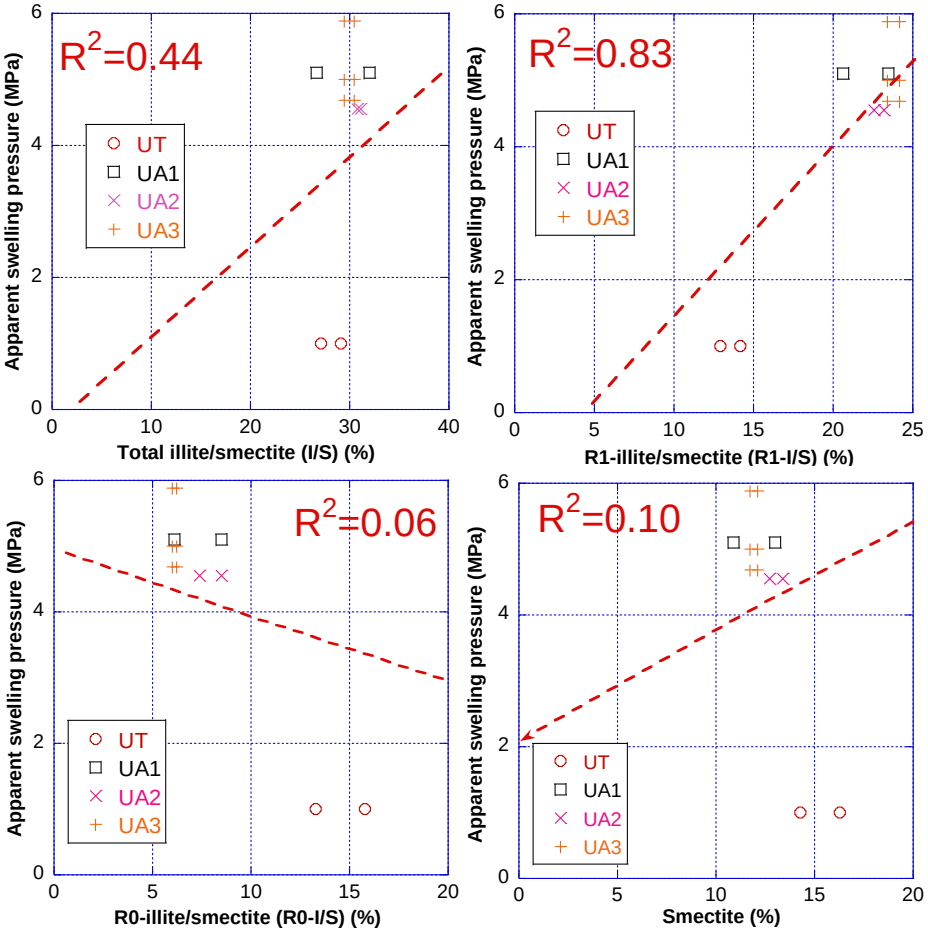

Figure 4.9. Apparent swelling pressure vs. specific clay mineral content

To verify this argument, nitrogen adsorption tests were carried out and two important properties were obtained, namely the Gurvich pore volume ($V_{Gurvich}$) and the specific surface area (SSA). $V_{Gurvich}$ and SSA reflect the ability of water molecules to come into contact with minerals (particularly with smectite). The $V_{Gurvich}$ pore volume corresponds to the total amount of water molecules that can fill the interlayer pores. The specific surface area SSA represents the surface area of water molecules that can be adsorbed on clay minerals. The nitrogen adsorption results ($V_{Gurvich}$ and SSA) are linearly correlated with the apparent swelling pressure P_{app} (Figure 4.10). P_{app} is linearly correlated with $V_{Gurvich}$ and SSA, with R^2 of 92% and 81% respectively, see Figure 4.10 (a) and (b). If we relate the R1-I/S content (which revealed to be the most strongly correlated with Papp) with $V_{Gurvich}$ and SSA, a remarkably linear relationships was found with both nitrogen sorption properties (R^2 = 97% and 87% respectively), see

Figure 4.10 (c) and (d). As smectite is not present as a single phase in the COx claystone (Andra, 2005), a plausible explanation is that the smectite present in R1-I/S is more favorable for water-smectite contact, because it would bring to the claystone a greater pore volume and a larger specific surface area. Therefore, it can be supposed that the spatial arrangement of smectite seems to be more important than its content. Hence using CEC values to assess the swelling capacity is inaccurate, as regards the macroscopic swelling of COx claystone.

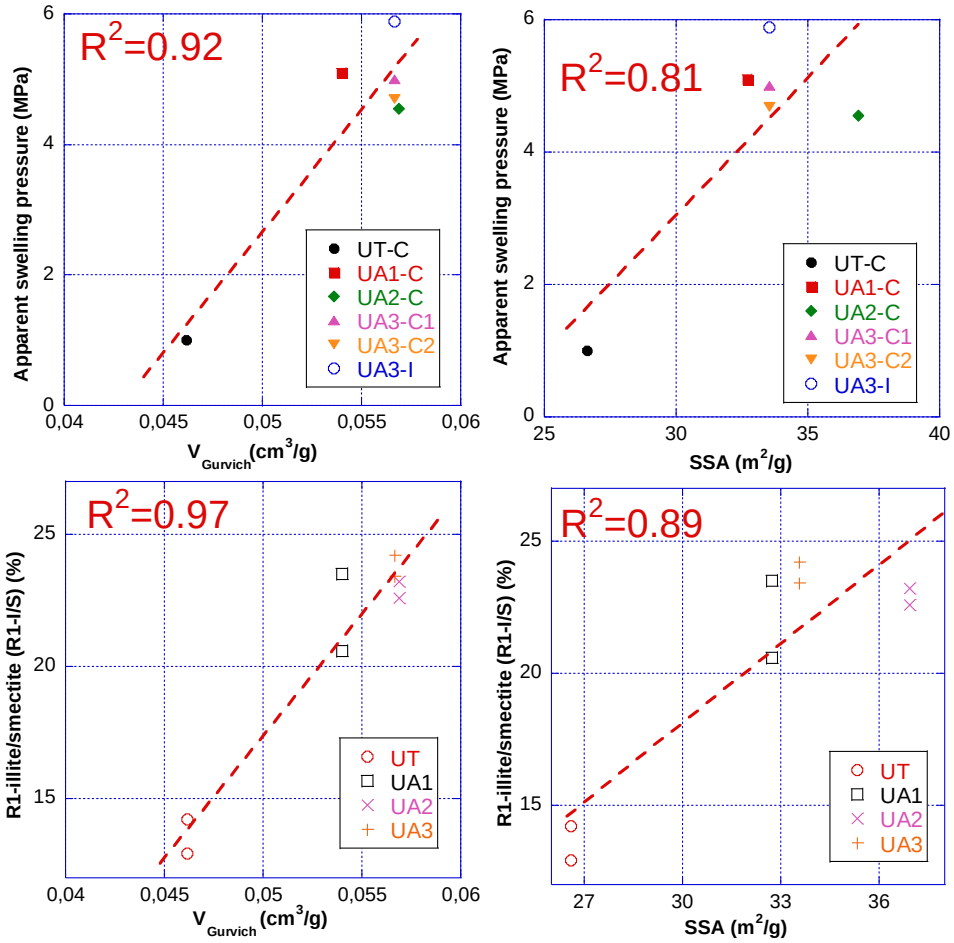

Figure 4.10. Correlation of nitrogen adsorption data with apparent swelling pressure: (a) P_{app} vs. $V_{Gurvich}$ (b) P_{app} vs. SSA (a) R1-I/S vs. $V_{Gurvich}$ (b) R1-I/S vs. SSA

Moreover, a nitrogen sorption test is easier to be carried out than QXRD. The linear relationship of $V_{Gurvich}$ vs. P_{app} and SSA vs. P_{app} is consistent with those of $V_{Gurvich}$ vs. swelling strain and SSA vs. swelling strain that observed in Chapter 2.

4.3.3. Permeability assessment

Gas and water permeability (evolution) were used for two different purposes. Coupling gas permeability (Kg) with Poiseuille law is able to evaluate a “mean” crack initial width. Water permeability was mainly recorded to be compared to the water permeability of “intact” COx argillite.

If, after swelling, both values (i.e. macro-cracked sample and intact material) are close to each other, it would evidence an efficient self-sealing. Moreover, if water flow through the crack is assumed after swelling, the permeability can also lead to a "final" crack width. This is developed in the following.

4.3.3.1 Gas permeability

The initial value of K_g was measured under almost no lateral pressure, thanks to the presence of stainless steel tube. As a consenquence, K_g comes from a gas flow that is supposed to mainly take place through the macro crack. This assumption is logical as the obtained results gave gas permeability 3 to 4 orders of magnitude higher than the intact one, see Table 4.4 (also see Duan et al., 2021). As the lateral stress applied on the cracked sample is very low, the gas permeability occurs in an opened crack and can be analized to evaluate its initial width. The initial K_g of macro-cracked samples (Table 4.4) are between 10^{-13} m^2 and 10^{-15} m^2. It is noteworthy that the K_g of UA3-2 is not reported due to experimental measurement problem. For the intact sample UA3-I, the initial K_g is of 1.37×10^{-17} m^2 that is consistent with previous tests (Zhang and Rothfuchs (2004)).

Table 4.5. Initial gas permeablity and water permeability of the tested sample

	UT-C	UA1-C	UA2-C	UA3-C1	UA3-C2	UA3-I
Initial K_g (m^2)	3.85×10^{-13}	1.79×10^{-13}	6.04×10^{-14}	1.08×10^{-13}	-	1.37×10^{-17}
Initial aperture (calculated with initial K_g) (µm)	32.89	26.57	20.71	24.48	-	-
Initial K_w (m^2)	1.7×10^{-14}	2.88×10^{-14}	1.44×10^{-14}	1.18×10^{-14}	8.31	2.48×10^{-20}
Initial aperture (calculated with initial K_w) (µm)	18.11	21.58	17.14	16.02	14.26	-
Final K_w (m^2)	2.7×10^{-17}	7.44×10^{-20}	4.67×10^{-20}	3.72×10^{-20}	1.24×10^{-20}	1.24×10^{-20}
Final aperture (calculated with final K_w) (µm)	2.11	0.296	0.253	0.235	0.163	-

4.3.3.2 Use of Poiseuille law

Poiseuille Law was used in order to obtain what can be called the "crack equivalent aperture (*e*)". To this purpose, the crack is simply modeled as two parallel planes and *e* is the distance between both (Figure 4.11). It is obviously far from reality (Chen et al., 2021), but remains a useful assumption to compare samples and to follow crack aperture evolution.

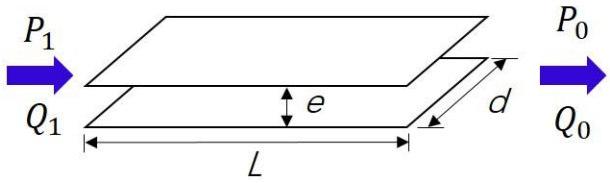

Figure 4.11. Simplified cracks consists of two parallel planes with a distance of *e*

Poiseuille Law leads to the fracture calculation of the fluid flow rate Q_1 and Q_0. For an imcompressible liquid in steady flow rate:

$$Q = Q_1 = Q_0 = \frac{d \cdot e^3}{12\mu L}(P_1 - P_0) \tag{4.5}$$

And for a compressible perfect gas:

$$Q_0 = \frac{P_1}{P_0} Q_1 = \frac{d \cdot e^3}{12\mu L} \cdot \frac{(P_1^2 - P_0^2)}{2P_0} \tag{4.6}$$

With rel. (4.3) and rel. (4.4) and when the material matrix permeability is low (compared to the crack "permeability"), it comes for both gas and liquid:

$$KA = \frac{d \cdot e^3}{12} \tag{4.7}$$

or:

$$e = \sqrt[3]{3K\pi d} \tag{4.8}$$

4.3.3.3 Water permeability

Gas permeability was a unique measure used to quantify the equivalent initial gas aperture. Water permeability was in fact used and recorded in parallel with P_{app} to identify the end of the swelling process. The latter is assumed as soon as both K_w and P_{app} are stable. Evolution of K_w can be found in Figure 4.12 and compared with Figure 4.8. On a global point of view, there was a strong and rapid swelling for UA-C type samples, and this is consistent with a sharp drop in permeability. After around 5 days, both phenomena stabilized slowly until 20 - 25 days. This observed parallelism is logical as swelling leads to crack closure. At the end of the process, water permeability of UA-C samples has decreased by 5 - 6 orders of magnitude. It is still slightly higher than initial values reported for intact sample but all in the range [10^{-19} m^2, 10^{-20} m^2]. This evidences the swelling efficiency on self-sealing. The UT-C sample exhibited a low swelling pressure (1 MPa) and it final water permeability stabilized at 10^{-18} m^2. This value is one order of magnitude higher than the one measured on intact UT sample. For this sample it can be concluded that the self-sealing is incomplete.

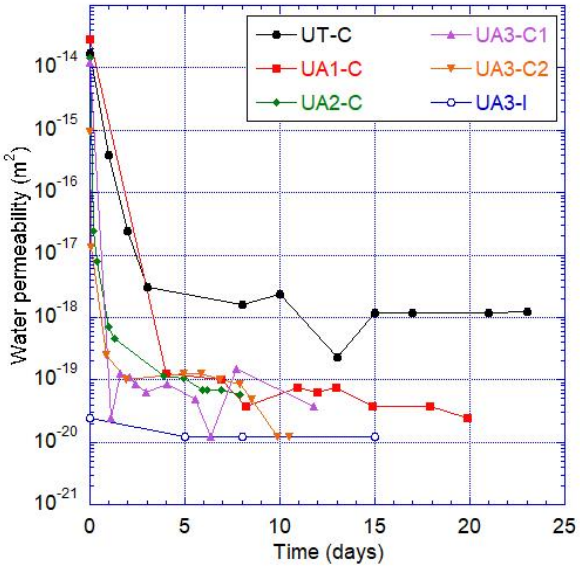

Figure 4.12. Variation of water permeability with time

Initial values of water permeability (at the beginning of water injection) are given in Table 4.4. They are all almost one order of magnitude less than the initial gas permeability. As a result, the initial crack aperture derived from K_w is smaller than what was calculated with K_g. Contrary to gas, water is chemically active with clay (also the case with concrete) and K_w smaller than K_g is usual with COx claystone. On the other hand, swelling is likely to occur very quickly therefore having an immediate impact on permeability. As aforementioned, the final values at the end of the swelling reveal an efficient self-sealing of the UA samples as they are now close to the intact material permeability.

4.3.4. Gas breakthrough pressure (GBP)

4.3.4.1 Laboratory results

When P_{app} and K_w were both stabilized, it was considered that the sample had reached full saturation and the gas breakthrough test was immediately performed. The GBP value of each test is shown in Table 4.5. After sealing, the GBP results for the saturated COx demonstrate distinctive features. The first one is that for macro-cracked samples, a significant difference in GBP values between UA and UT is observed. The GBP of UT COx is around 0 - 0.2 MPa, while the value of UA COx range from 0.8 to 1.46 MPa. This confirms that UA COx possesses a better sealing efficiency than UT COx claystone, which is consistent with the observation of the initial K_w and equivalent crack aperture. The other investigation is that by comparing UA3-C1, UA3-C1 and UA3-I, it is found that the GBP of intact sample is 4 - 6 times higher than those of sealed macro-cracked samples. This demonstrates for the UA COx that even if the induced self-sealing brings the sample back to a very low K_w (close to the intact one), the gas transfer properties do not meet those in the undisturbed state. As a result, coupled with P_{app} and K_w, GBP reveals to be a strong complementary tool to evaluate the sealing efficiency.

Table 4.6. Summary of equivalent capillary and gas breakthrough pressure

Sample label	sealed equivalent aperture (μm)	Equivalent capillary pressure (MPa)	GBP (MPa)
UT-C	2.11	0.06	0-0.2
UA1-C	0.296	0.49	0.8-0.89
UA2-C	0.253	0.58	1.3-1.46
UA3-C1	0.235	0.62	1.00-1.23
UA3-C2	0.163	0.893	1.0-1.2
UA3-I	-	-	6.2-6.4

4.3.4.2 Equivalent capillary pressure

The displacement of a gas phase in a saturated porous media is a complex process. Four gas migration mechanisms have been proposed by (Marschall et al., 2005), including diffusion, visco-capillary flow, pore dilatancy flow, and gas fracturing. A series of experiments carried out in our laboratory (such as M'Jahad et al., 2017) had led us to think that capillary phenomena (i.e. a part of the porous network is emptied from its saturating water by gas pressure) are preponderant for saturated COx claystone. Based on previous studies, it is reasonable to assume that the gas migration mechanism in the resealed macro-cracked COx would be capillary gas transport through the sealed crack. In order to evaluate whether this assumption is plausible, calculation of the equivalent crack aperture e_{gw} were performed with the final K_w (Figure 4.13 and Table 4.5). One can find that e_{gw} (both UA and UT COx) decreased from tens of microns to below one micron after sealing. Thus it can be supposed that, during a GBP experiment, gas would use the easier path to cross the sample, i.e. the sealed crack. Assuming again that this crack is composed of two parallel planes with a width equal to e_{gw}, Laplace Law is used to calculate the capillary pressure P_{cap}:

$$P_{cap} = \frac{2\gamma_{gw}}{e_{gw}} \cdot \cos\alpha \qquad (4.9)$$

Where γ_{gw} is the gas-water interfacial tension, 72.9×10^{-3} N/m at 20 °C; α is the gas/water contact angle, here it is taken at 0. P_{cap} is assumed to be the necessary gas pressure to push water away from the crack. It can then be compared with GBP (Table 4.5). Even if lower than the real measured value, it can be underlined that P_{cap} remains in the same order of magnitude than GBP. Given the simplicity (two parallel planes) of the crack geometry and the fact that the whole sample water permeability is due to water flow in the crack, these results can be regarded as quite convincing. On the other hand, they confirm the hypothesis of GBP due to capillary phenomena. The GBP value of intact sample UA3-I was also measured, which was between 6.2 and 6.4 MPa. A rough calculation with GBP value equal to P_{cap}, compared with Laplace's Law leads to a mean pore radius of the intact sample around 0.023 μm (23 nm). This result is consistent with what can be found in the literature (Song et al., 2015; 2016).

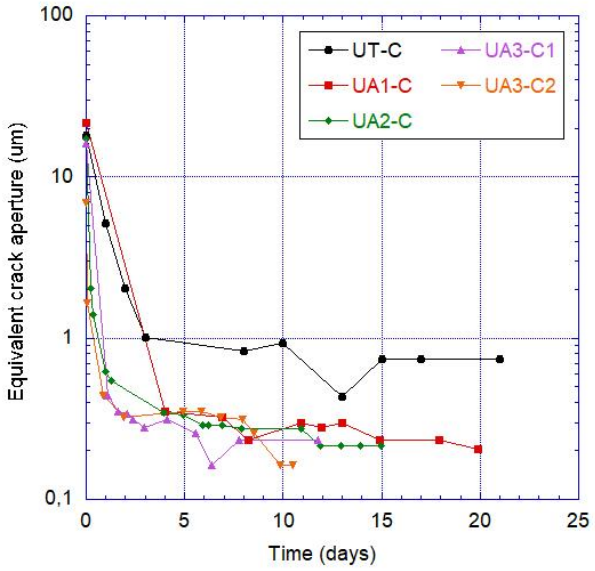

Figure 4.13. Equivalent single crack aperture evolution of all tested samples

4.4. Transition experiment: a preliminary free self-sealing test

4.4.1. Using silicone to replace epoxy

The aforementioned experiment provide a novel method for simultaneously measuring K_w and P_{app} of COx claystone. However, due to the epoxy stiffness, P_{app} is measured under "moderate confinement". This means that such test can only partially reduce the effect of confining pressure. As it can be seen in the different results the sample swelling induces an apparent swelling pressure in the device close to 5MPa. This is therefore a lateral pressure that participates to the permeability reduction and in some way gives optimistic results as regards this reduction. In order to solely study the contribution of clay mineral swelling to the self-sealing of COx claystone, a preliminary free self-sealing test was designed and carried out. This experiment was upgraded particularly by filling liquid silicone into the space between tube and sample. Thanks to the impermeability and high deformability of silicone, the volumetric swelling of the sample during re-saturation can be seen as in the absence of confinement (Figure 4.14). The material used in this experiment originated from core EST62665, with an initial saturation (after sampling) of 53%. The sample is 40 mm in length and 37 mm in diameter and pre-cracked by Brazilian Splitting test. The experiment procedures are similar to section 4.2 and the obtained data are the same as the former tests.

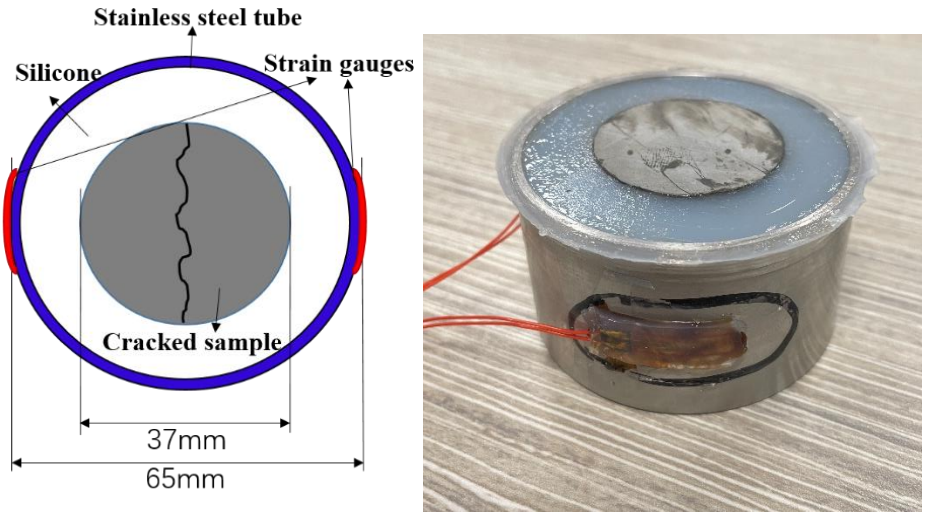

Figure 4.14: cross-sectional view of the special designed assemblage of "tube+silicone+sample"

4.4.2. Results observed

The initial gas permeability (K_{inigas}) is measured with argon gas under steady flow rate. The traditional "downstream method" was used to measure K_{inigas}. The upstream gas pressure is set to a very low value (i.e. 0.05 MPa) to avoid gas leakage between the silicone-COx sample interface. The measured K_{inigas} of the partially saturated sample (S_w=53%) is 1.51×10^{-18} m^2, which is in the same order of the non-damaged dried material (M'jahad et al., 2017). This means that the initial crack aperture is quite low (even not physically measured).

Based on the relationship between $P_{internal}$ & strain, the direct measurement strains data are constantly converted into P_{app}. P_{app} is followed until its stabilization. Figure 4.15 shows the P_{app} change with time. It can be found that the measured P_{app} of the two gauges are very close to each other and both values were stabilized at between 0.3 and 0.4 MPa. Considering the poro-mechanical coupling effect (P_i=0.1 MPa), the absolute swelling pressure is therefore smaller than P_{app}. This indicates that the use of silicone (instead of epoxy) resin is satisfactory, because of its weak stiffness, as the lateral pressure on the sample is considerably reduced (by one order of magnitude). This is also obvious that the swelling pressure is not an intrinsic property but strongly depends on external conditions (oedometric ones for example) – but this fact is very well known! On the other hand, this kind of experiment is likely to be more objective to analyze the self-sealing efficiency as it is almost not "polluted" by additional lateral (or confining) stress.

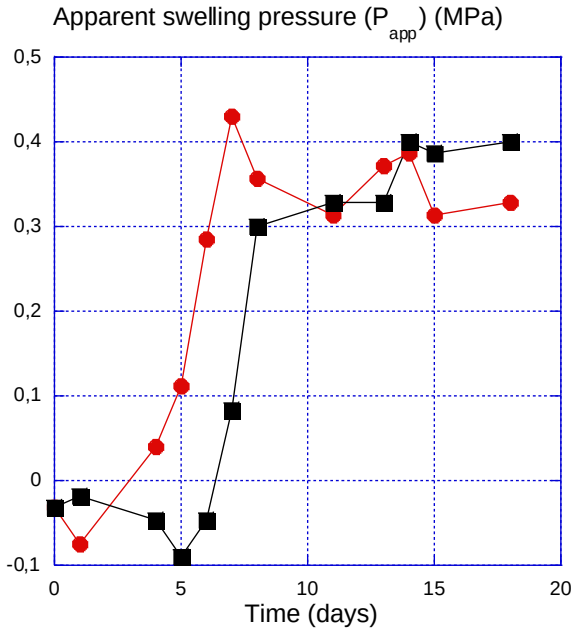

Figure 4.15. Evolution of apparent swelling pressure (P_{app})

By injecting water into the sample, water permeability was measured every one to two days, until the end of swelling i.e. stabilized permeability value. The drainage valve remained open during each permeability evaluation and was closed again as soon as the measurement was completed. Figure 4.16 exhibits the decrease of K_w with time. The injected water pressure is 0.1 MPa. One unexpected result is that the initial value of K_w is around four times higher than the K_{inigas} value. This can be interpreted that the initial K_w , which is deduced from water volume injected in the sample, is affected not only by the water flow through the sample but also by the water adsorption of material (with a low initial saturation). The stabilized K_w is in the order of 10^{-19} m^2 (precisely of 2.48×10^{-19} m^2), which is more than 10 times less than the initial value, can be regarded as the effective permeability after swelling. This result puts in light that a significant sealing process is still observed in the (quasi) absence of confining pressure. This indicates that the swelling of clay minerals can lead the cracked material to partially recover its water permeability under very low lateral pressure due to swelling. On the other hand, the permeability reduction does not allow the material to meet the values measured with the epoxy device (and are far from the reported intact values generally less than $10^{-20}m^2$). In other words, this test seems very promising as it could be used to evaluate, with a better objectivity, the self-sealing efficiency for sample with different crack (initial) opening or to quantify the confining pressure effect. Another important use should be to compare more accurately, between samples, the effect of their mineralogy.

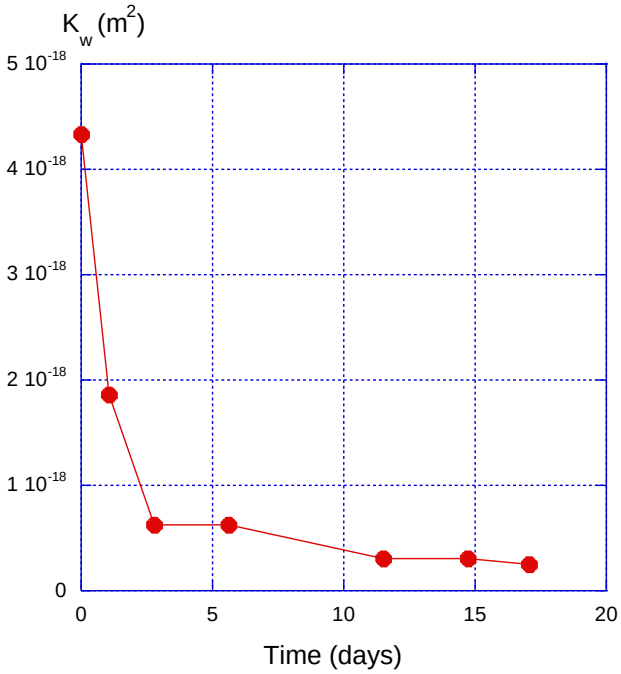

Figure 4.16. Evolution of water permeability (K_w)

After P_{app} and K_w were stabilized, gas breakthrough pressure (GBP) was measured on the saturated resealed sample. The drainage valve is initially closed. During the GBP test, argon is injected from the upstream side of the saturated sample, with a 0.02 MPa increment every 10 h. Detection is performed by placing an argon detector (accurate to ± 0.1 µl/s) close to the drainage valve. This valve is opened and the detector gives an indication of whether argon is present at the downstream side. GBP is defined as the upstream gas pressure when a continuous gas flow is detected at downstream. Because the upstream gas pressure increases very slow, thus to get the GBP is time-consuming. Based on the conclusion in section 4.3.4, GBP should be in the same order as the equivalent capillary pressure deduce from the stabilized K_w. According to the data in Figure 4.16 and relations (4.8) and (4.9), the value of GBP should be around 0.3 MPa. In fact, the measurement of GBP is quite delicate, because a relatively high pressure may lead to gas going through the silicone-COx sample interface. According to our experimental data, the gas breakthrough still does not occur when the injected gas pressure is equal to 2.2 bar. At this stage, this test is not achieved…

4.5. Chapter summary

This contribution investigates the self-sealing behavior of macro-cracked COx claystone, by using quantitative X-ray diffraction (QXRD), nitrogen adsorption measurements, and a series of originally designed swelling & sealing experiments. Both UT and UA COx claystone are used for QXRD and nitrogen adsorption tests: QXRD results give us a comprehensive understanding of the bulk mineral and subdivided clay mineralogical composition of different cores; nitrogen adsorption isotherms data

imply the information of pore volume ($V_{Gurvich}$) and specific surface area (SSA) of samples with different mineralogy composition. By using a specially designed experimental system, the swelling & sealing experiments of macro-cracked and intact samples are carried out in the absence of external confining pressure. Through this experiment, the change of apparent swelling pressure and permeability during re-saturation and the gas breakthrough pressure (GBP) after sealing have been measured. These direct measurement data would provide important references for numerical reproduction. Combining all the results from different experiments, several interesting results can be concluded as follow:

(1) During re-saturation, the apparent swelling pressure (P_{app}) of both macro-cracked and intact samples are all increased with time. By comparing macro-cracked samples from different geological positions, the P_{app} of UT COx is approximately 1 MPa, while it varies from 3 to 5 MPa for UA COx. By comparing samples from the same core, macro-cracked samples exhibit faster kinetics than the intact sample, while intact sample exhibits a slightly higher P_{app} than macro-cracked samples. Such difference is mainly attributed to the presence of cracks that increases the water-clay minerals contact area and generates more space for swelling.

(2) Relating P_{app} to specific clay mineral content, the smectite (swelling mineral) content does not seem to be the main influential factor, while the content of R1-I/S exhibits good linearity with P_{app}. Nitrogen adsorption data demonstrate that both $V_{Gurvich}$ and SSA are well linearly related to P_{app} and R1-I/S content, which implies that the effective water-mineral contact space and specific surface area are the key factors for COx swelling, and not simply the content of smectite fraction. That is to say, estimating the swelling capacity of COx by CEC values will lead to inaccurate results. From a viewpoint of testing technology, the $V_{Gurvich}$ and SSA that derived from nitrogen adsorption data have been proven to be simple and effective parameters for assessing COx swelling capacity. This should be verified and completed with other experiments.

(3) For both UT and UA COx, the presence of macro cracks results in a significant increment of permeability, up to 2 - 4 orders of magnitude for K_g and 5-6 orders of magnitude for Kw. Self-sealing of macro-cracked COx can cause significant reductions in water permeability (K_w) synchronously with the increase in P_{app}. The final water permeability of UA samples is reduced by five orders of magnitude and closed to that of the intact sample, while the final K_w of UT sample is reduced by four orders of magnitude and stabilized at around two orders of magnitude higher than the one for intact sample. Such results demonstrate that even in the absence of confinement, the clay mineral swelling can still lead to the macro-cracked COx claystone reseal to some degree. Besides, UA COx shows faster kinetics compared to UT COx, which can be attributed to the impact of R1-I/S content.

(4) After sealing, the results of gas breakthrough tests illustrate that the GBP of UT COx is around 0-0.2 MPa, while the value of UA COx range from 0.8 to 1.46 MPa. This confirms that UA COx possesses a better sealing efficiency than UT COx even for gas transport, which is consistent with the observation of K_w decrease. Compared with P_{app} and K_w, GBP is more sensitive to the sample integrity. Using Poiseuille Law, the GBP value of the sealed sample is in the same order of magnitude as the equivalent capillary pressure of residual cracks, which indicates that the gas migration in the sealed COx claystone would mainly occur through the residual sealed-crack and is controlled by capillary phenomena.

(5) A complementary test, with soft silicone instead of epoxy has brought first and interesting results on the sole effect of sample swelling (almost without any lateral stress). This led to strong reduction in water permeability that is nevertheless far from the intact material value. This promising test seems to be a convenient one to evaluate independently the swelling effect and the confining effect (toward the permeability reduction).

Note: This chapter had been written with a purpose of publication and accepted in 'Rocks Mechanics and Rock Engineering'

References

Al-Ani, Sarapää (2008) CLAY AND CLAY MINERALOGY. Geological survey of Finland

Amann-Hildebrand A, Dietrichs JP, Krooss BM (2016) Effective gas permeability of Tight Gas Sandstones as a function of capillary pressure – a non-steady-state approach. Geofluids 16:367–383

Anderson RL, Ratcliffe I, Greenwell HC, et al (2010) Clay swelling — A challenge in the oilfield. Earth-Science Reviews 98:201–216

ANDRA (2005) Dossier 2005 Argile. ANDRA, Collection les Rapports

Bernier F, Li XL, Bastiaens W, et al (2007) Fractures and Self-sealing within the Excavation DIsturbed Zone in Clays (SELFRAC). EIG Euridice GIE-BE

Cariou S, Duan Z, Davy CA, et al (2012) Poromechanics of partially saturated COx argillite. Applied Clay Science 56:36–47

Chen GJ, Maes T, Vandervoort F, et al (2014) Thermal Impact on Damaged Boom Clay and Opalinus Clay: Permeameter and Isostatic Tests with µCT Scanning. Rock Mech Rock Eng 47:87–99

Chen W, Han Y, Agostini F, et al (2021) Permeability of a Macro-Cracked Concrete Effect of Confining Pressure and Modelling. Materials 14:862. https://doi.org/10.3390/ma14040862

Conil N, Talandier J, Djizanne H, et al (2018) How rock samples can be representative of in situ condition: A case study of Callovo-Oxfordian claystones. Journal of Rock Mechanics and Geotechnical Engineering 10:613–623

Davy CA, Skoczylas F, Barnichon JD, Lebon P (2007) Permeability of macro-cracked argillite under confinement: Gas and water testing. Physics and Chemistry of the Earth, Parts A/B/C 32:667–680

de La Vaissière R, Armand G, Talandier J (2015) Gas and water flow in an excavation-induced fracture network around an underground drift: A case study for a radioactive waste repository in clay rock. Journal of Hydrology 521:141–156

Delvaux B (1992) Morphology, Texture, and Microstructure of Halloysitic Soil Clays as Related to Weathering and Exchangeable Cation. Clays and Clay Minerals 40:446–456. https://doi.org/10.1346/CCMN.1992.0400409

Duan Z, Skoczylas F, Wang C, Talandier J (2021) Hydric Cycle Impacts on COx Argillite Permeability and Young's Modulus. Rock Mech Rock Eng 54:1129–1147. https://doi.org/10.1007/s00603-020-02258-1

Giot R, Auvray C, Talandier J (2019) Self-sealing of claystone under X-ray nanotomography. Geological Society, London, Special Publications 482:213–223

Horseman ST, Harrington JF, Sellin P (1999) Gas migration in clay barriers. Engineering Geology 54:139–149

Lahn L, Bertier P, Seemann T, Stanjek H (2020) Distribution of sorbed water in the pore network of mudstones assessed from physisorption measurements. Microporous and Mesoporous Materials 295:109902

Liu J-F, Davy CA, Talandier J, Skoczylas F (2014) Effect of gas pressure on the sealing efficiency of compacted bentonite–sand plugs. Journal of Contaminant Hydrology 170:10–27

Marschall P, Horseman S, Gimmi T (2005) Characterisation of Gas Transport Properties of the Opalinus Clay, a Potential Host Rock Formation for Radioactive Waste Disposal. Oil & Gas Science and Technology - Rev IFP 60:121–139

Meier LP, Kahr G (1999) Determination of the Cation Exchange Capacity (CEC) of Clay Minerals Using the Complexes of Copper(II) Ion with Triethylenetetramine and Tetraethylenepentamine. Clays and Clay Minerals 47:386–388

Menaceur H, Delage P, Tang AM, Talandier J (2016) The Status of Water in Swelling Shales: An Insight from the Water Retention Properties of the Callovo-Oxfordian Claystone. Rock Mech Rock Eng 49:4571–4586

Mitchell JK, Soga K (2005) Fundamentals of Soil Behavior, 3rd Edition. John Wiley & Sons, Ltd, New Jersey

M'Jahad S, Davy CA, Skoczylas F, Talandier J (2017) Characterization of transport and water retention properties of damaged Callovo-Oxfordian claystone. Geological Society, London, Special Publications 443:159–177

Ongari D, Boyd PG, Barthel S, et al (2017) Accurate Characterization of the Pore Volume in Microporous Crystalline Materials. Langmuir 33:14529–14538

Rouquerol J, Llewellyn P, Rouquerol F (2007) Is the bet equation applicable to microporous adsorbents? In: Studies in Surface Science and Catalysis. Elsevier, pp 49–56

Saiyouri N, Hicher P-Y, Tessier D (2000) Microstructural Approach and Transfer Water Modelling in Highly compacted Unsaturated Swelling Clays. Mechanics of Cohesive-frictional Materials 5:41–60

Saiyouri N, Tessier D, Hicher P-Y (2004) Experimental study of swelling in unsaturated compacted clays. Clay Minerals 39:469–479

Seemann T, Bertier P, Krooss BM, Stanjek H (2017) Water vapour sorption on mudrocks. Geological Society, London, Special Publications 454:201–233

Song Y, Davy CA, Bertier P, et al (2017) On the porosity of COx claystone by gas injection. Microporous and Mesoporous Materials 239:272–286

Song Y, Davy CA, Bertier P, Troadec D (2016) Understanding fluid transport through claystones from their 3D nanoscopic pore network. Microporous and Mesoporous Materials 228:64–85

Song Y, Davy CA, Troadec D, et al (2015) Multi-scale pore structure of COx claystone: Towards the prediction of fluid transport. Marine and Petroleum Geology 65:63–82

Thommes M, Cychosz KatieA (2014) Physical adsorption characterization of nanoporous materials: progress and challenges. Adsorption 20:233–250

Van Geet M, Bastiaens W, Ortiz L (2008) Self-sealing capacity of argillaceous rocks: Review of laboratory results obtained from the SELFRAC project. Physics and Chemistry of the Earth, Parts A/B/C 33:S396–S406

Zhang C-L (2011) Experimental evidence for self-sealing of fractures in claystone. Physics and Chemistry of the Earth, Parts A/B/C 36:1972–1980

Zhang C-L, Rothfuchs T (2004) Experimental study of the hydro-mechanical behaviour of the Callovo-Oxfordian argillite. Applied Clay Science 26:325–336

Zhang C-L, Rothfuchs T (2008) Damage and sealing of clay rocks detected by measurements of gas permeability. Physics and Chemistry of the Earth, Parts A/B/C 33:S363–S373

Zhang F, Cui YJ, Conil N, Talandier J (2020) Assessment of Swelling Pressure Determination Methods with Intact Callovo-Oxfordian Claystone. 1879–1888

Zhang Y, Lebedev M, Sarmadivaleh M, et al (2016) Swelling effect on coal micro structure and associated permeability reduction. Fuel 182:568–576

Zhou X, Liu D, Bu H, et al (2018) XRD-based quantitative analysis of clay minerals using reference intensity ratios, mineral intensity factors, Rietveld, and full pattern summation methods: A critical review. Solid Earth Sciences 3:16–29

5. Conclusions and perspectives

This thesis focuses on experimentally investigating the self-sealing effect of Callovo-Oxfordian (COx) claystone, which is considered to be the host rock for long-lived and high-level radioactive waste storage in France. Six COx claystone cores originated from various depths (from the Meuse/Haute Marne Underground Research Laboratory) were tested with different experiments, including quantitative X-ray diffraction (XRD), cation exchange capacity analysis (CEC), nitrogen adsorption test, swelling & poro-mechanical test, and self-sealing test. This research was carried out from three different perspectives, namely multi-scale swelling mechanisms, poro-mechanical properties measurement with water, and the swelling and transport properties evaluation of the sealed material.

Multi-scale swelling mechanisms

This multi-scale swelling mechanisms of COx claystone was carried out by a series of swelling tests, supplemented by quantitative XRD, cation exchange capacity (CEC) and nitrogen adsorption. The tested material comes from five different geological locations, provided by Andra. XRD, CEC, and nitrogen sorption analysis were performed on powder samples, while the swelling tests were conducted on cylindrical samples. Cylindrical samples were re-cored from different T1-cores and pre-equilibrated at 75% RH to eliminate the effect of saturation. The effects of clay minerals contents and damage states (i.e. cracking) on swelling behavior (amplitude and kinetics) were investigated. During the swelling test, the sample was first placed in a triaxial cell at a constant confining pressure of 14 MPa. When the sample mass was stabilized, synthetic water was injected from both sample ends at a constant pressure of 5 MPa. The obtained experimental data is the evolution of sample expansion strain with time. The swelling amplitude and the swelling kinetics are evaluated by comparing between samples.

Mineralogical composition analysis illustrate that smectite is the only swelling mineral in COx, interspersing in two types of I/S aggregates in COx, namely R1-I/S (contains 30% smectite) and R0-I/S (contains 78% smectite). Nitrogen sorption data reveal that the swelling of COx is not only determined by the smectite content but also corresponds to the water-accessible pore volume and surface area. This conclusion is valid from nano-scale to μm-scale.

Anisotropic strains were measured during the swelling test. In particular, swelling strain parallel to bedding planes ($\varepsilon_{\parallel}^{S}$) is used to be related to smectite-related minerals. From the viewpoint of the swelling amplitude, the result reveals that $\varepsilon_{\parallel}^{S}$ has the highest correlation with R1-I/S, while has the

lowest correlation with R0-I/S. This illustrates that the effect of smectite distribution on the material swelling is still valid on the centimetric scale. Therefore, a conceptual model is proposed to give insights into the multi-scale swelling mechanism of this material. As for the swelling kinetics, there is no correlation was found between expansion time and mineral composition or pore properties, indicating that the kinetics corresponds to a more complex coupling process.

In addition, the effect of micro-cracks on swelling was studied by comparing the swelling of intact and micro-cracked samples. Results implied that micro-cracking causes the material to exhibit a greater swelling amplitude and higher initial swelling kinetics. And the compress-induced micro-cracks are more likely to be parallel to the bedding planes, leading to a more pronounced expansion in this direction.

Poro-mechanical properties measurement with water

When the above-mentioned swelling test is completed, the sample is fully saturated. A following poro-mechanical test was performed on the saturated material. The main objective of this work was to measure the Biot's coefficient using synthetic water (close to *in-situ* water) to control the pore pressure. Within the framework of poroelasticity, the Biot's coefficient is determined by strains measured during sequentially loading and unloading confining pressure (P_c) and pore pressure (P_i). This kind of test is very time-consuming due to the long saturation times to obtain pressure uniformity. Several tests were successfully performed for the past two years among which four representative ones are presented in this study.

Results clearly demonstrated that, despite a significant material anisotropy, the Biot's tensor is isotropic with a unique component "*b*". This important result, consistent with some theoretical calculations, does not mean that the strains, due to pore pressure change, are isotropic. An other important result is that "*b*" was found very close to 1. This means that, under the laboratory conditions, the COx claystone behaves as a Terzaghi material. This crucial result was obtained on water saturated claystone samples, which exhibited some kind of de-structuration after the tests. It is nevertheless consistent with numerous observations made with gas (helium) as being the fluid to control pore pressure, which more often led to quasi isotropic Biot's tensor with "*b*" in the range [0.9, 1]. In this case, gas experiments were performed on partially saturated materials (from dry to almost saturated) so without the de-structuration observed with water. All these important results can now be used in numerical simulations with a high level of confidence as they are also consistent with other recent published works.

Swelling and transport properties evaluation of the sealed COx

A series of "low confinement" self-sealing tests was designed and carried out to investigate the swelling and transport properties of the reseal COx claystone. Through this experiment, the change of apparent swelling pressure (P_{app}) and water permeability during re-saturation and the gas breakthrough pressure (GBP) after sealing have been measured. These direct measurement data would provide important references for numerical reproduction.

Results demonstrate that P_{app} increased with time and the *value* of the UT sample is approximately 1 MPa, while it varies from 3 to 5 MPa for UA ones. By comparing samples from the same core, macro-cracked samples exhibit faster kinetics than the intact one, while intact sample exhibits a slightly higher P_{app} than macro-cracked samples. Such difference is mainly attributed to the presence of cracks that increases the water-clay minerals contact area and generates more space for swelling. P_{app} also exhibits better linearity with R1-I/S than with R0-I/S. Such a result is consistent with the observation in swelling strain vs. smectite-related minerals (chapter 2). From a viewpoint of testing technology, nitrogen sorption is a simpler and more effective approach for assessing COx swelling capacity than XRD.

For both UT and UA material, the presence of macro cracks results in a significant increment of permeability, up to 2 - 4 orders of magnitude for K_g and 5-6 orders of magnitude for *Kw*. Self-sealing of macro-cracked COx can cause significant reductions in water permeability (K_w) synchronously with the increase in P_{app}. The final water permeability of UA samples is reduced by five orders of magnitude and closed to that of the intact sample, while the is reduced by four orders of magnitude. It worth underlining that the final K_w of UT sample is at around two orders of magnitude higher than the one for intact sample. Such results demonstrate that even in the absence of confinement, the clay mineral swelling can still lead to the macro-cracked COx claystone reseal to some degree. Besides, UA COx shows faster kinetics compared to UT COx, which can be attributed to the impact of high R1-I/S content.

After sealing, the results of gas breakthrough tests illustrate that the GBP of UT COx is around 0-0.2 MPa, while the value of UA COx range from 0.8 to 1.46 MPa. This confirms that UA COx possesses a better sealing efficiency than UT COx even for gas transport, which is consistent with the observation of K_w decrease. Compared with P_{app} and K_w, GBP is more sensitive to the sample integrity. Using Poiseuille Law, the GBP value of the sealed sample is in the same order of magnitude as the equivalent capillary pressure of residual cracks, which indicates that the gas migration in the sealed COx claystone would mainly occur through the residual sealed-crack and is controlled by capillary phenomena.

Perspectives

Our originally designed “self-sealing” experiment provides a solution for analyzing the swelling and the sealing effect of COx under certain pore fluid pressure. Experiments under “low confinement” indicate that the apparent swelling pressure increases simultaneously with the water permeability decrease. This gives us a preliminary concept that even under low confining pressure, the clay swelling (i.e. interstratified illite/smectite) has a certain effect on the sealing efficiency of damaged COx. In perspective, it would be very interesting to study the sealing efficiency of COx with (almost) complete elimination of the confining pressure. This could be performed with the device (with silicone) leading to the ‘free’ self-sealing test detailed in section 4.4. This is very useful for the better understanding of the sole contribution of clay swelling on sealing efficiency. Such a device would allow to make a clear distinction between the ‘intrinsic’ self-sealing effect due to the sole re-saturation and its amplification due to confining (or lateral) pressure – for example is there a critical initial crack aperture from which no intrinsic sealing is observed?

In addition, during the desaturation, pore water cations will be accumulated and remained in the clay particles, while only water molecules are evaporated from the material. Therefore, understanding the influence of pore water cations on clay swelling and material sealing during resaturation, is crucial. This will be an important portion of the continuation work of this thesis.

Cicatrisation et colmatage de l'argilite de Bure

Dans le cadre du stockage géologique des déchets nucléaires radioactifs en France, l'argilite du bassin de Bure (formation du Callovo-Oxfordien (COx)) est considérée comme la roche hôte. Ce matériau présente une importante capacité d'auto-étanchéité lors de la resaturation. Cependant, la contribution du gonflement des minéraux argileux à la cicatrisation n'est pas encore complètement comprise. Dans cette thèse, six carottes d'argilite COx ont été étudiées. La relation entre les minéral compositions et les propriétés des pores a été analysée par la diffraction quantitative des rayons (XRD), la capacité d'échange de cations (CEC) et la mesure de la sorption d'azote. Les résultats ont démontré que la distribution et la localisation de smectite affectent la structure des pores à l'échelle μm et nanométrique, ce qui est fortement associé à la capacité de gonflement du matériau. Les tests de gonflement sur les échantillons centimétriques ont mesuré directement les contraintes de gonflement pendant la resaturation, ce qui prouve que l'expansion d'arigilite à l'échelle macrotrique est affectée par l'effet combiné des mécanismes de gonflement à multi-échelles. Des études poromécaniques ont été réalisées sur les échantillons saturés. Malgré le matériau est fortement isotrope transversalement, le coefficient de Biot est isotrope et presque 1. En utilisant une cellule triaxiale modifiée, la cicatrisation des argilites endommagées a été étudié dans des conditions de "faible confinement". Les résultats ont indiqué que le gonflement des minéraux argileux entraîne une diminution significative de la perméabilité à l'eau. Après la cicatrisation, la pression de percée du gaz (GBP) est du même ordre de grandeur que la pression capillaire équivalente des fissures résiduelles, ce qui indique que la migration du gaz dans les argilite scellé se produirait principalement à travers la fissure scellée résiduelle et serait contrôlée par les effets capillaires.

Mots clés : argilite COx, gonflement, poromécanique, cicatrisation

Self-sealing and clogging of Bure claystone

In the context of geological storage of radioactive nuclear waste in France, claystone at the Bure basin (formation du Callovo-Oxfordien (COx)) is regarded as the ideal host rock. This material exhibits significant self-sealing capacity during resaturation. However, the contribution of clay mineral swelling to the material sealing efficiency is still not completely understood. In this thesis, six COx claystone cores from different geological locations were studied. The relationship between mineralogical compositions and pore properties was analyzed by quantitative X-ray diffraction (XRD), cations exchanged capacity (CEC) and nitrogen sorption measurement. Results demonstrated that the distribution and location of smectite particles affect the pore structure at μm-scale and nano-scale, which is highly associated with the material swelling capacity. Swelling tests on the centimetric samples directly measured swelling strains during resaturation, giving evidence for the macro scale expansion of COx is affected by the combined effect of multi-scale swelling mechanisms. Poro-mechanical studies were carried out on the saturated samples. It is found that even if the material is strongly transversely isotropic, the Biot's coefficient is consistently isotropic and almost equal to 1. By using a modified triaxial cell, the self-sealing of damaged COx claystone was studied under "low-confinement" conditions. Experimental data indicated that clay mineral swelling results in a significant decrease in water permeability. After sealing, the gas breakthrough pressure (GBP) of the resealed material is in the same order of magnitude as the equivalent capillary pressure of residual cracks, indicating that the gas migration in the sealed COx would mainly occur through the residual sealed-crack and is controlled by capillary phenomena.

Keywords: COx claystone, swelling, poro-mechanics, self-sealing